A Model-Independent Approach to Reconstruct the Expansion History of the Universe with Type Ia Supernovae

Dissertation submitted to the
Technical University of Munich
by
Sandra Benítez Herrera

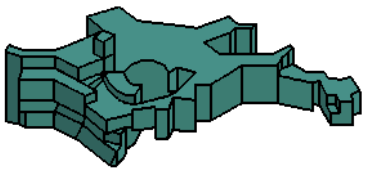

Max Planck Institute for Astrophysics

October 2013

TECHNISHCE UNIVERSITÄT MÜNCHEN

Max-Planck Institute für Astrophysik

A Model-Independent Approach to Reconstruct the Expansion History of the Universe with Type Ia Supernovae

Sandra Benítez Herrera

Vollständiger Abdruck der von der Fakultät für Physik der Technischen Universitt München zur Erlangung des akademischen Grades eines

Doktors der Naturwissenschaften (Dr. rer. nat.)

genehmigten Dissertation.

Vorsitzende(r): Univ.-Prof. Dr. Lothar Oberauer
Prüfer der Dissertation:

1. Hon.-Prof. Dr. Wolfgang Hillebrandt
2. Univ.-Prof. Dr. Shawn Bishop

Die Dissertation wurde am 23.10.2013 bei der Technischen Universität München eingereicht und durch die Fakultät für Physik am 21.11.2013 angenommen.

"Our imagination is stretched to the utmost, not, as in fiction, to imagine things which are not really there, but just to comprehend those things which are there."
Richard Feynman

"It is impossible to be a mathematician without being a poet in soul."
Sofia Kovalevskaya

Contents

1 Introduction **11**

2 From General Relativity to Cosmology **15**
2.1 The Robertson-Walker Metric 15
2.2 Einstein Gravitational Equations 17
2.3 The Cosmological Constant 19
2.4 The Expanding Universe 21
2.5 The Scale Factor and the Redshift 22
2.6 Distances in the Universe 23
2.6.1 Standard Candles and Standard Rulers 26
2.7 Cosmological Probes for Acceleration 27
2.7.1 Type Ia Supernovae as Cosmological Test 27
2.7.2 The Cosmic Microwave Background Radiation 28
2.7.3 Baryonic Acoustic Oscillations 32
2.8 The Concordance Model: ΛCDM 34
2.8.1 Dark Matter 34
2.8.2 Dark Energy 38
2.8.3 Cosmological Parameters: the Current Picture 41
2.9 Non-Standard Cosmologies: Modified Gravity 42
2.9.1 Brane Worlds 44
2.9.2 $f(R)$ Models 47
2.10 The Kinematic Approach 48

3 Supernovae: Candles In The Universe **51**
3.1 Supernovae Classification 51
3.2 Explosion Mechanisms 53
3.2.1 Thermonuclear Supernovae 54
3.3 Observational Characteristics 57
3.3.1 Light Curves and Spectra 58
3.3.2 Diversity and Correlations: The Phillips Relation 59
3.4 The Standardization Process of SNe Ia 63
3.4.1 The SALT Fitter 64
3.4.2 The MLCS Fitter 66
3.4.3 Comparison of MLCS and SALT2 Methods 67

3.5 Cosmology with SNe Ia: Basic Principles . . . 70
3.5.1 The Hubble Diagram . . . 71
3.5.2 The Expansion History and the Accelerating Universe . . 72
3.6 Current SN Ia Samples . . . 77
3.6.1 Observational Strategy . . . 77
3.6.2 State-of-the-Art SN Ia surveys . . . 79
3.6.3 The Union Compilation . . . 80
3.6.4 Systematic Uncertainties . . . 83
3.7 Space Versus Ground . . . 87
3.8 Future Samples and Surveys . . . 89

4 The Model-Independent Method 93
4.1 Motivation: Why Model Independent? . . . 93
4.2 Mathematical Formalism . . . 94
4.2.1 Background . . . 94
4.2.2 Model-Independent Determination of the Expansion Rate Function . . . 95
4.2.3 Illustration of the Method: Reconstructing ΛCDM . . . 98
4.3 Principal Component Analysis . . . 99
4.3.1 Building the Basis with Principal Component Analysis. . 101
4.4 Error Analysis . . . 104
4.5 Convergence of the Neumann Series . . . 106
4.6 Combining Different Data Sets and Families of Models . . . 107
4.7 Improving the Reconstruction . . . 107

5 Testing the Method with Simulated Data 111
5.1 Different Cosmological Scenarios . . . 111
5.1.1 ΛCDM Simulations . . . 111
5.1.2 Non-ΛCDM Simulations . . . 114
5.2 SNANA: A Tool To Simulate High Quality SN Data. . . . 120
5.2.1 Simulated Data in MLCS and SALT2. . . . 122

6 Extracting the Expansion Rate from Real Data 127
6.1 The Union2.1 Sample Revisited . . . 127
6.2 Constraining Cosmological Scenarios . . . 130
6.2.1 Dark Energy Models . . . 131
6.2.2 Beyond the wCDM Cosmology . . . 132
6.3 Alternative Cosmological Probes . . . 136
6.4 Other Interesting Applications . . . 138
6.4.1 Checking for Systematics in the Supernova Samples . . . 138
6.4.2 Testing Redshift Ranges for Supernova Campaign Planning . . . 141
6.5 Ongoing Work . . . 143

7 Conclusions and Perspectives **147**

8 Acknowledgments **153**

Bibliography **154**

1. Introduction

Humankind, given its own nature, has always tried to understand the Universe and its place in it. Since the beginning of history, cosmology has been the science through which women and men have tried to find answers to those fundamental questions by peering into the sky. Problems such as the motion of the planets, the nature of the space between stars, or the formation and evolution of galaxies, have been progressively understood thanks to the efforts of many generations of scientists.

For millennia, humans have often observed *new stars* appearing in the night sky. As early as in 1006, Arabic and Chinese astronomers recorded the observation of a bright newly-born star that shone in the sky for nearly two years and disappeared afterwards. Over the years scientists became aware that some of these events were remarkably more luminous. Moreover, estimated distances to these objects indicated that they had an extragalactic origin. Especially important were the observations of the (*super*)*nova* S Andromedae in the Andromeda galaxy in 1885. It was reckoned, that these bright events were different from any other object ever observed before. The origin and nature of those stars remained a mystery until the beginning of the 20th century. Considered as beacons in the Universe from which relative distances can be measured, Type Ia supernova explosions play a key role, not only in cosmology, but in other fields of astrophysics. Our understanding of these magnificent objects is fundamental to comprehend the Universe in which we live in.

Gravity and its effect on planetary orbits, has equally attracted a great deal of interest over history. From the theoretical, almost spiritual, beliefs of ancient Greek philosophers to the efforts of Galileo Galilei designing experiments with inclined planes, understanding the gravitational interactions which govern our planet and our Universe has been a priority for scientists. The first scientist who described gravity in quantitative terms, was Isaac Newton, who formulated the universal inverse-square law and provided extraordinary simple and accurate explanations of a wide range of terrestrial and celestial phenomena. Newton's laws were the accepted paradigm for gravity for the following two hundred years. In 1916, Albert Einstein presented his General Relativity, introducing revolutionary concepts that led to a new era in physics and cosmology. Einstein described the curvature of space-time to be responsible of the effects of gravity but believed that the expansion detected by Edwin Hubble in 1925 would slow down over time, according with the Newtonian ideas.

However, the past fifthteen years have brought mounting evidence that the expansion of the Universe is nowadays in an accelerated phase. Amongst the several observational probes that led to such conclusion, and the first to reveal such a striking finding, are Type Ia supernovae.

The currently adopted paradigm accounts for the acceleration but it requires the presence of an unknown component, dark energy, which is in fact the major constituent of our Universe. Present understanding of this component is uncomfortably close to nothing, which calls for a significant effort both at an observational and experimental front and on theoretical grounds. Because of the important implications of the acceleration, ambitious experimental efforts are being developed to measure the expansion history and growth of structure in the cosmos with percent-level precision or better.

A relatively large number of non-standard theories have been proposed to tackle the nature of dark energy. Indeed, cosmic acceleration is the most profound puzzle in contemporary physics and can lead to new ideas about the interaction between gravity and the quantum vacuum, the existence of extra spatial dimensions or the nature of quantum gravity.

A *model-independent* approach to directly interpret the data is arguably essential, if one would like to avoid introducing prejudices or biases from theoretical frameworks. The work in this thesis consists in implementing a recently developed methodology to derive the expansion history of the Universe in a model-independent fashion, using currently available Type Ia supernova data. Such reconstructions not only allow to recover the expansion history of the of the Universe, but also provide means to test cosmological models of the nature of dark energy. A number of tests on the improvement that future samples should provide or the effect of the different calibration methods are also presented. These studies shed light on the next necessary steps, from the observational side, to ensure progress.

This work is but a first step in the direction of providing tighter constraints on the expansion history of the Universe and some comprehension on the properties of dark energy. Model-independent methodologies are far from trivial, and a better understanding of their power and drawbacks is fundamental. The work presented here extends previous developments in this context. Future work will see to apply these methods to an increasing body of observational data, not only quantitatively, by including results from new observational campaigns, but also qualitatively, allowing for the introduction of data such as the Baryonic Acoustic Oscillations detected in the Cosmic Microwave Background.

This thesis is organised as follows. The Chapter 2 summarizes the main aspects of General Relativity and other alternative cosmological models needed to understand the tests and discussions presented here. The standard cosmological scenario, the ΛCDM model, and the main cosmological probes that led to the detection of the acceleration, are also reviewed here. Chapter 3 discusses our current theoretical understanding and observational evidence of Type Ia supernova physics, and, based on that, to what extent one can rely

on these objects to constrain cosmological models. Also, a description of the calibration process and the different data sets available in literature, with special interest on potential systematic errors, is included. In Chapter 4, the essential mathematical aspects of the model-independent methodology to obtain the reconstruction of the expansion history of the Universe is presented. The results from applying such methodology to mock data simulated in different calibration frameworks and theoretical backgrounds, are presented and discussed in Chapter 5. In Chapter 6, the reconstruction of the expansion rate extracted from real data and compared with the most recent cosmological results is reported. This chapter also includes tests on the gains from future surveys and additional checks for systematic uncertainties within current supernova samples. Moreover, a discussion on how well a number of current theoretical models are able to reproduce the observational results is provided. Finally, conclusions and future perspectives are presented.

2. From General Relativity to Cosmology

General Relativity is the most complete theory for gravity we have currently at hand. Published by Albert Einstein in 1916 (Einstein, 1916) after almost ten years of work to incorporate gravity into his new special theory of relativity, it unifies Special Relativity and Newton's law of universal gravitation, and describes gravity as a geometric property of space and time, or space-time. This theory is based on the so-called Principle of Equivalence which states that it is not possible to distinguish the effects of a gravity field from those of an accelerated movement, locally, in a given reference frame. Einstein's theory has important physical and astrophysical implications such as gravitational time dilation, deflection of light and gravitational lensing, gravitational waves, precession of apsides and orbital decay, gravitational redshift of light, and the existence of Black Holes (see e.g. Narlikar, 2002). These predictions have been confirmed, directly or indirectly, in all observations and experiments to date. Although General Relativity is not the only relativistic theory of gravity, it is the simplest theory that is consistent with experimental data. However, unanswered questions remain, the most fundamental being how general relativity can be reconciled with quantum physics to produce a complete and self-consistent theory of quantum gravity.

Cosmology focus on the evolution of the Universe at very large scales, where it is governed solely by gravity. In this context, General Relativity provides a great theoretical framework to which refer most of the physical processes.

In this Chapter, basic notions of what is known as the standard cosmological model will be reviewed. Also, alternatives to General Relativity are presented. For deeper insights into General Relativity and its observational tests we refer the reader to the text books of Narlikar (2002) and Carroll & Ostlie (1996).

2.1 The Robertson-Walker Metric

One of the most ingenious ideas in General Relativity is the interpretation of the ever-present nature of gravitation as an intrinsic feature of the Universe. Einstein identified this fundamental property as the geometry of the

space-time, suggesting that any effects we ascribe to gravitation actually arise because of distortions in geometry. We recall that the geometry of space can be extended to the geometry of space and time by Einstein's Special theory of relativity. Let us consider two events in space and time labelled by the coordinates (x, y, z, t) and $(x+dx, y+dy, z+dz, t+dt)$, where (x, y, z) denote spatial coordinates and t is the time measured by an observer O at rest in an inertial frame. The square of the *distance* between them is given by

$$ds^2 = c^2dt^2 - dx^2 - dy^2 - dz^2. \tag{2.1}$$

where c is the speed of light. The quantity ds is invariant under general coordinate transformation, i.e. another observer O' will measure the same distance in a different reference frame with (x', y', z', t'). When going from Special to General Relativity, an expression equivalent to Eq. 2.1 is employed for the invariant line element in a more general form

$$ds^2 = \sum_{\mu,\nu=0}^{3} g_{\mu\nu}dx^\mu dx^\nu, \tag{2.2}$$

where the coordinates are now called x^μ, with $\mu = 1, 2, 3$ representing the three spatial directions and $\mu = 0$ the time. The term $g_{\mu\nu}$ is the metric tensor of space-time, which is symmetric (only 10 of its 16 components are independent).

In order to specify the metric an important assumption is usually adopted: the Cosmological Principle, which states that on large spatial scales, at any given cosmic time, the Universe is, statistically, isotropic and homogeneous. This assumption implies that an observer viewing the Universe from any vantage point will find it looks the same in all directions. Moreover, he will realize it presents the same aspect from all vantage points. The Cosmological Principle is well justified by observations, in particular by the spatial distribution of galaxies, the spatial distribution of radio sources and the Cosmic Microwave Background (CMB) radiation.

Isotropy and homogeneity greatly simplify the mathematical specification of the metric, making non-zero only the time-time and space-space components (otherwise a preferred direction could be identified). Moreover, clock synchronisation arguments imply $g_{00} = c^2$, which is usually referred to as the cosmic time. The line element can then be written as

$$ds^2 = c^2dt^2 + \sum_{i,j=0}^{3} g_{ij}dx^i dx^j. \tag{2.3}$$

Einstein believed the space to be a closed surface and described by spherical coordinates. On top of it, he assumed space-time to be static. This allowed him to choose a time coordinate t such that the line element of space-time could be given by Eq. 2.3. In the Einstein Universe, the space sections are 3-surfaces of hyperspheres having constant positive curvature. The constancy

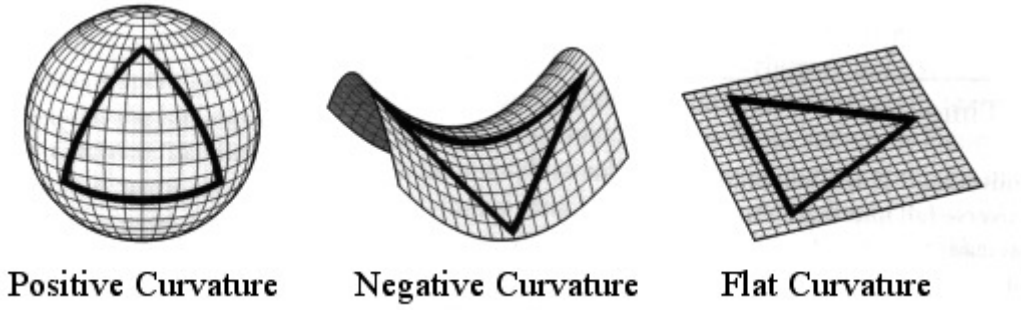

Figure 2.1: The three possible geometries of the Universe depending on the value of K: closed geometry corresponds to $K = +1$, flat geometry to $K = 0$ and open geometry to $K = -1$.

of curvature is essential in order to ensure the properties of homogeneity and isotropy. However, there are two other alternatives that keep homogeneity and isotropy: 3-surfaces of constant negative curvature or of zero curvature (see Fig. 2.1). In this context, we can again rewrite the line element in terms of polar coordinates (χ, θ, ϕ), where χ is the radial coordinate and (θ, ϕ) are the polar angles:

$$ds^2 = c^2dt^2 - a^2(t)[d\chi^2 + f_K^2(\chi)(d\theta^2 + \sin^2\theta d\phi^2)]. \tag{2.4}$$

The function $a(t)$ is called the *scale factor* and, due to homogeneity, depends only on cosmic time. The function $f_K(\chi)$ gives the curvature of the spatial hyper-surfaces and has the form

$$f_K(\chi) = \begin{cases} \sin\chi & (K = 1, \text{ spherical}) \\ \chi & (K = 0, \text{ flat}) \\ \sinh\chi & (K = -1, \text{ hyperbolic}). \end{cases} \tag{2.5}$$

The line element in Eq. 2.4, often called the `Robertson-Walker metric` (Robertson, 1933; Walker, 1933), describes a homogeneous and isotropic Universe and will be used throughout this work.

2.2 Einstein Gravitational Equations

The dynamics of the metric is governed by Einstein's field equations which directly relate the geometry of space-time to the energy-momentum tensor (mass-energy and linear momentum) of the matter and radiation present in the Universe. They are a system of non-linear partial differential equations whose solution is by no means trivial

$$G_{\mu\nu} \equiv R_{\mu\nu} - \frac{1}{2}g_{\mu\nu}R = \frac{8\pi G}{c^4}T_{\mu\nu}, \tag{2.6}$$

where the tensor $G_{\mu\nu}$ contains the geometry of the Universe. The Ricci curvature tensor $R_{\mu\nu}$ is a combination of first and second derivatives of $g_{\mu\nu}$, and the Ricci scalar R is the trace of the Ricci tensor, $R \equiv g^{\mu\nu}R_{\mu\nu}$. The energy-momentum tensor $T_{\mu\nu}$ accounts for the matter and energy content of the Universe. The universal gravitational constant G has the value $G = 6.67384 \times 10^{-11}$ m^3 kg^{-1} s^{-2}. From the above expression, we see that the geometry of the Universe (left-hand side of Eq. 2.6) is determined by its energy content (right-hand side of Eq. 2.6). It is worth noting that Einstein's equations tend to Newton's law in the limit of weak fields and $c \to \infty$.

The astrophysicist Karl Schwarzschild found the first non-trivial exact solution to the Einstein equations in 1916, the so-called Schwarzschild metric. This solution allowed to describe the final stages of gravitational collapse and the objects known today as black holes (Schwarzschild, 1916).

In 1922, a more general solution was derived by Alexander Friedman. Starting from the Robertson-Walker metric, where the dynamics of the metric reduces to the dynamics of the scale factor $a(t)$, and assuming the energy-momentum tensor to be that of a perfect fluid (with pressure p and energy density ρ depending only on time), he arrived at two independent Einstein equations. From the first one and a combination of both he was able to write

$$\left(\frac{\dot{a}}{a}\right)^2 = \frac{8\pi G}{3}\rho - \frac{Kc^2}{a^2}, \tag{2.7}$$

$$\frac{\ddot{a}}{a} = -\frac{4\pi G}{3}\left(\rho + \frac{3p}{c^2}\right), \tag{2.8}$$

known as Friedman equations. In this way, $a(t)$ can be determined by solving both equations, once its value at a certain point is fixed. By convention, the value of the scale factor today is set equal to 1. Moreover, in the following we will adopt $c^2 = 1$ for the sake of simplicity.

An important quantity, which is extensively used in cosmology, is the ratio between pressure and energy density, also referred to as the equation of state

$$w \equiv \frac{p}{\rho}, \tag{2.9}$$

For all cosmological relevant fluids, $w = 0$ corresponds to collisionless, non-relativistic matter, and $w = 1/3$ to radiation (or relativistic matter, e.g. neutrinos). The Friedman equations can be solved exactly in a few, simple cases. In terms of the equation of state w, Eq. 2.8 can be equivalently written as

$$\frac{\ddot{a}}{a} = -\frac{4}{3}G\rho\pi(1 + 3w). \tag{2.10}$$

An interesting property of Universes with $-1/3 < w < 1$ is the so called Big Bang singularity, that is, a point in time for which $a = 0$ and ρ diverges. In such cases $a(t)$ is a concave function (i.e. $\ddot{a} < 0$ in 2.10), and its first derivative is positive, $\dot{a} > 0$, yielding an expanding Universe. The observational

confirmation of the expansion of the Universe reveals that such singularity indeed exits. The deceleration is then due to the gravitational attraction acting against the expansion. Equation 2.10 also shows that universes made from fluids with $w < -1/3$, such as a cosmological constant, accelerate the cosmic expansion instead of decelerating it.
A combination of the Friedman equations provides the conservation of mass-energy

$$\frac{d}{dt}(a^3\rho) = -p\frac{d}{dt}(a^3). \tag{2.11}$$

which, together with Eq. 2.10, allows to determine the evolution of the energy density as a function of the scale factor

$$\rho \propto a^{-3(1+w)}. \tag{2.12}$$

This translates into $\rho_m \propto a^{-3}$ for matter and $\rho_r \propto a^{-4}$ for radiation. The dependence of density on the scale factor for the several components of the Universe can be understood if we consider the cosmic evolution as a succession of various epochs, with a different component dominating each of them (see Fig. 2.2). Due to its dependence on the scale factor as $\rho_r \propto a^{-4}$, radiation dominated the early Universe and the evolution of $a(t)$ was given by $a \propto t^{1/2}$ (this result is obtained by plugging the scaling relation into Eq. 2.7 and integrating over time). Later in time, the radiation contribution became less and less important and matter started dominating. The point of transition, that is, where radiation and matter density are equal, is referred to as $a = a_{eq}$. During the matter-dominated epoch, the scale factor evolves as $a \propto t^{2/3}$ (known as *Einstein-de Sitter limit*). An era dominated by an energy density is encountered at recent times. In this case, the Universe expands exponentially, i.e. $a \propto e^t$ (called the *de Sitter limit*).

2.3 The Cosmological Constant

The Friedman equations describe an expanding or contracting Universe, where $a(t)$ is a scale factor and $\dot{a}(t)$ acts as an expansion or contraction factor. However, Einstein believed the Universe to be static and was disturbed by the fact that his equations led to dynamical solutions. Therefore, he introduced an extra term in the field equations, the so called cosmological constant Λ, in an attempt to achieve a static solution. The modified Einstein's equations read:

$$G_{\mu\nu} = \frac{8\pi G}{c^4}T_{\mu\nu} + \Lambda g_{\mu\nu}. \tag{2.13}$$

The cosmological constant, Λ, is an expansion term, providing a repulsive field to balance the attractive gravity of matter.

We can use thermodynamic arguments to illustrate the effect of a component with constant energy density in an expanding Universe. The first law of

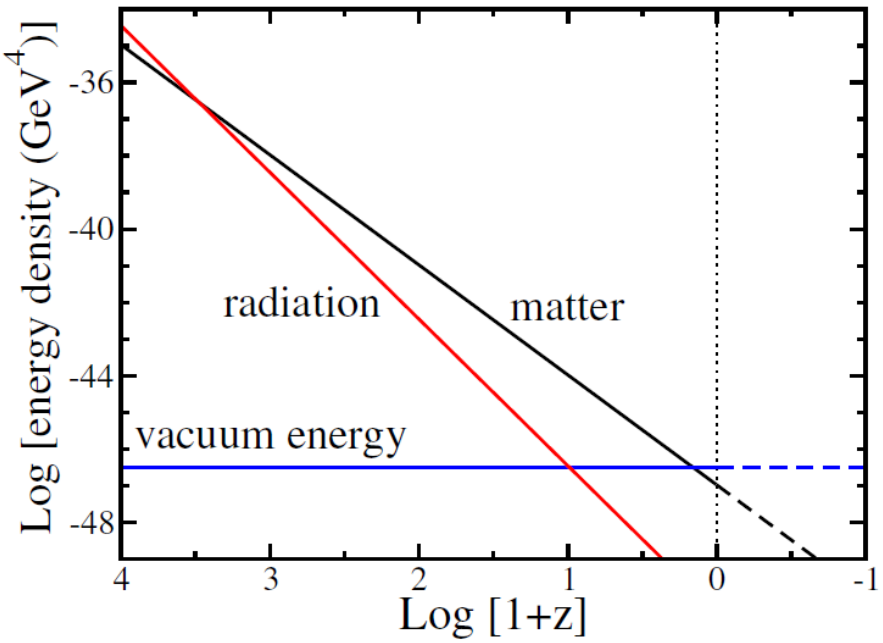

Figure 2.2: The evolution of the energy density as a function of redshift (in logarithmic scale) for the different components of the Universe. Earlier than $z \sim 3000$ radiation dominates (red line), thereafter and up to $z \sim 0.5$ (dark) matter dominates (black line). During this period structure forms and grows. Then dark energy dominates and the expansion accelerates. The matter-radiation equality, a_{eq}, occurs when matter intersects radiation. The matter-Λ equivalence is visible in the rightmost part of the plot. Taken from Turner & Huterer (2007).

thermodynamics implies that when a comoving volume element expands by an amount of dV, the corresponding change in energy is related to the pressure via $-pdV = dU = udV$. However, for a constant energy density $dU = \rho dV$, resulting in $p = -\rho$ or $w = -1$ (for $c^2 = 1$). This means, that a form of energy that is constant in space and time must necessarily have a repulsive gravitational effect.

The nature of the cosmological constant has been related to the zero-point fluctuations of all quantum fields, a property of the space-time itself. According to quantum field theory, *empty* space is filled with a sea of virtual particles. In this context, Λ would be the gravitational signature of this vacuum energy with energy-momentum tensor

$$T_{\mu\nu}^{vac} = \frac{\Lambda c^2}{8\pi G} g_{\mu\nu}. \tag{2.14}$$

During the past fifteen years the cosmological constant has been pointed out as a plausible explanation for dark energy. However, uncertainties remain

on its magnitude, as attempts to determine it have led to divergent results. Since virtual particles come to existence for very short periods of time, the *natural* value for the quantum vacuum density is given in units of one Planck mass per cubic Planck length. However, this density is about 120 orders of magnitude larger than the value of Λ suggested by the cosmic expansion (see Sec. 2.8.2).

2.4 The Expanding Universe

In 1929, Sir Edwin Hubble found observational evidence that the Universe is by no means static, but actually expanding. The discovery of the expansion of the Universe confirmed the validity of Friedman equations and led Einstein to claim Λ as his "greatest blunder". The term

$$H \equiv \frac{\dot{a}}{a}, \tag{2.15}$$

appearing in Eq. 2.7 is the cosmic expansion rate of the Universe, usually called the *Hubble parameter*. The *Hubble constant* H_0 is the value of the Hubble parameter at present time (i.e., at $a = 1$), and the most accurate measurement so far, made by the Planck Satellite collaboration (Planck Collaboration et al., 2013), gives $H_0 = 67.3 \pm 1.2$ km s^{-1} Mpc^{-1}. Nonetheless, this is not an independent measurement and usually implies the combination of several cosmological probes, as we will discuss in Sec. 2.7. Other teams have found different values for the Hubble constant. For instance Riess et al. (2011) found a value of $H_0 = 73.8 \pm 2.4$ km s^{-1} Mpc^{-1} by using optical and infrared observations of over 600 Cepheid variables with the Hubble Space Telescope (HST). The nine-year Wilkinson Microwave Anisotropy Probe data alone provided a values of $H_0 = 70.5 \pm 1.6$ km s^{-1} Mpc^{-1} (Hinshaw et al., 2012). More recently, using high-resolution CMB maps from the Atacama Cosmology Telescope together with BAO data, a value of $H_0 = 71.2 \pm 2.1$ km s^{-1} Mpc^{-1} (Sievers et al., 2013) was obtained. It is clear that a significant discrepancy between the Planck results and other studies exist. This is currently a matter of intensive debate among the astrophysical community. In this context, a model-independent methodology, as the one presented here, could shed some light on the problem, as we will discuss in Chapter 6.

From the first Friedman equation, Eq. 2.7, a particular value of the energy density can be found, such that curvature vanishes ($K = 0$). This is called the critical density, $\rho_{\rm crit}$, and can be written as

$$\rho_{\rm crit} = \frac{3H^2}{8\pi G}. \tag{2.16}$$

Due to the evolution of H in time, the critical density also changes through different epochs. Its present-day value is $\rho_{0,\rm crit} \simeq 1.9 \times 10^{-29}\ h^2$ g cm^{-3}, where h is a dimensionless parameter ($H_0 = 100h$ km s^{-1} Mpc $^{-1}$) to account for the

fact that we do not know the true value of the Hubble constant. This value of the critical density is normally used to scale the density of each component of the Universe. We define the density parameter

$$\Omega_i \equiv \frac{\rho_i}{\rho_{\rm crit}} \tag{2.17}$$

as the abundance of a substance in the Universe in units of $\rho_{0,\rm crit}$. In this context, the expansion rate can be expressed by means of the density parameter by inserting them into Eq. 2.7:

$$H^2 \equiv H_0^2 E^2(a) = H_0^2 \left[\frac{\Omega_{r0}}{a^4} + \frac{\Omega_{\rm M0}}{a^3} + \frac{\Omega_{k0}}{a^2} + \Omega_{\Lambda 0} F(a) \right] \tag{2.18}$$

where $E(a)$ is the normalised expansion function [$E(a = 1) = 1$] and Ω_{r0}, $\Omega_{\rm M0}$, Ω_{k0} and $\Omega_{\Lambda 0}$ are the present-day density parameters for radiation, matter, curvature and cosmological constant, respectively. A possible time-dependence of the cosmological constant is captured by the function $F(a)$. Usually the impact of curvature on Eq. 2.18 is expressed as

$$\Omega_k \equiv 1 - \Omega_{\rm M} - \Omega_r - \Omega_\Lambda, \tag{2.19}$$

which is also referred to as the normalisation condition. The total value of the density parameter Ω, including all contributions but curvature, is related to the spatial geometry of the Universe. In terms of Ω, the Friedman Equation can also be written as

$$\Omega - 1 = \frac{K c^2}{a^2 H^2}, \tag{2.20}$$

from which three alternatives arise summarised in Table 2.1. If $\Omega < 1$ (i.e. $\rho < \rho_{\rm crit}$) we obtain an open universe $K = -1$; $\Omega = 1$ (i.e. $\rho = \rho_{\rm crit}$) yields a flat geometry $K = 0$; and for $\Omega > 1$ (i.e. $\rho > \rho_{\rm crit}$) the universe is closed $K = +1$. This implies, that the evolution of the scale factor is strictly given by geometry (if one assumes a universe without cosmological constant).

As we see in Fig. 2.3, flat and open models ($\Omega \leq 1$) expand forever with a constant deceleration in the flat case and with an asymptotically linear expansion in the open case. Conversely, for closed models ($\Omega > 1$) the expansion stops at $a = a_{max}$. Thereafter the scale factor starts to decrease, and the Universe recollapses. In the presence of a cosmological constant, the Universe accelerates after some point in time.

2.5 The Scale Factor and the Redshift

We have already outlined that $\dot{a}(t)$ acts as an expansion or contraction factor in Eq. 2.7. We now explain its direct relation to a measurable quantity associated also with the expansion rate, the redshift.

Table 2.1: Possible curvature in cosmological models based on the value of the density, ρ, in terms of critical density, ρ_c.

$\rho < \rho_{\rm crit}$	$\Omega < 1 \rightarrow K = -1$	open
$\rho = \rho_{\rm crit}$	$\Omega = 1 \rightarrow K = 0$	flat
$\rho > \rho_{\rm crit}$	$\Omega > 1 \rightarrow K = 1$	closed

As the light from an emitting source propagates through an expanding Universe, the cosmic expansion makes its wavelength, λ, to be redshifted by the same amount by which the scale of the universe has been augmented while the light travels to us. The emitted wavelength (at any generic time) λ_e and the observed wavelength (today, i.e. $a_0 = 1$) λ_o are then related by

$$\frac{\lambda_o}{\lambda_e} = \frac{a_0}{a} = \frac{1}{a}. \tag{2.21}$$

Thus, the relative change in wavelength is defined as the redshift

$$z \equiv \frac{\lambda_o - \lambda_e}{\lambda_e} = \frac{1}{a} - 1, \tag{2.22}$$

The redshift z and the scale factor a can be used in a totally equivalent fashion by means of Eq. 2.22 or similarly

$$a = \frac{1}{1+z}. \tag{2.23}$$

where, evidently, $z = 0$ corresponds to present time. Redshifts can be measured from spectroscopic or photometric observations. The former compares the wavelength of the radiation coming from the astronomical sources to their rest-frame wavelength, which is measurable in the laboratory. The latter combines observations in different wavelengths passbands to infer redshift values. Spectroscopic redshifts are affected by smaller uncertainties but they are more difficult to acquire than photometric redshifts (read Section 3.3 for a detailed description of observations.)

2.6 Distances in the Universe

We have seen, that the most straightforward route to map the evolution of the Universe is through the $H(z)$ function. There are different ways to directly measure this quantity, e.g. via Baryonic Acoustic Oscillations (see Sec. 2.7.3). However, in most of the cases only indirect observations can be achieved through the well-known *distance-redshift relationship*.

General Relativity allows to formulate the laws of physics using arbitrary coordinates. The physical distance, also known as the *proper distance*, evolves proportionally to the scale factor $a(t)$. The proper distance between an emitting source at redshift z_2 and an observer at $z_1 < z_2$ is the distance measured

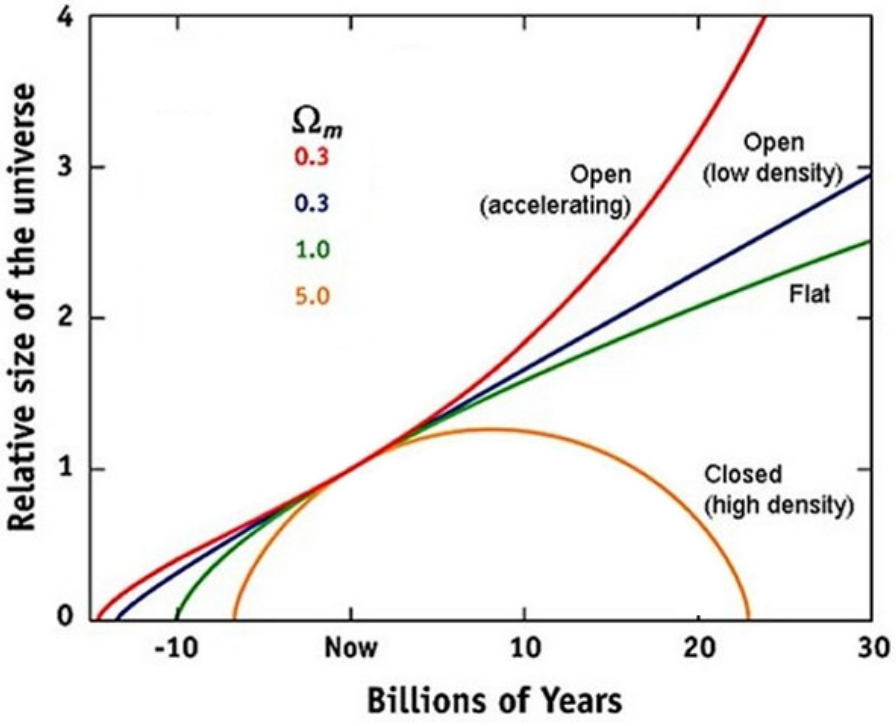

Figure 2.3: An illustration of the evolution of the scale factor. Eternal expansion happens for universes with $\Omega \leq 1$, i.e. flat (green line) or open (blue and red lines). The red curve corresponds to an accelerating universe. An eventual recollapse occurs in a closed universe with $\Omega > 1$ (yellow line). From http://www4.nau.edu/meteorite/Meteorite/Book-GlossaryD.html

by the light-travel time, that is $dD_{\rm prop} = -cdt$. Plugging in the expansion rate $H = \dot{a}/a$ this transforms into

$$dD_{\rm prop} = -c\frac{da}{\dot{a}} = -c\frac{da}{aH(a)}, \tag{2.24}$$

and integrating we obtain

$$D_{\rm prop}(z_1, z_2) = \frac{c}{H_0}\int_{a_2}^{a_1} \frac{da'}{a'E(a')}. \tag{2.25}$$

There is even a more convenient choice of coordinates which, conversely to the proper distance, are unaffected by cosmic expansion. These are the *comoving* coordinates. They assign constant spatial coordinate values to observers who perceive the Universe as isotropic. Such observers are called comoving observers because they move along with the Hubble flow. Thus, isotropy defines a special local frame of reference, the *comoving frame*.

The coordinate χ in Eq. 2.4 is usually referred to as comoving distance and it is defined by $dD_{\rm com} = -cdt/a$ or

$$D_{\rm com}(z_1, z_2) \equiv \chi(z_1, z_2) = \frac{c}{H_0} \int_{a_2}^{1} \frac{da'}{(a')^2 E(a')}, \tag{2.26}$$

where $a_1 = 1$ is the scale factor of the observer at present day. In addition to the proper and comoving distance, we will mention here another distance which is generally used in astronomy, the *angular-diameter* distance $D_{\rm A}$. It is defined, analogously with the Euclidean case, as the relation between the solid angle δw subtended by an object and the area δA, i.e. relating the comoving size of an object with its angular size. In non-Euclidean geometry, the solid angle of a sphere of constant radial coordinate χ has to be scaled by $a^2 f_K^2(\chi)$ leading to

$$D_{\rm A}(z_1, z_2) = \left(\frac{\delta A}{\delta w}\right)^{1/2} = a_2 f_K \left[\chi(z_1, z_2)\right] \tag{2.27}$$

and thus, the angular-diameter distance is

$$D_{\rm A}(z_1, z_2) = a_2 f_K \left[D_{\rm com}(z_1, z_2)\right] = a_2 \frac{c}{H_0} f_K \left[\int_{a2}^{1} \frac{da'}{(a')^2 E(a')}\right]. \tag{2.28}$$

We now consider an object of known intrinsic luminosity L. It is clear that from the total light emitted by a distant source, only a small part of it reaches the observer. The energy flux, F, i.e. the fraction of the luminosity collected per square meter at a certain distance D from the source, is given by the inverse square of the distance law

$$F_{\rm bol} = \frac{L_{\rm bol}}{4\pi D_{\rm L}^2}, \tag{2.29}$$

where the subscript `bol` refers to the flux and luminosity emitted over all wavelengths or frequencies and $D_{\rm L}$ is the so called *luminosity distance*.

The luminosity distance and the angular-diameter distance are related by the Etherington relation which holds for any space-time and is independent of cosmology (Etherington, 1933)

$$D_{\rm L}(z_1, z_2) = \left(\frac{1}{a_2}\right)^2 D_{\rm A}(z_1, z_2). \tag{2.30}$$

Combining this last equation with Eq. 2.28, the luminosity distance can be written as

$$D_{\rm L}(z_1, z_2) = \left(\frac{1}{a_2}\right)^2 \frac{c}{H_0} f_K \left[\int_{a_2}^{1} \frac{da'}{(a')^2 E(a')}\right]. \tag{2.31}$$

Another way to determine the luminosity distance, used frequently by astronomers, is from the comparison between *apparent* magnitude m (proportional to the log of the flux received by the observer) of an astronomical object,

and its *absolute* magnitude M (proportional to the log of the intrinsic luminosity of the object as seen from a distance of 10 parsecs)

$$m - M = 5log_{10}(D_{\rm L}/10\ pc), \tag{2.32}$$

which gives

$$D_{\rm L} = 10^{\frac{\mu}{5}+1}. \tag{2.33}$$

The term $\mu = m - M$ is the *distance modulus*, which has units of magnitudes. Astronomical objects of known physical size located at different z allow to probe the evolution of the angular-diameter distance; such objects are referred to as *standard rulers*. Similarly, objects which probe the redshift evolution of the luminosity distance are generally called *standard candles*.

It is worthy to note that for small redshifts, $z \ll 1$, the four distance measurements mentioned above coincide:

$$D = \frac{cz}{H_0} + O(z^2) \tag{2.34}$$

with the first element representing the linear Hubble expansion (the so-called *Hubble law*), and the deviation from a linear relation revealing the deceleration (or acceleration). The factor c/H_0 or *Hubble radius*, defines the present value of the horizon's size (given by $r_H = c/H(a)$), that is, the maximum distance that photons can have traveled in the time since the Big Bang.

2.6.1 Standard Candles and Standard Rulers

Standard candles are a class of astronomical objects whose intrinsic brightness is known. By comparing the luminosity of such an object to its observed (apparent) magnitude, one can infer the distance to the object using the inverse square law in Eq. 2.29.

Two problems arise for any class of standard candle. The principal one is calibration, i.e. determining the absolute magnitude of the candle with sufficient accuracy. This involves finding a class of objects whose physical properties are well understood and modeled, as well as a robust strategy to avoid mis-classifications and contamination (especially important at high redshifts). Additionally, means to account for interstellar extinction, which makes objects appear fainter and redder, are needed in the calibration procedure.

Until the 1950s, the preferred standard candles were the so-called Cepheid, i.e. variable stars with very regular pulsation periods directly correlated with their luminosity. However, Walter Baade soon discovered that the nearby Cepheid variables used to calibrate the cosmic distance ladder were of a different type than the ones used to measure distances to more distant galaxies (Baade, 1956). Most of the nearby Cepheid variables were population I stars with higher metal content than the distant population II stars. In fact, the population II stars were fainter than believed (~ 1.5 mag), and the corresponding

derived distances were greatly underestimated. All astronomical observations nowadays seem to indicate that Type Ia supernovae, once their light curves are properly calibrated, are the best standard candles up to 10^3 Mpc. As we have seen in previous Sections, the $H(z)$ expansion function can be derived from the luminosity distance of a standard candle through Eq. 2.31.

Analogously, a standard ruler is an astronomical object whose approximate size is known. By measuring its apparent angular diameter in the sky, one can determine its distance from Earth. In general, the angular size of an object can be defined as

$$\theta = \frac{r}{D_{\rm A}} \tag{2.35}$$

where r is the *true* size of the object and $D_{\rm A}$ is the angular-diameter distance.

In comoving coordinates, the sizes of an object along the line of sight and the traverse direction can be written in terms of the expansion rate and the angular-diameter distance, respectively

$$r_{\parallel} = \frac{c\Delta z}{H(z)}; \qquad r_{\perp} = (1+z)D_{\rm A}(z)\Delta\theta. \tag{2.36}$$

where Δz is the observed size in redshift. This means, that an estimate of $H(z)$ and $D_{\rm A}(z)$ can be determined if the *true* scales are know and the observed sizes Δz and $\Delta\theta$ can be measured.

2.7 Cosmological Probes for Acceleration

The physics of the accelerating Universe can be analysed in the light of several cosmological probes. In particular, the parameters of the ΛCDM scenario can be precisely determined if different observational probes are combined. We will review three of the probes which are the most relevant for the work presented here. These are Type Ia supernovae (SNe Ia), Baryonic Acoustic Oscillations (BAO) and the Cosmic Microwave Background (CMB).

2.7.1 Type Ia Supernovae as Cosmological Test

Supernovae Ia are violent stellar explosions which occur when a carbon-oxygen white dwarf (the final evolutionary stage of low-mass stars, with $M < 8\ M_{\odot}$) reaches the Chandrasekhar limit ($M_{\rm Ch} = 1.4\ M_{\odot}$) while accreting mass from a companion or via a violent merger with another white dwarf, and undergoes a thermonuclear runaway. The luminosity produced in these events is so large ($L \sim 10^{10}\ L_{\odot}$ at peak), that they can outshine an entire galaxy. The existence of a fixed amount of mass, $M_{\rm Ch}$, responsible to trigger the explosion, suggests that the amount of energy released during the process is approximately fixed. A substantial scatter in peak luminosity has been observed in SNe Ia. However, once their light curves are calibrated through the absolute *magnitude-decline rate empirical relation*, SNe Ia become good candidates for standard candles.

In the late 1990s, SNe Ia gave the most direct evidence for cosmic acceleration and the existence of dark energy. Chapter 2 will be fully dedicated to explain the physics behind SN explosions and the application of these magnificent events as standard candles in cosmological studies. A method to "extract" the information concerning the expansion history of the Universe imprinted in SN Ia data will be presented in Chapter 3.

2.7.2 The Cosmic Microwave Background Radiation

The cosmic microwave background is the oldest light we can see in the Universe, and therefore the most powerful probe of its infant evolution. This light provides direct information on the physical conditions when the Universe was only 380,000 years old ($z = 1090$), that is, when photons, until then tightly bound to electrons, last scattered off electrons and started traveling freely through space.

The existence of a background radiation originating from the propagation of photons in the early Universe (once they decoupled from matter) was theoretically predicted by George Gamow and his collaborators Ralph Alpher and Robert Herman in 1948 (Alpher & Herman, 1948; Alpher et al., 1948). They argued that if there was a Big Bang – that is, a system evolving from a highly compressed state with an inflationary phase at very early epochs (Guth, 1981; Linde, 1982) – the expansion of the Universe would have stretched and cooled the high-energy radiation of the early Universe into the microwave region and to a temperature of about 5 K. Twenty years later, this radiation was discovered by the radio astronomers Arno Penzias and Robert Wilson while working with a new antenna at the Bell T&T Telephone Labs in New Jersey. They measured a slightly lower temperature for the CMB radiation (~ 2.7 K) and were awarded the Nobel Prize in 1978.

The interpretation of the CMB was a controversial matter of debate during the 1960s with some supporters of the steady state theory arguing that the microwave background was the result of scattered starlight from distant galaxies. However, during the 1970s the consensus was established that the CMB is a remnant of the Big Bang. Within the Big Bang paradigm, inflationary cosmology predicts that after about 10^{-37} seconds the Universe underwent an exponential growth that smoothed out nearly all inhomogeneities, leading to an Universe as isotropic and homogeneous as we observe it today (on large scales). Nevertheless, some authors such as Harrison, Peebles, Yu and Zel'dovich realized that a certain degree of anisotropy (at the level of 10^{-4} or 10^{-5}) should remain in the CMB radiation, caused by quantum fluctuations that led to the inflation event (Harrison, 1970; Peebles & Yu, 1970). These fluctuations were responsible for over- and underdensities which, via gravitational instability, formed the seeds of all current cosmic structure (Zeldovich, 1972). A few years later, Sunyaev calculated the observable imprint that these inhomogeneities would have on the CMB (Sunyaev, 1978). The NASA COBE mission success-

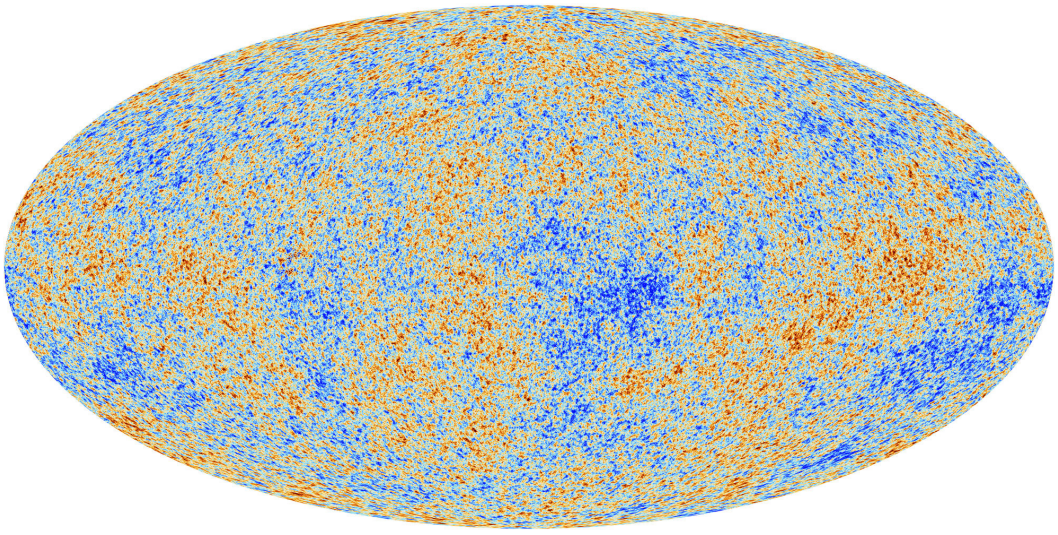

Figure 2.4: Sky Map of the CMB radiation temperature from the Planck Satellite mission (Planck Collaboration et al., 2013). Blue spots represent cooler temperatures. Red corresponds to higher temperatures. The scale is in μK.

fully confirmed the primordial anisotropies, which had been long sought for, using the Differential Microwave Radiometer instrument (Smoot et al., 1992). The team was awarded the Nobel Prize in Physics in 2006 for this discovery.

The Physics of the CMB

The CMB is known to follow with extraordinary precision the spectrum of a blackbody

$$B_\nu(T_{\rm CMB}) = \frac{2h\nu^3}{c^2}\frac{1}{exp(h\nu/k_{\rm B}T_{\rm CMB})-1} \tag{2.37}$$

corresponding to a temperature of $T_{\rm CMB} = 2.725$ K (Noterdaeme et al., 2011). As expected, the distribution of the CMB on the sky has proven to be remarkably isotropic to the precision of 10^{-3}. Most of the residual anisotropy, at the level of a few mK, is due to the motion of our Solar system with respect to the rest frame of the CMB (what is usually called the *dipole anisotropy*). After removing the dipole component, we are left with the primary anisotropy at the level of 10^{-5} with $\Delta T_{\rm CMB} \approx 30\mu K$.
Mathematically, temperature anisotropies are expressed as

$$\frac{\delta T}{T}(\theta,\phi) = \sum_{l=2}^{+\infty}\sum_{-l}^{+l} a_{lm}Y_{lm}(\theta,\phi) \tag{2.38}$$

where $Y_{lm}(\theta,\phi)$ are spherical harmonics (in this expansion, $l = 0$ would represent the monopole or mean temperature and $l = 1$ the motion of the Solar

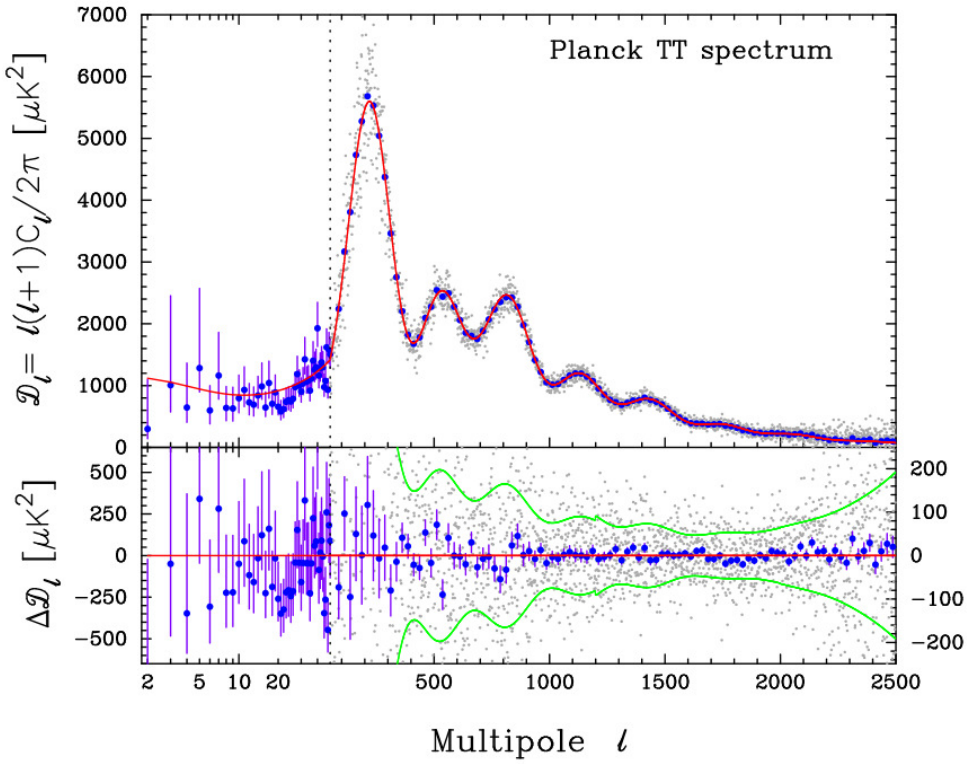

Figure 2.5: Upper panel: Multipole power spectrum of the CMB temperature fluctuations from the Planck Satellite. The light grey points show the power spectrum multipole-by-multipole. The blue points are the average in bands of width $\Delta l = 31$ together with 1-σ errors. The red curve is the theoretical prediction of the concordance cosmology. Lower panel: The power spectrum residuals with respect to the theoretical model. The green curves correspond to 1-σ errors on the individual power spectrum estimates (Planck Collaboration et al., 2013).

System). The variance C_l of a_{lm} is usually referred to as the power spectrum of the CMB

$$C_l \equiv < |a_{lm}^2| > \equiv \frac{1}{2l+1} \sum_{m=-l}^{l} |a_{lm}|^2. \tag{2.39}$$

If the temperature fluctuations are Gaussian (as appears to be the case) all information contained in the CMB sky maps, such as the one shown in Fig. 2.4, can be compressed into the power spectrum, essentially describing the behaviour of C_l as a function of l (Fig. 2.5).

It seems now clear, that the early Universe was composed of a hot and dense primordial plasma of interacting photons, electrons, and baryons. As the Universe expanded, *adiabatic* cooling made the energy density of the plasma

decrease sufficiently in order for electrons to be captured by protons, forming neutral hydrogen atoms

$$p + e^- \longrightarrow H + \gamma. \tag{2.40}$$

This recombination event happened when the temperature was around 3000 K (or equivalently, when the universe was approximately 380,000 years old). After this point, photons were able to travel freely through space, resulting in the decoupling of matter and radiation.

Observed anisotropies in the cosmic microwave background are usually divided into two categories: *primary anisotropy*, due to effects on the last scattering surface (and before); and the *secondary anisotropy*, due to interactions effects of the background radiation with hot gas or gravitational potentials, occurring between the last scattering surface and the observer. Two main physical mechanisms are visible in the CMB power spectrum, which conform the primordial anisotropy: `Baryonic Acoustic Oscillations` (BAO) and `diffusion damping` (also called collisionless damping or Silk damping; Silk, 1968).

BAO will be described in greater detail in next Section 2.7.3. They essentially arise before the epoch of recombination when the overdensities compressed the cosmic fluid due to gravity, whereas the radiation pressure of the coupled baryon-photon fluid acted against gravity, driving the fluctuations apart. These two competing effects gave rise to the acoustic oscillations with the characteristic peak and through pattern. The Silk damping refers to the suppression of anisotropies on small scales. This is mainly due to the increase of the photon mean free path during decoupling, which is not an instantaneous process. Essentially, photons diffused from the hot, overdense regions of plasma to the cold, underdense ones dragging along the protons and electrons and causing temperatures and densities to be averaged. Structures smaller than the diffusion scale (8 h^{-1}Mpc or 10 arcmin) are inevitably damped.

An important secondary anisotropy observed in the CMB, which relates to propagation effects of photons, is the so-called `Sunyaev-Zel'dovich effect`. It originates from the Thomson scattering of CMB photons off electrons in the hot gas of galaxy clusters, modifying the spectrum of the CMB observed in the line of sight of a cluster (Sunyaev & Zeldovich, 1970). Also the `Sachs-Wolfe effect` (Sachs & Wolfe, 1967), which causes photons from the Cosmic Microwave Background to be gravitationally redshifted or blueshifted due to changing gravitational fields, is considered as a secondary anisotropy.

The CMB is also expected to have a polarization intensity of order 10% of the total intensity, which carries additional information on the properties of the early Universe. This polarization arises from Thomson scattering and is radial/tangential around temperature spots.

Since the first detection of the CMB anisotropies with the COBE satellite, further experiments have been carried out reaching much higher precision. A series of ground and balloon-based experiments have measured the

CMB anisotropies on smaller angular scales over the past two decades, for instance DASI (Leitch et al., 2002) or BOOMERanG (de Bernardis et al., 1999). The primary goal of these experiments was to measure the scale of the first acoustic peak, which COBE did not have sufficient resolution to resolve. The subsequent peaks in the power spectrum were tentatively detected by several experiments before being definitively confirmed by the Wilkinson Microwave Anisotropy Probe (WMAP) launched in 2001. The analyses based on the 5-year (Komatsu et al., 2009) and the 7-year data (Komatsu et al., 2011) showed striking evidence of an almost flat ΛCDM Universe and provided tighther constraints on the cosmological parameters.

The most up to date constraints on CMB were released early in 2013 by the Planck Satellite Mission from ESA. The extended frequency coverage and angular resolution (of about 5 arcmin) of the Planck mission has allowed to probe the power spectrum of the CMB to much smaller scales with very high sensitivity. Moreover, it has set an unprecedent control over the subtraction of foregrounds, especially delicate in CMB analyses, and has detected thousands of galaxy clusters through the Sunyaev-Zel'dovich effect (Planck Collaboration et al., 2013).

Other ground-based experiments to improve measurements of the polarization and resolution on small angular scales, such as the projects based on the Atacama Cosmology Telescope, the South Pole Telescope and the QUIET telescope, are currently ongoing.

2.7.3 Baryonic Acoustic Oscillations

Baryonic acoustic oscillations are a feature imprinted in the power spectrum of the CMB. As we saw in the last Section, prior to $z \sim 1000$ the primordial gas was ionized due to the high temperature and density. The mean free path of electrons at this time was less than the *Hubble time* $(1/H)$ resulting in a close coupling between electrons, nuclei (baryons) and photons. The radiation pressure of the photons was comparable to the gravitational forces in the over-densities, with the result that the perturbations in the baryon-photon fluid oscillated as sound waves. Mathematically, the BAO effect can be seen as a standing wave in Fourier space where the acoustic scale gives rise to a harmonic sequence of oscillations in the power spectrum. Fig. 2.5 shows the acoustic peaks of the power spectrum of the CMB temperature fluctuations. The angular scale of the first peak determines the curvature of the Universe, indicating spatial flatness. The ratio of the first to second peak determines the baryonic density and the third peak gives us a hint about the dark matter component density. The locations of the peaks also give important information about the nature of the primordial density perturbations.

The imprint left by these sound waves in the early Universe provides a characteristic angular scale which can be used as a standard ruler (Blake & Glazebrook, 2003; Seo & Eisenstein, 2003). Since only fluctuations smaller

than the comoving sound horizon r_s at recombination are affected by acoustic oscillations, the acoustic scale can be calculated as the comoving distance that the sound waves could travel from the Big Bang until recombination:

$$r_s = \int_0^{t_*} \frac{c_s(t)}{a(t)} dt = \int_{z_*}^{\infty} \frac{c_s(z)}{H(z)} dz \tag{2.41}$$

where t_* and z_* refer to the time and redshift of recombination, respectively, and c_s is the sound speed of the waves. From Equation 2.41 it is clear that the acoustic scale is uniquely determined once the epoch of recombination and the sound speed of the fluid (which depends on the baryon-to-photon ratio) are known. These two quantities are very precisely obtained from CMB measurements yielding a value of $r_s = 150h^{-1}$ Mpc.

Within the BAO theory, separations along the line of sight correspond to differences in redshift that depend on the Hubble parameter $H(z)r_s$. Analogously, separations traverse to line of sight correspond to differences in angle that depend on the angular diameter distance $D_{\rm A}(z)/r_s$. This means, that measuring the acoustic scale over a wide redshift interval allows to access both $H(z)$ and $D_{\rm A}(z)$, making BAO an exceptional probe of dark energy and cosmic geometry. It is worth noting that the acoustic features are not only imprinted in the CMB but also in the spatial distribution of baryonic and, eventually, non-baryoninc dark matter.

The challenge of measuring BAO is purely statistical. Since it is a weak signal at large scales, one needs to map enormous volumes of the sky to detect them. The BAO signature was first discovered by Eisenstein et al. (2005) using a spectroscopic sample of over 40,000 luminous red galaxies (LRG) from the the Sloan Digital Sky Survey (SDSS, York et al., 2000). The LRG are the brightest and reddest galaxies in the Universe and can be easily seen up to intermediate redshifts ($z > 0.2$). The detection provided a standard ruler to measure the distance to a single redshift $z = 0.35$. Subsequently, Percival et al. (2007) also measured the BAO signal using a combination of the Two-degree Field Galaxy Redshift Survey (2dFGRS Colless et al., 2001) and SDSS main galaxy samples. They used it to measure the distance to $z = 0.2$. This measurement together with the one from Eisenstein et al. (2005) was used to place constraints on the cosmological parameters and probe ΛCDM as the standard model for cosmology.

Future galaxy surveys (spectroscopic and photometric) are expected to detect the BAO signature in several redshift bins and measure the acoustic scale both in the radial and transverse directions. An example is the Baryon Oscillation Spectroscopic Survey (BOSS) which is mapping out the BAO signature with unprecedented accuracy using observational time at the Apache Point Observatory (APO) 2.5-m telescope as part of Sloan Digital Sky Survey III. Over the period 2009-2014, the BOSS survey will obtain the redshifts of 1.5 million LRGs out to $z \sim 0.7$ over 10,000 square degrees. Simultaneously, it will map quasars at $z \sim 2.5$ allowing to measure the acoustic oscillations in

the Lyman-α forest.[1]

2.8 The Concordance Model: ΛCDM

The Λ-Cold Dark Matter (ΛCDM) is the currently adopted cosmological model. The model assumes the Friedman-Lemaître-Robertson-Walker (FLRW) metric, i.e., it obeys isotropy, homogeneity and the R-W metric (Eq. 2.4), the Einstein (Eq. 2.6) and Friedman (Eq. 2.7) equations and the conservation of energy (Eq. 2.11). Furthermore, it is based on the Big Bang scenario and the Standard Model of particle physics.

Till now, it is the best and simplest model that is in general agreement with observations, ranging from the Big Bang relic radiation (the CMB), and the abundances of light elements, to the large-scale structures of galaxy clusters and filaments. It involves two key concepts: Cold Dark Matter and Dark Energy (usually identified with Λ). These are currently the dominant components of the Universe, accounting for around 70% and 25% of the total energy budget as seen in Fig 2.6.

2.8.1 Dark Matter

Dark Matter refers to an unknown matter component originally proposed to explain discrepancies between calculated masses of galaxies and clusters of galaxies (obtained through dynamical and general relativistic considerations), and inferred masses of the visible *luminous* matter contained in them (stars, gas and dust). Already in the 1930s, Fritz Zwicky, applying the virial theorem[2] to the Coma cluster, estimated a difference of a factor 10^2 depending on whether the mass of the cluster was obtained from the motion of galaxies near its edge or via the visible number of galaxies and total brightness (Zwicky, 1937).

The most convincing proof of the existence of dark matter, given by Vera Rubin in the late 1970s, came from observations of the rotation curves of spiral galaxies. Observed rotation curves usually exhibit a characteristic flat behaviour at large distances from the center, even far beyond the edge of the visible disks (see Figure 2.7). Rubin discovered that the stars in spiral galaxies orbit roughly at the same speed, implying that the mass densities of the galaxies are uniform well beyond the central regions containing most of the stars (Rubin et al., 1980). From Rubin's analysis it seemed clear that

[1]The Lyman-α forest is the sum of the absorption lines arising from the Lyman-α transition of neutral hydrogen in the spectra of distant galaxies and quasars. For a detailed description of the Lyman-α forest as a cosmological probe see Weinberg et al. (2003).

[2]The virial theorem states that, for a stable, self-gravitating, spherical distribution of equal mass objects (stars, galaxies, etc), the total kinetic energy of the objects must equal the gravitational energy, within a factor of two. For an introduction on astrophysical applications of the virial theorem see Collins (1978).

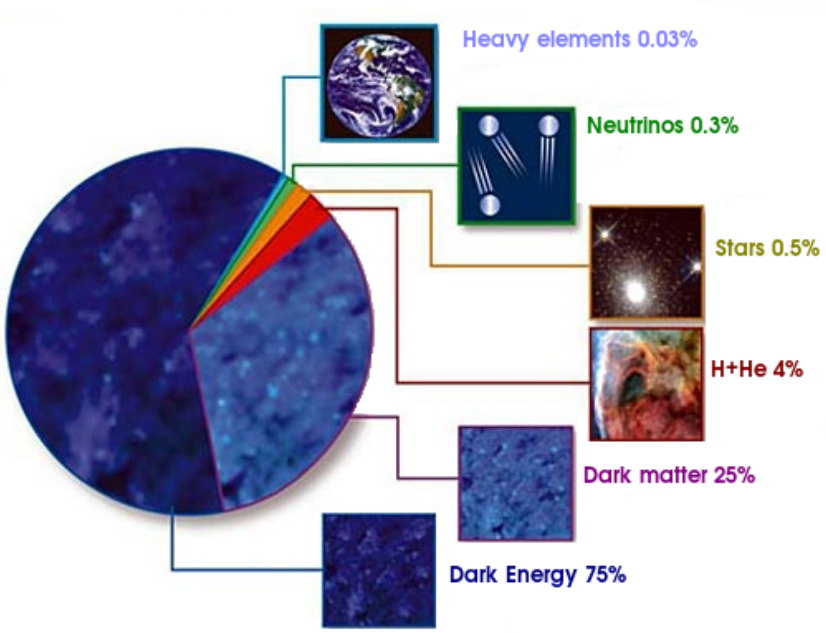

Figure 2.6: The different components of the current Universe. Ordinary matter (including neutrinos and baryons) accounts only for around 5% of the total energy content. The remaining is made up of dark matter ($\sim 25\%$) and dark energy ($\sim 70\%$).

the considered galaxies contained about six times more mass than could be accounted for by their visible mass.

Additionally, high resolution neutral hydrogen (HI) observations – detectable via the $\lambda = 21$ cm line in low-density regions of the interstellar medium – confirmed that, for the majority of spiral galaxies, their rotation curves remained flat beyond the optical disks (Roberts & Rots, 1973; Begeman, 1989). This led to the conclusion that a massive dark halo surrounded the disks of spiral galaxies. Later on, this result was further corroborated by gravitational lensing of background objects by galaxy clusters – such as the Bullet Cluster (Clowe et al., 2006) or Abell 1689 (Taylor et al., 1998) –, and more recently, the temperature distribution of hot gas in galaxy clusters (Hansen et al., 2011) and the pattern of anisotropies in the CMB (Komatsu et al., 2009).

Dark matter particles are supposed to be cold, non-relativistic at the epoch of radiation-matter equality, non-baryonic, dissipationless, adiabatic and collisionless.[3] There are several lines of evidence for this set of physical properties. For instance, it is known that dark matter particles should be non-baryonic, since the cosmic microwave background and cosmic web of structure would

[3]Other hypotheses for dark matter consider it to be hot or warm with different physical properties, though these theories seem less plausible. For a review on the topic see Bertone et al. (2005).

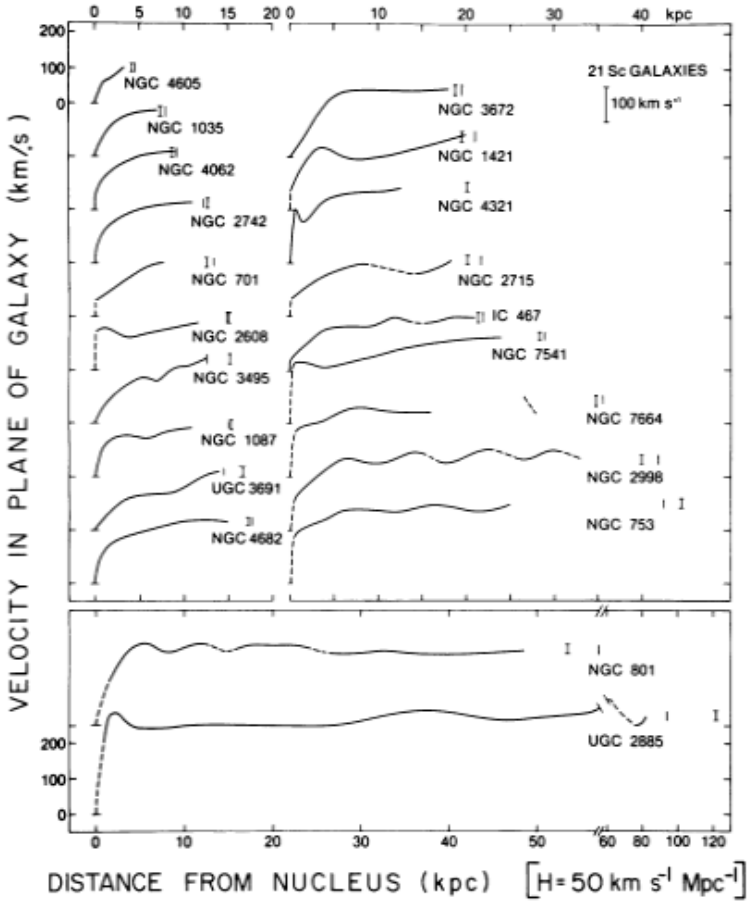

Figure 2.7: Rotation curves for several spiral galaxies presenting the typical flat pattern. This proofs that the density matter does not decrease with distance to the galactic centre, and that some undetectable dark matter is present in all galaxies. From Rubin et al. (1980).

look radically different if baryons would build up all the dark matter. Additionally, the abundance of light elements – created during Big Bang nucleosynthesis – depends strongly on the baryon density (more precisely, on the baryon-to-photon ratio) of the Universe (see e.g. Cyburt, 2004; Iocco et al., 2009). Observed abundances of deuterium and ^{4}He give similar constraints on the baryon density in the Universe as those coming from cosmic microwave background observations (Steigman et al., 2007). Also, dark matter cannot consist of light (below the keV regime in mass) particles, because they are relativistic at early times, and thus stream out of small-scale density perturbations. Current measurements of the Lyman-α forest, at $z \sim 3$, constrain the dark-matter particle mass to be $m \gtrsim 2$ keV (Boyarsky et al., 2009). Moreover, there is strong evidence on the electromagnetic neutrality of dark matter (Sigurdson et al., 2004). If dark matter had a small charge or a small electric

or magnetic dipole moment, it would couple to the photon-baryon fluid before recombination, altering the features of the CMB as well as the matter power spectrum.

The most plausible candidates for dark matter are the so called WIMPs or Weakly Interacting Massive Particles, which are affected only by gravity and the weak force. There are currently many ongoing projects to search for WIMPs, including direct or indirect detection experiments. The former look for the scattering of dark matter particles off atomic nuclei within the detector, the latter search for products, gamma rays and standard particle-antiparticle pairs, of WIMP annihilation. Examples of direct detection experiments are CDMS (Cryogenic Dark Matter Search), EDELWEISS (Experience pour Detecter Les Wimps En Site Souterrain) or CRESST (Cryogenic Rare Event Search with Superconducting Thermometers). These experiments usually consist on gigantic laboratories deep underground in order to reduce the background from cosmic rays. They make use of two detector technologies: cryogenic detectors, which operate at temperatures below 100 mK and detect the heat produced when a particle hits an atom in a crystal (e.g. germanium); or noble liquid detectors, which detect the scintillation light produced by a particle colliding in liquid xenon or argon. So far, though a few detection events have been reported (Ahmed et al., 2009; Angloher et al., 2012), no compelling proof has still been offered. The Fermi Gamma-ray Space Telescope launched in 2008 is currently searching for gamma-rays from dark matter decay.

An alternative approach is to try to produce dark-matter particles in the laboratory, something that is being carried out in the Large Hadron Collider (LHC). A number of state of art N-body simulations have been implemented by the international Virgo Consortium led by the Max Planck Institute for Astrophysics, in an attempt to give theoretical understanding of the dark matter density field and the formation of structure at large scales in the Universe. A snaphot of one of the most famous simulations, the Millennium Run (Springel, 2005), can be seen in Fig. 2.8, showing the characteristic dark-matter distribution, i.e. the filamentary structure in which dark matter clusters.

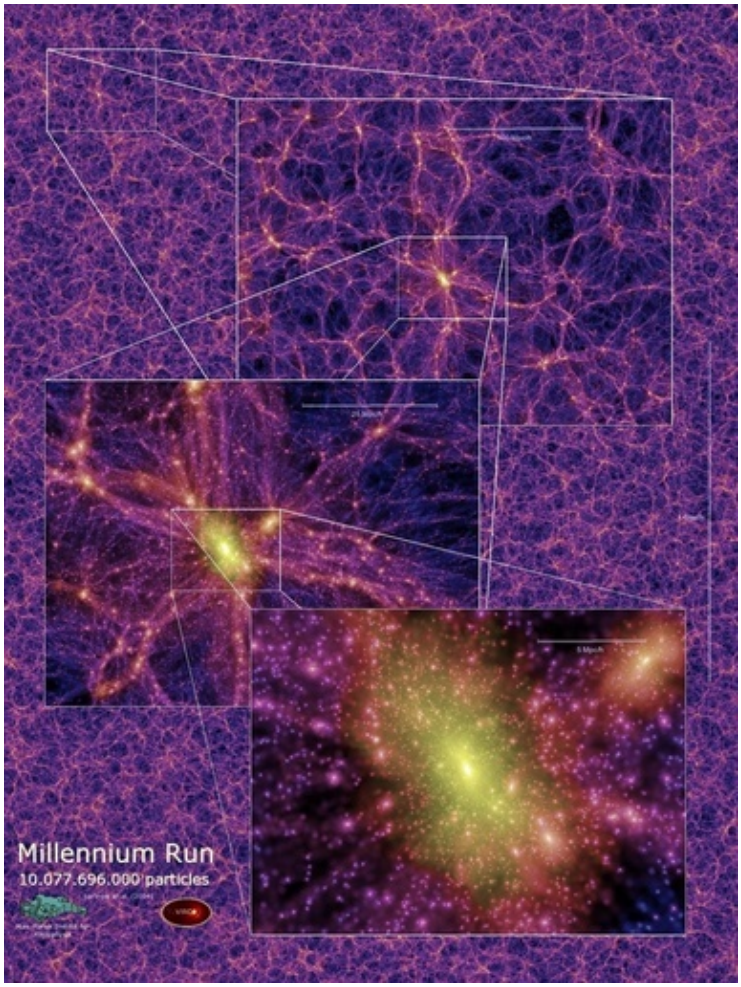

Figure 2.8: Snapshots at different distance scales of the dark matter Millennium Simulation performed by researches at the Max Planck Institute for Astrophysics. The cosmic web of filaments and voids is seen as well as the growth of structure in the nodes connecting the filaments (Springel, 2005).

2.8.2 Dark Energy

Before the 1990s, it had become evident that matter (including dark and baryonic) could only account for $\sim 30\%$ of the Universe's critical density (Turner, 1999). We know from Sec. 2.4 that spatial flatness (strongly favoured by cosmological observations) requires the total energy density to be close to one unity ($\Omega \equiv \sum_i \Omega_i = 1$). This remarkable fine-tuning is usually referred to as the *flatness problem*, which was first mentioned by Robert Dicke in 1969, and indicates a very specific value for the critical density (recall that $\Omega \equiv \rho/\rho_{\rm crit}$). A solution to this problem could be the before-mentioned cosmic inflation (see Olive, 1990, for a review). A direct consequence of inflation is that the primitive Universe originated in a tiny causally connected region which later on

expanded smoothing out spacetime and making it flat, isotropic and homogeneous. If, as observations and inflationary considerations suggest, the cosmic energy budget equals unity, there seems to be a missing portion of about $\sim 70\%$ which should be different than matter. Some authors considered that this new component could exist in form of vacuum energy (or cosmological constant) being uniformly distributed in space and not clumping as ordinary matter (Turner et al., 1984). The (re-)introduction of the cosmological constant solved partially the Ω problem, and presented relatively good agreement with CMB data as well as the large-scale distribution of galaxies. This led theoretical cosmologists to include a Λ into the simpler CDM model, with density parameters $\Omega_{\rm M} \sim 0.3$ and $\Omega_\Lambda \sim 0.7$ (Turner, 1991, 1997, 1999; Ostriker & Steinhardt, 1995; Liddle et al., 1996). However, a Universe with $\Omega_\Lambda \sim 0.7$ would accelerate the cosmic expansion instead of decelerating it, having $\ddot{a} > 0$ in the second Friedman equation (Eq. 2.8). At that time, as no observational evidence was available, this idea was rather disturbing and was only kept as a possibility. Nonetheless, in 1998 the acceleration of the Universe was observationally confirmed, providing evidence of a smooth, dark energy component whose nature was a complete mystery.

Since that time, many different dark-energy models have been proposed, but none of them have given a satisfactory answer to the nature and origin of the cosmic acceleration. As we already mentioned, within General Relativity, the simplest explanation is a cosmological constant with equation of state $w = p/\rho = -1$. In this case, the dark energy would be an elastic and smooth fluid exerting a repulsive gravitational force which, if present in sufficient quantity, could lead to the observed accelerated expansion.

However, all attempts to identify the cosmological constant with the vacuum energy density predicted by quantum field theory have failed so far: the latter is between 55 and 120 orders of magnitude larger than the observationally inferred value $\rho_{\rm vac} = \Lambda/8\pi G \simeq 10^{-47}{\rm GeV}^4$ (Sahni & Starobinsky, 2000; Sahni, 2002). A Universe with such a large value of Λ as the one implied by theory would have expanded so rapidly that galaxies and stars (and thereby, life) would never have formed. The idea of a symmetry which sets the value of Λ to either zero or a very small value has gained attention in the past few years. However, no experimental evidence has been found until now.

Other possibilities allow for a non-constant dark energy equation of state, varying with time. These are the so called *Quintessence* or *Phantom* models (Wetterich, 1995, 1998). Both assume the vacuum energy to be a dynamical, evolving scalar-field (Freese et al., 1987; Frieman et al., 1995; Turner & White, 1997; Caldwell et al., 1998; Steinhardt, 1999). The general idea is that the energy of the true vacuum is zero, but not all fields have evolved to their state of minimum energy. Thus, the fields are classically unstable and are rolling toward their lowest energy state. In this case, the density and pressure are given by

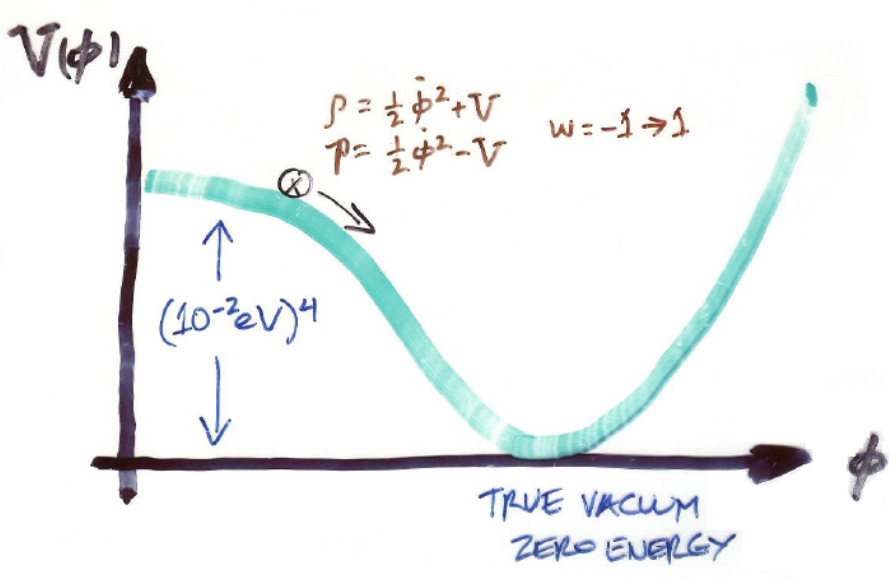

Figure 2.9: Sketch representing a scalar field slowly rolling towards its minimum energy state. From Turner (1999).

$$\begin{aligned} p &= \tfrac{1}{2}\dot{\phi}^2 + V(\phi) \\ \rho &= \tfrac{1}{2}\dot{\phi}^2 - V(\phi), \end{aligned} \tag{2.42}$$

where $V(\phi)$ is the potential energy of the scalar field and the evolution of the field ϕ is governed by

$$\ddot{\phi} + 3H\phi + V'(\phi) = 0. \tag{2.43}$$

If the scalar field evolves slowly, that is $\dot{\phi}^2 \ll V$, then $p \simeq -\rho$ and the scalar field behaves like a slowly varying vacuum energy (see e.g. Turner, 1983, 1999). For Quintessence fields $V(\phi) > 0$ and $-1 < w < -\frac{1}{3}$. Conversely, in Phantom fields $V(\phi) < 0$ and $w < -1$. The limit $w = -1$ is referred to as the *Phantom divide line* (Perivolaropoulos, 2005). Dynamical scalar fields have been introduced in an attempt to ameliorate the fine-tuning problem faced by Λ (Turner & White, 1997). However, several difficulties remain, the major problem being that the scalar field must be very light and, in this way, long-range forces can mediate (Carroll, 1998). The sketch of Fig. 2.9 illustrates the idea of a scalar field slowly rolling towards its minimum energy state.

In this context, the simplest parameterisation of the equation of state parameter as a function of scale factor $w(a)$ reads

$$w(a) = w_0 + w_a(1 - a), \tag{2.44}$$

where w_0 is be the present-day value of the equation of state. It was proposed by Chevallier & Polarski (2001) and Linder (2003). For this specific

parametrization, the expansion rate can be written as

$$H^2(a) = H_0^2 \left[\frac{\Omega_{r0}}{a^4} + \frac{\Omega_{\rm M0}}{a^3} - \frac{\Omega_{k0}}{a^2} + \Omega_{\Lambda 0} \exp \left\{ -3 \int_a^1 [1 + w(a')] \frac{da'}{a'} \right\} \right], \quad (2.45)$$

which for flat curvature reduces to

$$H^2(a) = H_0^2 \left[\frac{\Omega_{\rm M0}}{a^3} + \Omega_{\Lambda 0} \exp \left\{ -3 \int_a^1 [1 + w(a')] \frac{da'}{a'} \right\} \right]. \quad (2.46)$$

2.8.3 Cosmological Parameters: the Current Picture

The common strategy when deriving specific values for the cosmological parameters relies on the combination of several independent probes. In this way, complementary information is offered for the analyses and a high impact of systematic errors is avoided. This is particularly important, as we will see for the case of SNe Ia, since systematics can lead to ambiguous estimations of the cosmological parameters. As an illustration, the combination of constraints from the three probes discussed in this section is shown in Fig. 2.10 (see also Fig. 3.18 for a more modern version of the same plot).

In Table 2.2, constraints of the ΛCDM main parameters model combining CMB, BAO and Type Ia Supernova measurements are given. It is noteworthy that CMB, BAO and Supernovae are considered as geometrical probes, meaning that they involve only measurements of distances and volumes to derive the evolution of the scale factor. There are other interesting constraints which come from dynamical probes, such as Weak Lensing, which is a very powerful technique for mapping dark matter and its clumping. This involves the slight distortion of galaxy shapes due to gravitational bending of light by intervening large-scale structures.

Table 2.2: Cosmological density parameters and Hubble constant obtained from the combination of the 5-year WMAP data (Komatsu et al., 2009), the BAO constraints of Percival et al. (2007) and Type Ia Supernovae (Kowalski et al., 2008). As a comparison the recent results obtained from the Planck mission are also reported (Planck Collaboration et al., 2013).

Parameter	**WMAP+BAO+SN**	**Planck**
$\Omega_{\rm M}$	0.274 ± 0.015	0.315 ± 0.017
Ω_b	0.0456 ± 0.0015	0.0485 ± 0.0015
Ω_Λ	0.726 ± 0.015	0.686 ± 0.020
H_0	70.5 ± 1.3	67.4 ± 1.4

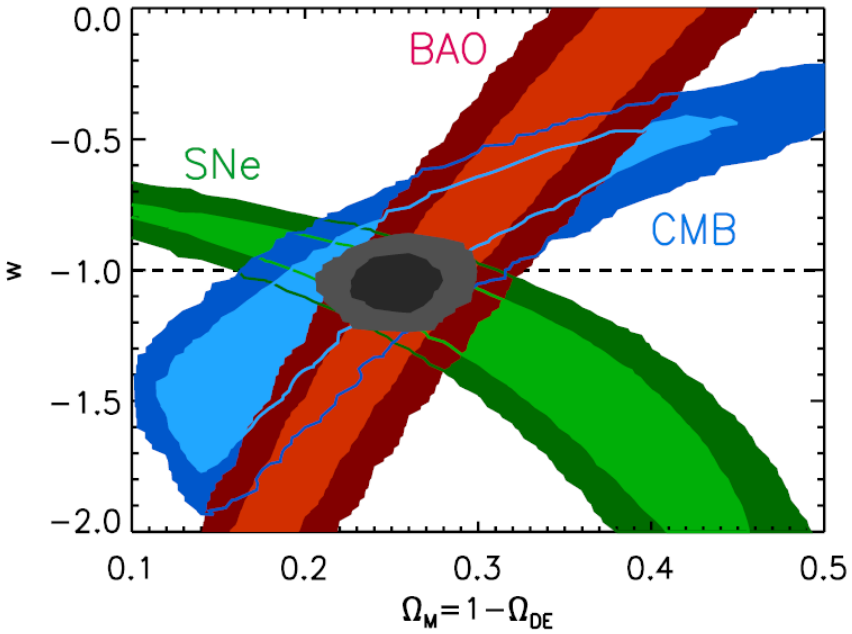

Figure 2.10: Parameter space of Ω_M and w with 68% and 95% confidence level contours of three independent cosmological probes: SNe Ia, BAO and CMB. Each cosmological probe populates a different area of this parameter space. Combining them reduces a great deal the confidence contours producing tight constraints on the cosmological parameters. From Turner & Huterer (2007).

The distribution and abundance of Galaxy Clusters at different epochs are also sensitive probes of dark energy. They measure structure growth on much smaller scales providing complementary information about the contribution of matter and dark energy to the total energy density Ω, as can be seen in Fig. 2.11. In order to determine the age of the Universe and as a further probe of dark energy it is useful to employ the oldest stars in Globular Clusters as shown in Fig. 2.12.

2.9 Non-Standard Cosmologies: Modified Gravity

The ultimate goal of the method proposed in this thesis is to differentiate between cosmological scenarios in an attempt to break the parameter degeneracy of ΛCDM. Since our method directly tests the geometry of the Universe without reverting to any assumptions made on its energy content, it provides an independent and consistent way to compare different cosmological models (or more precisely, the expansion history predicted by those models) based on rather disparate physical assumptions.

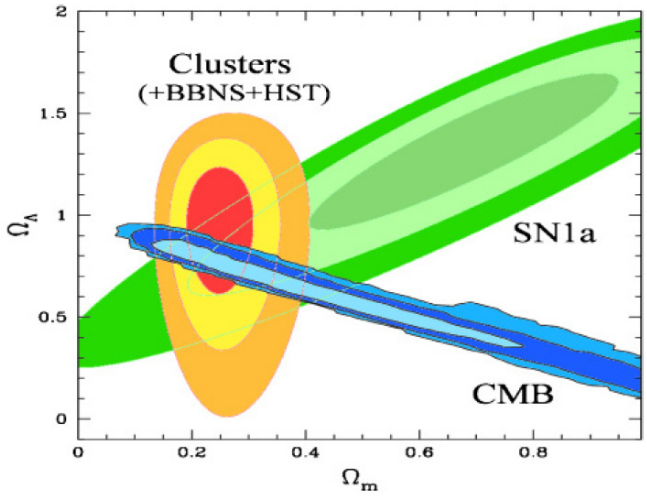

Figure 2.11: Age of the Universe as a function of the matter energy density, assuming a flat Universe and four different values of the dark energy equation of state w. The combination of constraints from globular clusters and from CMB is shown. Taken from Turner & Huterer (2007).

The standard model (and its theoretical foundation, General Relativity) described in Sec 2.8, though remarkably successful, breaks down at higher energies than the Planck scale $E \gtrsim M_p \sim 10^{16}$ TeV. Therefore the ΛCDM model can only give limited insights into the very early Universe. Moreover, General Relativity can accommodate accelerated expansion but cannot provide deeper understanding of the phenomenon or on the nature of the dark energy. Over the last few years, different approaches claiming that cosmic acceleration is a manifestation of new gravitational physics and not dark energy, have received increasing attention. Instead of adding an extra term (dark energy) to the stress-energy momentum on the right side of Einstein's equations, one can also modify the left side in order to reproduce the observations. In general, independent measurements of distance and redshift (as those seen in Section 2.11) can probe the expansion history $H(z)$ but cannot tell whether this comes from a *true* extra fluid in the cosmos budget, or from a change in the laws of gravity.

Modified gravity offers an alternative to break the observational parameter degeneracy of dark energy models and shed some light on the *fine-tuning* and *coincidence* (the fact that the dark energy is approximately exactely double as the total amount of matter) problems.

However, when modifying gravity one has to be extremely careful so as not to violate high precision tests of gravity in the local Universe, like the Solar System, and also not to introduce unphysical features in the theory, such as phantoms, which are fields with negative kinetic energy density (ghosts). Moreover, the new theory must satisfy some minimal mathematical properties

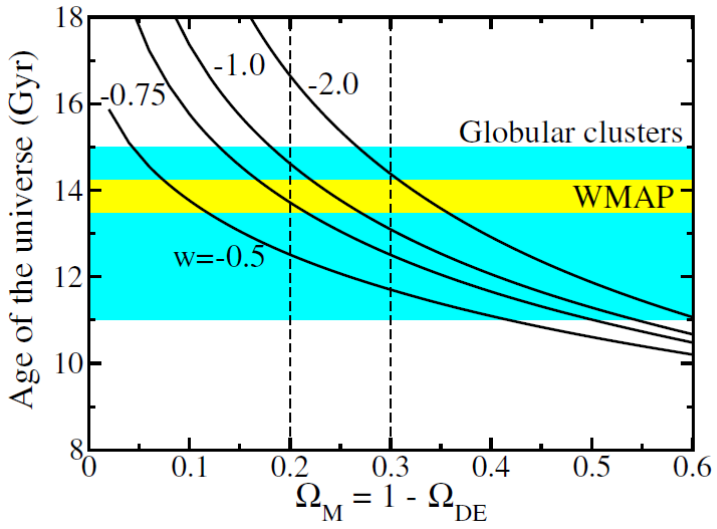

Figure 2.12: Parameter space of Ω_M and Ω_Λ of three independent cosmological probes: SNe Ia, galaxy cluster inventory and CMB. From Turner & Huterer (2007).

such as to allow a Lagrangian formulation, being Lorentz invariant or obey causality. Although many possibilities have been proposed, we will briefly consider only those that have been directly used in this work. For further details, the reader is referred to the studies quoted below.

2.9.1 Brane Worlds

Braneworld cosmologies are inspired by string theory and can be regarded as low energy effective models of a more fundamental theory. They suggest that the observable Universe could be described as a four-dimensional surface or *brane* embedded in higher dimensional spacetime (also called `bulk`). Branes are extended objects of higher dimensions than strings where the matter and radiation fields are localized. All matter particles and fields are trapped on the brane, i.e. conservation of mass-energy holds. In contrast, gravity is free to propagate in the brane as well as in the bulk.

The most common examples of braneworlds are the Randall-Sundrum models (Randall & Sundrum, 1999), where a 4D brane is embedded in a 5D de Sitter bulk. At low energies, General Relativity is recovered to a good approximation, whereas at high energies gravity behaves increasingly five-dimensional. This behaviour implies that a given energy density produces a greater rate of expansion than in General Relativity. This introduces significant changes to gravitational dynamics and perturbations, with interesting and potentially testable implications for high-energy astrophysics, black holes and cosmology.

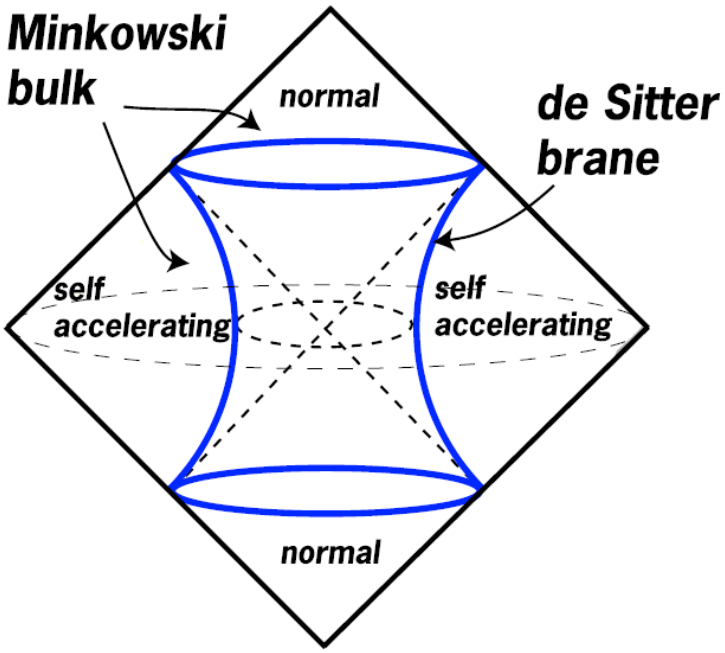

Figure 2.13: A representation of the embedding of a self-accelerating and normal branches of the DGP brane in a Minkowski bulk. From Durrer & Maartens (2008).

Alternatively, the Dvali-Gabadadze-Porrati (DGP) model (Dvali et al., 2001) modifies General Relativity at low energies. Here the bulk is assumed to be a 5D Minkowski space-time of large volume (see Fig 2.13). The Einstein-Hilbert action (Hilbert, 1924)

$$S = \frac{-1}{16\pi G} \int d^4x R\sqrt{-g} \tag{2.47}$$

is modified to

$$S = \frac{-1}{16\pi G} \left[\frac{1}{r_c} \int_{bulk} d^5x \sqrt{-g^{(5)}} R^{(5)} + \int_{brane} d^4x \sqrt{-g} R \right] \tag{2.48}$$

where r_c is the crossover scale, that sets the scale beyond which the laws of 4D gravity breakdown and become 5-dimensional. $g = |g_{\mu\nu}|$ is the determinant of the metric tensor. At large scales, $r \gg r_c$, gravity "leaks" off the 4D brane into the bulk whereas on small scales gravity is bound to the brane and 4D dynamics is recovered. The generalisation of this model to a Friedman-Robertson-Walker brane produces a *self-accelerating* solution (Deffayet, 2001) due to the weakening of gravity at low energies.

The resulting Friedman equation is a modification of the general-relativistic case

$$H^2 - \frac{H}{r_c} = \frac{8\pi G\rho}{3}, \tag{2.49}$$

with r_c defined as

$$r_c = \frac{1}{H_0(1-\Omega_{\rm M})}. \tag{2.50}$$

The additional term H/r_c in Eq. 2.49 behaves like dark energy with an equation of state that evolves from $w = -1/2$ for $z \gg 1$ to $w = -1$ in the distant future. The ΛCDM normalisation condition for the different components of the total energy density Ω is now given by

$$\Omega_k + \left(\sqrt{\Omega_{r_c}} + \sqrt{\Omega_{r_c} + \sum_i \Omega_i}\right)^2 = 1, \tag{2.51}$$

where

$$\Omega_{r_c} \equiv \frac{1}{4r_c^2 H_0^2} \tag{2.52}$$

and the index i refers to the different components of the energy density budget. The Friedman Equation in terms of the density parameters is

$$\frac{H^2(z)}{H_0^2} = \left[\Omega_k(1+z)^2 + \left(\sqrt{\Omega_{r_c}} + \sqrt{\Omega_{r_c} + \sum_i \Omega_i(1+z)^{3(1+w_i)}}\right)^2\right]. \tag{2.53}$$

Equations 2.49 and 2.49 imply that whenever the Hubble radius, H_0^{-1}, is small with respect to r_c the cosmological evolution follows that of General Relativity. When $r_c \sim H_0^{-1}$ a transition to an accelerated expansion occurs. The cosmological constant is replaced by the cross over scale, with the advantage that r_c is stable under quatum corrections.

The DGP model offers a full description of the expansion history as well as of the growth of large scale structure. However, recently-performed tests with current cosmological data allude to some tension and theoretical problems for this model, such as ghosts and 5D effects (see e.g. Song et al., 2007).

Going beyond DGP as an isolated theory one may consider a phenomenological model which is motivated by the concept of extra dimensions of infinite extent and arbitrary number of dimensions. This is the mDGP model, first introduced by Dvali & Turner (2003). It interpolates between ΛCDM and the DGP model and allows for the presence of extra dimensions through corrections to the Friedman equation with the addition of a parameter α. The modified Friedman equation reads

$$H^2 - \frac{H^\alpha}{r_c^{2-\alpha}} = \frac{8\pi G\rho}{3}, \tag{2.54}$$

where r_c is again the crossover scale defined by

$$r_c = (1 - \Omega_m)^{\frac{1}{\alpha-2}} H_0^{-1}. \tag{2.55}$$

It is easy to see that ΛCDM is recovered when $\alpha = 0$ and pure DGP when $\alpha = 1$. For $\alpha = 2$ In the case $\alpha < 0$ an effective equation of state less $w < -1$ is obtained while for $\alpha \geq 1$ the matter era necessary for structure formation and limits set by big bang nucleosynthesis are violated. The extreme $\alpha = 2$ corresponds to a "renormalization" of the Friedman equation and $\alpha > 2$ leads to early universe braneworld modifications. This model can be useful when attempting to distinguish between ΛCDM, general dark energy and modified gravity. Further information about the two models introduced above can be found in Tang et al. (2006), Thomas et al. (2009) and the review by Durrer & Maartens (2008).

2.9.2 $f(R)$ Models

A different alternative when modifying gravity are the $f(R)$ models, which do not assume the existence of extra dimensions. These theories generalize the Einstein-Hilbert action in Eq. 2.47 by adding a more general function of the Ricci scalar, e.g. terms proportional to powers of R,

$$S = \frac{-1}{16\pi G} \int f(R)\sqrt{-g}d^4x. \tag{2.56}$$

The field equations describing the geometry and energy density of the Universe are then derived from this action. $f(R)$ gravity was first proposed by Buchdahl (1970) and it has become an active field of research mainly due to Starobinsky's work (Starobinsky, 1980).

Different approaches may be followed in order to specify the form of the function $f(R)$ – see e.g Sotiriou & Liberati (2007). Some functional forms are inspired by corrections arising from a quantum theory of gravity and explain the accelerated expansion and structure formation of the Universe without invoking dark energy.

The simplest parameterisations lie within the Palatini approach which usually leads to second order differential field equations that produce acceleration at late times. The Palatini variational approach refers to a particular way in which the field equations are derived from the action. It assumes that the *affine connection* is independent of the metric (Palatini, 1919). Within this formalism also several parameterisations of $f(R)$ are possible. We consider, due to its simplicity, the one presented in Carvalho et al. (2008). For details on other parameterisations see e.g. Amarzguioui et al. (2006) or Hu & Sawicki (2007).

Here, the functional $f(R)$ is assumed to have the form

$$f(R) = R - \frac{\beta}{R^n}, \tag{2.57}$$

where R in the Rici scalar, and n and β, together with $\Omega_{\rm M}$ (see below), are the parameters of the model. The expansion rate can be written as

$$H^2(z) = H_0^2 \left[\frac{3\Omega_{\rm M0}(1+z)^3 + f/H_0^2}{6 f_R \xi^2} \right], \tag{2.58}$$

with

$$\xi = 1 + \frac{9}{2}\frac{f_{RR}}{f_R}\frac{H_0^2 \Omega_{\rm M0}(1+z)^3}{R f_{RR} - f_R}, \tag{2.59}$$

and where the notation $f_R = df/dR$, $f_{RR} = d^2 f/dR^2$ has been adopted.

Recent studies have shown that power-law functional forms of $f(R)$, such as the above-mentioned, are capable of reproducing the three phases of the cosmological evolution: radiation domination, matter domination and late time acceleration (Amarzguioui et al., 2006; Fay et al., 2007). However, it is still subject of debate whether $f(R)$ theories satisfy the Solar System tests and recover the Newton limit (Faraoni et al., 2006; Olmo, 2007; Barausse et al., 2008).

2.10 The Kinematic Approach

A different method to access the history of the cosmic expansion is by means of the so-called kinematic models, which avoid a dynamical description of the Universe and do not depend on the matter-energy content of the observed Universe. The only assumption is the validity of the cosmological principle (homogeneity and isotropy) so that the FLRW metric is still valid. We describe here the models discussed by Elgarøy & Multamäki (2006) and Guimarães et al. (2009), which are based on different parameterisations of the deceleration parameter, q, and the jerk parameter, j (second and third order contribution in the expansion, respectively). The deceleration parameter in terms of z is defined as

$$q \equiv -\frac{1}{H^2}\frac{\ddot{a}}{a} = \frac{1}{2}(1+z)\frac{(H(z)^2)'}{H(z)^2} - 1 \tag{2.60}$$

where $' \equiv d/dz$. Similarly the jerk parameter is given by

$$j \equiv -\frac{1}{H^3}\frac{1}{a}\left[\frac{d^3 a}{dt^3}\right] = -\left[\frac{1}{2}(1+z)^2\frac{(H^2)''}{H^2} - (1+z)\frac{(H^2)'}{H^2} + 1\right]. \tag{2.61}$$

In what follows we will use five realizations. The first and simplest model, M_0, is given by a constant deceleration parameter, $q(z) = q_0$. The second

model, M_1, is a linear expansion of the deceleration parameter $q(z) = q_0 + q_1 z$. Model M_2 has two phases of constant deceleration, separated by an abrupt transition redshift, i.e. $q(z) = q_0$ for $z \leq z_t$ and $q(z) = q_1$ for $z > z_t$. The fourth model, M_3 is a constant jerk parameterisation, $j(z) = j_0$. The last model, M_4, assumes an expansion of the luminosity distance with free q_0 and j_0 parameters such as

$$D_{\rm L}(z) = \frac{c}{H_0}\left[z + \frac{1}{2}(1-q_0)z^2 - \frac{1}{6}(1-q_0-3q_0^2-j_0)z^3\right] + O(z^4). \qquad (2.62)$$

All these models provide an equivalent description of the cosmic expansion and are very interesting in the sense that no assumption about the matter-energy content present in the Universe is required. The value of the jerk parameter today can be used as a measure of a possible deviation from the ΛCDM model.

3. Supernovae: Candles In The Universe

Supernova explosions constitute one of the most spectacular events in the Universe. They are mainly responsible for the creation of heavy elements as well as the enrichment of the interstellar medium. The amount of energy they release is so extreme (about $\sim 10^{53}$ erg), that they are able to trigger or suppress star formation in neighboring regions. Their luminosity at maximum sometimes outshines the entire host galaxy in which they explode. In less massive galaxies, the effects of supernova explosions may even change their structural properties.

Given their intense luminosity, supernovae are being used as favourite candidates to measure cosmological distances in the Universe (see Sec. 3.4). Furthermore, they have been used to determine dust properties and the star formation history of galaxies. They are also the major source of neutrinos after the Big Bang and the strong shock waves formed in their remnants produce and accelerate cosmic rays.

Roughly speaking, a supernova is the violent end of a star in which it ejects most of its material into the interstellar medium by means of a shock wave. This shock wave creates an expanding shell of gas and dust, which eventually forms the supernova remnant. Valuable information on stellar evolution and stellar composition can be obtained through these magnificent explosions. By properly modeling supernovae, insights on the physics, hydrodynamics, nucleosynthesis and radiation transport of the explosions can be achieved (see Leibundgut, 2008, for a review on the subject). Since they can be observed at large distances, they range amongst the objects we are able to see even at high look-back times.

3.1 Supernovae Classification

In the 1930s, the astrophysicists Baade and Zwicky made the first differentiation in an attempt to distinguish classical *novae* from supernovae (Baade & Zwicky, 1934). Observations showed that the spectra of `supernovae` looked very similar at the peak of their luminosity as well as at later phases. This evidence led Wilson to point them out as distance indicators (Wilson, 1939).

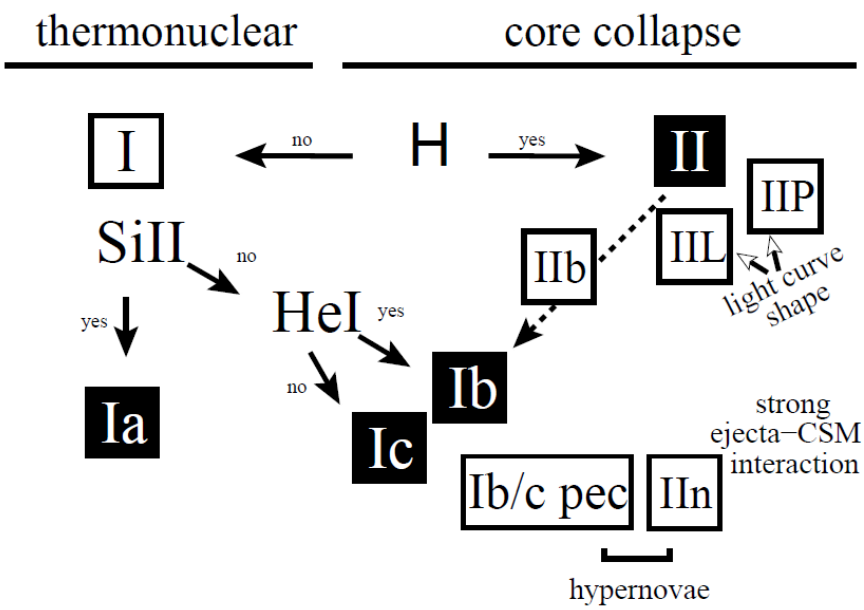

Figure 3.1: Classification scheme for supernovae from Turatto (2003). Type Ia SNe are associated with the thermonuclear explosion of white dwarfs. Other SN types are linked with the core collapse of massive stars. Some type Ib/c and IIn SNe with very high explosion energies are often called hypernovae and connected to Gamma Ray bursts.

A decade later, in 1940 the event SN 1940C in NGC 4725 was detected. This particular object showed many differences in the spectrum, the most significant being the presence of Balmer hydrogen lines near maximum. Soon it became obvious that not all supernovae had exactly the same characteristics and a new classification scheme for them was introduced by Minkowski (Minkowski, 1941).

The modern classification scheme was based entirely on the optical spectra at maximum light denoting as Type I those objects with no traces of hydrogen lines near maximum, and as Type II those which did show the Balmer hydrogen lines (Minkowski, 1941, 1964). With increasing number of observations a further separation was necessary within the first class. Those events that exhibited strong transitions of singly ionised silicon (Si II) near maximum light were designated as as Type Ia (Wheeler & Harkness, 1990), while supernovae with no prominent silicon lines were denoted as Type Ib/c (Filippenko et al., 1986; Filippenko, 1997a). The presence or absence of helium lines was used to further distinguish between Type Ib and Type Ic (Filippenko, 1997a; Wheeler & Levreault, 1985).

Figure 3.1 displays the most up-to-date classification diagram from Turatto (2003). It is worth mentioning that Type II SNe have been likewise divided into sub-groups attending to their light curve profiles or their relation to Gamma

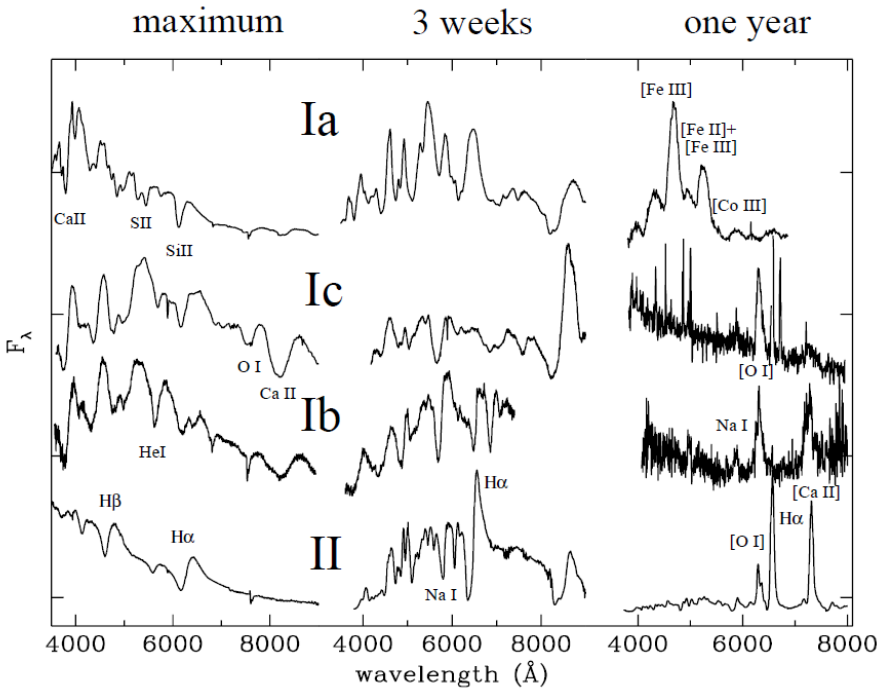

Figure 3.2: Spectra comparison of the main SN types at maximum, three weeks, and one year after maximum. The spectra correspond to the supernovae SN1996X for type Ia, SN1994I (left and center) and SN1997B (right) for type Ic, of SN1999dn (left and center) and SN1990I (right) for type Ib, and SN1987A for type II. At late times the contamination from the host galaxy is evident as an underlying continuum plus unresolved emission lines (Turatto, 2003).

Ray bursts (see Turatto, 2003, for a full review on supernova classification). In Fig. 3.2 characteristic spectra for the different supernova types are shown.

3.2 Explosion Mechanisms

Physical interpretation of the spectral classification is far from trivial and has founded a lively field of research aiming to explain the very different processes involved in supernova explosions.

The events corresponding to the right part of Fig. 3.1 are supposed to come from core collapse in massive stars (about $\sim 8-10M_\odot$). In these stars, hydrostatic equilibrium is maintained by burning to heavier elements at increasing temperatures and densities. Once the stellar core has burnt its fuel to iron and no further exothermic reactions are possible, radiation pressure can no longer support the core and it collapses under its own gravitational pull. The collapse is only halted when the material reaches nuclear densities where electrons and protons merge via inverse beta decay to create neutrons and neutrinos. At

this stage, a compact remnant, or a proto-neutron star, is formed. The gravitational binding energy of the neutron star is released by the neutrinos with a small fraction of their energy being transferred to the stellar envelope, which is then ejected in a violent explosion (Hoyle & Fowler, 1960). The mechanism in which this process occurs is still under investigation. If the star is more massive than $\sim 40 M_{\odot}$, the final product of the explosion might be a black hole, that is to say, an object of such great density that light is not able to escape from it.

Type Ia supernovae (SNe Ia hereafter) are observed in all types of galaxies (Turatto et al., 1994), in contrast with Type II and Ib/c which are predominantly observed in late-type galaxies. Since they are also present in elliptical galaxies, usually associated with very old stellar populations, SNe Ia cannot be the product of the core collapse of a massive star. Instead, SNa Ia are thought to be powered by the thermonuclear explosion of a degenerate star (most likely a carbon-oxygen white dwarf). Therefore, no traces of hydrogen and helium are observed in these explosions, which indicate a highly evolved progenitor. This also accounts for the lack of compact objects in their remnants. The thermonuclear origin of SNe Ia was first suggested by Hoyle & Fowler (1960). Since then, a great deal of models have been developed and tested with more and more refined simulation techniques, trying to identify the progenitor systems and the explosion conditions.

3.2.1 Thermonuclear Supernovae

It is well known that a Sun-like star consumes its nuclear fuel over 5 to 10 billion years. Afterwards, it reaches the red giant stage ejecting gradually the outer layers through strong winds. Finally, it shrinks to a carbon-oxygen white dwarf, with electron degeneracy pressure as the only means to avoid further collapse. If the star is isolated, it quietly and slowly cools down and fades away. But if the star happens to be in a binary system, with a main-sequence or another degenerate star as companion, dynamical interactions between them may lead to instabilities which can eventually trigger an explosion. The nature of these systems is still a matter of debate.

The two broad classes of possible progenitors are the *single degenerate* scenario, in which a white dwarf accreting from a binary companion is pushed to a certain mass limit which ignites the explosion; and the *double degenerate* scenario in which gravitational radiation causes an orbiting pair of white dwarfs to violently merged disrupting the system.

For decades, the single degenerate channel was the accepted paradigm to explain SN Ia explosions. However, in the last few years there is growing evidence for the double degenerate channel being the responsible mechanism for a considerable part (if not the majority) of the thermonuclear events (Pakmor et al., 2012).

The standard picture for the great luminosity observed in SN explosions is known to arise from the γ-photons produced in the radio-active decay of ^{56}Ni through ^{56}Co to ^{56}Fe (Truran et al., 1967; Colgate & McKee, 1969; Kuchner et al., 1994). ^{56}Ni (most tightly bounded α nucleus) is abundantly synthesized in thermonuclear burning at high densities. By electron-capture processes it decays to unstable ^{56}Co with a half time of $\sim$6.1 days and further to stable ^{56}Fe with a half time of $\sim$77 days. The γ-rays originating from these decays interact with the ejecta via Compton scattering and photo-electric absorption and are thermalized to optical light (see Sec. 3.3.1 for details on SN Ia light curves).

Different flame-propagation modes during the explosion have been proposed in the literature. There are pure `deflagration` models where a burning front, or flame, propagates more slowly than the local sound speed (Niemeyer et al., 1996; Reinecke et al., 1999), and `detonations` with supersonic flame propagation (Arnett, 1969). The former scenario, however, does not produce the correct amount of ^{56}Ni and yields too strong mixing of the intermediate mass elements, in contradiction with observations. The latter scenario, on the other hand, produces too much ^{56}Ni for a standard Chandrasekhar-mass explosion.

A third possibility, are `delayed detonations`, where the flame transitions to a detonation after starting as deflagration (e.g. Khokhlov, 1991; Röpke et al., 2007). The last few years have seen an increasing activity in extending the simulations to three dimensions to explore the effects of asymmetries (Reinecke et al., 2002; Gamezo et al., 2003; Röpke & Hillebrandt, 2005; Röpke et al., 2007) and to account for peculiar supernovae in the different scenarios. We highlight here only two models, which are regarded as the most plausible explanations for SN Ia explosions. For an overview on the topic we refer the reader to the reviews of Hillebrandt & Niemeyer (2000) and Hillebrandt et al. (2013).

Delayed Detonation of a Carbon-Oxygen White Dwarf

The delayed detonation model is the most promising realization of the *single-degenerate* scenario and one-dimensional simulations have been very successful in reproducing normal SNe Ia (Blondin et al., 2013).

In this particular model, a white dwarf in a binary system steadily accretes material from its non-degenerate companion (still on the main sequence) through the inner Lagrange point of the system. When the critical mass of 1.4 $M_\odot$ (the Chandrasekhar limit; Chandrasekhar, 1931) is reached, the density in the center becomes large enough to ignite carbon fusion and eventually a thermonuclear runaway occurs. This leads to the ignition of a thermonuclear flame that propagates through the star and burns its carbon and oxygen to heavier elements. The energy released is enough to disrupt the star in a supernova explosion.

As mentioned above, it was noted that a pure deflagration would not burn

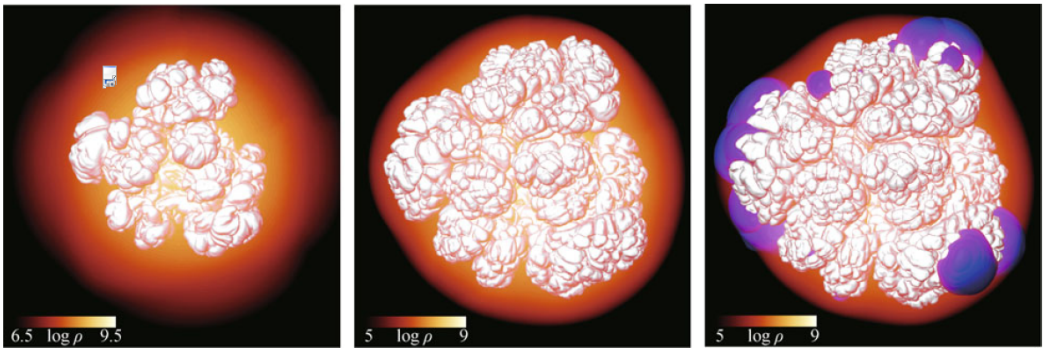

Figure 3.3: Snapshots of a 3-D simulation of a Chandrasekhar-mass delayed detonation. The white surface and the blue colors represent the deflagration front and the detonation flames, respectively. From Hillebrandt et al. (2013)

enough material and release sufficient nuclear energy, and that it does not reflect the proper amount of mixing observed in SN ejecta. A detonation occurring at some late stage after the deflagration phase could solve this shortcoming. In this case, the combustion starts out in a deflagration mode bringing the white dwarf out of hydrostatic equilibrium and pre-expanding the fuel. Subsequently, a spontaneous transition of the burning front from the (sub-sonic) deflagration to the (super-sonic) detonation occurs (Khokhlov, 1991). This mechanism allows for the necessary amount of ^{56}Ni while also synthesizing a substantial amount of intermediate mass elements in the outer layers of the exploding white dwarf, as suggested by observations. An example of this model is shown in the simulation of Fig. 3.3.

Violent mergers of two White Dwarfs

Alternative explosion models for SN Ia have also been discussed in literature, within both the *single* and *double degenerate* scenarios. Within the latter, it has been shown that a violent merger of two carbon-oxygen white dwarfs can lead to a SN Ia explosion (Pakmor et al., 2012).

At an early stage, the two stars within the binary system evolve separately while exchanging mass through their Roche-lobes in a stable manner. A common envelope phase may occur in which both stars are brought to a closer binary orbit. After this, gravitational-wave emission makes the binary system to orbit in a slow inspiral and mass transfer becomes unstable. In the last few orbits before the actual merger, tidal forces heavily deform the less massive of the white dwarfs. Hot spots, formed on the surface of the primary white dwarf, are sufficiently dense to ignite a detonation. Subsequently, the detonation front burns the merged object almost entirely. Figure 3.4 shows the hydrodynamic evolution and thermonuclear explosion of two white dwarfs with initial masses 0.9 and $1.1 M_{\odot}$.

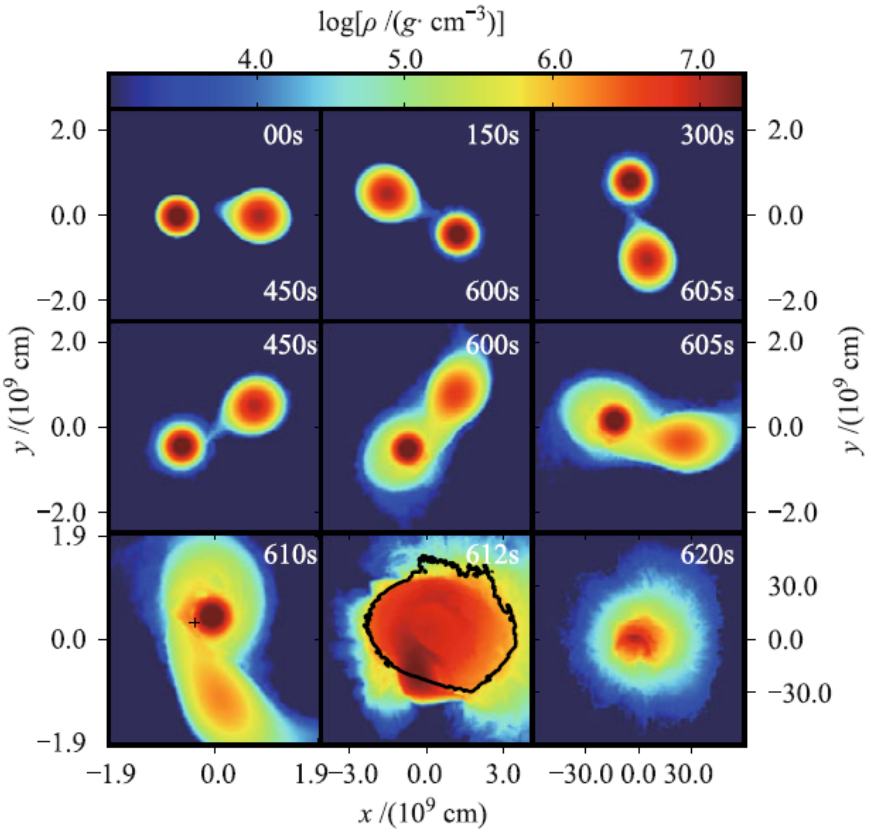

Figure 3.4: The merger of a pair of white dwarfs with 1.1 $M_\odot$ and 0.9 $M_\odot$ simulated with the SPH GADGET and the LEAFS codes. Redder colors correspond to higher densities. From (Pakmor et al., 2012).

3.3 Observational Characteristics

As stated in Section 3.1, SNe Ia are defined observationally by the absence of hydrogen and helium and the presence of a strong silicon absorption line (Si II, $\lambda \sim 6150\mathring{A}$) in their early-time spectra (Filippenko, 1997a). The last few years have seen great progress in observing SNe Ia, and identifying some events that are clearly different. Many nearby supernovae are now observed with exquisite detail by intensive surveys such as the Nearby Supernovae Factory (Aldering et al., 2002a) or the Palomar Transient Factory (Law et al., 2009). Observations have revealed the great homogeneity in luminosity as well as the identical spectral evolution that SNe Ia exhibit at maximum light (Branch & Tammann, 1992; Hamuy et al., 1996; Branch, 1998). This uniformity offers standard spectral and light-curve templates, which are very useful in singling out other supernovae with peculiar features. The differences can be attributed, most likely, to variations in the progenitor star, in accretion and rotation rates, or in different carbon-to-oxygen ratios and flame ignition. All these factors are

highly dependent on the scenario which is chosen to model SN Ia explosions.

Moreover, it is worth noting that the distant objects appear to follow the same spectral evolution throughout the explosion, and afterwards, as their nearby counterparts (Blondin et al., 2006; Garavini et al., 2007).

3.3.1 Light Curves and Spectra

Typically, SN Ia light curves are measured using the standard broad-band filters from the Bessel system: U, B, V, R, I for the optical spectrum, and J, H, K for the near-infrared (NIR) part (Bessell, 1990).

Standard SNe Ia, also called *Branch-normal* (Branch et al., 1993), reach their maximum luminosity about 20 days after the explosion, with an absolute magnitude of approximately $M \sim -19$ in both the B and V passbands (Riess et al., 1999). Then a rapid decline of around 2-3 magnitudes in one month occurs, followed by an exponential downfall about 50 days post maximum (Leibundgut, 2000). A second maximum usually arises 20 to 30 days after the first one in NIR bands (Meikle & et al., 1997). The colors in SN Ia evolve from blue before peak magnitude to red thereafter. This transition is especially evident in the $B - V$ color changing from $\sim$0.1 at 10 days before maximum to $\sim$1.1 around 30 days after maximum light. Characteristic light curves of several SNe Ia in four different passbands are displayed in Fig. 3.5.

As we mentioned before, the most prominent feature of optical SN Ia spectra is the blue-shifted doublet of Si II around 6150$\mathring{A}$ (see Fig. 3.6). Additionally, several lines of other intermediate-mass elements such as Ca, Mg, S, and O can be seen at maximum light. Their densities and excitation states are the same from one supernova to another (Filippenko, 1997b). At early phases, the ejecta of SNe Ia is optically thick and expanding at velocities of about 20 000 km s^{-1} (Branch et al., 2005). This is confirmed by the P-Cygni profiles of the absorption lines, which form the characteristic pattern of resonant line scattering in an expanding atmosphere. As the gas moves outward, the outer layers become transparent allowing to look deeper inside the ejecta. Observations reveal that absorption features of different elements originate at different depths of the ejecta and that its velocity decreases from outside-in. Studies of the observed abundance stratification can help to constraint the spectral evolution of SNe Ia (Stehle et al., 2005). Two weeks after maximum iron-group elements (mostly Fe II and Co II) start to dominate the spectra (Harkness, 1991). At even later phases, around 100 days after maximum, forbidden emission lines of Fe III and Co III appear, indicating the beginning of the so called *nebular phase*. At this stage, the ejecta has become optically thin due to the expansion and radiative cooling in forbidden lines occur. This, and the fact that the ratio of [Co III] to [Fe III] corresponds to the characteristic abundance ratio of cobalt and iron for radioactive decay, supports the idea that the light curve in SNe Ia is powered by the radioactive decay of ^{56}Ni $\rightarrow$ ^{56}Co $\rightarrow$ ^{56}Fe (Truran et al., 1967; Colgate & McKee, 1969).

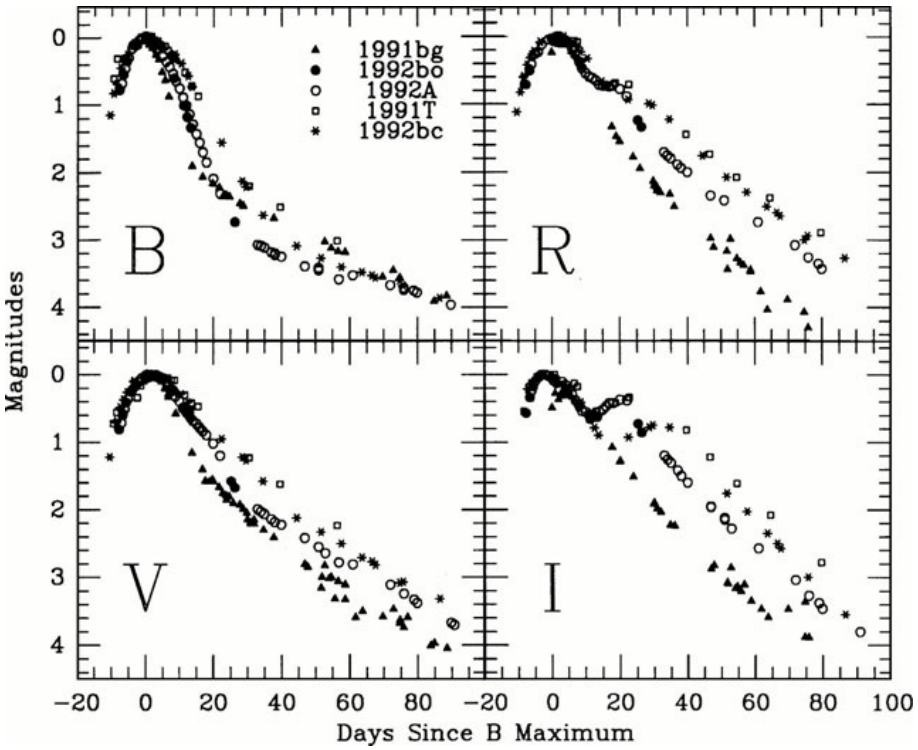

Figure 3.5: Light curves of several SNe Ia in the B, V, R and I bands. From Suntzeff (1996) and Filippenko (1997a).

Despite the genereal absence of hydrogen and helium signatures in SN Ia spectra, some events, such as 2002ci (Hamuy et al., 2003) or 2007le (Simon et al., 2009), do present narrow Hα emission lines which have been identified with circumstellar material surrounding the supernova. These observations contribute to the understanding of the relation between progenitor systems and dust properties, essential for cosmological distance determinations (Goobar, 2008; Folatelli et al., 2010).

3.3.2 Diversity and Correlations: The Phillips Relation

Differences in spectra and light curves of SNe Ia are, actually, strongly correlated (Hamuy et al., 1996; Filippenko, 1997a). The most important of these correlations was established by Mark Phillips at the Cerro Tololo Interamerican Observatory in Chile. It relates the width of the light curve to the absolute magnitude, showing that SN Ia brightnesses deviate from that of a template light curve in a very predictable way (Phillips, 1993). Supernovae with faster declining light curves are fainter and redder at their peak. On the other hand, SN with higher peak luminosities decline more slowly after the peak and show, in general, bluer colors (Branch 1998 - see Fig. 3.7). This empirical correlation of peak luminosity with light curve shape, which theoretically seems to arise

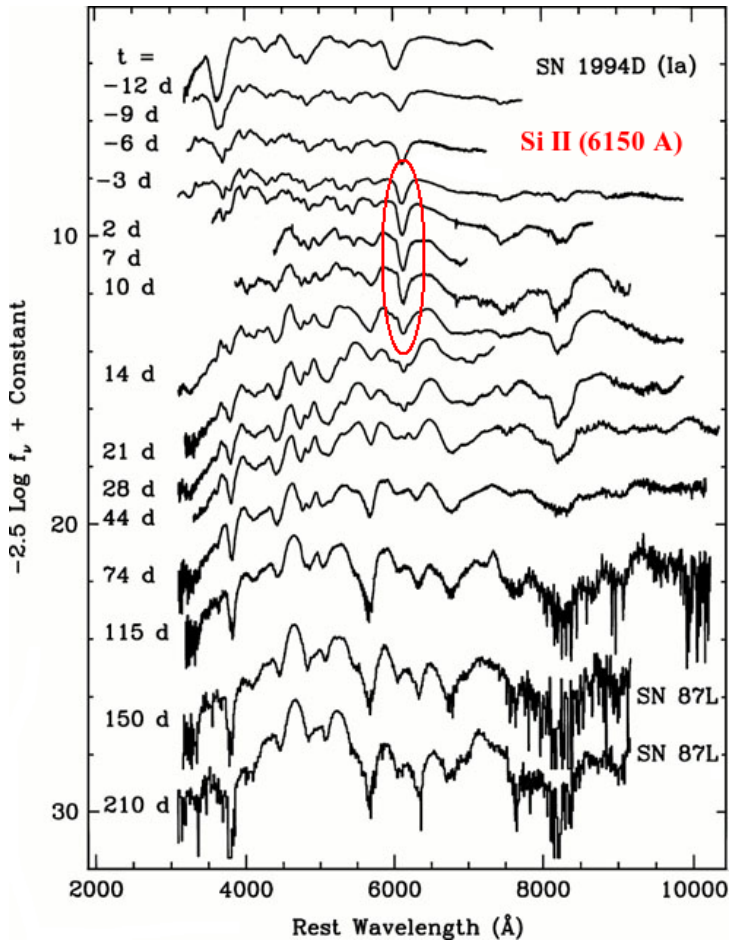

Figure 3.6: Time-series spectra of SN Ia 1994D. Epochs (days) are given relative to maximum B brightness. The main spectroscopic feature, the Si II double at 6150$\mathring{A}$, is highlighted in red. From Patat et al. (1996) and Filippenko (1997a).

from radiative transfer effects (Höflich & Khokhlov, 1996; Kasen & Woosley, 2007), can be used to renormalise the peak magnitudes of a sample of objects and recalibrate each supernova to infer its intrinsic brightness (Phillips, 1993; Perlmutter et al., 1997; Riess et al., 1996).

This calibration is in fact crucial for cosmological surveys that use SNe Ia as distance indicators (e.g. Perlmutter et al., 1999; Schmidt et al., 1998; Riess et al., 1998). Phillips (1993) parameterised the light-curve shape with the parameter Δm_{15} which is the decay in B-band magnitude 15 days after the peak. He first quantified the correlation using a handful of objects including the archetypes of low and high luminosity SN Ia: SN 1991bg and SN 1991T highlighted in Fig. 3.8. Supernova 1991bg is a good example of red and subluminous (about ∼2 mag dimmer) event with a fast declining light curve. No second maximum in the I-band light curve was observed in this supernova, and

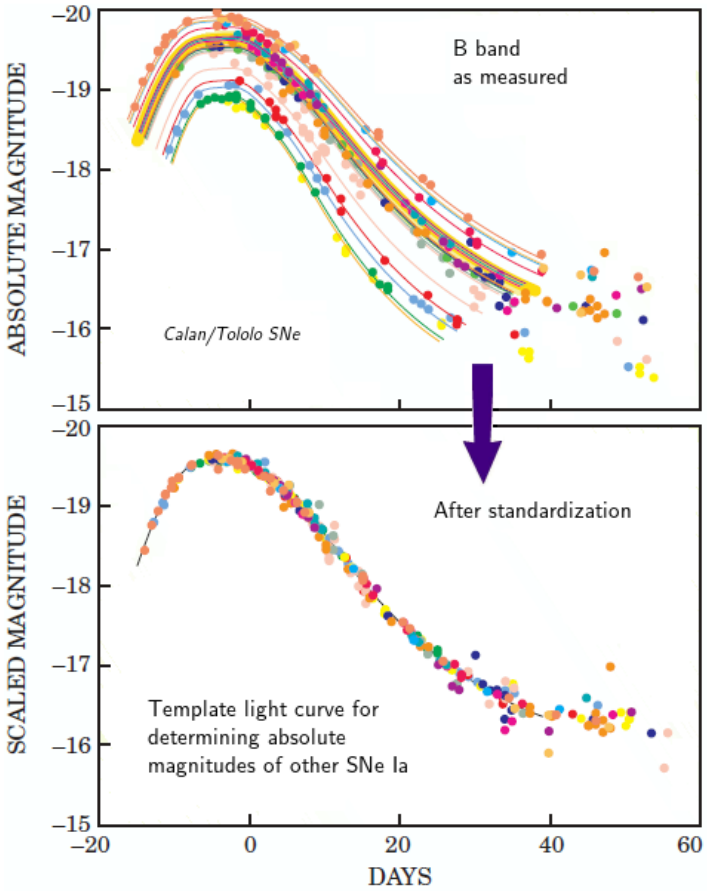

Figure 3.7: SN Ia light curves from the Calán Tololo Observatory. In the upper plot the scatter in absolute luminosity and the correlated light-curve width is shown. In the bottom plot the scatter is reduced after stretching the light curve and rescaling the luminosity accordingly. Taken from Perlmutter & Schmidt (2003).

the spectra showed very little iron but high abundance of intermediate mass elements with low expansion velocities (Filippenko et al., 1992; Leibundgut et al., 1993; Hamuy et al., 1994; Turatto et al., 1996). In contrast with normal SNe, a strong absorption feature corresponding to a blend of lines of Ti II was observed in the spectra of this object. Modeling of both spectra and light curve show that the total amount of ^{56}Ni present in the ejecta was about 0.07 solar masses, very low compared with *Branch-normal* supernovae (Mazzali et al., 1997).

On the contrary, SN 1991T appeared to be more luminous (by ∼0.3 mag) and energetic with broad light curves and strong lines of Fe III dominating the early spectrum, instead of the expected Si and Ca features (Jeffery et al., 1992; Filippenko et al., 1992; Ruiz-Lapuente et al., 1992). Moreover, other even brighther (about ∼1 mag) events have been detected within the SN zoo

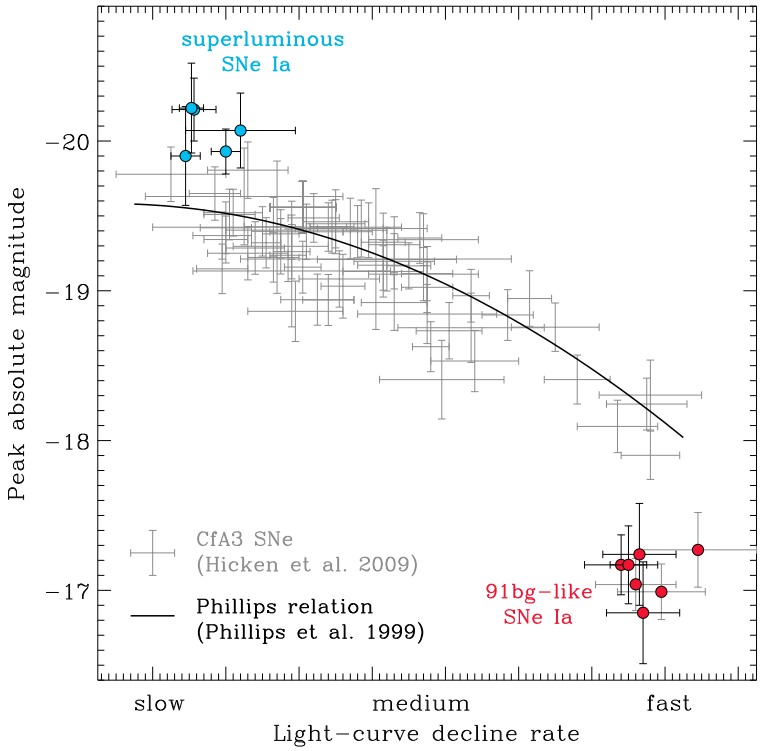

Figure 3.8: Phillips relation for the CfA3 SN data (Hicken et al., 2009a). Blue points represent superluminous events. Red points correspond to the underluminous class of SN 1991bg-like SNe. Courtesy of S. Taubenberger.

(see Fig 3.8). These are thought to arise from super-Chandrashekar mass explosions (see e.g. Jeffery et al., 2006; Hachinger et al., 2012).

The diversity in SN Ia light curves is even nowdays not fully understood, though much progress has been achieved. The peculiar supernovae appear to produce 5% non-Gaussian tails in the SN Ia fraction distribution (Li et al., 2011) and it is still unclear whether they come from different progenitors or are products of distinct explosion mechanisms.

After filtering out the peculiar SNe spectroscopically and correcting the light curves, little dispersion is found in well measured optical band peak magnitudes of SNe Ia and luminosity-distance estimates with around 6% uncertainty can be obtained. The development of corrections for the correlation between SN color and extinction (Riess et al., 1996; Tripp, 1998; Phillips et al., 1999) and *K-corrections* for redshift effects (Kim et al., 1996; Nugent et al., 2002) has proven very important for the accurate determination of cosmological distances.

Another interesting correlation is the one relating the type of host galaxy in which the explosion occurs with the colors and velocities of SNe. It has been shown (Hamuy et al., 1995, 1996; Sullivan et al., 2010) that fainter supernovae

with lower ejecta velocities are usually found in red, early-type galaxies; conversely, brighter supernovae are more common in blue or late-type galaxies (usually in inner regions of spiral galaxies).

3.4 The Standardization Process of SNe Ia

To a rough approximation, SNe Ia are standard candles (see Section 2.6.1), with a dispersion of approximately 0.4 magnitudes in V-band at maximum brightness (Hamuy et al., 1996; Riess et al., 1996). This scatter can be sharply reduced by means of the Phillips relation mentioned in the previous Section and depicted in Fig. 3.8. All current methods to standardize SN light curves are based upon the empirical correlation between light-curve width and peak luminosity, with different parameterizations for it.

Generally speaking, SN Ia color depends on the light-curve parameter, altough variations in color are also present for a fixed light-curve shape. This variation is believed to arise from different explosion mechanisms, host galaxy dust and the surrounding environment of the SNe, but its origin and nature is still not well understood. Independently from the process producing differences in color, an appropriate correction needs to be applied to improve the distance measurements from SN Ia. The most common approach is to fit the light curves with one parameter family of templates and add a color law describing variations in color.

The color excess, generally expressed as $E(B-V)$, can be easily determined from multiband photometry and a specific color law. The color correction is related to the extinction correction via the parameter

$$R_V = \frac{A_V}{E(B-V)}. \tag{3.1}$$

where A_V is the extinction in the V-band. This is the well-know parameterisation of Cardelli et al. (1989) where the parameter R_V can be estimated by measuring A_V or by comparing the relative extinction in different filters. Studies of the extinction in the Milky Way yield an averaged value of $R_V = 3.1$ (Sneden et al., 1978). However, other SN analyses have indicated a lower value for it. For instance, Kessler et al. (2009) investigated color variations and found $R_V = 2.8 \pm 0.14$ with the Sloan Digital Sky Survey II SN data (Frieman et al., 2008). Also, Nobili & Goobar (2008) found a smaller value of $R_V = 1.75 \pm 0.27$, though this analysis was qualitatively different.

The two mainstream light-curve fitters to standardize SNe are the Multicolor Light Curve Shape (MLCS; Riess et al., 1996; Jha et al., 2007) technique used by the High-z Supernova Search Team (Schmidt et al., 1998) and the stretch-factor formalism SALT (Spectral Adaptive Light curve Template Guy et al., 2005), employed by the Supernova Cosmology Project (Perlmutter et al., 1997).

MLCS fitters create a set of light-curve templates in multiple passbands using well-observed nearby SNe Ia to determine the relationships between multiband light curve shapes and peak absolute magnitudes. The different parameters of the analysis, such as intrinsic color, rate of decline, peak brightness, V-band extinction in the host galaxy and distance modulus, are determined by fitting each multiband set of distant supernova light curves to redshifted versions of these templates (Jha et al., 2007; Wood-Vasey et al., 2007)

In contrast, SALT-style fitters perform a global, simultaneous fit of parameters describing cosmology and the relationship between supernova light curves and absolute magnitude. The main difference between these two methods is the treatment they perform on supernova colors. While MLCS links the differences in color in SNe Ia at maximum light to dust reddening (adopting an explicit prior for the distribution of the reddening), the SALT approach allows scatter in intrinsic color and does not attempt to separate intrinsic variations from dust (Weinberg et al., 2012).

At the level of precision of current data samples, the differences in techniques fitting the light curves are significant. Therefore, a better understanding is necessary to fully explain the light-curve shape and color corrections and is currently an area of active research (Weinberg et al., 2012). We will summarize here the characteristics of both MLCS and SALT and highlight the main differences concerning SN light-curve and cosmological results.

3.4.1 The SALT Fitter

Essentially, in the SALT2 approach (the update of SALT, Guy et al., 2007) the photometry of each SN is fitted to an empirical model to determine the correction parameters. The SN rest-frame spectrum – $F(\mathrm{SN}, p, \lambda)$ – is modeled as a function of both wavelength, λ, and time since B-band maximum, p, and derived through a pseudo-principal component analysis based on both photometric and spectroscopic data. Most of these data come from nearby SN Ia data, but higher redshift data as the Supernova Legacy Survey SNe (Astier et al., 2006) are also included. The model consists of three components, namely a term for the time-dependent spectral average, $M_0(p, \lambda)$, a term for the variation from the average, $M_1(p, \lambda)$, accounting for the correlation of peak brightness and color with light-curve shape, and a wavelength-dependent color law $\mathrm{CL}(\lambda)$. The three components are determined from the training process and combined as

$$\begin{aligned} F(\mathrm{SN}, p, \lambda) &= x_0 \times [M_0(p, \lambda) + x_1 \times M_1(p, \lambda)] \\ &\quad \times \exp\left[c \times \mathrm{CL}(\lambda)\right]. \end{aligned} \tag{3.2}$$

In this context, x_0 describes the flux normalization, x_1 is the shape-luminosity parameter accounting for the deviation from the average decline rate, and c is the color parameter which encodes the difference in measured color and the

mean color for a given x_1. These parameters are determined for each observed SN by fitting the model to the available data. The fit is carried out in the observer frame by redshifting the model, correcting for Milky Way extinction (using the law from Cardelli et al., 1989, with the usual value of $R_V = 3.1$) and multiplying by the effective filter transmission functions provided by the different observatories.

The distance modulus is then obtained by combining the three parameters $m_B^{max} = -2.5\log_{10}[\int_B F(\mathrm{SN}, 0, \lambda)..\lambda d\lambda]$, x_1 and c for each SN through the equation:

$$\mu_B = m_B^{\max} + \alpha \cdot x_1 - \beta \cdot c + \delta \cdot P(m_\star^{\mathrm{true}} < m_\star^{\mathrm{threshold}}) - M_B\,, \tag{3.3}$$

where M_B is the absolute B-band magnitude, and α, β and δ are the correction parameters for shape, color and host mass, respectively. The global parameters α, β, δ and M_B describe the SN Ia population and are estimated simultaneously with the cosmological parameters by carrying out the following χ^2 minimization (Conley et al., 2006):

$$\chi^2_{\mathrm{stat}} = \sum_{\mathrm{SNe}} \frac{\left[\mu_B(\alpha, \beta, \delta, M_B) - \mu(z; \Omega_M, \Omega_w, w)\right]^2}{\sigma^2_{\mathrm{ext}} + \sigma^2_{\mathrm{sys}} + \sigma^2_{\mathrm{lc}}}, \tag{3.4}$$

where

$$\sigma^2_{\mathrm{lc}} = V_{m_B} + \alpha^2 V_{x_1} + \beta^2 V_c + 2\alpha V_{m_B,x_1} - 2\beta V_{m_B,c} - 2\alpha\beta V_{x_1,c} \tag{3.5}$$

is the propagated error from the covariance matrix, V, of the light-curve fits.

There is evidence that SN Ia luminosity correlates with the mass of the host galaxy, even after the corrections for color and light-curve width have been applied (Kelly et al., 2010; Sullivan et al., 2010). Low-redshift SNe Ia usually come from surveys that observe catalogued galaxies and generally have brighter absolute magnitudes, due to the fact that host galaxies of SNe Ia in these surveys are, on average, more massive than the host galaxies of distant SNe Ia. It has been proven that this correlation biases cosmological results (Sullivan et al., 2010) and can be relatively easily corrected by fitting a step in absolute magnitude at $m_\star^{\mathrm{threshold}} = 10^{10} M_\odot$. Within the Union2 compilation (see Sec 3.6.3), a probabilistic approach to determine the proper host-mass correction for each SN is adopted, since host-mass data are not available in the literature for all SN hosts.

Finally, uncertainties due to host galaxy peculiar velocities, Galactic extinction corrections and gravitational lensing are included in the term σ_{ext} in Eq. 3.4. Additionally, a dispersion term, σ_{sys}, which contains potential sample-dependent systematic errors and the observed intrinsic SN Ia dispersion, is also included. Computing a separate σ_{sys} for each sub-sample appears beneficial, since it prevents samples with poorer-quality data from increasing the errors of the whole sample. A number of systematic errors are also considered for the

full cosmology analysis within the SALT2 paradigm. These are taken into account by constructing a covariance matrix for the entire sample. For a detailed explanation on systematic errors see Sec. 3.6.4.

3.4.2 The MLCS Fitter

The MLCS method, and its update MLCS2k2 (Riess et al., 1996; Jha et al., 2007), describes the variation among SN Ia light curves with a single shape parameter Δ. The color variations relative to the model are assumed to be the result of extinction by dust in the host galaxy and in the Milky Way. The MLCS model magnitude is defined as

$$\begin{aligned} m^{e,f}_{\rm model} &= M^{e,f'} + p^{e,f'}\Delta + q^{e,f'}\Delta^2 \\ &\quad + X^{e,f'}_{\rm host} + K^{e}_{ff'} + \mu + X^{e,f}_{\rm MW}, \end{aligned} \tag{3.6}$$

where e is an epoch index that runs over the observations, f are observer-frame filter indices, f' are the rest-frame filters for which the model is defined, Δ is the shape-luminosity parameter that accounts for the correlation between peak luminosity and the shape/duration of the light curve. $X_{\rm host}$ is the host-galaxy extinction (which is assumed to behave similarly to dust in the Milky Way), $X_{\rm MW}$ is the Milky Way extinction, $K_{ff'}$ is the K-correction between rest-frame and observer-frame filters, and μ is the distance modulus. The extinction is described using the parameterization of Cardelli et al. (1989).

The coefficients $M^{e,f'}$, $p^{e,f'}$, and $q^{e,f'}$ are model vectors evaluated using a training set of around 100 well-observed low-redshift SNe. The parameter $M^{e,f'}$ refers to the absolute magnitude for a SN Ia with $\Delta = 0$ and the p and q vectors translate the shape-luminosity parameter Δ into a change in the SN Ia absolute magnitude. Essentially, intrinsically faint (bright) SNe have positive (negative) values of Δ.

Via adequate K-corrections, the MLCS rest-frame magnitudes are transformed to the magnitudes of a redshifted SN in a particular observed passband. K-corrections are usually computed following the prescription of Nugent et al. (2002), which requires a SN spectrum at each epoch, the spectrum of a reference star, and the reference star magnitude in each passband.

Performing the light-curve fit determines the likelihood function $\mathcal{L}$ of the observed magnitudes (or fluxes) as a function of four parameters for each SN Ia. These are the time of peak luminosity in the rest-frame B-band, t_0, the shape-luminosity parameter, Δ, the host-galaxy extinction in the V-band, A_V, and the distance modulus, μ. The redshift, z, is accurately determined from the spectroscopic analysis, and therefore it is not used as a parameter in the fit. However, the uncertainty in redshift is included in the error estimates. For each SN, the χ^2 statistic function is given by

$$\chi^2 = -2\ln\mathcal{L}({\rm data}|t_0, \Delta, A_V, \mu) - 2\ln P_{\rm prior}(z, A_V, \Delta), \tag{3.7}$$

where $P_{\rm prior}$ is a Bayesian prior and the log-likelihood is given by

$$-2\ln\mathcal{L} = \left\{ \sum_i \frac{\left[F_i^{\rm data} - F_i^{\rm model}(t_0, \Delta, A_V, \mu)\right]^2}{\sigma_{i,\rm stat}^2 + \sigma_{i,\rm model}^2} \right\}. \tag{3.8}$$

In this last equation, the index i runs over all measured epochs and observer-frame passbands, and $F_i^{\rm data}$ is the observed flux for each measurement i. The term $\sigma_{\rm stat}$ is the statistical measurement uncertainty and $\sigma_{\rm model}$ is the model uncertainty estimated from the spread in the training sample of SNe.

Since A_V is a physical parameter that is always positive, and since it is not well constrained when the signal is low compared to the noise, or when the observations do not cover a large wavelength range, the MLCS fit includes a Bayesian prior on the extinction. The prior forbids negative values of A_V and encodes information about the distribution of extinction in SN host galaxies as well as the selection efficiency of the survey. It has been shown (Kessler et al., 2009) that the prior does not have a significant impact on the inferred parameters. MLCS provides an estimate of the distance modulus, μ, for each SN via Eq. 3.7. Subsequently, the cosmological parameters are derived by minimizing the following χ^2 statistic function for the entire SN Ia sample,

$$\begin{aligned} \chi^2_\mu &= \left\{ \sum_i \frac{[\mu_i - \mu(z_i; w, \Omega_{\rm M}, \Omega_{\rm DE}, H_0)]^2}{{\sigma_\mu}^2} \right\} \\ &\quad + \chi^2_{\rm BAO} + \chi^2_{\rm CMB}, \end{aligned} \tag{3.9}$$

where $\mu(z_i; w, \Omega_{\rm M}, \Omega_{\rm DE}, H_0)$ is the model distance modulus. The terms $\chi^2_{\rm BAO}$ and $\chi^2_{\rm CMB}$ incorporate information from BAO (Eisenstein et al., 2005) and CMB measurements (Larson et al., 2011), respectively. The minimum of χ^2 is marginalized over H_0 in the global fit due to the degeneracy between the Hubble parameter and the peak rest-frame model magnitude. The distance-modulus error is given by combining in quadrature the statistical uncertainty from MLCS with an additional (intrinsic) error and the redshift uncertainty.

3.4.3 Comparison of MLCS and SALT2 Methods

It is worth noting, that on a per-object basis, both SALT2 and MLCS light-curve fits are qualitatively very similar. However, recently published comparisons between SALT2 and MLCS concerning cosmological inferences for a compilation of several data sets resulted in an estimate of the equation-of-state parameter w that differed by 0.2 (Kessler et al., 2009). This difference exceeded both statistical and systematic error budgets. Figure 3.9 shows the mean difference in distance modulus, $\Delta\mu = \mu_{\rm SALT2} - \mu_{\rm MLCS}$, as a function of redshift. The two methods yielded consistent distance estimates for nearby and intermediate redshift data, with the scatter in $\Delta\mu$ being comparable to the intrinsic scatter of each sample. When including higher redshift data in

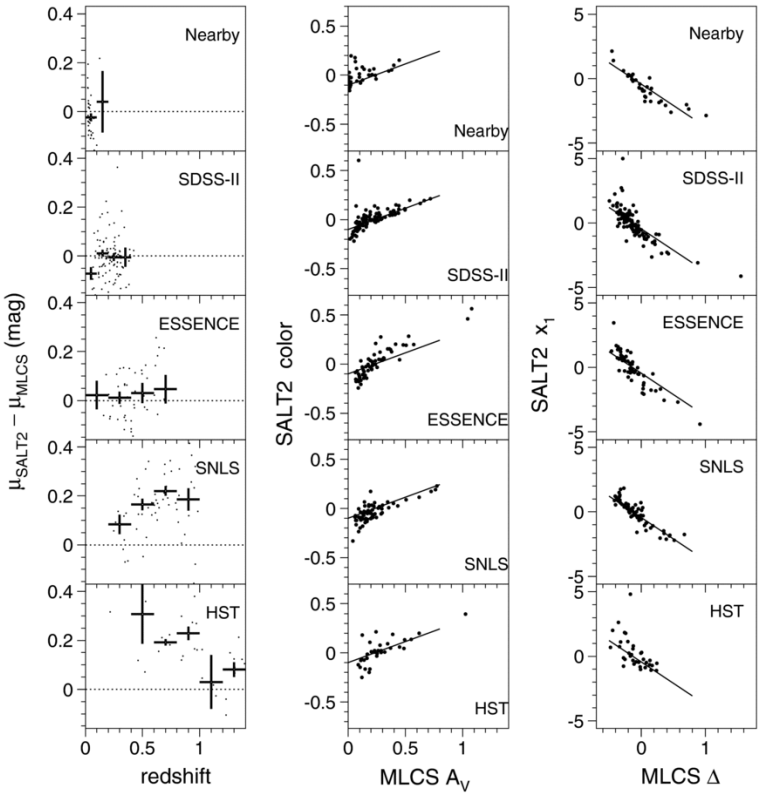

Figure 3.9: Difference in the distance modulus, $\Delta\mu$, and correlation between the corrections parameters of SALT2 (x_1 and c) and MLCS (Δ and A_V), for several public data sets. Crosses in the left column show the average and the uncertainty in redshift bins. The solid straight lines (middle and right panels) represent the fitted slopes, dc/dA_V and $dx_1/d\Delta$, for the various data samples (Kessler et al., 2009).

the analysis, such as SNLS or HST samples – see Sec. 3.6– the difference in distance modulus increased and a clear trend for $\Delta\mu$ with redshift appeared (Kessler et al., 2009).

The deviation appears to originate from the difference between the two fitters in the rest-frame U-band region, and the color prior used in MLCS. Also, MLCS seems to be less accurate in predicting the rest-frame U-band using data from filters at longer wavelengths (Weinberg et al., 2012). This difference in U-band performance is not hard to understand, since observations carried out in the observer-frame U-band are in general associated with a high level of uncertainty due to atmospheric variations. We recall that MLCS is exclusively trained on observations of nearby SNe, while the SALT2 training set also includes higher-redshift data. This means that the dependence on the nearby sample is reduced and better constraints on the rest-frame ultraviolet region of the spectrum can be obtained.

Effectively, the SALT2 parameters x_1 and c are analogous to the MLCS parameters Δ and A_V. The parameters x_1 and Δ are essentially equivalent in describing the correlation between SN light-curve shape and brightness. However, as we already mentioned, the color parameters c and A_V have different physical meanings. MLCS makes the assumption that all intrinsic SN color variation is captured in the model by the shape-luminosity correlation and that any additional observed color variation is due to reddening by dust. The color term c in SALT2 describes the excess color (red or blue) relative to a SN with fixed stretch parameter x_1. The excess color can be from host-galaxy extinction, from variations in the SN color that are independent of x_1, or from other effects, which SALT2 does not attempt to separate.

The global SALT2 parameter β, which gives the correction for B-band and, is the analog of the global MLCS dust parameter R_V, which gives the correction for V-band. Both parameters can be compared via the relation $\beta = R_B = R_V + 1$ and, in fact, one would expect both of them to be equal if the color variation was purely due to host-galaxy extinction. However, the SALT2 β parameter is determined from the global fit to the Hubble diagram for the entire SN Ia sample under analysis, while the MLCS R_V parameter is obtained by modeling the observed colors of a specific subset of the SN data.

Within the MLCS framework, each light-curve fit yields an estimate for the distance modulus together with its estimated error, independent of cosmological assumptions. Differently, in SALT2 the distance modulus for a given SN is based on a global fit to the whole sample assuming a specific cosmological model. This might induce biases in a particular redshift range to propagate over the entire redshift range of the sample, and make them more difficult to identify.

The fit with MLCS incorporates a Bayesian prior ($P_{\rm prior}$ in Equations 3.7 and 3.8) in order to reduce the scatter in the Hubble diagram (by including information about the underlying A_V distribution). This prior excludes values of $A_V < 0$, because of the assumption that excess color variation is due to extinction by dust. This means that SNe with very blue apparent colors (bluer than the template) are assigned $A_V \simeq 0$, and the discrepancy in color between the model and the data is attributed to fluctuations. In SALT2, apparently blue SNe have negative colors ($c < 0$) resulting in larger luminosities and distance moduli compared to MLCS. Within the SALT2 framework, the scatter in the Hubble diagram is minimized via the simultaneous fit of the global SN parameters with the cosmological parameters.

Recent studies (Mandel et al., 2009; Barone-Nugent et al., 2012) suggest that SNe Ia are truly standard candles in the near-IR, needing no standardization process. The peak luminosities in the rest-frame H-band have only about 0.1 magnitudes dispersion, independent of light curve shape. This small dispersion in NIR peak luminosities compared to the optical ones is consistent with theoretical predictions from radiative transfer models (Kasen, 2006).

3.5 Cosmology with SNe Ia: Basic Principles

Supernovae Ia are the most straightforward tool for studying cosmic acceleration, providing the first observational evidence of the accelerated expansion of the Universe already more than a decade ago (Riess et al., 1998; Perlmutter et al., 1999, both using local calibration samples from the Calán/Tololo survey, Hamuy et al. 1996). Already in the 1920s, Hubble, while studying the cosmic expansion of the Universe, had used galaxies as beacons in the cosmos to measure cosmological distances (out to 1000 Mpc). However, it was soon discovered that galaxies are not suitable for this purpose, since they present very different shapes and sizes and are not uniform in luminosity. Over the second half of the last century, other distance indicators were found to be much more adequate for cosmological applications.

The idea of using supernovae to determine the present expansion rate of the Universe dates back to 1939, when Wilson advanced the idea that they could be considered as standard candles due to their uniformity in luminosity (Wilson, 1939). Since then, an increasing interest in using SNe to determine the Hubble constant and the expansion history of the Universe has arisen.

In the late 1970's, Tammann and Colgate predicted that light curves from distant supernova would be affected by time dilation (Tammann, 1978; Colgate, 1979). We previously saw that the expansion of the Universe causes light to be redshifted during its journey from distant objects to an observer. Distances between galaxy clusters, and the wavelengths of the photons are increased by the same incremental factor z by which the cosmos has been stretched in the time interval since the light left its source. Here, the time interval is the speed of light times the object's distance from Earth, which can be determined by comparing its apparent brightness to that of a nearby supernova of the same intrinsic brightness. Therefore, a collection of measurements of SNe Ia over a wide range of distances would provide the entire expansion history of the Universe (Perlmutter & Schmidt, 2003). This was tested on a large sample by Goldhaber et al. (1997) and Goldhaber et al. (2001). The confirmation was extremely important for cosmology, because it led to the rejection of alternative *tired light* theories.

At that time, matter was believed to be the primary energy component of the cosmos and therefore, the main goal was to determine the matter density parameter Ω_{M} in order to check different cosmological models. Furthermore, through the measurement of the expansion rate, the curvature of space and the finite/infinite nature of the Universe could be evaluated.

Essentially, to measure cosmic expansion with SNe Ia, one has to compare the corrected peak apparent magnitudes of distant supernovae to those of local calibrators (usually within the interval $0.03 < z < 0.1$) whose distances are large enough to be insensitive to peculiar velocities and small enough to be insensitive to the assumed densities of dark matter and dark energy.

3.5.1 The Hubble Diagram

The luminosity distance $D_{\rm L}(z)$ is sensitive to the expansion rate through Eq. 2.31. Therefore the cosmological parameters governing the expansion of the Universe in Friedmann-Robertson-Walker models can be determined with precise values of luminosity distances (Sandage, 1961, 1988; Peebles, 1993; Peacock, 1999). We recall here briefly the importance of the Hubble law which relates the redshift, z, of a nearby galaxy to its distance D from us:

$$V = cz = H_0 D, \tag{3.10}$$

where V is the galaxy radial velocity, and H_0 is the Hubble constant, or the present expansion rate of the Universe. This law led to the remarkable result that the velocities of galaxies are increasing with distance as if they were moving apart from each other. In other words, Hubble found the first evidence of the expansion of the Universe. The low-redshift linearity of Hubble's law is a consequence of the Cosmological Principle, that is, on large scales the Universe is isotropic and homogeneous. This means that we must not consider ourselves in any special position in the Universe and that if we observed the galaxies from any other position we would notice the same expansion (Hubble, 1936; Narlikar, 2002).

Originally, Hubble plotted in his diagram the recession velocity of galaxies against their distances (see Fig. 3.10; Hubble, 1936; Sandage, 1961). He obtained a value for H_0 of 530 km s^{-1} Mpc^{-1} (Hubble, 1936), much larger than the present estimations lying in the range 60-80 km s^{-1} Mpc^{-1}. This large difference is due to the circumstance that Hubble greatly underestimated the distances to the galaxies in his observations. He used Cepheids as distance indicators, but he did not account for the fact that there are two classes of Cepheids, one belonging to population I-stars and the other to population II-stars. The former are about four times brighter than the latter. Moreover, this standard candles are only good estimators for distances up to ~ 10 Mpc (Narlikar, 2002).

The *Hubble diagram* is an extension of the linear Hubble law to higher redshifts. Three fundamental quantities can be derived from such a diagram: the slope of the expansion line, which provides an estimation of the local expansion field; the scatter around the expansion line, which gives an indication of the accuracy of the relative distances (in contrast to absolute scales), of deviations from the smooth cosmological expansion and measurement errors; and finally, the value of the local Hubble constant, that is calculated from the interception of the line at zero redshift (Branch & Tammann, 1992; Leibundgut & Pinto, 1992; Riess et al., 1996; Branch, 1998). The first attempts of producing a Hubble diagram using SN Ia data (instead of galaxies) showed that their brightnesses followed the Hubble relation quite well (Kowal, 1968; Tammann & Leibundgut, 1990; Leibundgut & Pinto, 1992), although considerable scatter was still present.

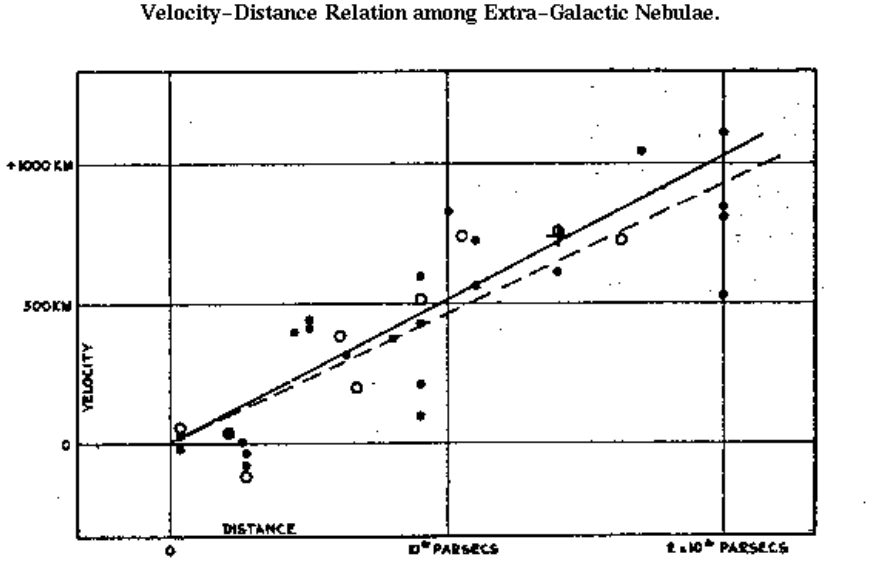

Figure 3.10: Original Hubble diagram. The recession velocities (in km s^{-1}) are plotted against distance (in parsecs). The filled disks and solid line represent a solution using the galaxies individually; the circles and dashed line a solution combining the galaxies into groups. From Hubble (1936).

Modern Hubble diagrams of SNe Ia usually show redshift instead of radial velocity, and distance modulus instead of absolute distances. Moreover, redshifts are usually now referred to the Cosmic Microwave Background rest frame (Tonry et al., 2003; Knop et al., 2003; Barris et al., 2004; Riess et al., 2004, 2007; Astier et al., 2006; Wood-Vasey et al., 2007; Jha et al., 2007). In these modern versions, the scatter of the normalized SNe Ia (through the light curve recalibration discussed in Section 3.3.1) around the expansion line is about 0.2 magnitudes or 10% in distance (Jha et al., 1999, 2007; Tonry et al., 2003). This means that although our knowledge of the explosion mechanisms and radiative transport in the explosions is still limited, SNe Ia can be used as good relative distance indicators in the local Universe.

Figure 3.11 displays the most recent homogeneously treated sample of SNe Ia: the Union2.1 data set (see next Section for a full description of this sample; Suzuki et al., 2012). In Fig. 3.12 we see the Hubble diagram with data from Davis et al. (2007) and different models overplotted.

3.5.2 The Expansion History and the Accelerating Universe

The importance of the Hubble diagram lies in the fact that the cosmic expansion history can be reproduced and studied in detail, providing us the matter

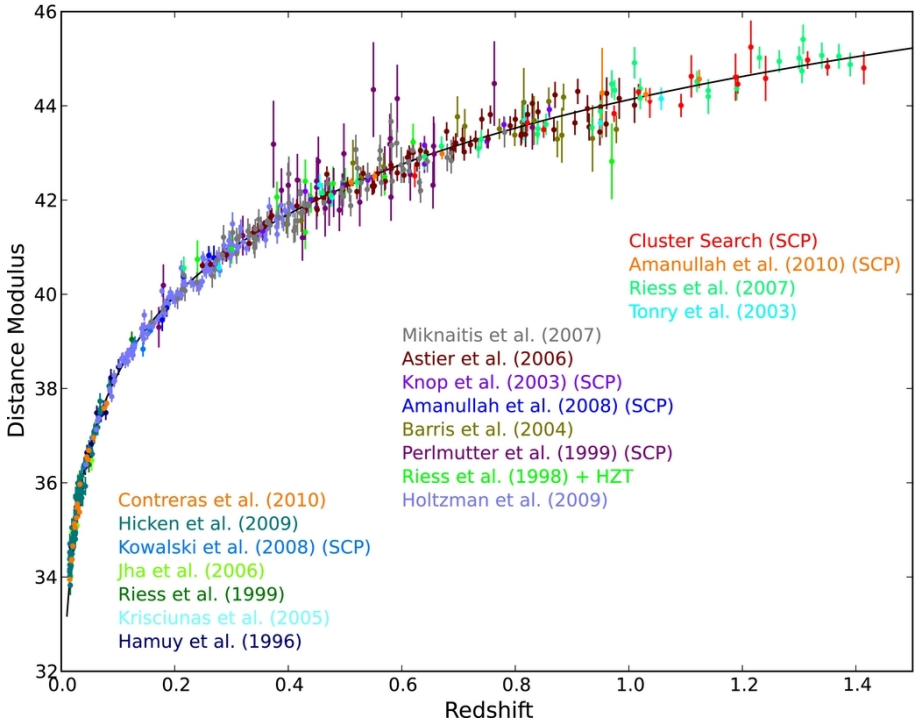

Figure 3.11: Hubble diagram of the largest SN Ia sample to date, the Union2.1 compilation (Suzuki et al., 2012). Here the distance modulus ($\mu = m - M$ in units of magnitude) is plotted against redshift. The solid line is the best ΛCDM fit.

and energy contributions during the different epochs of the Universe (Linder, 2003). Only relative distances are required to trace the expansion history in such a diagram, if a class of cosmological objects with the same intrinsic luminosity is available (that means, one is independent of the distance ladder). That is the reason why SNe are such a powerful tool: they can be observed up to redshifts of $z \sim 1.5$, providing insights into the distant past of our Universe (when it was 2/3 of the current age, approximately) and constituting, at least till now, the best distance indicators we have in hand.

We discussed in Sec. 2.8 that, in the light of the ΛCDM model, some dark energy component accelerates the expansion of the Universe. Theoretical cosmologists had already anticipated that the missing energy in the cosmic budget could be in form of vacuum energy, something that would lead to a late time acceleration phase (Turner, 1991, 1997; Ostriker & Steinhardt, 1995; Liddle et al., 1996). However, at that time, there was no observational probe that could confirm such predictions. In 1998, the most surprising discovery was made. Two independent groups, the Supernova Cosmology Project (Hook et al., 2005; Knop et al., 2003; Perlmutter et al., 1995, 1999) and the High-Z Supernova Search Team (Leibundgut et al., 1996; Riess et al., 1997, 1998, 2000; Garnavich et al., 1998; Coil et al., 2000; Barris et al., 2004; Clocchi-

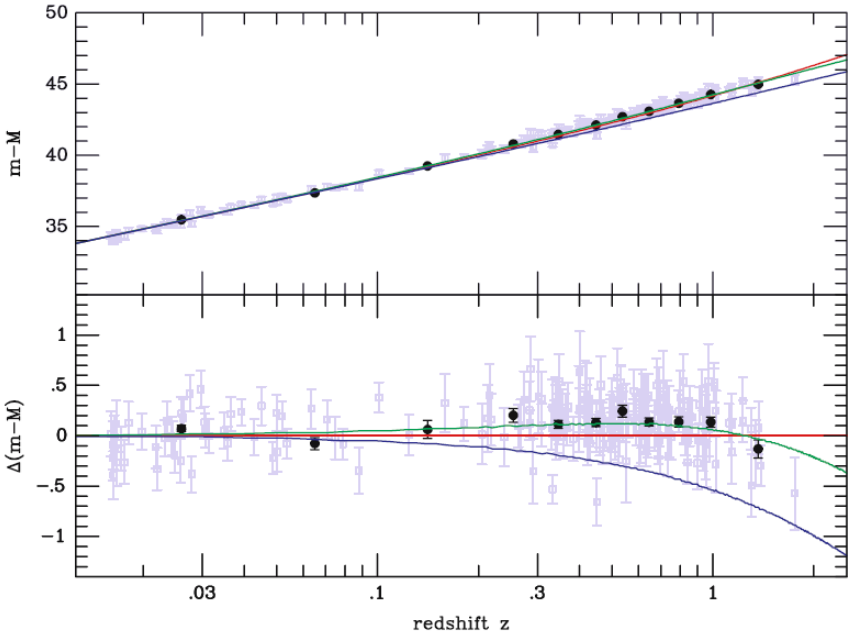

Figure 3.12: Hubble diagram using SNe Ia from Davis et al. (2007). The data for the individual SNe are plotted as shaded points, while the binned data are shown in black. The red line corresponds to an empty universe with $\Omega_{\rm M} = \Omega_\Lambda = 0$, the blue line to an Einstein-de Sitter model with $\Omega_{\rm M} = 1, \Omega_\Lambda = 0$, and the green line to the standard ΛCDM model with $\Omega_{\rm M} = 0.3, \Omega_\Lambda = 0.7$. The bottom panel shows all distances relative to the empty Universe model. From Leibundgut (2008).

atti et al., 2006), found strong indications that the distant ($z \geq 0.5$) SNe Ia appeared about 0.25 magnitudes fainter than predicted even for a massless, empty universe (see Figs. 3.13 and 3.14). However, since we live in a Universe with matter, there should be a limit on how low the mass can be. This argument led to the interpretation that the faint (distant) SNe are actually further away than expected, meaning that distances are increasing more rapidly than presumed, or equivalently, that the expansion of the Universe is accelerating!

The best fit achieved back in 1998 gave the following values for the cosmological parameters: $\Omega_{\rm M} = 0.3$ and $\Omega_\Lambda = 0.7$ (for a flat Universe with no large-scale curvature), confirming that a non-zero vacuum energy component or cosmological constant was indeed present in the Universe and was, moreover, larger than the matter density.

The detection of the accelerated expansion is of extraordinary importance as it gives a credible explanation of the missing 70% of the critical density, in form of a dark energy component with negative pressure, $p = -\rho$. In this context, an interesting question arises: when did the universe start accelerating? We recall from General Relativity that the components of the energy

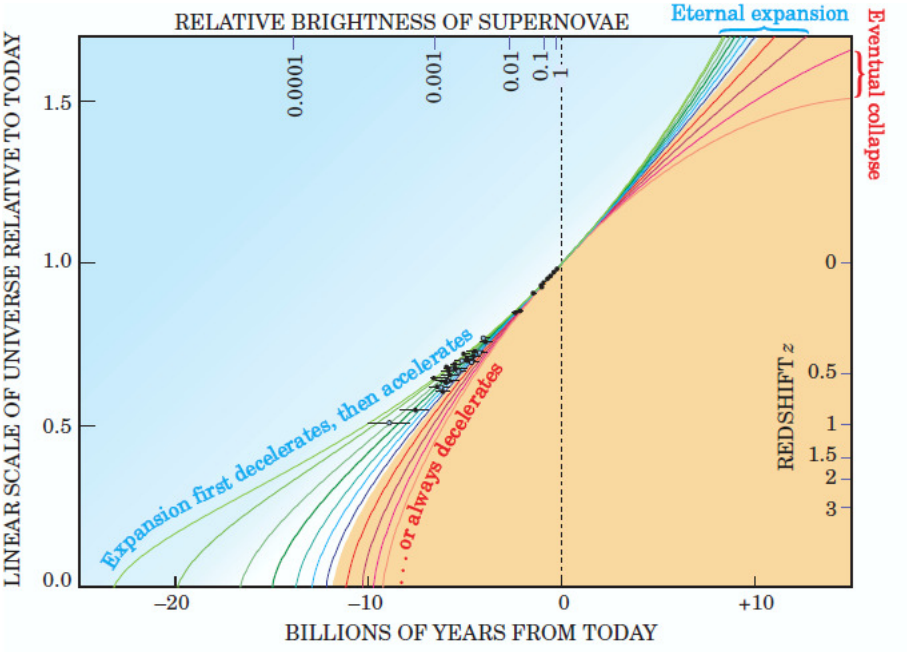

Figure 3.13: History of the cosmic expansion measured with high-z SNe assuming a flat geometry. The curves in the blue shaded region represent cosmological models in which the acceleration due to vacuum energy overcomes the deceleration caused by matter. In the yellow shaded area, the curves represent models with permanent deceleration due to high mass density. For the last two curves, the expansion eventually halts and the Universe recollapses. Taken from Perlmutter & Schmidt (2003).

density evolve in time following Eq. 2.12. Since the end of the inflation epoch (where matter and radiation were equal), the matter contribution to the total energy density has fallen many orders of magnitude. But the vacuum energy density or Ω_Λ, a property of empty space itself, stays constant. This implies that the dark energy component was less important in the past than it is today (something also independently required by large scale structure formation and CMB measurements). Until recently ($z \approx 0.5$) the universe was decelerating due to matter domination, but now (when the dark energy dominates) it is, in fact, accelerating. Riess et al. (2004) observationally confirmed this transition from a past deceleration epoch to the current acceleration phase using very high redshift SNe Ia (Fig. 3.15).

It seems indeed stunning that the Universe is accelerating exactly today, and that the dark energy density is about twice of the matter density, showing that we live during a very special epoch. This is the so-called cosmic *coincidence problem*, which suggests that something might be wrong with current observations or with the cosmological models proposed so far.

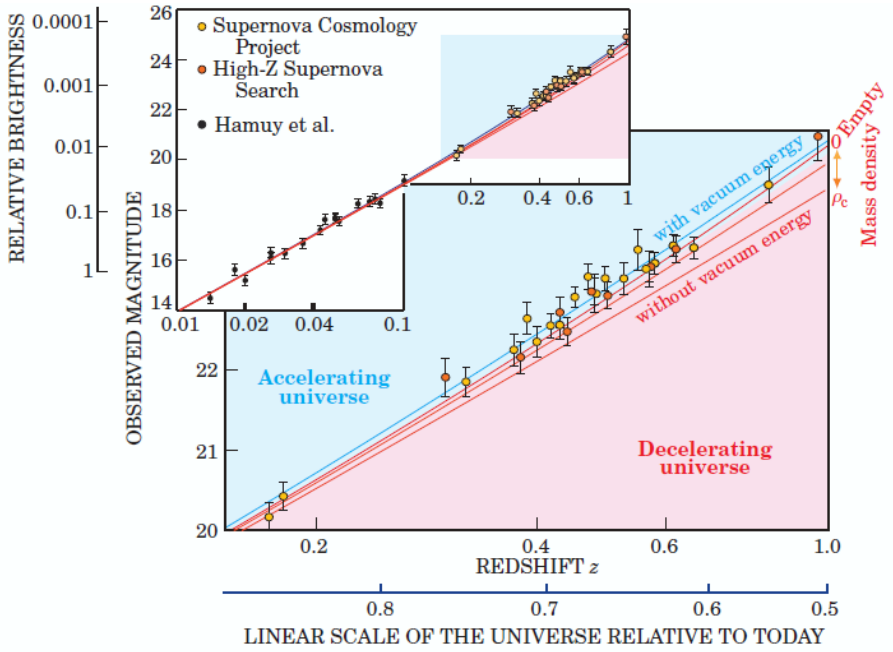

Figure 3.14: Hubble diagram using distant SNe Ia from the SCP and the High-Z Supernova Search and nearby SNe from (Hamuy et al., 1993). At redshifts beyond $z = 0.1$ the cosmological predictions begin to diverge, depending on the assumed cosmic densities. The red curves are models with zero vacuum energy and mass densities ranging from the critical density ρ_c to zero. The best fit (blue line) is an accelerating Universe with a vacuum energy about twice the mass density. Taken from Perlmutter & Schmidt (2003).

An alternative explanation of the SN data without an accelerated expansion could be that faint supernovae are dimmed by the intervening dust of the host galaxy. However, color measurements sensitive to a color-dependent dimming indicate that this does not play a major role (Riess et al., 1998; Perlmutter et al., 1999). This leads to the question whether supernovae might have been intrinsically fainter in the past, but no evidence for evolution in spectral properties has been found when comparing nearby and distant supernovae (Perlmutter et al., 1997, 1999).

However, as we will explain in the following sections, systematic uncertainties are still quite big in current data. Therefore, it is very important to understand their effect in the data. Searching for a larger number of distant supernovae from the epoch when $\Omega_{\rm M}$ was dominating and cosmic expansion was still slowing down, would be a very good test of systematics. In the ΛCDM model, supernovae from that time are not as dimmed as they should be if dust or intrinsic evolutionary changes were causing their faintness.

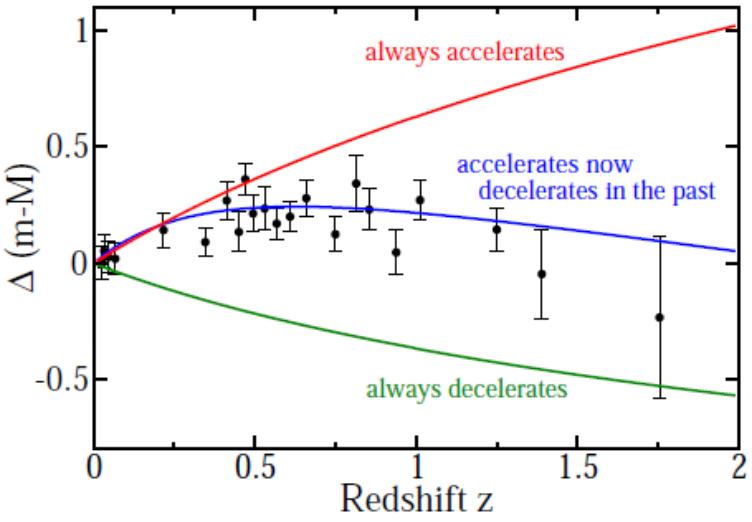

Figure 3.15: Hubble diagram with binned SNe data from Riess et al. (2007). It shows evidence for a transition from acceleration today corresponding to the current dark energy domination epoch, to deceleration in the past due to the matter-domination era. From Turner & Huterer (2007).

3.6 Current SN Ia Samples

An average galaxy hosts just a couple of explosions per millennium, making the occurrence of SNe highly random and impossible to predict their location and time. When a supernova explosion is detected, it has to be immediately followed to cover the phase of maximum brightness (essential for their calibration) and the subsequent weeks. This becomes a hard task since the observing time at the largest telescopes is usually pre-scheduled more than half a year before. Thus, when a explosion is discovered, it is already too late to submit any observing proposal. This is, in fact, one of the reasons why SN Ia samples have increased slowly.

3.6.1 Observational Strategy

In the early 1990s, Saul Perlmutter and collaborators at the University of California and the Lawrence National Laboratory, in Berkeley, conceived a new observing strategy for supernova cosmology campaigns that has proven very successful. This strategy consists of four main steps: discovery, monitoring, spectroscopic confirmation, and calibration against low redshift samples.

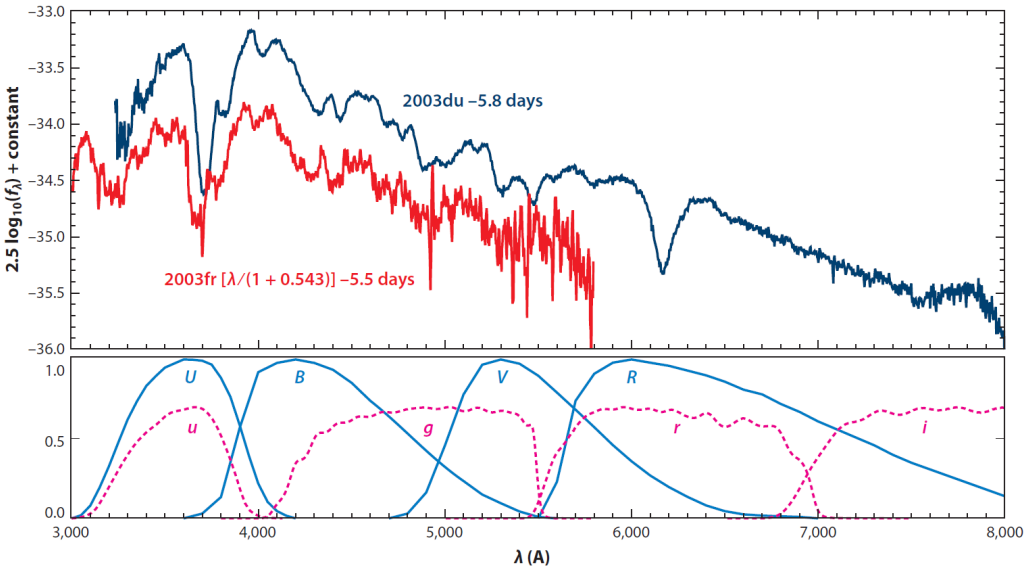

Figure 3.16: Upper panel: observed spectrum of SN 2003du compared with the rest-frame spectrum of SN 2003fr at $z = 0.543$. Both spectra are approximately six days prior to the B-band maximum. The absorption and emission features are remarkably similar. Currently available data do not demonstrate any clear difference between the spectra of distant Type Ia supernovae and those of their local counterparts. Bottom panel: optical bands for the Bessel $UBVR$ system (Bessell, 1990), as well as the SDSS $ugri$ filter set (Fukugita et al., 1996). From Goobar & Leibundgut (2011).

In large surveys, discovery and monitoring are usually done together, through repeated imaging of a large field of view in multiple bands. If a set of images of adjacent sections of sky with thousands of galaxies in it is taken just after new moon and again after one month, the images will provide at least a dozen of bright spots that were not there in the first images. These fresh supernovae are certainly near peak brightness.

Usually, a minimum rest-frame cadence of one observation per 5 days is needed to get adequate measurements of the light curve shape, such that statistical errors are dominated by the intrinsic dispersion of SN luminosities and not by observational errors. At least two bands are needed to measure SN colors and infer dust extinction, though more are better to distinguish different forms of extinction (interstellar, circumstellar, and intergalactic) from each other and from intrinsic color differences.

A survey with periodic and uniform exposures observing supernovae at a given redshift should aim at a signal-to-noise ratio (S/N) of around 15 at peak, so that one can still measure the SN before or after peak when it is around 1.5 magnitudes fainter. After discovering SNe, one must determine their type and redshift through accurate photometry and spectroscopy, using state-of-

the-art observational facilities and telescopes (e.g. the 10m-class telescopes in Hawaii or Chile). The most reliable approach for classification is to obtain SN spectra to match their spectral features with known templates. However, spectroscopic follow-up is typically expensive in a supernova campaign. For the same telescope aperture, an epoch of spectroscopy requires an order of magnitude more time than an epoch of photometry (Weinberg et al., 2012). In principle, photometric redshifts can be used instead of spectroscopic redshifts, though this would probably mean a degradation in statistical accuracy. Due to the degeneracies between redshift, SN color, and dust extinction, it is not clear that cosmological SN surveys can obtain the required accuracy using only photometric monitoring (Weinberg et al., 2012).

An intermediate approach would be to obtain eventual spectroscopic observations of host galaxies but not attempt real-time spectroscopy of all candidates. This scheme would yield precise redshifts and provide host galaxy data that can be used to measure correlations between supernova and host galaxy properties. Using this method, Bernstein et al. (2012) forecast a degree of purity of around 98% in a survey such as the Dark Energy Survey (DES, The Dark Energy Survey Collaboration, 2005) for photometric observations.

For type identification, one can also check for a second peak in the rest frame infrared light curve, a morphological feature that is unique to SNe Ia, though rest-frame IR measurements are hard to access at high redshifts.

A difficulty that arises in supernova campaigns is that, with increasing redshifts, the brightness of very distant supernovae measured in a given filter can not be easily compared with the brightness of closer supernovae in the same filter. By doing so, one would be probing different parts of the spectrum for each supernova, due to the redshift effect. This is called the *K-correction problem*, which can be solved with the above-mentioned methodology, by measuring each supernova in an adequate redshifted filter and combining them in a later step.

3.6.2 State-of-the-Art SN Ia surveys

Supernova surveys have been a major area of activity in observational cosmology over the last decade. The largest high-redshift ($z \sim 0.4 - 1.0$) data sets are currently those from the ESSENCE survey (Wood-Vasey et al., 2007) with around 200 spectroscopically confirmed SNe and the CFHT Supernova Legacy Survey (SNLS, Astier et al., 2006; Conley et al., 2011; Sullivan et al., 2011) with 500 spectroscopically confirmed SNe in the three-year data set SNLS3. At very high redshifts ($z > 1$), the *Hubble Space Telescope* (Riess et al., 2004, 2007; Suzuki et al., 2012, HST,) has yielded around 25 objects which confirm that the Universe is decelerating at high redshift and limit possible systematic effects from evolution of the supernova population or intergalactic dust extinction. At intermediate redshifts ($0.1 < z < 0.4$), the SDSS-II supernova survey (Frieman et al., 2008; Sako et al., 2008) has discovered and monitored around

500 spectroscopically confirmed SNe Ia. So far, only the first-year data set (103 SNe) has been analysed (Kessler et al., 2009), but Campbell et al. (2013) present cosmological results from a sample of 752 photometrically classified SDSS-II SNe with spectroscopic host galaxy redshifts.

Important efforts have been made to expand the sample of local calibrators and improve their measurements, including rest-frame IR and rest-frame UV photometry. Besides the well-known collection of nearby supernovae from Cerro Tololo (Hamuy et al., 1996), other contributions have been added to the nearby family such as the large sample from the CfA team (Jha et al., 2006; Hicken et al., 2006). Also worth noting are the forthcoming low redshift samples from the Katzman Automatic Imaging Telescope (KAIT; Li et al. 2000; Filippenko et al. 2001), the Carnegie SN Program (Hamuy et al., 2006) and the Nearby Supernova Factory (Wood-Vasey et al., 2004; Copin et al., 2006).

The most efficient strategy for SN cosmological analyses is to use numerous samples that span a wide range in redshift. To limit systematic errors introduced by combining disparate SN surveys, it is often advisable to recompile the data from these surveys as homogeneously as possible. Early attempts of constructing such SN Ia compilations were made by Riess et al. (2004, 2007) with the so-called *Gold* samples. However, these selections mainly consisted of intermediate or high-redshift samples from single studies, together with a low-redshift dataset from a different source. In the next Section, we describe the compilation performed by the Union team, which involves applying consistent criteria for inclusion in the sample, light curve fitting with a single algorithm, propagation of errors via covariance matrices and consistent use of K-corrections.

3.6.3 The Union Compilation

The Union2.1 dataset (the most recent update of the original Union sample by Kowalski et al., 2008) is a compilation of 580 type Ia supernovae combining the recently extended datasets of distant supernovae observed with HST, SNLS, ESSENCE and SDSS with new low-redshift SNe in the smooth Hubble-flow ($z \sim 0.02$) from Hicken et al. (2009a), the Supernova Cosmology Project (SCP) Spring 1999 Nearby Supernova Campaign (Aldering et al., 2000) and nearby data from Contreras et al. (2010). Also, older samples from the literature are included in this compilation.

A robust analysis based on outlier rejection and resistant against contamination is applied. Outlier rejection can reduce the bias as well as the intrinsic dispersion by a factor of three, leading to stronger cosmological constraints. By putting less weight on the SN samples with significant statistical and systematic uncertainties, poor quality data do not affect the precision of the high-quality samples (e.g. SNLS or ESSENCE). Moreover, the same light-curve fitter SALT2 is applied to all datasets within the compilation, so that the calibration procedure is the same for all supernovae.

Objective criteria to separate the good SNe Ia from the questionable and outlier events are also adopted. First of all, accepted supernovae must have data in at least two bands lying between the rest-frame U and R-bands, and should have at least five data points available. Second, at least one observation before B-band maximum is required for the candidates. For the nearby SNe, a lower limit of $z > 0.015$ is set in order to avoid the effect of the host galaxy peculiar velocity. Finally, any object spectroscopically classified as SN 1991bg-like is removed from the sample, as these SNe Ia are a distinct subclass that is not properly modeled by SALT2.

Figure 3.11 shows the sub-samples which compose the Union2.1 dataset. Seventeen supernovae from Hamuy et al. (1996), 11 from Riess et al. (1999), 16 from Jha et al. (2006), 6 from Krisciunas et al. (2001) and Krisciunas et al. (2004), 8 new SCP supernovae and the 102 low-redshift SNe Ia from the CfA3 survey (Hicken et al., 2009a) constitute the low redshift sample. The distant sample is formed by 72 SNe from SNLS (Astier et al., 2006), 75 from ESSENCE (Wood-Vasey et al., 2007), 11 from Knop et al. (2003), 30 from Perlmutter et al. (1999), 12 from the High-Z Search Team (HZT – Riess et al. 1998; Garnavich et al. 1998; Schmidt et al. 1998), 22 from Barris et al. (2004) and 8 from Tonry et al. (2003). The 29 SNe from Riess et al. (2004, 2007) and the 6 new high-redshift SNe Ia from Suzuki et al. (2012) constitute the highest redshift events in the compilation. The intermediate-redshift interval has been recently populated by Sloan Digital Sky Survey (SDSS) SN data (Holtzman et al., 2008), and 5 additional intermediate-redshift SNe Ia discovered from La Palma (Amanullah et al., 2008).

A diagnostic plot, used to study possible inconsistencies between the various SN samples, is displayed in Figure 3.17. The median of the dispersion can be used as a measure of the intrinsic dispersion, which reveals how well the empirical models correct for the observed dispersion in SN luminosities. The median for this sample is 0.15 mag indicated by the leftmost dashed vertical line in the left panel.

For the cosmological fit, a blind analysis is carried out following the approach of Conley et al. (2006), where the best fitting cosmological parameters are hidden until the analysis is finished and systematic errors in the estimation of the parameters are avoided. Each sample is fitted to a flat ΛCDM cosmology independently of the other samples (with the correction parameters α, β, δ and M_B having their global values). This means that each sample is fitted independently with its own Hubble line minimizing the effects of outliers. This technique offers an optimal framework to include future samples from different instruments and surveys. The best fit for the dark energy density obtained with this data set is (as reported in Suzuki et al., 2012)

$$\Omega_\Lambda = 0.729 \pm 0.014 \quad (\Lambda\mathrm{CDM} : \mathrm{SN} + \mathrm{CMB} + \mathrm{BAO} + H_0). \tag{3.11}$$

The current SN data alone do not provide definitive constraints on the equation of state parameter w because the measurements are degenerate with Ω_M.

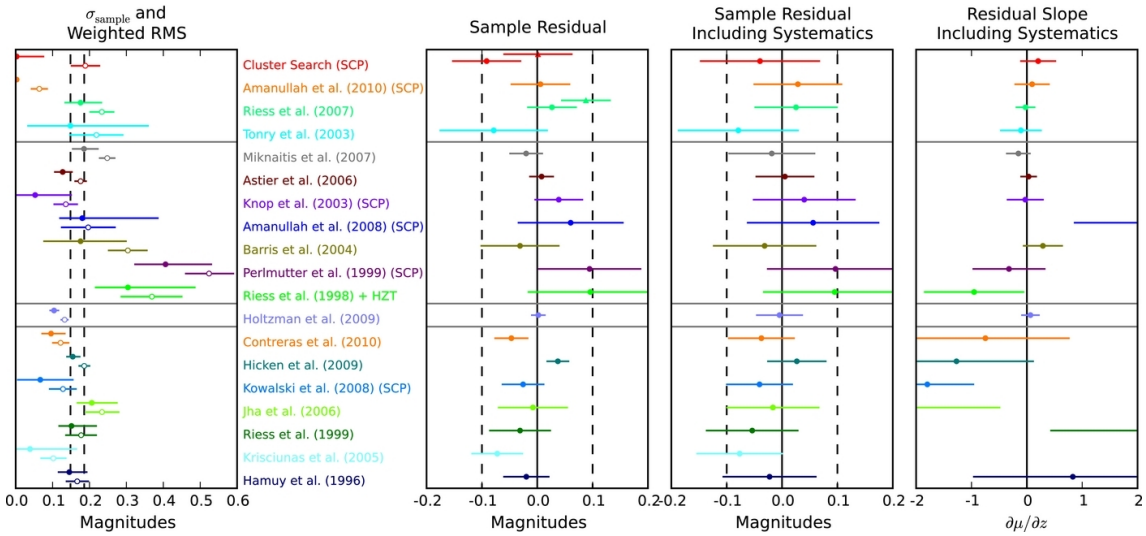

Figure 3.17: Diagnostics plot for the individual data sets. Left panel: sample dispersion (filled circles) and variance-weighted root-mean-square about the best-fit model (open circles). The leftmost dashed vertical line indicated the median of the dispersion for the entire sample. Middle panels: the average sample residual from the best-fit model ($\mu_{\rm measured} - \mu_{\rm model}$) with and without systematic errors. Right panel: best-fit slope of the Hubble residuals (in magnitudes) vs. redshift. From Suzuki et al. (2012).

However, combining the SN data with constraints from BAO (Eisenstein et al., 2005) and the CMB (Dunkley et al., 2009) which also involve $\Omega_{\rm M}$, the results are greatly improved and the degeneracy is broken. The value of w for this sample is

$$w = -1.013^{+0.068}_{-0.073}. \tag{3.12}$$

The joint constraints for a flat Universe from SN data, BAO and CMB are shown in Fig. 3.18. Relaxing the assumption of flatness, the combined constraints are still consistent with a flat ΛCDM Universe, as seen also in Fig. 3.19. With the combination of the three cosmological measurements, the statistical error is greatly reduced, although a significant systematic error still remains. It is noteworthy that CMB and SN Ia constraints are almost orthogonal, making this combination of cosmological probes very powerful for investigating the nature of dark energy. We conclude this Section by noting, that, at low redshifts, SNe can achieve a precision unmatched by other methods. However, at higher redshifts they cannot compete with the dark energy sensitivity of the large BAO surveys unless the statistical, and especially the systematic, errors are greatly reduced.

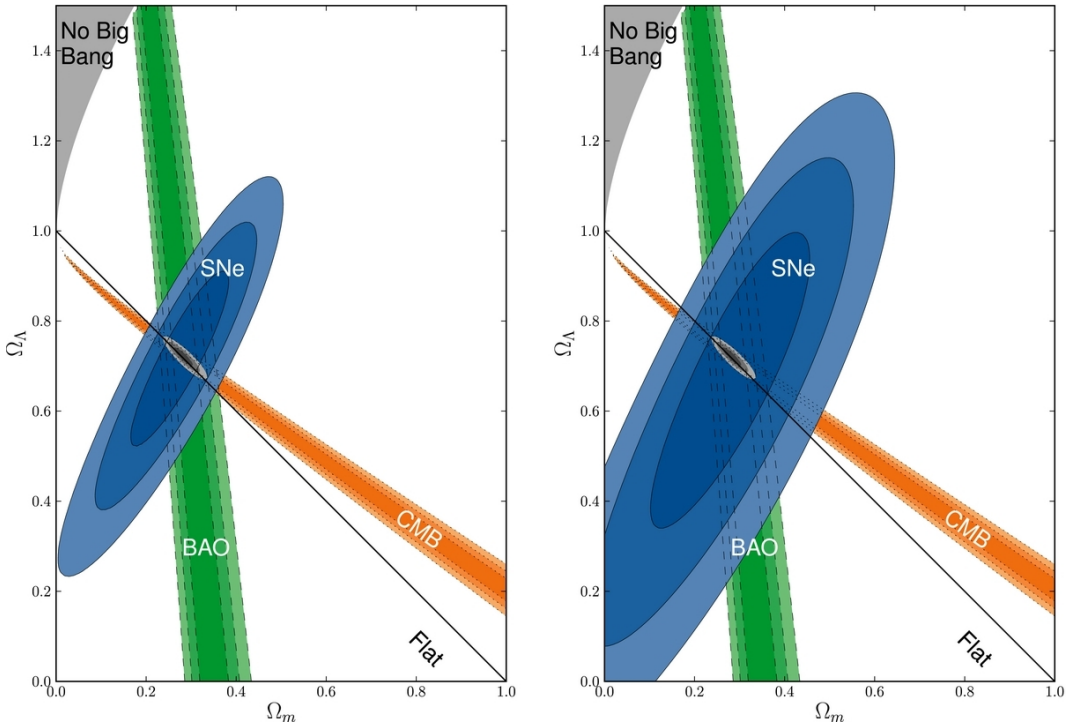

Figure 3.18: Left panel: 68.3%, 95.4%, and 99.7% confidence regions in the (Ω_M, Ω_Λ) plane from SNe Ia, BAO, and CMB with statistical uncertainties only. Right panel: idem including both statistical and systematic uncertainties. From Suzuki et al. (2012).

3.6.4 Systematic Uncertainties

The accuracy with which we can infer the cosmological parameters from SN data is limited by several systematic effects. Some are directly related to supernova physics, but most of them account for the fact that we live in a non-empty Universe with dark and baryonic matter that distorts the light we receive from distant objects. The effects on data quality – which include flux calibration errors, uncertainties associated with SN colors and dust extinction, possible evolution of the supernova population with redshift or gravitational lensing, amongst others – are necessary to comprehend if we want to understand the cosmological implications imprinted in the SN data.

Future surveys hope to discover and monitor thousands of supernovae, sufficient to reduce statistical errors to only 0.01 mag (see Section 3.8), meaning that systematic uncertainties will have the greatest impact on supernova studies. We will highlight in this Section the most relevant problems and mention some possible solutions to overcome them. For a detailed review on systematics we refere the reader to Kessler et al. (2009) and Amanullah et al. (2010).

One of the main systematic effects afflicting SN data is the extinction due to dust occurring on the host galaxy and/or the Milky Way. Different assump-

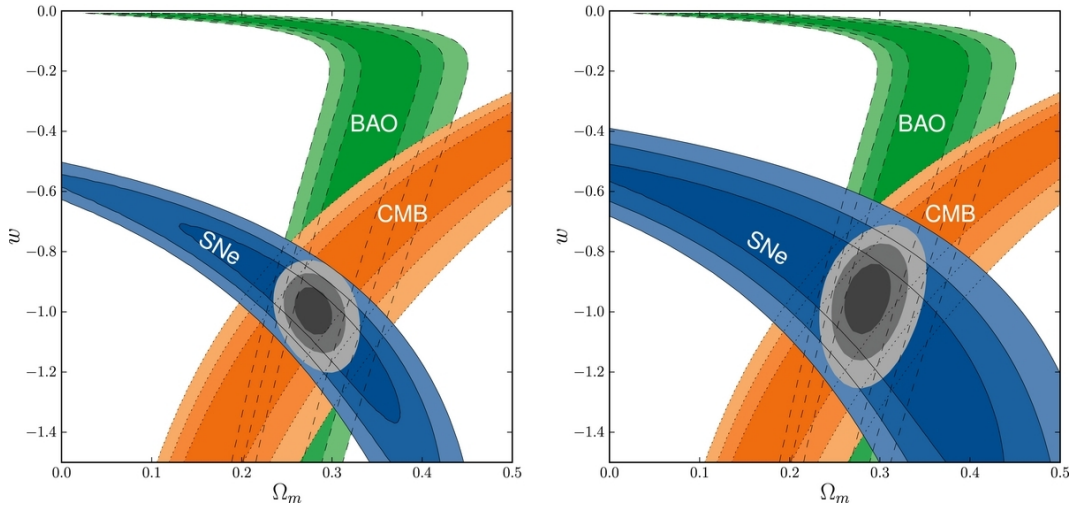

Figure 3.19: Left panel: 68.3%, 95.4%, and 99.7% confidence regions in the ($\Omega_{\rm M}$, w) plane from SNe Ia, BAO, and CMB with statistical uncertainties only. Right panel: idem including both statistical and systematic uncertainties. From Suzuki et al. (2012).

tions about dust extinction may change the inferred value of the cosmological parameters. For the extinction in our own Galaxy, the correction of Cardelli et al. (1989) for the diffuse interstellar medium is usually applied. Nevertheless, as mentioned in Sec. 3.4, it is not clear whether this local reddening law can be applied to distant galaxies. Moreover, the difference in the value of R_V could be a reflection of different kinds of dust along the line of sight to the supernova (e.g. circumstellar dust), but it could also arise from intrinsic color differences among SNe Ia with similar light curve shapes (Hicken et al., 2009b; Kessler et al., 2009; Sullivan et al., 2011). In this context, some authors have analysed the variation of SN reddening/colors, finding little dependence of the color on host galaxy properties (Kessler et al., 2009; Sullivan et al., 2010). The recent study of Chotard et al. (2011), using spectroscopic indicators of luminosity in nearby SNe, infers an extinction law with $R_V = 2.8 \pm 0.3$, consistent with the Galactic value. Techniques which eliminate the most highly reddened SNe can reduce extinction systematics if they can be applied in a way that does not introduce selection biases. An extreme approach would be to employ only SNe in early-type galaxies (which contain small amounts of interstellar dust) within distant galaxies clusters (Sullivan et al., 2003). However, this has the difficulty that no good comparison with a nearby sample is available. Probably, the best strategy for reducing extinction systematics is to focus on obtaining data in the IR region, where extinction is low compared to optical wavelengths and SNe Ia show very small scatter in the peak luminosity.

It has been suggested that the dimming observed in distant SNe could be due to intergalactic grey dust (i.e. weak extinction variation over the optical

wavelengths) instead of a dark energy component (Aguirre et al. 2009). Note that, although so far there is no evidence for such an extinction and simple dust scenarios without cosmological constant have been ruled out by Riess et al. (2004), it is not correct to exclude this possibility completely.

The differences between telescopes and filter pass bands, which vary from one observatory to another, constitute other important sources of systematic errors, making it difficult to combine observations from different telescopes, and to obtain the required accuracy in photometry (Stubbs & Tonry, 2006). For instance, for nearby supernovae, a correction (the so-called S-correction, Stritzinger et al., 2002) has to be introduced when combining data from multiple telescopes. A way to avoid this, is to carry out the photometric measurements on single instruments as the SNLS and ESSENCE surveys have done, though this only helps if the photometry is also calibrated on the natural telescope/instrument system.

Light-curve fitting methods are equally relevant for calibration and, as we saw in Sec. 3.4, they may cause discrepancies in the cosmological parameters for the same data sets. Usually, the Phillips relation – parameterized by, e.g., the decline rate – is employed to fit the light curves. However, there are other methods based on different normalisation of the peak luminosities which could add additional information. These approaches have been investigated by the Supernova Cosmology Project (see Perlmutter et al., 1997, 1999; Knop et al., 2003). Also, *self-calibration* is an alternative to flux-calibration, which can reduce the systematic error (Kim & Miquel, 2006), but at the price of increasing the statistical error.

The uncertainties in intrinsic colors and photometric calibration can be reduced with detailed, well calibrated, multiwavelength observations of large numbers of low redshift SNe. In this way, it is possible to characterize separately the dependence of SN color on luminosity, light curve shape and time since explosion, and provide constraints on dust extinction laws that are independent from cosmological inferences. Moreover, locally observed SNe map a wide range in age, metallicity, and current star formation rate (SFR) of their host stellar populations. This provides ideal conditions for investigation of the possible evolution of SNe Ia with redshift and host galaxy properties (Kelly et al., 2010; Sullivan et al., 2010; Hicken et al., 2009b; Hayden et al., 2012). In relation to this, it is worth mentioning the efforts of the ongoing Nearby Supernova Factory project (Aldering et al., 2002a), which aims to provide a network of standard stars for calibration and plans to address some of the relevant systematic errors, such as the host-mass correction (the range of host masses will become comparable to that of high redshift SNe for the first time in a local sample) and the modeling of the light curves (through a better understanding of SN Ia spectral time series).

The possible evolution of SNe with redshift could be another source of systematic errors. The question of whether distant SNe have the same spectral evolution as their nearby counterparts has been widely studied in the literature

(Coil et al., 2000; Lidman et al., 2005; Howell et al., 2005; Blondin et al., 2006) and it remains a matter of discussion. This could mean that different populations of SNe Ia exist, depending maybe on host-galaxy morphology or color (Sullivan et al., 2006; Gallagher et al., 2008), on progenitor metallicity or explosion mechanism (*single* versus *double degenerate* scenario; Sarkar et al., 2008). So far, no significant differences have been found among the local and distant SN Ia samples (Hook et al., 2005; Lidman et al., 2005; Matheson et al., 2005; Blondin et al., 2006; Astier et al., 2006; Riess et al., 2007; Wood-Vasey et al., 2007), and also the progenitor metallicity appears to be a minor contribution to the systematics (Röpke et al., 2006).

A strategy for limiting evolution systematics is to break the SN sample into subsets defined by spectral features, light curve shape, or host properties and check for consistency of the cosmological results, because evolution is unlikely to affect all populations in the same way. A complementary method is to observe supernovae at $z > 2$, where SN fluxes should be insensitive to the dark energy parameters (Riess & Livio, 2006). Discrepancies would then indicate evolutionary effects.Once more, it is worthy to note that any evolutionary corrections may be weaker in the NIR, both because of the narrower range of luminosities and because of the weaker sensitivity to metal lines and reddening laws.

The difficulty in determining the SN rest frame from observed photometry also affects SN measurements (Jha et al., 2007). Most ground-based surveys work at rest-frame B or V (between $0.4-0.6$ μm) wavelengths, which transform to observed-frame I-band ($0.7 - 0.9$ μm) at $z = 0.5 - 0.8$. The Carnegie Supernova Project (Freeman et al., 2009) has produced a SN Hubble diagram to $z > 0.7$ in the rest-frame I-band, where systematic errors due to uncertainty in the reddening laws are roughly half of those in the V-band. Moreover, Mandel et al. (2009) find that the intrinsic dispersion of peak luminosities is only 0.11 mag in the rest-frame H-band ($1.5-1.7$ μm), where systematics due to extinction are of the order of 1/6 of those in V. However, obtaining rest-frame NIR photometry for high redshift supernovae requires space observations due to the high background from the ground.

A different systematic effect is the gravitational lensing caused by intervening large scale structure, which introduces scatter in observed SN fluxes, at a level of 0.05 magnitudes for sources at $z = 1$ (Frieman, 1996; Wang, 1999). On average, the flux of the SN population does not change, but it is beneficial to check for selection effects which could bias the results, especially as the magnification distribution is highly non-Gaussian (Sarkar et al., 2008). Since lensing effects are small and calculable, they are unlikely to become a limiting systematic even for future surveys. Analyses that average fluxes of SNe in redshift bins or model the flux distribution can minimize lensing systematics and may reduce some other systematic effects as well (Amendola et al., 2010; Wang et al., 2012).

Equally important is the fact that the local expansion field is not smooth and some deviations from the local Hubble flow – attributed to density inhomogeneities – exist, which makes it hard to set the zero-point of the expansion rate, i.e. H_0 (Riess et al., 1995, 1997; Zehavi et al., 1998; Jha et al., 2007). This limitation translates into a systematic uncertainty that seriously affects our constraints on cosmological parameters (Hui & Greene, 2006; Cooray & Caldwell, 2006; Jha et al., 2007; Wood-Vasey et al., 2007). Therefore, larger samples of nearby supernovae are required in order to overcome these obstacles and obtain a better understanding of the local density distribution and the local velocity field (Riess et al., 1995; Haugbølle et al., 2007). Studies about the possibility of a *Hubble bubble* (local underdensity where the expansion rate is lower than the global one) could also be carried out with a higher number of nearby supernova (see a discussion on the subject in Hicken et al., 2009a).

In the Union2 paradigm, systematic errors that directly affect SN distance measurements (calibration or Galactic and host-galaxy extinction, for instance) are treated as nuisance parameters to be fitted simultaneously with the cosmology. Minimizing these nuisance parameters gives additional terms to add to the covariance matrix of the distance modulus

$$U_{ij} = \sum_{\epsilon} \frac{d\mu_i(\alpha,\beta,\delta)}{d\epsilon} \frac{d\mu_j(\alpha,\beta,\delta)}{d\epsilon} \sigma_\epsilon^2 \ , \tag{3.13}$$

where the sum is over each of the systematic errors considered in the analysis and α, β and δ are the light-curve correction parameters.

Systematic errors that affect sample composition or the color and shape correction coefficients cannot be parameterized supernova by supernova. These are incorporated by assigning to each data set its own constant covariance. Amanullah et al. (2010) showed that adding each covariance in the covariance matrix rather than summing the derived cosmological impacts in quadrature, yielded smaller systematic errors for the Union2 analysis (see Table 3.1). This is due to the difference redshift dependence of each systematic error.

In the last versions of the Union compilation, two new systematic errors are studied. A systematic error on the host-mass-correction coefficient and uncertainties in the effective wavelengths and zero points of the filters. A table summarizing the main systematic errors considered in the Union2.1 sample can be found in Table 3.1.

3.7 Space Versus Ground

The Earth's atmosphere is another important cause of systematic uncertainties, which appreciably affect the data (Davis et al., 2006). The very strong and variable absorption due to water molecules in the atmosphere makes the sky opaque to significant parts of IR radiation. Problems derived from atmospheric absorption can be completely avoided if a telescope is placed in space,

Table 3.1: Main systematic errors analysed for the Union2.1 sample. Adapted from Suzuki et al. (2012).

Source	**Error on w**
Vega	0.033
All instrument calibration	0.030
Color correction	0.020
Mass correction	0.016
Contamination	0.016
Intergalactic extinction	0.013
Galactic extinction	0.010
Light curve shape	0.006
Quadrature sum	0.061
Summed in covariance matrix	**0.048**

obtaining greater accuracy and precision in flux calibration. Other systematic errors affecting cosmological studies can also be overcome with higher-quality photometry (magnitude measurements with errors less than 0.02) and spectroscopy (essential for classification) obtained from space.

The technical advantages of space-based telescopes for supernova cosmology were already emphasized early on by Aldering et al. (2002b). They describe the improvement in stability of the point-spread function (PSF) achievable from space, increasing the sensitivity to faint, variable point sources and the higher precision and accuracy of photometry (especially in the presence of a host galaxy environment). In contrast, the use of *adaptive optics* (Beckers, 1993) from the ground can yield a sharp PSF, but it is not likely to produce photometry with 1% precision and an image stable enough to allow host subtraction at random positions in the sky away from bright guide stars.

Concerning the low sky background in the NIR in space, Weinberg et al. (2012) regard it as a critical point, since no improvements in ground-based technology or observing strategy will ever remove the IR sky noise. For instance, photometry in the rest-frame J-band (1.2 μm) of SNe at $z = 0.8$, with high signal-to-noise at peak magnitude, can be obtained using a 1.3-m space telescope (such as the one proposed for WFIRST, see next Section) in about 20 minutes. However, a ground-based 4-m telescope with 0.8 arcsec seeing[1] and a typical IR sky background would require multiple nights, and still the accuracy of the photometry would be affected by the variable sky (Weinberg et al., 2012). These considerations make space missions important and necessary.

[1]The astronomical seeing is a relative measure of the optical quality of the Earth's atmosphere and refers to the steadiness and absence of distortion in a telescopic image across an interval of observation. For a review on seeing solutions and adaptive optics see Beckers (1993).

3.8 Future Samples and Surveys

Different observational strategies are presently being implemented. One of the approaches is to extend the current supernova samples towards higher redshifts. The sample of SNe Ia beyond $z > 1$ is rather small at present (Riess et al., 2007), and several teams, such as the High-Z Search Team, using the HST, are focusing on observing SNe at redshifts $z > 1.5$ to provide additional constraints on the Hubble diagram and SN evolution.

Another ongoing NASA enterprise is the future successor of the HST, the *James Webb Space Telescope* (JWST) to be launched in 2014. This space observatory will make it possible to find many distant SNe (up to $z \sim 2$) in the NIR, leading to a more precise Hubble diagram. Moreover, it will improve the distance measurements and reduce light curve shape and reddening corrections, which limit the accuracy of current data. This will present a critical test of the current results and a significant improvement with respect to systematics.

Other teams focus on the study of nearby supernovae, which can be observed with higher precision and are fundamental for our understanding of the present expansion rate. Large campaigns to discover and monitor local supernovae (e.g., PTF or the SN Factory) should yield better understanding of potential systematics, as well as a better local calibration.

Improving ground-based surveys with new instrumentation, in particular wide-field cameras, and dedicated telescopes is also important for increasing the quantity and quality of the data. The next year or two should see the publication of the final results from the SDSS-II SN survey, the five-year SNLS sample, and ESSENCE. The measurements from these large surveys should substantially reduce the statistical errors in the Hubble diagram. Systematic errors are also expected to be reduced due to the high sampling cadence, wide wavelength range and careful photometric calibration of these surveys. One of the largest projects on the near horizon is the ongoing Dark Energy Survey (DES, The Dark Energy Survey Collaboration, 2005) that started operations in late 2012 and is using the CTIO Blanco 4-m telescope. This survey will observe ~ 2000 SNe Ia in the redshift interval $0.3 < z < 0.8$. The DES strategy and forecast discovery rate can be found in detail in Bernstein et al. (2012), but essentially they hope to find up to 4000 Type Ia SNe out to redshift $z = 1.2$. DES aims to observe $10 - 20\%$ of their high-z supernovae spectroscopically but to obtain nearly complete spectroscopic host galaxy redshifts for their cosmological sample.

Another ground-based survey telescope that is expected to find thousands (or even tens of thousands) of SNe is the Panoramic Survey Telescope & Rapid Response System[2] (Kaiser & Pan-STARRS Team, 2002), which in its first phase (with the 1.8-m PS1 telescope on Haleakala in Hawaii) has already detected hundreds of SNe. Both Pan-STARRS and DES are being carried out by international, multi-institutional collaborations and will cover a large area

[2]http://pan-starrs.ifa.hawaii.edu/public

with multiband imaging surveys, going a factor of ten deeper in flux than the SDSS imaging survey (Abazajian et al., 2009). Looking ahead, the Large Synoptic Survey Telescope[3] (LSST Science Collaboration et al., 2009) will use a wide-field 8.4-m optical telescope equipped with a 3.2-Gigapixel camera, that would enable deep weak lensing and optical cluster surveys over a large area of the sky and would detect and measure tens of thousands of supernovae.

However, it is still not clear to which extent this outstanding number of SNe will be used for dark energy studies. It will be practically impossible to obtain spectroscopy for the classification of all these objects, and the errors will be mostly dominated by systematics, though for LSST, with its high photometric precision in the optical, they should be below those of PS1 and DES.

Finally, if the space mission Wide Field InfraRed Survey Telescope (WFIRST) is completed and launched following the Astro2010 recommendations (Astro2010 Decadal Survey report, New Horizons in Astronomy and Astrophysics) the access to the rest-frame NIR should be of great advantage for SN cosmology.

The European Space Agency (ESA) recently selected the Euclid satellite as a medium-class mission for its Cosmic Vision 2015-2025 program, with launch planned for 2020. Though primarily intended for weak lensing and BAO measurements, Euclid will also provide optical and NIR imaging and spectroscopy of a few thousand Type Ia supernovae to intermediate z, covering a sky area of roughly 14,000 deg^2.

[3]http://www.lsst.org

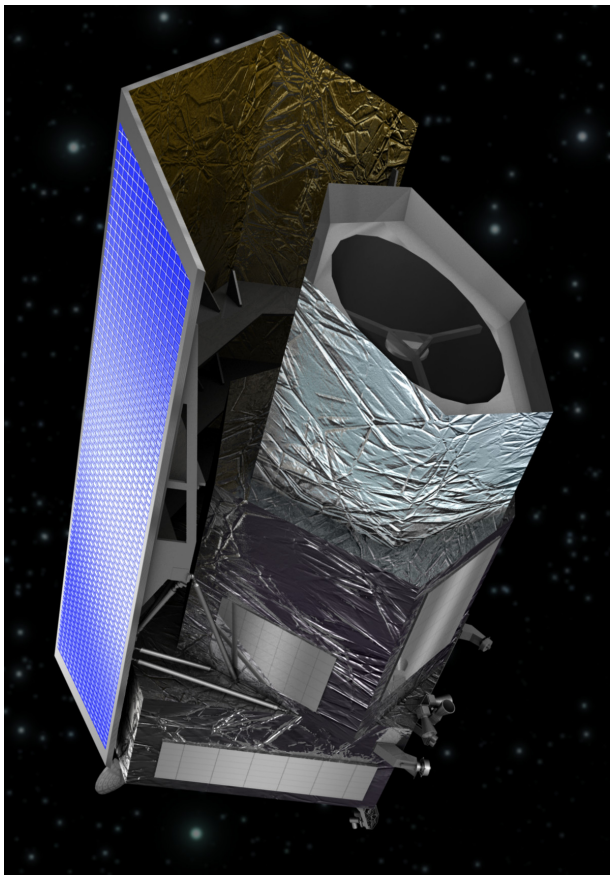

Figure 3.20: Artistic impression of the future ESA satellite Euclid. Taken from http://www.euclid-ec.org/.

4. The Model-Independent Method to Reconstruct the Expansion Rate

In this Chapter, we review the reconstruction technique that has been used for the work presented in this thesis. The details of the method and the assumptions it relies on, together with the improvements added concerning Principal Component Analysis, are described.

4.1 Motivation: Why Model Independent?

Since the discovery of the accelerating expansion a decade ago, both theoretical and observational studies have attempted to search for further evidence of dark energy. A matter-dominated universe at the present epoch seems to be inconsistent when various cosmological probes, such as SNe, BAO or CMB, are combined, implying that a dark component of unknown nature is present in the Universe. As we saw in Chapter 2, there is a large variety of cosmological models that account for acceleration, and this degeneracy is still difficult to break with current data. Usually, these models are based on a specific parameterisation of the equation of state which is introduced into the Friedmann equations to obtain the cosmic expansion rate. Then, each model is confronted with observations to estimate the best cosmological parameters. In contrast with the common approach, the method employed in this work makes no assumption on the energy/matter content of the Universe and looks only for the geometry, therefore it is a model-independent method.

The idea of a model-independent reconstruction extracted straight from the data was already addressed in Starobinsky (1998). Other authors such as Huterer & Turner (1999, 2000); Tegmark (2002); Wang & Tegmark (2005) have worked since then to find the best methodology and procedure to properly smooth the data in redshift bins. Recently, reconstructions of this kind have been carried out by Shafieloo et al. (2006, 2007) using SNe data; Fay & Tavakol (2006) adding BAO constraints to the SNe; and Daly & Djorgovski (2003, 2004) combining SNe Ia luminosity distances with angular-diameter distances from radio galaxies. Seikel & Schwarz (2009) have also tested the significance

of cosmic expansion directly from SN Ia data in a model-independent way. Other non-parametric approaches to reconstruct the expansion history and equation of state of dark energy use Gaussian Processes for smoothing the data (see e.g. Seikel et al., 2012).

Other suggestions of model-independent analyses involve kinematic considerations, trying to avoid references to the matter/energy content of the Universe. However, they do assume special parameterisations of the deceleration parameter $q(z)$ (e.g. Turner & Riess, 2002; Riess et al., 2004; Elgarøy & Multamäki, 2006), the scale factor $a(t)$ (Wang & Tegmark, 2005) or the Hubble rate $H(z)$ (e.g. John, 2005) at some point. Also expansions of the deceleration parameter, q, into principal components (Shapiro & Turner, 2006) or the jerk parameter, j, into a series of orthonormal functions have been proposed (Rapetti et al., 2007) .

The method described here was first developed by Mignone & Bartelmann (2008). It provides a purely geometrical test to derive the expansion history of the Universe as a function of redshift z, or equivalently, the scale factor a. No reference to any specific Friedmann model is made in this approach; that is, no presumption of a special parameterisation for the matter and energy of the Universe is made. The minimal assumptions involved are that the Universe is topologically simply connected, homogeneous and isotropic, described by the Robertson-Walker metric as expressed in Eq. 2.4, and that the expansion rate is a smooth function.

In this context, SNe Ia are very suitable observables, for they allow us to directly map the accelerated cosmic expansion (once they have been calibrated, as discussed in Sect. 3.4). Luminosity-distance measurements over a wide range of the scale factor, $D_{\rm L}(a)$, obtained from SNe Ia, can be directly related to the Hubble function by specifying only the metric. Contrary to other ways of analyzing cosmological data, where usually a specific Friedman cosmology is a priori defined, this method does not make any assumptions on the energy content of the Universe nor its dynamics.

4.2 Mathematical Formalism

4.2.1 Background

We recall from Chapter 2 that Friedman equations can be written as a function of the present-day density parameters for radiation (Ω_{r0}), matter ($\Omega_{\rm M0}$), curvature (Ω_{k0}) and dark energy ($\Omega_{\Lambda 0}$):

$$E(a) = \left[\frac{\Omega_{r0}}{a^4} + \frac{\Omega_{\rm M0}}{a^3} - \frac{\Omega_{k0}}{a^2} + \Omega_{\Lambda 0} F(a)\right]^{1/2}, \tag{4.1}$$

where $E(a)$ is the expansion function normalised to unity today, $a = 1$, so that $H^2(a) = H_0^2 E^2(a)$. The function $F(a)$ depends on the time-varying equation of state of the dark energy as

$$F(a) = \exp\left[-3\int_1^a 1 + w(x)\frac{dx}{x}\right]. \tag{4.2}$$

In the usual approach, one would assume this expression (or variations of it) for the expansion rate as true and would try to constrain the density parameters by confronting the model with some cosmological probes, such as SNe, BAO or CMB. However, instead of assuming a specific Friedmann model and constraining the parameters contained in $E(a)$, the method applied here advocates a parameter-free recovery of the expansion rate as a function of the scale factor a.

From the Robertson-Walker metric it is possible to define the angular-diameter distance by

$$D_A(a) = a f_K[\chi(a)], \tag{4.3}$$

with the comoving angular-diameter distance

$$f_K(\chi) = \begin{cases} \sin\chi & (K=1, \quad \text{spherical}) \\ \chi & (K=0, \quad \text{flat}) \\ \sinh\chi & (K=-1, \quad \text{hyperbolic}). \end{cases} \tag{4.4}$$

and the comoving distance

$$\chi(a) = \frac{c}{H_0}\int_a^1 \frac{dx}{x^2 E(x)}. \tag{4.5}$$

From the equations above we can write the luminosity distance as an integral of the inverse of the expansion rate

$$D_{\rm L}(a) = \frac{c}{H_0}\frac{1}{a}\int_a^1 \frac{dx}{x^2 E(x)} \equiv \frac{c}{H_0}\frac{1}{a}\int_a^1 \frac{dx}{x^2} e(x), \tag{4.6}$$

with $e(a) \equiv E^{-1}(a)$ and $K = 0$ set in Eq. 4.4 for simplicity of notation (note that this first-order approximation could be abandoned when necessary without any change of principle). H_0 is the Hubble constant and c/H_0 is the Hubble length which shall be removed in further discussion also for simplicity (i.e. the luminosity distance is scaled to the Hubble length).

4.2.2 Model-Independent Determination of the Expansion Rate Function

Starting with Eq. 4.6, we then differentiate it with respect to a to obtain

$$D'_{\rm L}(a) = -\frac{1}{a^2}\int_a^1 \frac{dx}{x^2} e(x) - \frac{e(a)}{a^3}. \tag{4.7}$$

This expression can be transformed into a Volterra integral equation of the second kind for the unknown function $e(a)$

$$e(a) = -a^3 D'_{\rm L}(a) + \lambda \int_1^a \frac{dx}{x^2} e(x), \tag{4.8}$$

with the inhomogeneity $f(a) \equiv -a^3 D'_L(a)$ and the simple kernel $K(a,x) = x^{-2}$. The general parameter λ will later be fixed to $\lambda = a$. For now it is introduced to make the connection to a class of equations for which solutions are known to exist and to be uniquely described in terms of a Neumann series (see Arfken & Weber, 1995):

$$e(a) = \sum_{i=0}^{\infty} \lambda^i e_i(a). \tag{4.9}$$

A possible choice for the function e_i would be

$$e_0(a) = f(a) \tag{4.10}$$

$$e_n(a) = \int_1^a K(a,t) e_{n-1}(t) dt, \tag{4.11}$$

where, for the guess of e_0, the approximation of either the integral or λ to be small has been made in Eq. 4.8. This approximation is valid in all important cosmological cases and it is subsequently improved until convergence is reached. It essentially means that starting, for instance, from the ΛCDM cosmology observations, deviations must be small, if they exist at all.

Equation 4.8 involves the derivative of the luminosity distance with respect to the scale factor a. Observations of SNe Ia provide measurements of the distance modulus, μ_i, and redshifts, z_i (or scale factors $a_i = (1+z_i)^{-1}$), and we know from Sec. 2.6 how to calculate the luminosity distances $D_{\rm L}(a_i)$ from these observables.

Thus, one could think of taking the derivative of the luminosity distance directly from the data. However, this is the most inconvenient procedure since the result would be extremely noisy and the determination of $D'_{\rm L}(a)$ would be unreliable. This is due to the measurement errors and scatter of the data about the fiducial model, which makes the differentiation of the luminosity distance directly from the data difficult. Therefore, it is necessary to suitably smooth the data in the first place by fitting an adequate function $D_{\rm L}(a)$ to the measurements $D_{\rm L}(a_i)$ and approximating the derivative in Eq. 4.8 through the derivative of $D_{\rm L}(a)$. In this way, the derivative of the fitted data is taken as a representation of the derivative of the real data. The method employed here achieves this goal via the expansion of the luminosity distance $D_{\rm L}(a)$ into a series of arbitrarily chosen orthonormal functions $p_j(a)$:

$$D_{\rm L}(a) = \sum_{j=1}^{J} c_j p_j(a). \tag{4.12}$$

Suitable orthonormal function sets can be constructed by Gram-Schmidt orthonormalisation from any linearly independent function set. The J coefficients c_j are those which minimise the χ^2 statistic function when fitting to the data.

$$\chi^2 = (\mathbf{D}_{\rm obs} - \bar{D}(\mathbf{a}))^T C^{-1} (\mathbf{D}_{\rm obs} - \bar{D}(\mathbf{a})), \tag{4.13}$$

where the covariance matrix C^{-1} is assumed to be symmetric, $\mathbf{D}_{\rm obs}$ is a vector of the measured luminosity distances, $\mathbf{a}$ is a vector of the measured scale factors, and $\bar{D}(a_i)$ is the vector of model luminosity distances, defined by

$$\bar{D}(a_i) \equiv \sum_{j=1}^{J} c_j p_j(a_i) \equiv (Pc)_i. \tag{4.14}$$

We define P as a $N \times J$ matrix with elements $P_{ij} \equiv p_j(a_i)$ and $\mathbf{c}$ is the J-dimensional vector of the expansion coefficients. Thus, the set of coefficients that minimise χ^2 is

$$\mathbf{c} = (P^T C^{-1} P)^{-1} (P^T C^{-1}) \mathbf{D}_{\rm obs}. \tag{4.15}$$

With this representation of the data, the derivative of the luminosity distance function is simply given by

$$D'_{\rm L}(a) = \sum_{j=1}^{J} c_j p'_j(a). \tag{4.16}$$

Due to the linearity of Eq. 4.8, it is possible to solve it for each mode j of the orthonormal function set. Introducing the derivative of a single basis function $p'_j(a)$ instead of $D'_{\rm L}(a)$ into Eq. 4.8, we find that its contribution to the (inverse) expansion rate in terms of Neumann series is

$$e^{(j)}(a) = \sum_{k=0}^{\infty} a^k e_k^{(j)}(a), \tag{4.17}$$

with

$$e_0^{(j)}(a) \equiv -a^3 p'_j(a), \tag{4.18}$$

$$e_n^{(j)}(a) = \int_1^a e_{n-1}^{(j)}(x) x^{-2} dx. \tag{4.19}$$

These modes of the inverse expansion function can be computed iteratively for any given orthonormal function set $p_j(a)$. The final solution is then

$$e(a) = \sum_{j=1}^{J} c_j e^{(j)}(a), \tag{4.20}$$

that is, the measured coefficients of the series expansion directly give the solution for the expansion function. The only condition here is that the number of coefficients required to fit the data should be minimal. Moreover, the truncation of the series in Eq. 4.12 is based entirely on the quality of the data. This sets a limit on how many of the required coefficients we are able to get for an accurate reconstruction. We will discuss this aspect further in the following sections.

4.2.3 Illustration of the Method: Reconstructing ΛCDM

As an illustration of the technique, a synthetic sample is simulated in a flat ΛCDM cosmology with $\Omega_{\rm M} = 0.3, \Omega_\Lambda = 0.7$ and a Hubble constant of $H_0 = 70$ km s^{-1} Mpc^{-1}. From Friedman Eq. 4.1 we determine that the expansion function for such a cosmology is

$$E(a) = (\Omega_{\rm M} a^{-3} + \Omega_\Lambda)^{1/2}. \tag{4.21}$$

The corresponding luminosity distance $D_{\rm L}(a)$ for this model can be determined via Eq. 4.6. A suitable choice for the orthonormal function set could be the linearly independent set

$$u_j(x) = x^{j/2-1}, \tag{4.22}$$

which can be orthonormalised by the Gram-Schmidt method. The orthonormalisation interval will be $[a_{\rm min}, 1]$ where

$$a_{min} = (1 + z_{\rm max})^{-1} \tag{4.23}$$

is the scale factor of the maximum redshift $z_{\rm max}$ in the synthetic supernova sample. In this way, an arbitrary set of orthonormal functions $p_j(a)$ is obtained. When projecting the luminosity distance $D_{\rm L}(a)$ onto these basis functions, we can solve for the expansion coefficients. For a ΛCDM universe with the values of the parameters specified above, the minimal number of coefficients significantly different from zero is five. In Fig. 4.1 the model luminosity distance is compared to its reconstruction using the basis functions proposed above and calculating the coefficients of its expansion. If only three or four coefficients are used for the reconstruction, it clearly deviates from the model.

The problem arises here when one considers the SNe Ia data presently at hand. Unfortunately, a reconstruction with only the first three coefficients can be obtained from the real $D_{\rm L}(a_i)$ data, since the errors on the fourth and fifth coefficients are too large and they loose significance. This is due to the errors in the data, which limit our ability to accurately determine the expansion function. Figure 4.2 shows the reconstructed expansion function with three coefficients for a simulated sample with the same observational characteristics as the first-year SNLS data (Astier et al., 2006) compared to the expansion rate of the underlying ΛCDM model. We see there is *apparent*

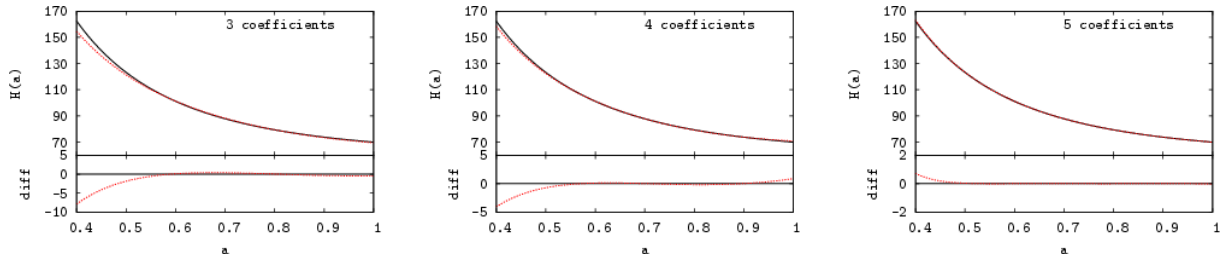

Figure 4.1: The expansion rate in a ΛCDM model with $\Omega_{\rm M} = 0.3$ and $\Omega_\Lambda = 0.7$ (solid line) and its reconstruction using three, four, and five coefficients (red curves). The bottom panels show the residuals between the reconstruction and the model. $H(a)$ is given in units of km s^{-1} Mpc^{-1}. From Mignone & Bartelmann (2008).

good agreement between the model and the reconstruction, though we know from the theoretical calculation that the reconstruction is incomplete.

The strong dependence of the number of terms in the expansion on data quality represents an important drawback of the method. Moreover, the choice of the orthonormal basis also influences the number of coefficients to be included in the reconstruction. In fact, although the basis would, in principle, be arbitrary with ideal data, it is not in practice. It surely is possible to choose a convenient function set which would minimize the number of coefficients we need for the reconstruction. We address this issue in the next Section by introducing an optimal basis system based on Principal Component decomposition.

4.3 Principal Component Analysis

In this Section, we revise the mathematical algorithm to derive the Principal Components from a generic data set (for a careful review on this topic see Jollife, 2002).

Principal Component Analysis (PCA) is a well known statistical tool which aims at reducing the dimensionality of an initially very large parameter space. The PC procedure looks for directions of maximum *variance*[1] within the data and constructs an orthonormal basis representing directions (the PCs) of maximum clustering, or along which most of the information is contained. After the PCs are determined, the original data can be re-written as a linear combination of some PCs, usually a number much smaller than the dimensionality of the original parameter space. This new set of variables are *uncorrelated* and have the property that the first few already retain most of the information in the data.

Imagine a data set $\mathbf{X}$ with p variables and n objects. Calculating the PCs from such as data set involves the definition of a *covariance matrix* Σ

[1] *Variance* is a measure of the spread of the data usually defined as $Var = \frac{\sum_{i=1}^{n}(x_i - \bar{x})^2}{n-1}$.

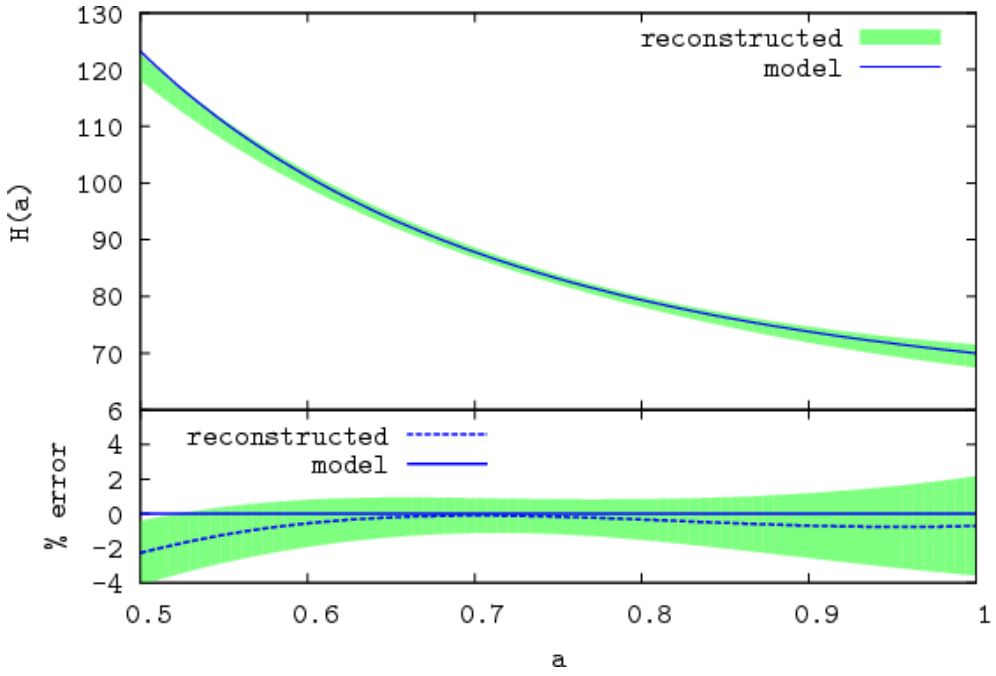

Figure 4.2: The reconstructed expansion rate with 1σ errors for a simulated sample of SNe in a ΛCDM universe (blue line) with observational characteristics resembling those of the 1st year SNLS data. The bottom panel shows the residuals between the reconstruction and the model. $H(a)$ is given in units of km s^{-1} Mpc^{-1}. From (Mignone & Bartelmann, 2008).

$$\Sigma = \begin{bmatrix} \sigma_{11} & \sigma_{12} & \cdots & \sigma_{1p} \\ \sigma_{21} & \sigma_{22} & \cdots & \sigma_{2p} \\ \vdots & \vdots & & \vdots \\ \sigma_{p1} & \sigma_{p2} & \cdots & \sigma_{pp} \end{bmatrix}. \tag{4.24}$$

where the covariance between the two variables i and j is given by

$$\sigma_{ij} = \sigma_{ji} = \frac{1}{n-1}\sum_{k=1}^{n}(x_{ki} - \bar{x}_i)(x_{kj} - \bar{x}_j). \tag{4.25}$$

The covariance matrix is then diagonalized by solving

$$|\Sigma - \lambda I|\mathbf{v} = 0, \tag{4.26}$$

where $\lambda_1 > \cdots > \lambda_p$ are the `eigenvalues` and $\mathbf{v}_1(\lambda_1), \cdots, \mathbf{v}_p(\lambda_p)$ the corresponding `eigenvectors`. The *first* principal component is the eigenvector with the largest eigenvalue, which accounts for the maximal amount of total variance. The *second* component is the eigenvector with the second largest eigenvalue, accounting for the amount of variance that was not accounted for by the first component and so on. Moreover, the derived PCs are uncorrelated

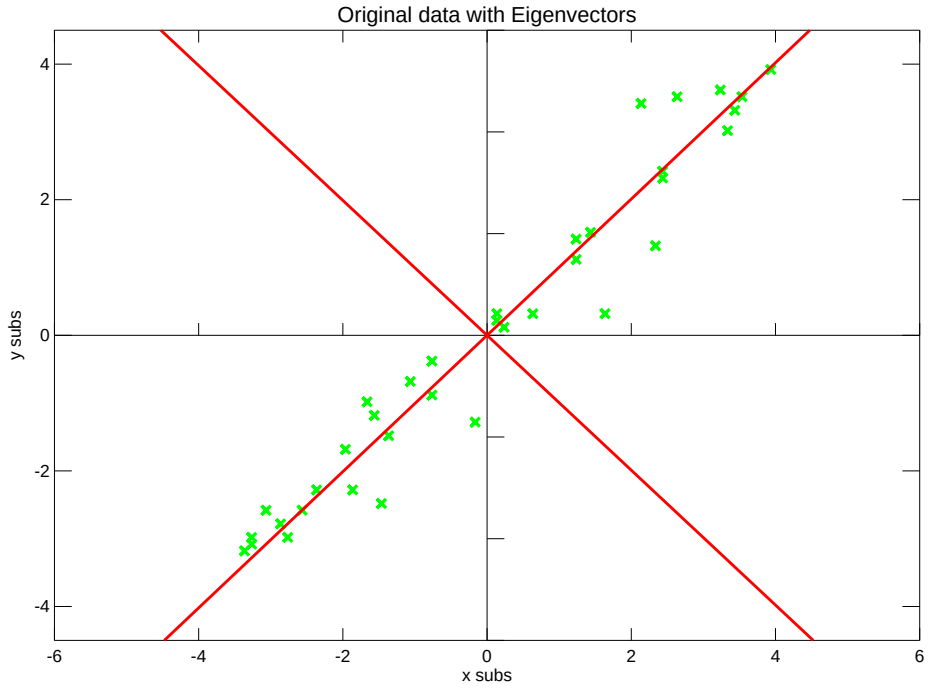

Figure 4.3: A 2-D normalised data (mean subtracted) plotted together with the Principal Components. The first PC points to the direction of maximum clustering with analogous meaning as a line of best fit. The second eigenvector gives the spread around that direction.

(*orthogonal*) to the preceding components. It is obvious that the number of components extracted equals the number of observed variables being analyzed, that is p. However, in most analyses, only the first few components account for meaningful amounts of variance, so only these first few components are retained, allowing for a significant reduction in dimensionality.

Figure 4.3 illustrates the PCs (red axis) found for a 2-D data set. In this simple example, the linear transformation associated with the principal components can be seen as a rotation of axis in the direcction of higher variance. Note that in any PC prescription, the original data have to be normalised before computing the covariance matrix, by subtracting the mean from each of the data dimensions.

4.3.1 Building the Basis with Principal Component Analysis.

PCA is a beneficial technique to be used together with a *model-independent* approach as the one proposed in this thesis. In this Section, we shall substitute the arbitrary orthonormal basis mentioned in Section 4.2.3 by a new basis system derived from PCA.

Different approaches using PCA have been proposed to reconstruct the dark energy equation of state w (e.g. Huterer & Starkman, 2003; Simpson & Bridle, 2006; Huterer & Peiris, 2007), the Hubble parameter (Ishida & de Souza, 2011) and the cosmic star formation history (Ishida et al., 2011). Here we follow the method described in Maturi & Mignone (2009) to obtain an optimal basis system for a given cosmological data set, in this case a luminosity-distance SNe Ia catalogue.

We start by defining a 1D vector $\mathbf{d} \in \Re^n$ which collects the redshift or scale factor values for which there is a luminosity distance measurement in our catalogue

$$\mathbf{d} = [D_{\rm L}(a_1), D_{\rm L}(a_2), ..., D_{\rm L}(a_n)]. \tag{4.27}$$

The next step is to choose a group of models we believe spans the set of viable cosmologies. Suppose we chose initially M different cosmologies: for each one of them we calculate the luminosity distance for the value of scale factor given in $\mathbf{d}$, producing for each model a vector $\mathbf{t}_i$. This ensemble of models, referred to as the *training set*, initializes the method and is defined as follows:

$$\mathbf{T} = (\mathbf{t}_1, \mathbf{t}_2, ..., \mathbf{t}_M), \tag{4.28}$$

where each training vector $\mathbf{t}_i$ $\{\mathbf{t}_i \in \Re^n \mid i = 1, ..., M\}$ corresponds to a particular behaviour of the observable as a function of scale factor. The matrix $\mathbf{T}_{n\times M}$ represents a convolution of all our expectations towards the underlying cosmology and will act as a synthetic data set in order to determine an ideal orthonormal basis.

Once the training set of models is defined, we build the so called *scatter matrix* (analogous to a covariance matrix)

$$\mathbf{S} = \Delta\Delta^T \in \Re^{n\times n} \tag{4.29}$$

with

$$\Delta = (t_1 - \bar{\mathbf{t}}, t_2 - \bar{\mathbf{t}}, ..., t_M - \bar{\mathbf{t}}) \tag{4.30}$$

containing the differences between each training vector and a given reference vector that defines the origin of the parameter space. This reference model may be any combination of models within $\mathbf{T}$, and is usually set to be the mean of the training set $\bar{\mathbf{t}} \equiv \langle t \rangle$. A different choice for the reference model can be used instead, depending on the specific problem at hand. An interesting choice could be the best fit to a given cosmological model, so that all other models would be described as its perturbed states (see Chapter. 5 for a discussion of this issue).

The principal components are found by solving the usual eigenvalue problem

$$\mathbf{w}_i = \lambda_i \mathbf{S}\mathbf{w}_i, \tag{4.31}$$

where λ_i and $\mathbf{w}_i$ are the eigenvalues and the eigenvectors, respectively. The linear transformation W leading to these PCs is defined in such a way that it concentrates, in only a few features, all the information (or variance) regarding the deviations of the models in the training set from the reference vector. The eigenvector with the largest eigenvalue corresponds to the direction of maximum variance (first PC). The second PC corresponds to the direction defined by the eigenvector with the second largest eigenvalue and so on. Figure 4.4 shows how cosmologies are represented in the new parameter space. The first two principal components of an ensemble of non-flat ΛCDM models are plotted together with the projection of the real data.

As was mentioned in previous Section, an important issue when working with PCA is the determination of how many PCs one should take into account (Jollife, 2002, chapter 6). The number of terms to be included in our reconstruction is based on the *cumulative percentage of total variance* represented by a set of L PCs,

$$t_L = \left(\frac{\sum_{i=1}^{L} \lambda_i}{\sum_{j=1}^{N_{\rm PC}} \lambda_j} \times 100 \right), \tag{4.32}$$

where $N_{\rm PC}$ is the total number of PCs and L the number to be included in the reconstruction. In this way, the question of how many Principal Components to use (i.e. number of coefficients in our reconstruction) translates into what percentage of variance we are willing to consider.

After constructing the orthonormal basis and deciding how many PCs to include in the final analysis (L), we express the corrections for the luminosity distance to the reference model ($D_{\rm L}|_{\rm ref}$, from now on) as linear combinations of the first L PCs,

$$D_{\rm L}(a) \equiv D_{\rm L}|_{\rm ref} + \sum_{j=1}^{L} c_j w_j(a). \tag{4.33}$$

Following what was done in the previous section, the final values for the coefficients c_j are determined by confronting this expression for the luminosity distance with the data through a χ^2 minimisation. Subsequently, we approximate the derivative in Eq. 4.8 as

$$D'_{\rm L}(a) = \sum_{j=1}^{L} c_j w'_j(a). \tag{4.34}$$

As an illustration, the first four PCs computed for the Union2.1 sample (see Sec.3.6.3) are plotted in Fig. 4.5. Additionally, Fig. 4.6 shows the power of the corresponding eigenvalues in a Scree plot test (Cattell, 1966). This plot is

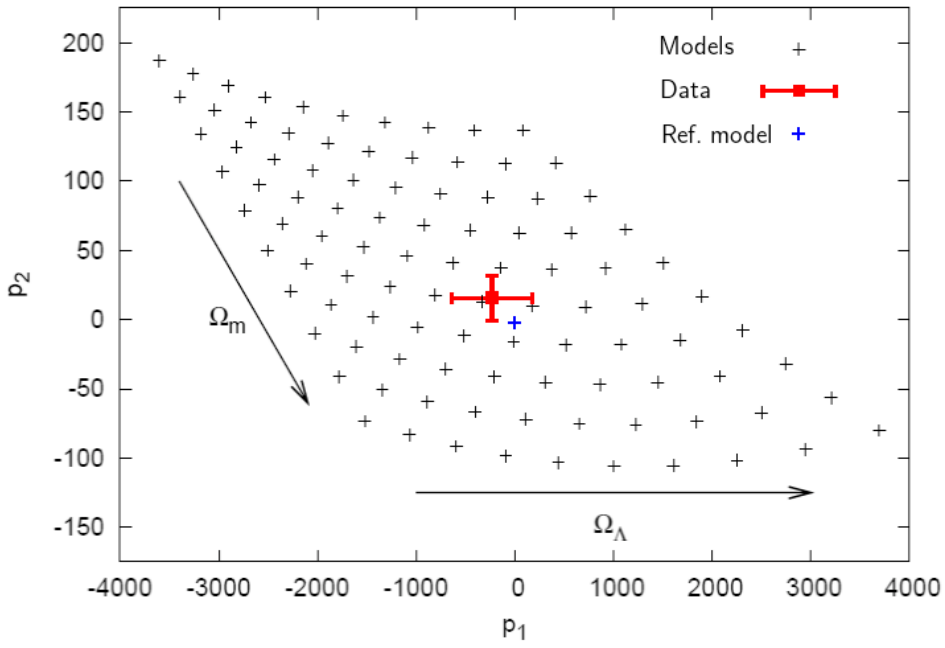

Figure 4.4: The first two principal components of a training set consisting of non-flat ΛCDM models. Each point in this plot represents a ΛCDM cosmology with cosmological parameters lying in the range $0.1 < \Omega_M < 0.5$ and $0.5 < \Omega_\Lambda < 0.9$. The redshift coverage used to generate this training set is taken from the 1st year SNLS data. The red point without error bars marks the space origin (reference model) and the red point with error bars shows the projected data set (Maturi & Mignone, 2009).

traditionally used as a tool to discriminate how many PCs to include in PCA studies. In the following Chapters, we will use basis built in the way described in this Section to reconstruct the expansion rate of the Universe.

4.4 Error Analysis

The errors in our method arise mainly from the uncertainty in the determination of the expansion coefficients, c_j, and the Hubble constant, H_0 (which is left as a free parameter in the analysis), due to the minimisation.

The errors in the coefficients c_j are calculated through error propagation of the SN distance measurements. The Fisher information matrix of the χ^2 statistic function is generally given by (Pratt, 1976)

$$F_{ij} \equiv \left\langle \frac{\delta^2 \chi^2}{\delta c_i \delta c_j} \right\rangle \tag{4.35}$$

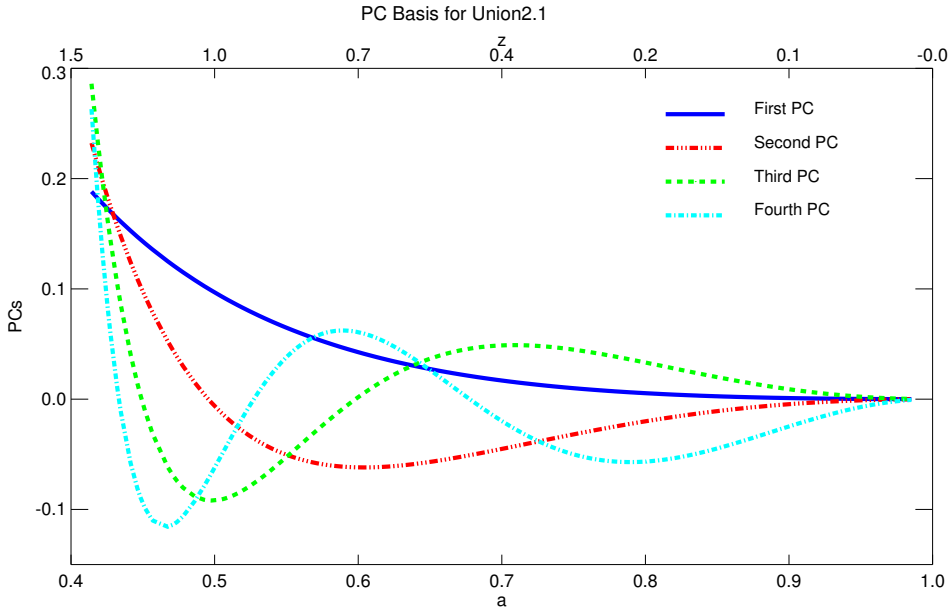

Figure 4.5: The four first components calculated with the formalism proposed in this Section, using the redshift distribution of the Union2.1 sample.

which for this particular case can be written as

$$F_{ij} \equiv \sum_{k=1}^{N_{\rm SNe}} \frac{p_i(a_k)p_j(a_k)}{\sigma_k^2}, \tag{4.36}$$

where k runs over all SN measurements and σ_k^2 are the individual errors on the luminosity distances. By definition, the errors in the coefficients, Δc_i, satisfy the Cramér-Rao inequality

$$(\Delta c_i)^2 \geqslant (F^{-1})_{ii} \tag{4.37}$$

and propagate into the estimate of $e(a)$ as follows

$$[\Delta e(a)]^2 = \sum_{j=1}^{J} \left[\frac{\delta e(a)}{\delta c_j}\right]^2 (\Delta c_j)^2 = \sum_{j=1}^{J} \left[e^{(j)}(a)\right]^2 (\Delta c_j)^2. \tag{4.38}$$

The final errors on the expansion rate $E(a) = 1/e(a)$ are then

$$[\Delta E(a)]^2 = \frac{[\Delta e(a)]^2}{e^4(a)} \tag{4.39}$$

The error contribution due to the minimisation of H_0 is added to the previous one in quadrature. Moreover, the uncertainty in our ability to determine the Principal Components is given by (Ishida & de Souza, 2011; Jollife, 2002)

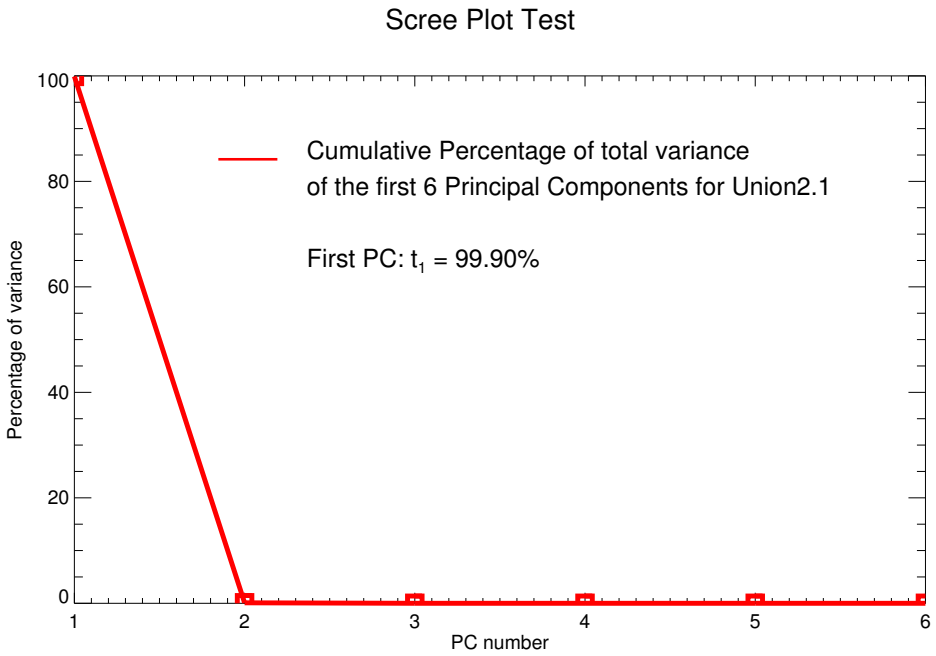

Figure 4.6: Scree plot test showing the cumulative percentage of total variance for the first PCs calculated for the Union2.1 sample.

$$\sigma_{\mathrm{PC}_i} \sim \frac{1}{\sqrt{\lambda_i}}. \tag{4.40}$$

In this way, the total error budget is expressed as

$$\sigma_T^2 = \sigma_{\mathrm{coeff}}^2 + \sigma_{H_0}^2 + \sigma_{\mathrm{PC}_i}^2. \tag{4.41}$$

4.5 Convergence of the Neumann Series

A different, though related matter, is to consider where the Neumann series should be truncated, i.e. up to what power k of the scale factor a the expansion in Equation 4.17 should proceed. Convergence of the series is achieved at different powers k for different redshift intervals. In order to achieve convergence on the interval $0.5 \leq a \leq 1$, the series can be truncated after $k = 4$. However, as it was proven by Mignone & Bartelmann (2008), the inclusion of the four-order term produces a difference to the preceding three orders which is already within the error bars, and can therefore be neglected. This is also true for the Union2.1 sample. Moreover, the Neumann series converge to zero at $a = 1$ to be consistent with the Principal Component basis.

4.6 Combining Different Data Sets and Families of Models

It is important to emphasise that, although we only present results of applying the method to SNe Ia data in this thesis, it could be also used to analyse any other observable which delivers standard candle or standard ruler measurements (e.g. CMB or BAO). A general parameterization, with independent parameters regardless the underlying physical assumptions, could be achieved by considering the Principal Components as *eigen-cosmologies*. In this context, observations would "excite" (i.e. make visible) a given number of modes according to their accuracy.

For example, if one wants to combine the luminosity distances of SNe Ia, angular-diameter distances and the CMB angular power spectrum, the data vector $\mathbf{d}$ should be organised as follows

$$\mathbf{d} = \left[D_{\rm L}(z_1)...D_{\rm L}(z_{N_{\rm SNe}}), D_{\rm A}(z_1)...D_{\rm A}(z_{N_{\rm BAO}}), C_{l_1}...C_{l_{N_{\rm CMB}}} \right] \tag{4.42}$$

whose dimension N is given by the sum of all data set sizes

$$N = N_{\rm SNe} + N_{\rm BAO} + N_{\rm CMB}. \tag{4.43}$$

In this case, it is probably useful to work with non-dimensional quantities which reflect the signal-to-noise ratios. This means that the different observables should be re-normalised with respect to their variance. Figure 4.7 shows an example of the PC approach applied to CMB data. Here the PC parameter space for an identical training set as the one used in Fig. 4.4 is plotted using the five-year WMAP data (Komatsu et al., 2009) instead of luminosity distance measurements.

It is also possible to make the training set less specialized by including different cosmological models than ΛCDM. For instance, one could include other dark energy scenarios that allow its equation of state to vary in time or alternative cosmologies based on several physical frameworks, such as the $f(R)$ or DGP theories discussed in Sec. 2.9.

4.7 Improving the Reconstruction

There are several advantages of using the PC orthonormal basis defined previously to construct a parameter space characterising observable behaviour instead of underlying physical quantities. First of all, the projections (Principal Components) of the training set into the new parameter space via the linear transformation W, are independent by definition and avoid any degeneracy in the observable description (which might not be the case in physical parameterizations). Moreover, the first few of them already contain all the

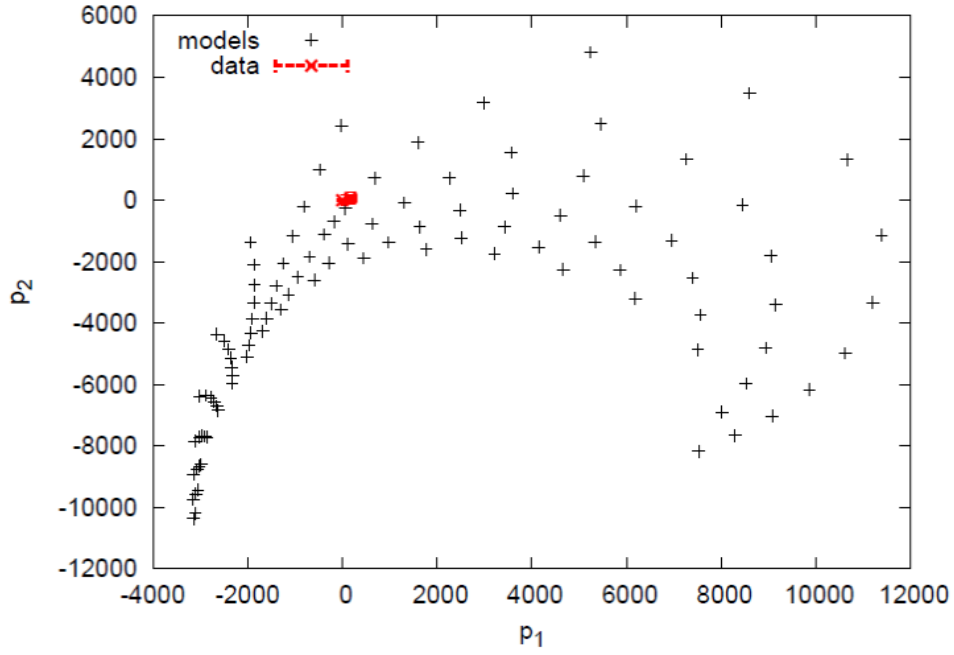

Figure 4.7: The first two principal components of a training set consisting on non-flat ΛCDM models for the five-year WMAP data (Komatsu et al., 2009). The red point mark the space origin (reference model) and the red point with error bars shows the projection of the data. Taken from (Maturi & Mignone, 2009).

available information since they are derived by Principal Components decomposition. Additionally, they provide the best discriminatory power for the family of cosmologies comprised in the training set, though this property does not preclude the method to recover cosmologies not included in the initial matrix of behaviours (see Sec. 5.1.2).

Figure 4.8 compares the reconstructed expansion history from the Union2.1 data using the old version of the method (green area) – that is, the arbitrary basis given by Eq. 4.22 and orthonormalised via the Gram-Schmidt process – against the new implementation using the PC basis (orange region).

The improvement in the reconstruction is obvious fore several reasons. In first place, we are now able to recover the expansion history from the data with one parameter only, instead of the three needed with the arbitrary basis. With the PC approach proposed in Sec. 4.3.1, we have a strong criterion for the number of coefficients to include in the reconstruction of the expansion rate. Moreover, we are also certain that the number of these is minimal and ordered according to their information content. By using the optimal basis system derived from a Principal Component analysis we are able to recover the *true*

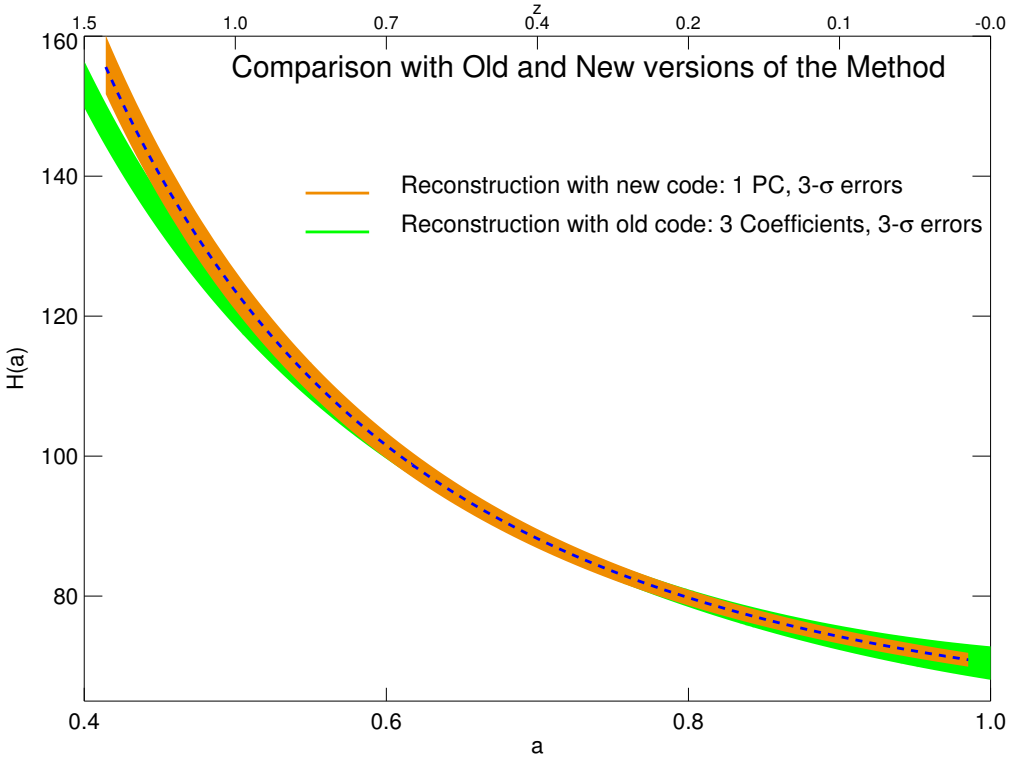

Figure 4.8: Comparison between the reconstructed expansion rate using the old version of method with arbitrary basis (green area, 3 coefficients) and the one obtained using the new basis system derived from PCA (orange region, 1 coefficient) for the Union2.1 data sample.

behaviour of the expansion rate removing any possible bias introduced by the choice of the basis. This is evident from the observed systematic trend on the slope of the $H(a)$ function, specially evident at high redshifts, when calculated with the old basis indicated. This clearly indicated that the estimation of the derivatives was not accurately determined with the old prescription, Finally, the reduction of the error bars at low redshift is quite significant, the scatter in H_0 being reduced by 50%.

It is worth stressing that (in contrast with other approaches in the literature) the complete methodology described here avoids both the binning in redshift while smoothing the SN data and any cosmological assumption on the matter/energy of the Universe. Since it relies only on the expansion of the luminosity distance into an orthonormal basis, it provides a model-independent determination of the expansion rate. The fact that the PC basis is computed by using an ensemble of *behaviours* (models) does not affect the model-independent nature of this method as we will see in following Chapters.

5. Testing the Method with Simulated Data

Here we describe the multiple tests performed to assess the robustness of the method presented in Chapter 4. Simulations of SN data were generated in several cosmological scenarios and standardized with the two light curve fitters discussed in Sec. 3.4. Also mock data covering different redshift ranges was simulated. In all cases, the underlying expansion rate of the simulated data was successfully recovered, indicating that the method performs well and can be reliably applied to real data.

Throughout this Chapter we will be referring a great deal to Union2.1-like data simulated in different contexts. For an illustration, the real Union2.1 (Suzuki et al., 2012) is plotted in Fig. 5.1, where $D_{\rm L}(a)$ is given in units of parsecs. The mock data discussed in this Chapter will cover the same redshift range and follow equal error distribution as the Union2.1, unless otherwise specified. In what follows we will give the values for the Hubble constant H_0 and the reconstructed expansion $H(a)$ in units of km s^{-1} Mpc^{-1}.

5.1 Different Cosmological Scenarios

5.1.1 ΛCDM Simulations

In first place, we calculated the luminosity distances consistent with equation Eq. 4.6 for a flat ΛCDM universe with cosmological parameters $\Omega_{\rm M} = 0.3$, $\Omega_\Lambda = 0.7$ and $H_0 = 63$ km s^{-1} Mpc^{-1}. Moreover, we generated random errors with uncertainties according to Suzuki et al. (2012). The random number was drawn from a normal distribution with mean zero and a standard deviation of one. A mock data set derived this way and consisting of about 600 SNe is plotted in Fig. 5.2 together with our estimation of $D_{\rm L}$.

To build the Principal Component basis, a training set consisting on non-flat ΛCDM models was produced by sampling the parameter space in the interval $0.1 \leq \Omega_{\rm M} \leq 0.5$ and $0.5 \leq \Omega_\Lambda \leq 0.9$. The reference model of the new parameter space was chosen to be the mean of the training set, i. e. $\Omega_{\rm M} = 0.3$, $\Omega_\Lambda = 0.7$. The reconstruction of the Hubble expansion with one PC and $3-\sigma$ errors is shown in Fig. 5.3. From the calculation of the cumulative percentage of total variance t_L (defined by Eq. 4.32) for each eigenvalue,

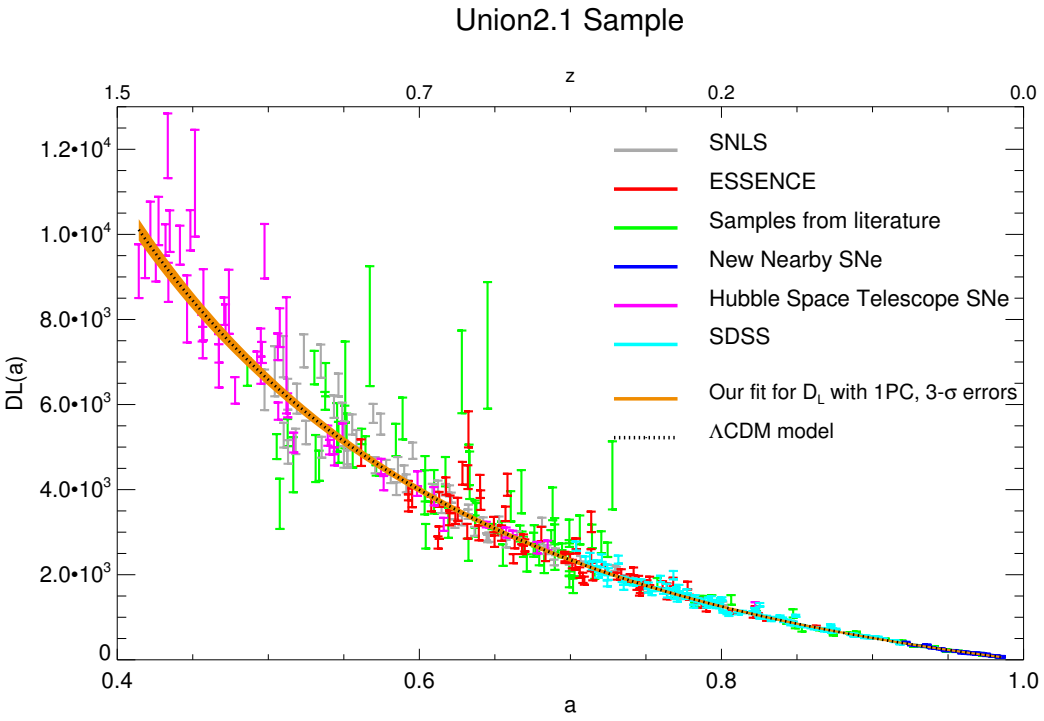

Figure 5.1: Luminosity distance versus scale factor a for the larger SN samples contained in Union2.1. Our fit for $D_{\rm L}(a)$ using 1 Principal Component and with 3-σ errors is shown in orange. The black dotted line represents a ΛCDM model shown here only for comparison. $D_{\rm L}(a)$ is giving in units of parsecs.

we determined that one PC is sufficient to fully reconstruct the expansion rate for this simple case. We found that the first eigenvalue (and hence, its corresponding eigenvector) already accounts for 99.90% of the total variance contained in the data. To asses how close our reconstruction is to the simulated data, we performed a simple χ^2-test, yielding a value of $\chi^2 = 1.025$ for the reduced χ^2 statistical function. In our approach, the Hubble constant is left as a free parameter to be minimised together with the expansion coefficients. We obtain a value of $H_0 = 63.03 \pm 0.12$, very close to the *true* value of the simulated data.

Subsequently, a more unrealistic model (still within the ΛCDM paradigm) was assumed to simulate the data. In this case, the underlying cosmological parameters were set to $\Omega_{\rm M} = 0.2$, $\Omega_\Lambda = 0.8$ and $H_0 = 70$. For the reconstruction of both $D_{\rm L}$ and H, the same basis as in the previous example was used. The result is plotted in Fig. 5.4. A value of $H_0 = 70.015 \pm 0.15$, consistent with the *true* value of the simulated data, was found in the minimisation with $\chi^2 = 1.01$. In this case we found that one PC was also enough to produce an accurate reconstruction, containing most of the percentage of total variance.

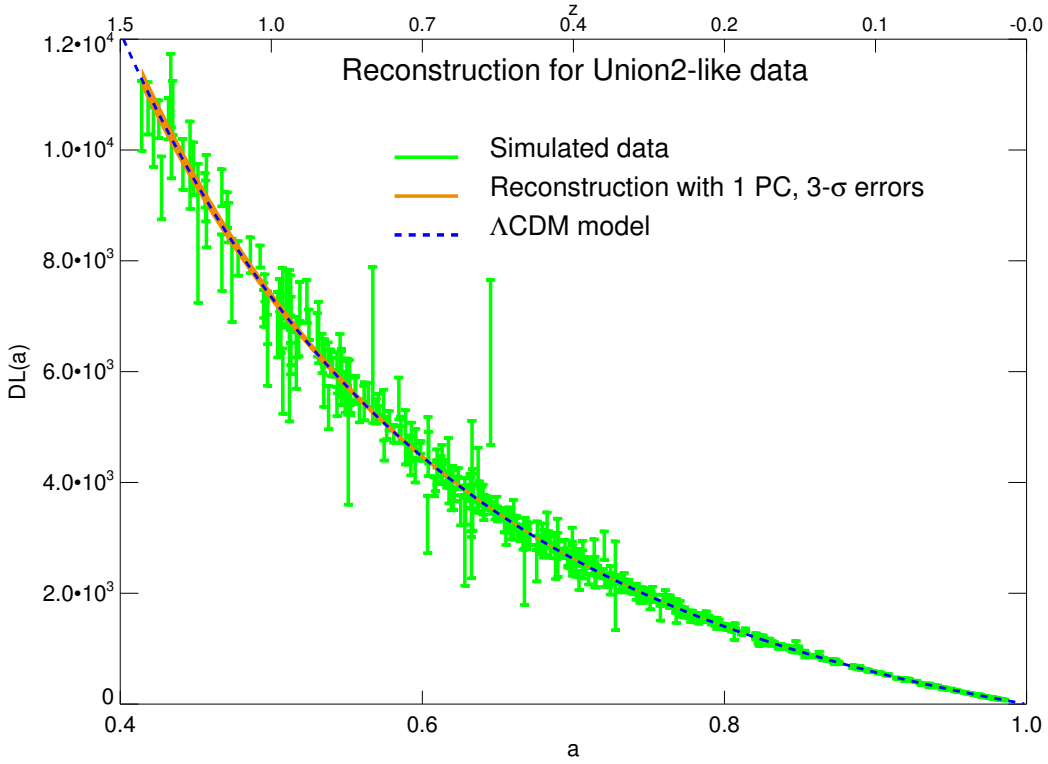

Figure 5.2: Mock data simulated in a ΛCDM scenario with $\Omega_{\rm M} = 0.3$, $\Omega_\Lambda = 0.7$ and $H_0 = 63$. Our reconstruction of $D_{\rm L}(a)$ with 1 Principal Component and 3-σ errors is shown in orange. The PC basis was produced by sampling the parameter space in the range $0.1 \leq \Omega_{\rm M} \leq 0.5$ and $0.5 \leq \Omega_\Lambda \leq 0.9$. In blue, the underlying model of the simulated data is plotted.

But we will see that for mock data generated in more exotic and complex cosmological scenarios, higher number of components will be needed.

Additionally, the exercise was repeated with a basis produced by sampling the parameter space in the more restrictive range of $0.3 \leq \Omega_{\rm M} \leq 0.5$ and $0.5 \leq \Omega_\Lambda \leq 0.7$. This means that the *true* cosmology was not included in the training set. The reference vector was the same as in previous cases.

The underlying cosmology was recovered almost entirely, as seen in Fig. 5.5, although the reconstruction failed at very high-redshifts ($z > 1$), giving an indication that the *true* underlying model is not comprised in the original matrix of models (as we already knew) and that one should maybe consider a higher number of coefficients. This behaviour is enhanced when more complex models are adopted to simulate the data, as will be discussed in the next Section.

Nevertheless, it is worth noting, that the basis used for this example is highly restrictive and one would tend to do the opposite, that is, to increase the flexibility of the training set. This can be achieved by spanning the parameter

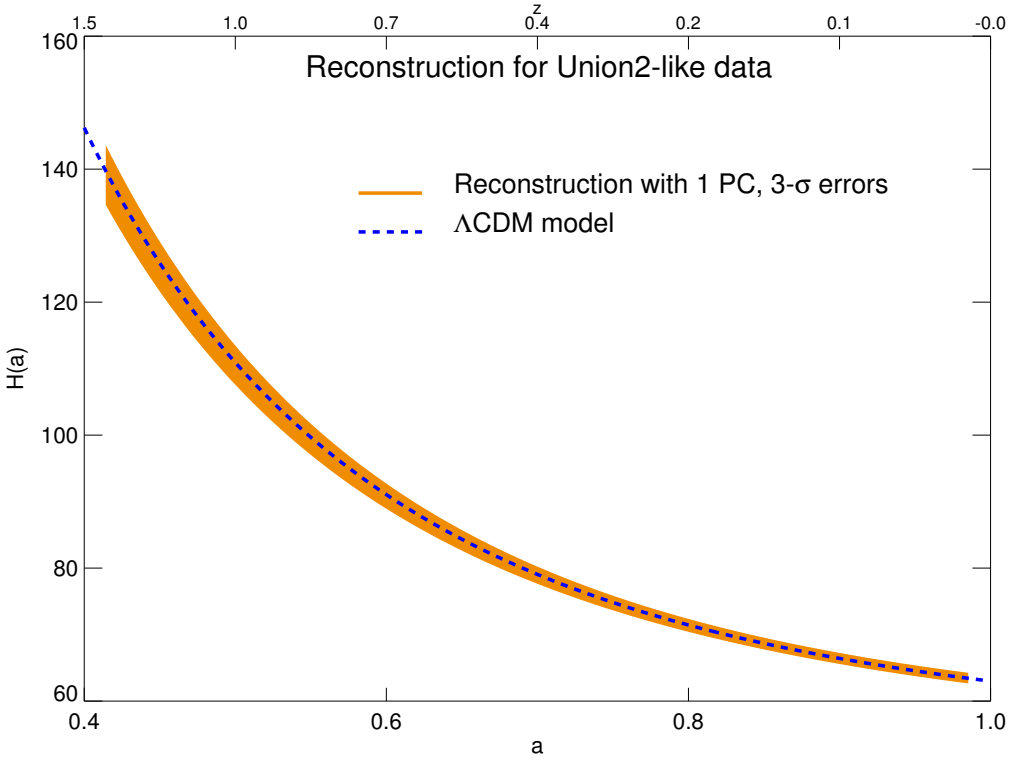

Figure 5.3: Recovered Hubble expansion function of the simulated data plotted in Fig. 5.2. Our reconstruction of $H(a)$ using 1 Principal Component and with 3-σ errors is shown in orange. The PC basis was produced by sampling the parameter space in the range $0.1 \leq \Omega_{\rm M} \leq 0.5$ and $0.5 \leq \Omega_\Lambda \leq 0.9$. In blue, the underlying cosmology of the simulated data is plotted.

space of a particular family of models as much as possible or, in general, by maximizing the number of different cosmologies included in the training set.

5.1.2 Non-ΛCDM Simulations

To further validate the method, we simulated SN data in several non-ΛCDM cosmologies. We present here two of these simulations, the first being a DGP brane world as described in Sec. 2.9. The second is a more exotic model proposed as a challenging test by Shafieloo, who has extendly worked on similar reconstruction techniques as the one described in this thesis over the past years (see e.g. Shafieloo et al., 2006, 2007, 2012).

The Dvali-Gabadadze-Porrati Brane-World Cosmology

We generated the mock data following Eq. 2.54 and having the same redshift and error distribution as the Union2.1 data set. The results shown in this

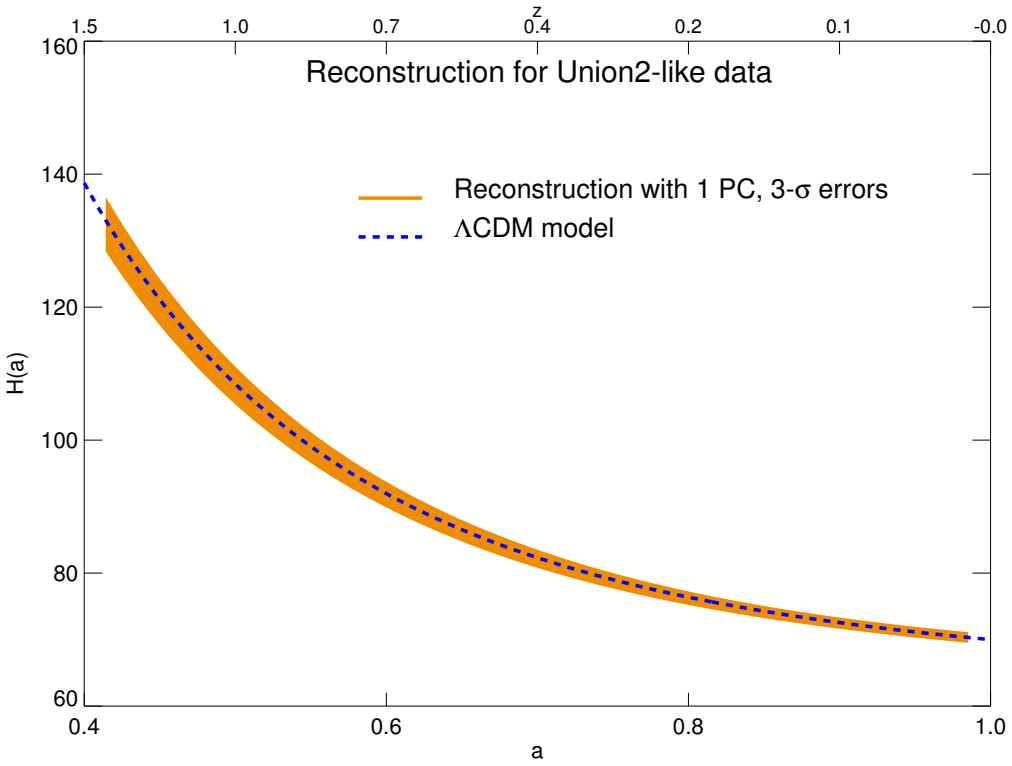

Figure 5.4: Recovered expansion rate of a mock data sample generated in a ΛCDM scenario with $\Omega_{\rm M} = 0.2$, $\Omega_\Lambda = 0.8$ and $H_0 = 70$. The reconstruction of $H(a)$ using 1 Principal Component and with 3-σ errors is shown in orange. In blue, the underlying cosmology of the simulated data is plotted.

Section correspond to a model with parameters set to $\alpha = 1$ and $\Omega_{\rm M} = 0.3$, but other realizations were studied yielding similar outcomes. The basis employed is the same as the one used in the previous Section, that is composed on solely ΛCDM models (with complete sampling of the $\Omega_{\rm M}$ and Ω_Λ parameters).

As seems evident from Fig. 5.6, more than one PC is needed to recover the underlying cosmology. In particular, we found that it was necessary to consider up to the third coefficient to fully reconstruct $H(a)$, as Fig. 5.7 illustrates. Indeed, when calculating the cumulative percentage we found that at least three eigenvalues contribute significantly to the total amount of variance.

Since the PC basis was constructed in a way that it highlights deviations from the models being comprised in the training set, having to compute higher orders indicates that the *underlying* background cosmology of the data cannot be the standard ΛCDM model. We encounter this result far from trivial and difficult to reproduce in traditional analyses where a specific parameterization of the Friedman Equation is assumed, and no freedom to detect deviations from this assumption is allowed. In fact, performing a χ^2-analysis this simulated sample is compatible with a ΛCDM model, which is of course a misleading

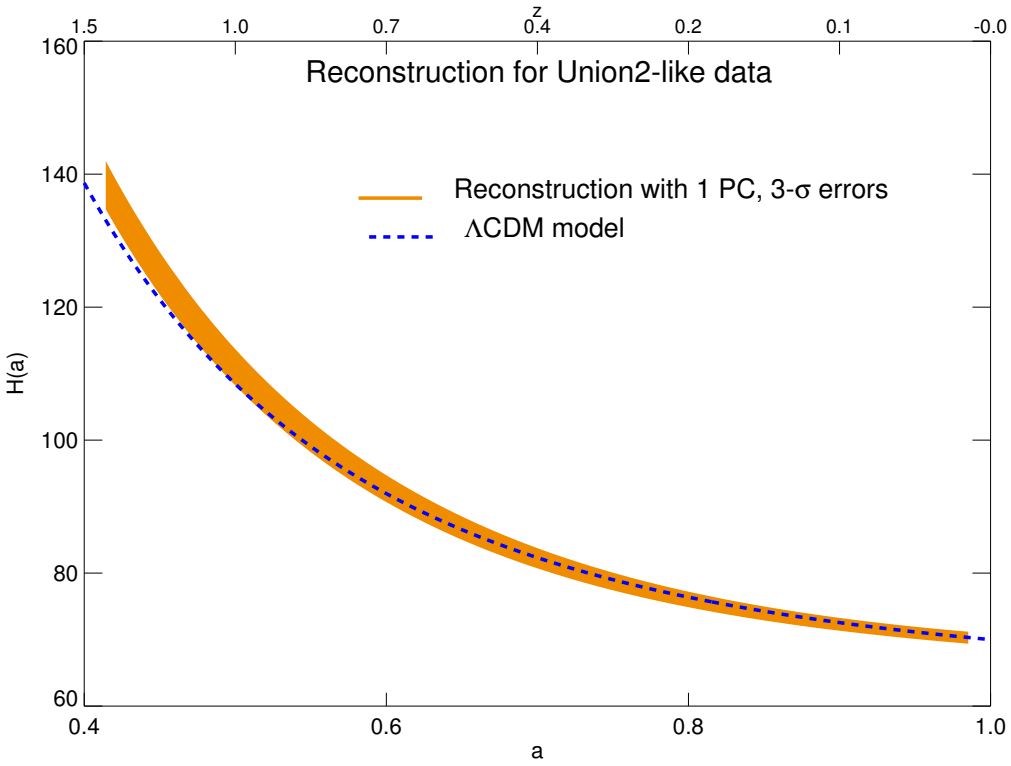

Figure 5.5: Recovered expansion rate of a mock data sample generated in a ΛCDM scenario with $\Omega_{\rm M} = 0.2$, $\Omega_\Lambda = 0.8$ and $H_0 = 70$. The reconstruction of $H(a)$ using 1 Principal Component and with 3-σ errors is shown in orange. The parameter sampling to build the PC basis was restricted to $0.3 \leq \Omega_{\rm M} \leq 0.5$ and $0.5 \leq \Omega_\Lambda \leq 0.7$. In blue, the underlying cosmology of the simulated data, not included in the training set, is plotted.

result since the underlying cosmology has a very different nature. This is a strong argument in favour of model-independent methods as the one proposed in this work.

Since more PCs (i.e. more variance) have to be included to recover $H(a)$, the error bars increase, specially at high redshift where there is less data available. We recall that the mock data have the same characteristics than Union2.1 and that the real sample only contains a handful of objects above $z > 1$ (see Fig. 5.1).

The Kink Quintessence Model

The Kink model is a particular kind within the evolving-dark-energy family of models described in Sec. 2.8.2. It was first proposed by Corasaniti et al. (2003) and has been used as a control check for other non-parametric approaches (see e.g. Holsclaw et al., 2010; Shafieloo et al., 2012). The model has a rapidly

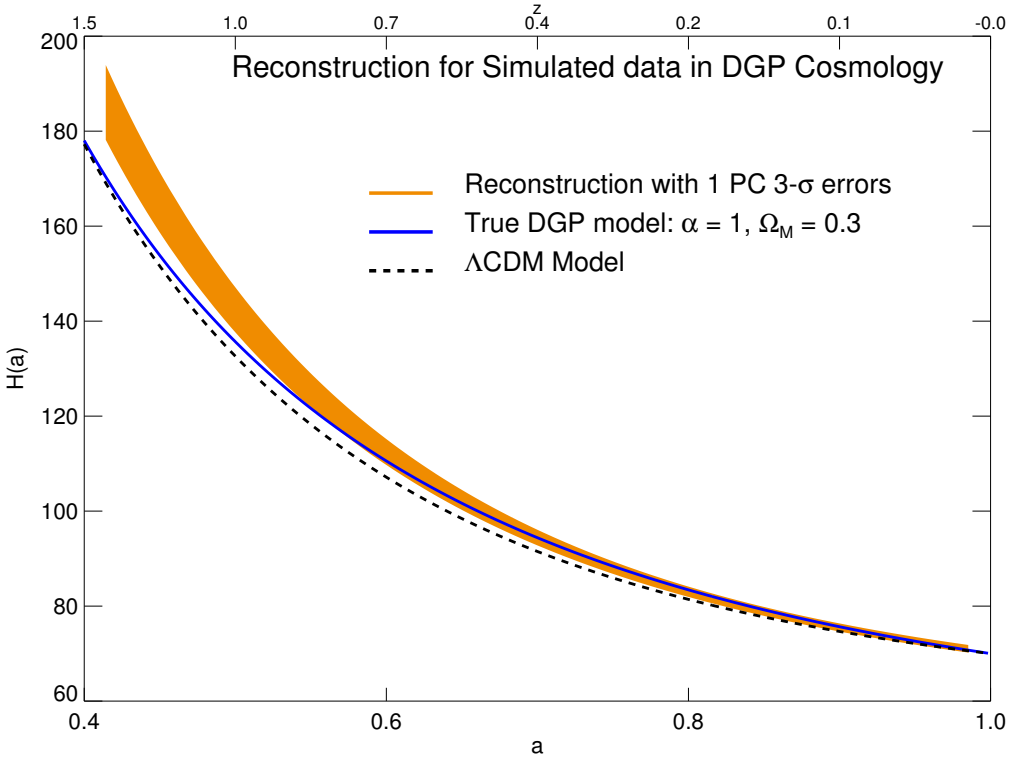

Figure 5.6: Recovered expansion rate of a mock data sample generated in a DGP cosmology with $\alpha = 1$, $\Omega_{\rm M} = 0.3$ and $H_0 = 70$. The reconstruction of $H(a)$ using 1 Principal Component and with 3-σ errors is shown in orange. In blue, the *true* underlying cosmology of the simulated data is plotted. The dashed black line is a ΛCDM model with $\Omega_{\rm M} = 0.3$ shown here for comparison. From this plot is it clear that higher number of components are necessary to achieve an accurate reconstruction.

varying equation of state given by the following Equation

$$w(z) = w_0 + (w_{\rm m} - w_0)\frac{1 + exp(\Delta_t^{-1}(1+z_t)^{-1})}{1 - exp(\Delta_t^{-1})} \tag{5.1}$$

$$\times \left[1 - \frac{exp(\Delta_t^{-1}) + exp(\Delta_t^{-1}(1+z_t)^{-1})}{exp(\Delta_t^{-1}(1+z)^{-1}) - exp(\Delta_t^{-1}(1+z_t)^{-1})}\right]$$

with the constants having the values $w_0 = -1$, $w_{\rm m} = -0.5$, $z_t = 0.5$ and $\Delta_t = 0.05$. This model has $w \geq -1$ everywhere and, therefore, can be considered as a quintessence field, though the transition is steeper than for most quintessence models.

Luminosity-distance data were simulated using Eq. 5.1 and with similar observational properties as the future WFIRST survey (see Sec. 3.8). For

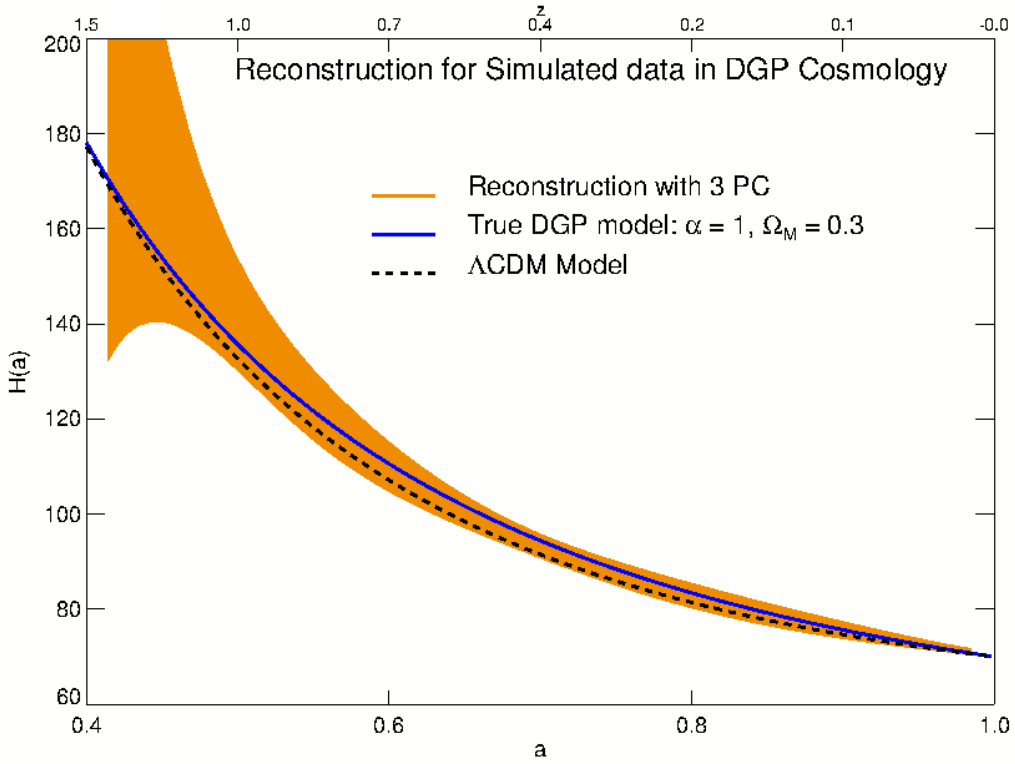

Figure 5.7: Recovered expansion rate of a mock data sample generated in a DGP cosmology with $\alpha = 1$, $\Omega_{\rm M} = 0.3$ and $H_0 = 70$. The reconstruction of $H(a)$ using 3 Principal Components and with 3-σ errors is shown in orange. In blue, the *true* underlying cosmology of the simulated data is plotted. The dashed black line is a ΛCDM model with $\Omega_{\rm M} = 0.3$ shown here for comparison.

the simulations, $\Omega_{\rm M} = 0.27$ and (small) uncertainties drawn from a gaussian distribution were assumed. The basis to perform the reconstruction is the same as the one used throughout this Chapter. In Fig. 5.8 we see the simulated data together with the true underlying cosmology and our reconstruction of $D_{\rm L}$. Analogously, Fig. 5.9 shows the reconstruction for $H(a)$ and the underlying model. In this case, we need to compute up to the fourth principal component to recover the *true* expansion history. And even so, the slope does not perfectly match that of the original model, indicating the basis is not optimal for these data. The error bars are smaller than those in the DGP example because the Kink data were generated with small (unrealistic) errors, in contrast to the DGP case, where errors follow the distribution of the real data.

Despite having to use higher number of PCs, we find our result reassuring, since we are able to recover a quite extreme cosmology using a simple basis composed of ΛCDM models only. We stress here again that, if the underlying model would be the standard ΛCDM, higher moment components would be zero because the basis was built specifically to highlight deviations from this

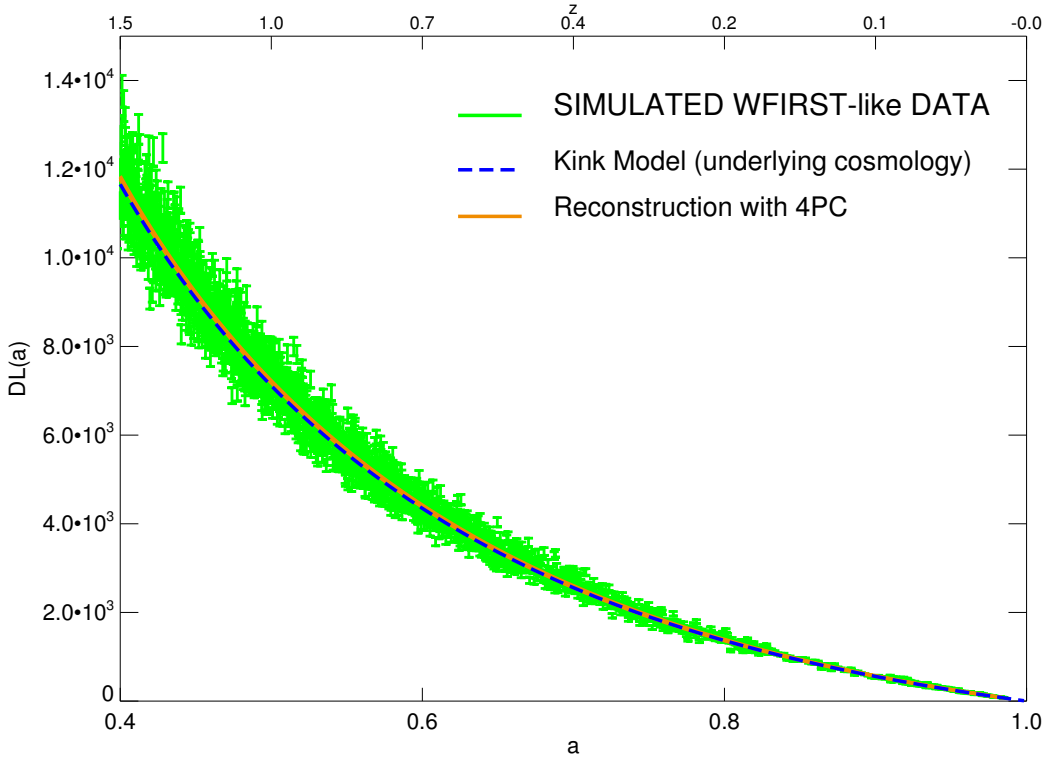

Figure 5.8: Luminosity distance versus scale factor of the Kink data. Our fit for the $D_{\rm L}(a)$ using 4 Principal Components and with 3-σ errors is shown in orange.

model. Since we need to compute four coefficients to fully reconstruct $H(a)$, this already tells us that the underlying model is not ΛCDM (though we cannot say what it is).

Including other cosmological models in the training set could help to discriminate the underlying cosmology of the simulated (and eventually the real) data, allowing to make assessments about the nature and physical properties of the background cosmology. This practice is beyond the scope of this thesis, but it will surely be developed in future work.

For comparison, the result from Shafieloo using a completely different non-parametric technique, Gaussian Processes (Shafieloo et al., 2012), to reconstruct the expansion history given the same simulated data, it is shown in Fig. 5.10 (red points). Our reconstruction, once properly scaled to match Shafieloo's units, looks exactely the same, only with slightly bigger errors. This result confirms again the robustness of our method with the advantage that it is conceptually and computationally much simpler than the Gaussian Process technique.

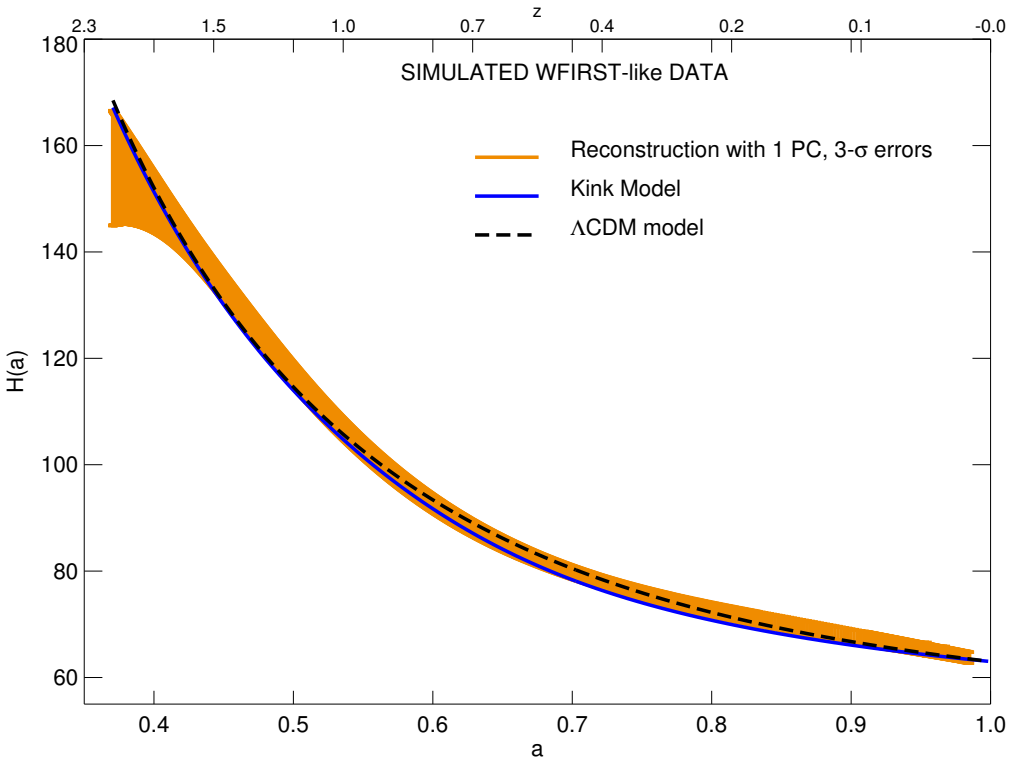

Figure 5.9: Recovered expansion rate of the Kink simulated data shown in Fig. 5.8. The reconstruction of $H(a)$ using 4 Principal Components and with 3-σ errors is shown in orange. In blue, the *true* underlying cosmology of the simulated data is plotted. The black dashed line is a ΛCDM model shown here for comparison.

5.2 SNANA: A Tool To Simulate High Quality SN Data.

SNANA (A Public Software Package for Supernova Analysis) is a software package for supernova analysis that allows to simulate light curves in a given framework, i.e. having the same observational implementation as several public surveys – such as SNLS or SDSS – and technical features corresponding to different telescopes and filter systems. Moreover, it contains various light-curve fitters within the same software architecture, granting K-corrections (to transform rest-frame model magnitudes into observer-frame magnitudes) and other technicalities to be consistently computed and used among multiple SN models, making it easier to compare them. Additionally, cosmology fitters to determine cosmological parameters are also available.

Essentially, each light-curve model is defined in a separate function that is used in both the light-curve fitter and in the simulation, making the fitter

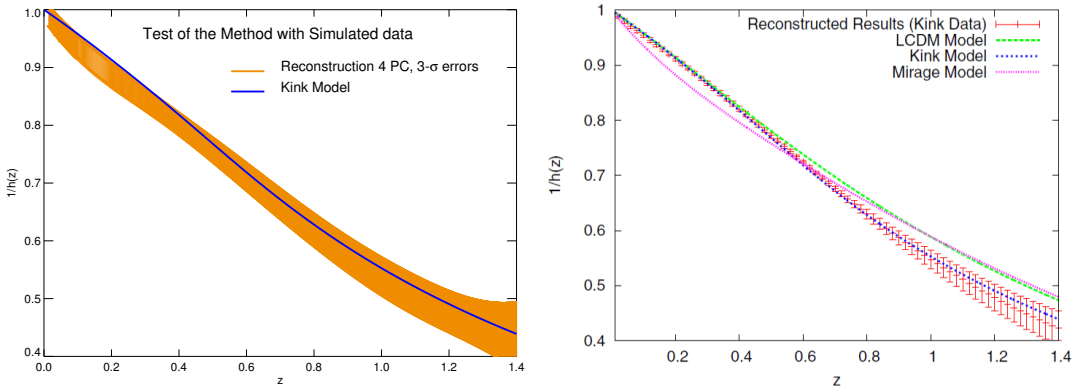

Figure 5.10: Left: Our reconstructed expansion history for the simulated Kink data with 4 Principal Components and with 3-σ errors (in orange). The reconstruction has been scaled accordingly to Shafieloo' units. Right: The result from Shafieloo et al. (2012), using Gaussian Processes.

and simulation to be synchronized with the same underlying model. A K-correction utility is used when the underlying model describes SNe Ia in the rest frame (as for example MLCS), and depends on the choice of the spectral template and filter bandpasses. If the underlying SN model describes SNe Ia in the observer frame (e.g. SALT2), the K-correction utility is ignored. The simulation of a given survey is done by means of an *observing-conditions* library that describes the cadence, seeing, atmospheric transparency, and readout noise for a particular survey. The simulation uses the measured observing conditions to generate realistic light curves that can be analyzed in the same way as real data. K-corrections, are computed following Nugent et al. (2002) and with the default spectral templates of Hsiao et al. (2007), though other templates are possible. An illustration of the quality and flexibility of the simulations is shown in Fig. 5.11, where the measured flux – with errors – of the simulated data for four different surveys is compared.

The light curve fitting program in SNANA reads SN light-curve files and applies specific criteria to select a subset of SNe and epochs. SNANA light curve fitters treat real data and simulated samples in exactly the same way.

SNANA includes a basic cosmology fitter that reads a table of redshifts and distance moduli generated by the light curve fitter, and determines cosmological parameters for a Friedmann-Robertson-Walker cosmology. To obtain tighter constraints on the cosmological parameters, it is possible to include priors from measurements of Baryon Acoustic Oscillations and the Cosmic Microwave Background.

For a complete overview of the SNANA capabilities we refer to the reader to Kessler et al. (2009) and the manuals at http://www.sdss.org/supernova/SNANA.html.

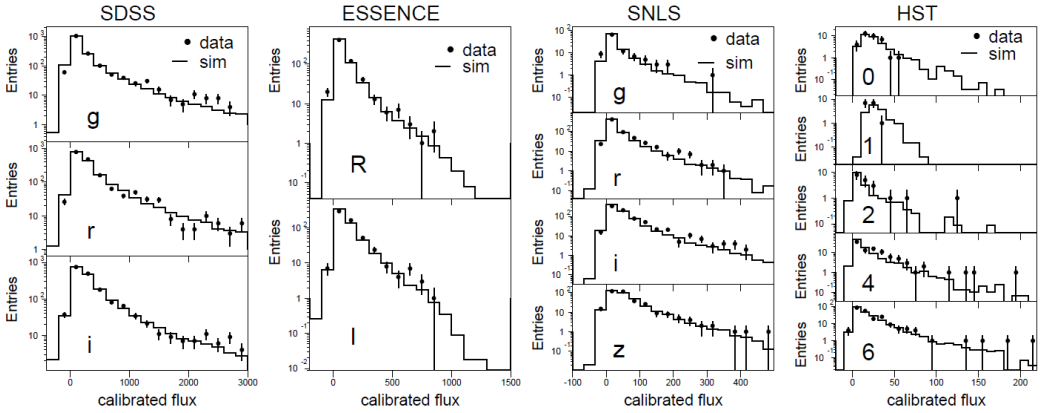

Figure 5.11: Comparison of flux distribution for real data (dots) and simulations (histograms) for the SDSS, ESSENCE, SNLS, and *HST* surveys. The observer-frame filters are also indicated on each plot. From Kessler et al. (2009)

5.2.1 Simulated Data in MLCS and SALT2.

One of the potential applications of the method presented in this thesis, is to identify possible discrepancies within the SN data which could have been overlooked by traditional analyses. One of the most plausible sources of bias is the choice of a particular light curve fitter to infer cosmic distances. As we mentioned in Sec. 3.4.3, there is significant difference in the cosmological results obtained from the two main-stream light curve fitters when applied to the same data. This effect might be easier to identify by means of a geometrical approach as the one presented here, by analising the expansion history of data simulated in the context of different SN models. Hence, SNANA provides a consistent framework in which to both simulate and fit data according to the preferred light-curve fitters.

To explore this idea, we created *perfect* simulations using the MLCS and SALT2 formalisms inside SNANA consistent with a ΛCDM universe having $\Omega_{\rm M} = 0.3$ and $H_0 = 72$ and about 1000 SNe each. The samples were generated with the same proportions of low, high and intermediate redshift, and equal percentage of SNe per survey (SNLS, ESSENCE, SDSS...) as in the real Union2.1 sample. The values of the correction parameters are $R_{\rm V} = 2.18$ for MLCS, and $\alpha = 0.11$ and $\beta = 3.2$ for SALT2 were adopted.

The term *perfect* refers to light curves simulated with very good observing conditions, with no galactic extinction (Milky Way and host galaxy), and no intrinsic magnitude-smearing (i.e. no scatter in the Hubble diagram residuals, an additional feature included in SNANA). The determination of the shape and color parameters is done with very high precision when using *perfect* simulations, and any type of cosmological analysis should deliver the *true* underlying model with high degree of accuracy, making it an additional test

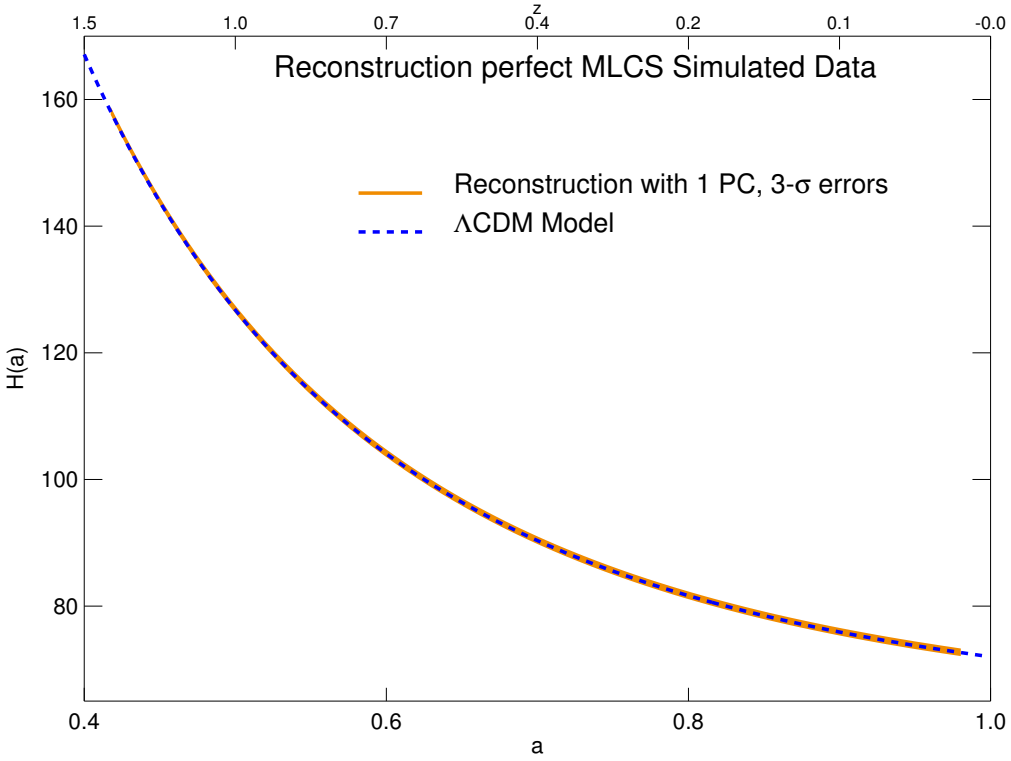

Figure 5.12: Recovered expansion rate for a MLCS *perfect* simulation. The reconstruction of $H(a)$ using 1 Principal Component and with 3-σ errors is shown in orange. In blue, the underlying ΛCDM cosmology is plotted. Note that the data was both simulated and fitted with MLCS.

for the method.

The PC basis consisted on an ensemble of ΛCDM models following the same redshift distribution as the simulated data and with the same parameter sampling as in Sec. 5.1.1. The reconstruction of the expansion rate for two of the simulations is plotted in Figures 5.12 and 5.13. As expected, the expansion history is recovered with very high precision in both examples, yielding $\chi^2|_{\rm MLCS} = 0.0183315$ and $\chi^2|_{\rm SALT2} = 0.00276868$. We find no difference in the expansion history procured by both light curve fitters for the same ideal data.

We note that for the SALT2 simulation, an intermediate step was necessary, since SALT2 does not directly provide distance moduli. To obtain those from the output of the light curve fitter, another program called SALT2mu (Marriner et al., 2011), implemented also within SNANA, was employed. The SALT2mu formalism reads the output files from the SALT2 light curve fitter and gives an independent fit to the parameters α and β decoupling them from cosmology and yielding a table of distance moduli. Moreover, a more detailed description of the intrinsic scatter of the fitted parameters is included in the algorithm.

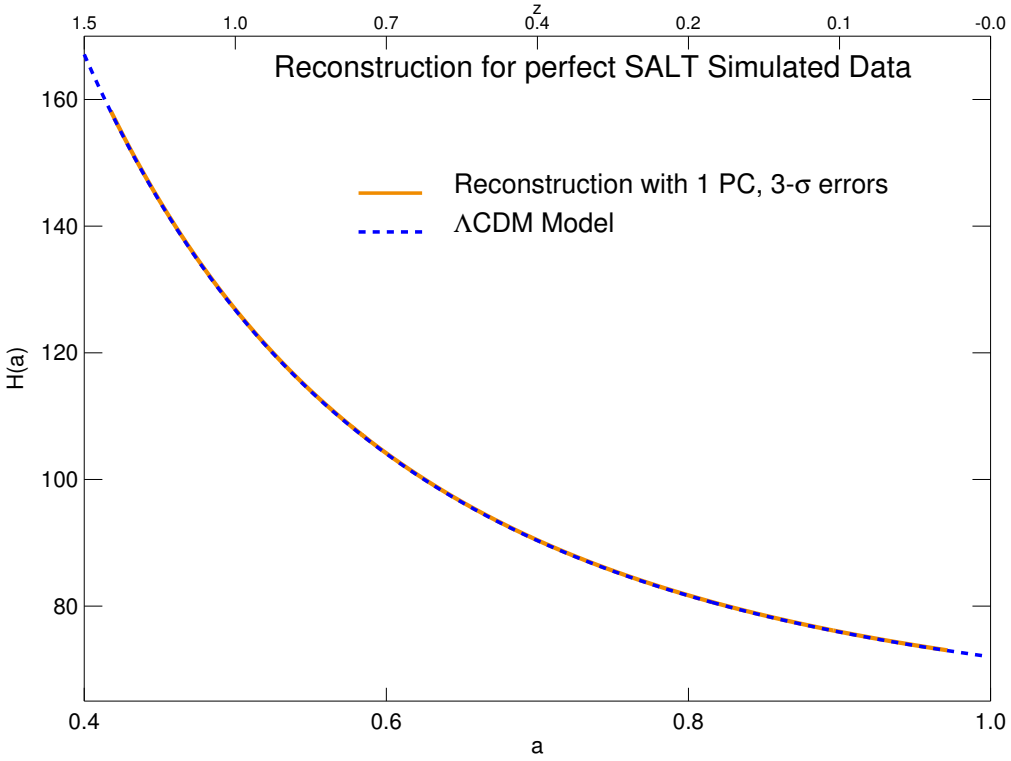

Figure 5.13: Recovered expansion rate for a SALT2 *perfect* simulation. The reconstruction of $H(a)$ using 1 Principal Component and with 3-σ errors is shown in orange. In blue, the underlying ΛCDM cosmology is plotted. Note that the data was both simulated and fitted with SALT2.

Next, we tried simulations with realistic cadence, measurements errors and selection effects, though still with high signal to noise (on average, higher than current data). The same proportions concerning reshift ranges and survey population as in Union2.1 were maintained.

To avoid the theoretical prejudice introduced by each fitter when simulating, we created a single data sample with a mixture of SNe, half of them simulated in MLCS, the other half in SALT2. Subsequently, the generated light curves were fitted with both models, independently. The results are shown in Fig. 5.14.

We see that the error bars are bigger than those of the *perfect* data. This is due to the fact the these simulations include uncertainties coming from extinction and non-photometric observing conditions. Nonetheless, the recovered expansion history is the same independently of the light-curve fitter used to calibrate the data. This means that both methods are consistent with each other and that, for ideal (or sufficiently high quality) data, they yield the same cosmological results. The observed deviations between both SN models, reported in other SN studies might come from limited understanding on sys-

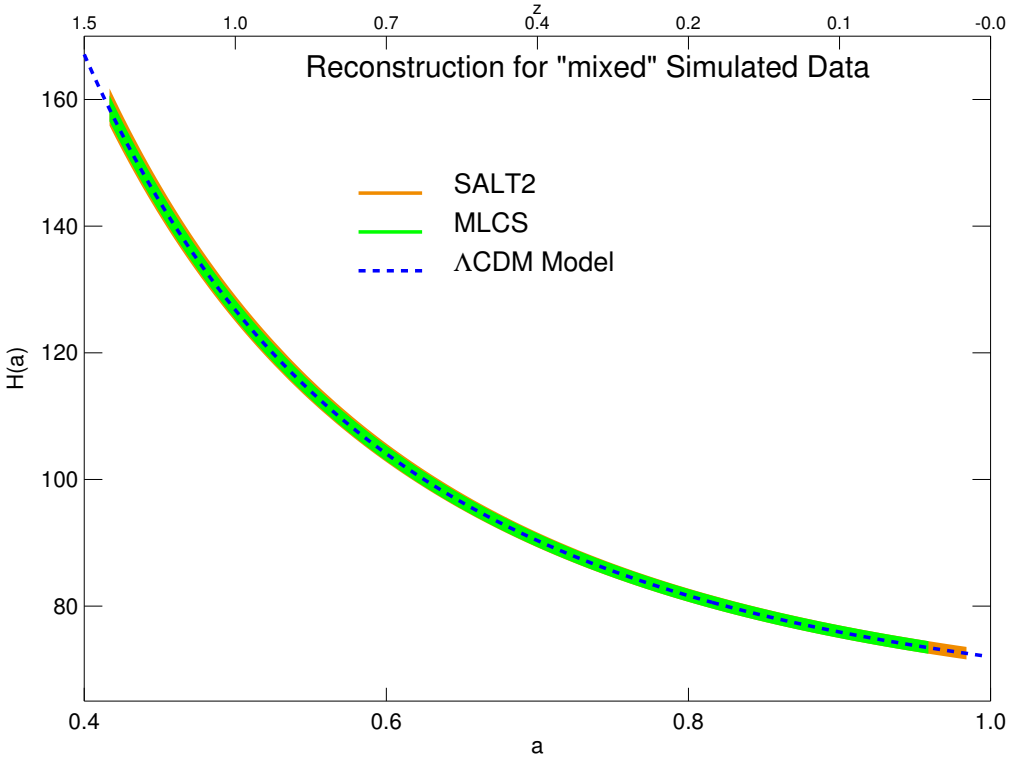

Figure 5.14: Recovered expansion rate for mixed simulations (half simulated in MLCS, the other half in SALT2) fitted with both SALT2 and MLCS. The reconstruction of $H(a)$ using 1 Principal Component and with 3-σ errors is shown in orange. In blue, the underlying ΛCDM cosmology is plotted.

tematics related to our technical capabilities or non-well understood physical properties of the SN Ia explosions, e.g. intrinsic scatter due to SN evolution with redshift. We will address the issue of systematic errors and possible ways to detect them within SN samples in the next Chapter.

6. Extracting the Expansion Rate from Real Data: Cosmological Implications

The main goal of this work was to apply the model-independent method to real SN Ia samples to derive constraints on the expansion rate of the Universe. Additionally, and due to the non-parametric nature of the method, we attempted to discriminate between dark energy and non-standard cosmological models, and draw some conclusions on the cosmological parameters occurring in those models.

In the following we present results some of which have been, or are about to be, published in Benitez-Herrera et al. (2012), Benitez-Herrera et al. (2013) and Benitez et al. (2014, in preparation). As done in the previous Chapter, the reconstructed $H(a)$ will be given in units of km s^{-1} Mpc^{-1}.

6.1 The Union2.1 Sample Revisited

We applied the method described in Chapter 4 to the largest homogeneously reduced SN Ia sample publicly available, the Union2.1 (Suzuki et al., 2012, – see Fig. 5.1). This sample contains 580 SNe and includes data from SNLS (Astier et al., 2006), ESSENCE (Miknaitis et al., 2007) and SDSS (Holtzman et al., 2008) surveys, low redshift samples (Hamuy et al., 1996; Hicken et al., 2009a) as well as *Hubble Space Telescope* data (Riess et al., 2007).

The PC basis for this data set was already shown in Fig. 4.5, consisting in a training set of flat ΛCDM models with the usual sampling $0.1 \leq \Omega_{\rm M} \leq 0.5$ and $0.1 \leq \Omega_{\Lambda} \leq 0.5$. The reference model was assumed to be the best fit cosmology for these data obtained by Suzuki et al. (2012), i.e. $\Omega_{\rm M} = 0.277$, $\Omega_{\Lambda} = 0.723$. As we know, the PC basis was constructed in a way that it highlights deviations from the reference model, meaning that, if we were to find deviations from this model in our reconstruction, it would imply that this "best fit" is probably misleading. We stress the importance of this statement because what it may appear as the best fit obtained with a χ^2-test or any other traditional (parametric) method, may not be the *real* underlying cosmology of the data and could lead to misleading results.

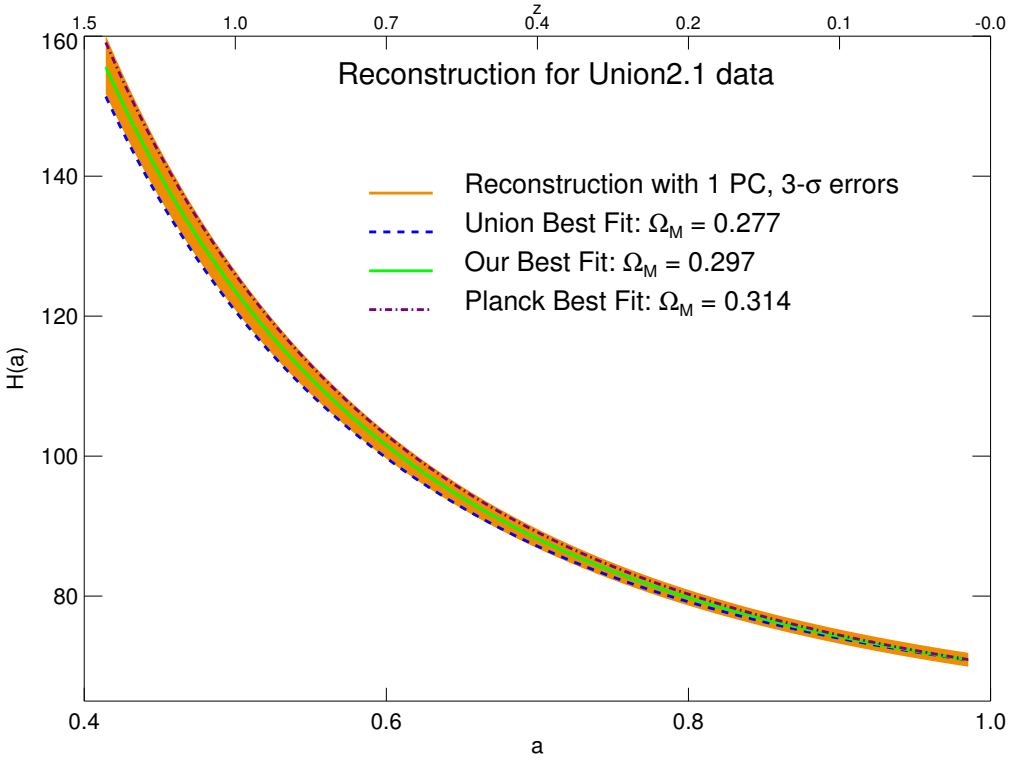

Figure 6.1: The reconstructed expansion history, with 3-σ error, extracted from the Union2.1 sample using the optimal basis system with one PC. The green line represents our best-fit to ΛCDM paradigm. The blue line is the best-fit obtained by the Union team (Suzuki et al., 2012) for this sample and the grey line corresponds to results from Planck (Planck Collaboration et al., 2013).

The first Principal Component for this sample already accounts for approximate 99.9% of the total variance and its determination carries an uncertainty of $\sigma_{\mathrm{PC}_1} \approx 2.5 \times 10^{-5}$. This means it already contains the main properties of the expansion of the Universe and accounts alone for a great part of the total variance sampled in the scatter matrix. Therefore, we restrict ourselves to only one principal component when performing the reconstruction. The reconstruction for $H(a)$ using the PC basis and with 3-σ errors is plotted in Fig. 6.1. For the sake of comparison, the figure also shows the best-fit cosmology found by the original Union2.1 analysis, $\Omega_{\mathrm{M}} = 0.277 \pm 0.022$ (Suzuki et al., 2012) – used as reference model – and the latest result reported by the Planck satellite team, $\Omega_{\mathrm{M}} = 0.314 \pm 0.020$ (Planck Collaboration et al., 2013). Both results are in marginal agreement with the behaviour we found for $H(a)$.

We recall that the Hubble constant, H_0, was left as a free parameter to fit together with the expansion coefficients. We stress once more that the SN data have to be standardized before extracting their absolute magnitudes, and subsequently distances. The standardization process of the Union2.1 sample

was a prior and separate step independent of the work presented in this Section. These data were calibrated by the Union team (Kowalski et al., 2008; Suzuki et al., 2012) within the SALT2 (Guy et al., 2007) paradigm. Fitting the luminosity distance data to the expression in Eq. 4.33 with one PC returns $H_0 = 70.43 \pm 0.33$ and $c_1 = 122.74 \pm 796.68$, for the first expansion coefficient. As expected from a geometrical approach, our method does not provide direct constraints on specific cosmological parameters. However, it returns an estimation on the form of the expansion rate as a function of redshift with corresponding uncertainties. Having such a function, we could compare our results with ΛCDM cosmologies and point to the most likely cosmological parameters able to reproduce the resulting Hubble parameter behaviour. Translating our results for a flat ΛCDM scenario lead to a cosmological constant model where matter energy density is in close agreement with the recently released Planck-satellite results for the cosmic microwave background (Planck Collaboration et al., 2013). Given the general agreement that the *true* underlying cosmological model should not differ much from a cosmological-constant model (at least as long as the cosmic dynamics is concerned), we believe our results show that going beyond the parametrized analysis is fundamental to tackle small deviations present in the data.

Indeed, putting our reconstruction in the context of ΛCDM models we calculated a range of $\Omega_{\rm M}$ values allowed by the behaviour we found for $H(a)$. Keeping fixed the value of H_0 extracted from the data, we obtained $\Omega_{\rm M} = 0.297 \pm 0.020$ (grey curve in Fig. 6.1). It is important to emphasise that the magnitude of the error of $\Omega_{\rm M}$ does not carry the same meaning as in any standard parametric analysis. The determination of a range of values for $\Omega_{\rm M}$ is merely a strategy to better compare our results. Unlike other analyses we are tracking only deviations from the reference vector and this causes the error bars to be small. The results we found are significantly higher than the best-fit value obtained by the Union2.1 team ($\Omega_{\rm M} = 0.277$ without systematics; blue dashed curve in Fig. 6.1), and are in close agreement with the value reported by the Planck Collaboration. As seems clear from Fig. 6.1, we do observe a deviation from the reference model (the Union2.1 fit) assumed to perform the reconstruction, suggesting that the underlying *true* cosmological model might deviate from the reported best fit to the data. We notice that we have also tested other reference models obtaining in all cases the same best fit value for our reconstruction $\Omega_{\rm M} = 0.297$ and minimised value for H_0.

Another way to express our results, allowing a more clear comparison with others from the SNe Ia literature (all using SALT2 light curve fitter; Guy et al., 2007) is shown in Fig. 6.2. We believe that the shift in our results towards the Planck values is a clear indication that SNe Ia cosmology should move beyond the parametrized approaches if it aims at dealing with small deviations from the standard values of the cosmological parameters present in the data.

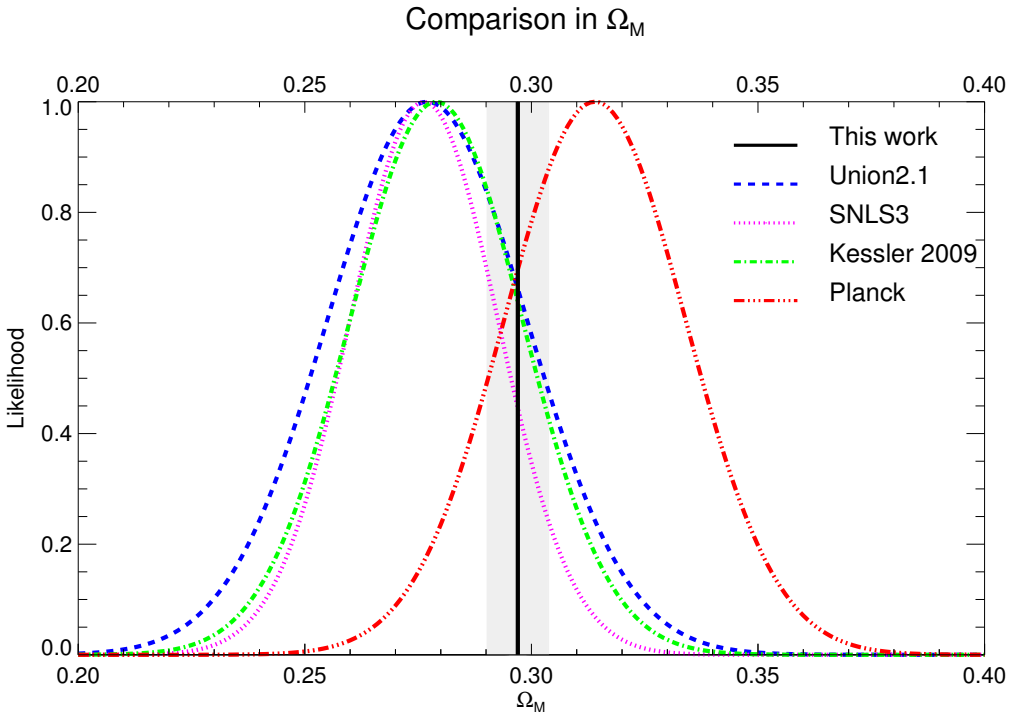

Figure 6.2: Comparison between our results when translated to a flat ΛCDM scenario, $\Omega_M = 0.297 \pm 0.020$ (black line and gray region), and others from the literature. The green (dot-dashed) line correspond to results reported by the first year of SDSS data, $\Omega_M = 0.279 \pm 0.019$ (Kessler et al., 2009). Cyan (dashed) line stands for results reported by Union2.1 team, $\Omega_M = 0.277 \pm 0.022$ (Suzuki et al., 2012), the pink (dotted) line represents outcomes from SNLS3, $\Omega_M = 0.276 \pm 0.016$ (Sullivan et al., 2011) and the red (dot-dot-dashed) line represents recent results from Planck, $\Omega_M = 0.314 \pm 0.020$ (Planck Collaboration et al., 2013). Only statistical errors and supernova fitted with SALT2 are considered in this plot.

6.2 Constraining Cosmological Scenarios

We have demonstrated that we are not biased by any theoretical opinion towards a cosmological model, since we do not assume any specific form for the expansion of the Universe. Our model-independent approach stands as an useful tool to analyse different cosmological scenarios in a consistent way, by looking at (geometrical) predictions on the Hubble function for various models. The goal of this Section is to illustrate how families of models, with completely different parameters, can be confronted with the data in order to assess their validity.

6.2.1 Dark Energy Models

We tried some dark energy models with different parameterisations of the dark energy equation of state w, going from flat and non-flat models to several a priori assumed transition redshifts, z_t (point of the Hubble diagram where the expansion makes a transition between acceleration and deceleration) for the model.

Relaxing the premise of constant equation of state, we analyzed a dark energy model proposed by Rapetti, Allen & Weller (2005). It is an extension of the parametrization in Eq. 2.44 proposed by Chevallier & Polarski (2001) and Linder (2003), which assumes a fixed transition redshift ($z_\mathrm{t} = 1$) between the current value of the equation of state and the value at early times, $w_\mathrm{et} = w_0 + w_1$. In contrast, the model discussed by Rapetti et al. (2005) introduces z_t as an extra free parameter so that the equation of state w can be written as

$$w(a) = \frac{w_\mathrm{et} z + w_0 z_\mathrm{t}}{z + z_\mathrm{t}} = \frac{w_\mathrm{et}(1-a)a_\mathrm{t} + w_0(1-a_\mathrm{t})a}{a(1-2a_\mathrm{t}) + a_\mathrm{t}}, \tag{6.1}$$

where a_t is the transition scale factor. From the Friedmann equation, the expansion function in terms of redshift is then given by

$$H(z) = H_0 \sqrt{\Omega_\mathrm{M}(1+z)^3 + \Omega_\mathrm{de} f(z) + \Omega_k (1+z)^2}, \tag{6.2}$$

with

$$f(z) = (1+z)^{3(1+w_\mathrm{et})} \mathrm{e}^{-3(w_\mathrm{et}-w_0)g(z;z_\mathrm{t})}; \tag{6.3}$$

Here, the function $g(z; z_\mathrm{t})$ is defined as

$$g(z; z_\mathrm{t}) = \frac{z_\mathrm{t}}{z_\mathrm{t} - 1} \ln\left(\frac{z_\mathrm{t}}{z_\mathrm{t} + z}\right). \tag{6.4}$$

Rapetti et al. (2005) constrained the best-fit cosmological parameters for different possibilities within this model, varying the number of free parameters. They made use of SN Ia (the Gold sample by Riess et al., 2004), X-ray galaxy clusters and CMB data for this analysis. In Fig. 6.3, we compare those possibilities to the model-independent reconstruction of the expansion function extracted from the Union2.1 sample. This is meant to illustrate that standard cosmologies within the wCDM paradigm with different choices of parameters do not fit the data in all cases. This is not easy to see in other analyses which are model-dependent. Our reconstruction of $H(z)$ can be a useful tool since it allows us to rule out cosmological models based entirely on the data. For example, the two most extreme models shown in Fig. 6.3 – one with a fixed $z_\mathrm{t} = 0.35$ (green solid line) which splits the SN and the cluster data sets into similarly low and high redshift subsamples, and the one with arbitrary z_t (blue dashed line) – are clearly inconsistent with our reconstruction. The other models (marginally) agree with the SN measurements within errors, though they have slightly different slopes.

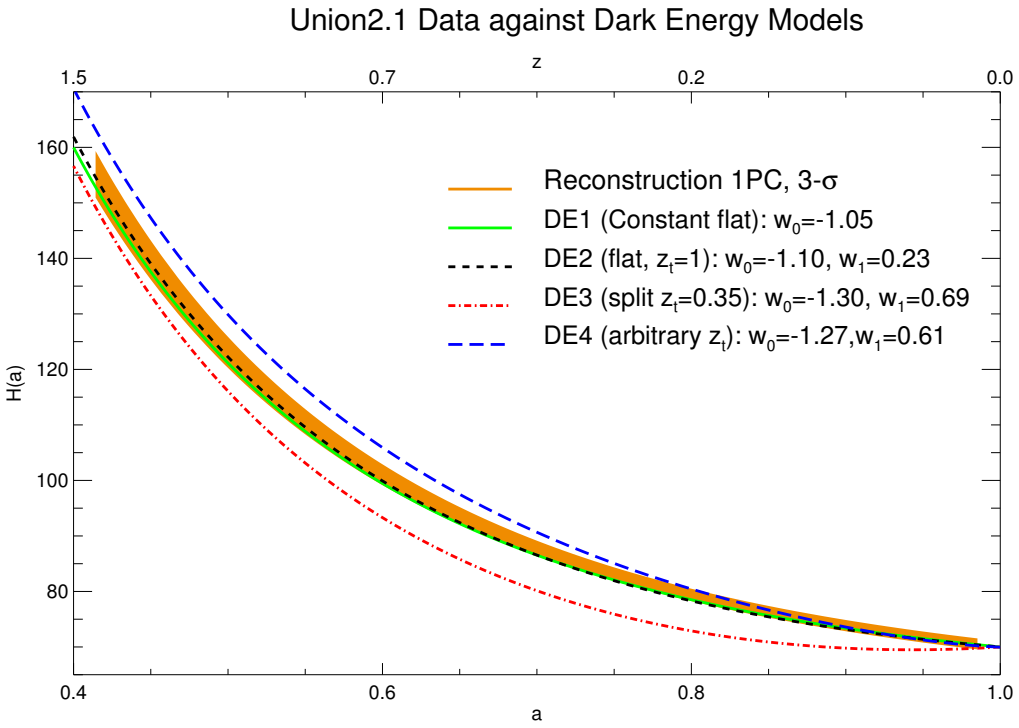

Figure 6.3: Recovered expansion rate extracted from the Union2.1 data with 1 PC and 3-σ errors (orange area) confronted with several dark energy models. The best fit parameter for the models were taken from previous studies in literature.

6.2.2 Beyond the wCDM Cosmology

In this Section, we have evaluated the alternative models explained in Section 2.9 by confronting them to our reconstruction of $H(a)$ from the Union2.1 data.

DGP Models

Firstly, we looked at the brane world DGP and mDGP models described in Section 2.9.1. In Fig. 6.4, the comparison of our model-independent reconstruction with some DGP and mDGP models is presented. The values of the model parameters are taken from previously reported fits to actual cosmological data. We evaluated two pure DGP models ($\alpha = 1$) adopting the best-fit values for $\Omega_{\rm M}$ reported in Guo et al. (2006) – magenta dotted-dashed line – and Liang & Zhu (2011) – black dotted line. In the first case, the constraints were obtained from the Gold and SNLS samples in combination with BAO. In the second, the best fit values are found by combining cosmology-independent Gamma Ray Burst and SNe Ia data, with BAO, CMB and $H(z)$ measure-

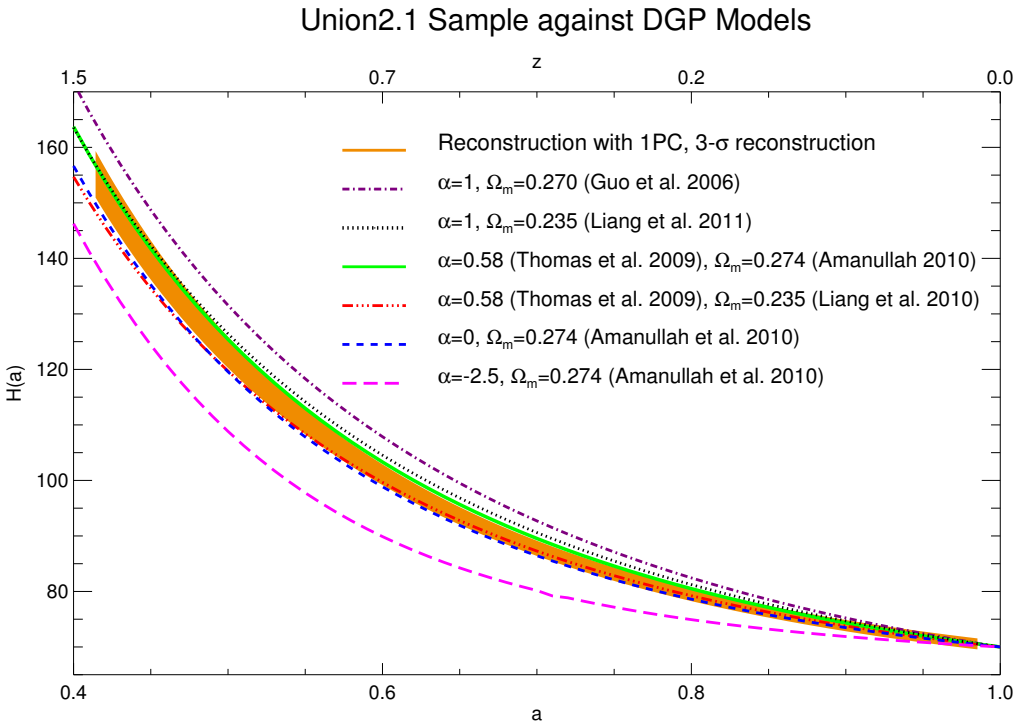

Figure 6.4: Recovered expansion rate extracted from the Union2.1 data with 1 PC and 3-σ errors (orange area) confronted with several DGP and mDGP models. We find the data to be consistent with $0 \lesssim \alpha \lesssim 0.50$.

ments. The latter constitutes so far the strongest constraint obtained for the DGP model.

For the mDGP model we considered the values inferred by Thomas et al. (2009) adding weak-lensing data to BAO and SNe (green solid line). In that particular study, the authors found an upper limit for the α parameter ($\alpha < 0.58$ at 68 per cent confidence level), but were not able to give constraints on the $\Omega_{\rm M}$ parameter. Therefore, and to better understand the effect of changing $\Omega_{\rm M}$ for a given α, we made use of the best-fit values reported in Liang & Zhu (2011) for the DGP model and in Amanullah et al. (2010) – for the standard ΛCDM model. This corresponds to $\alpha = 0$ and is also plotted in Fig. 6.4 f or the sake of comparison (blue dashed line). Additionally a model with negative α (magenta long-dashed line), resembling a highly non-physical model, is also included..

As was found in prior studies (see, for example, Maartens & Majerotto, 2006; Fairbairn & Goobar, 2006), a pure DGP cosmology is disfavored by the SNe data even at low redshifts. Models with negative values of α also disagree with our reconstruction. However, it is still too early to break the degeneracy betweeten ΛCDM and mDGP models with $0 \lesssim \alpha \lesssim 0.58$.

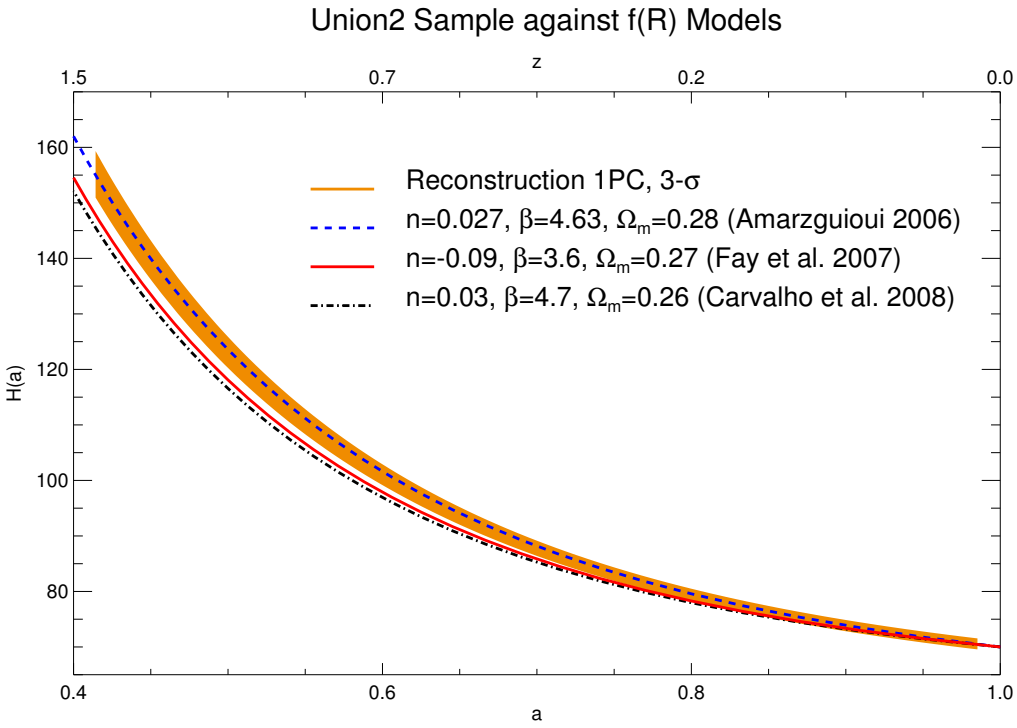

Figure 6.5: Recovered expansion rate extracted from the Union2.1 data with 1 PC and 3-σ errors (orange area) confronted with several $f(R)$ models. The best fit parameter for the models were taken from previous studies in literature.

$f(R)$ Theory

We now consider $f(R)$ cosmologies which, as we recall from Section 2.9.2, include a general function of the Ricci scalar in the Einstein equations. There are different parameterizations for $f(R)$, but here we assume the most simple one given by Eq. 2.57. By evaluating this equation at $z = 0$ it is possible to obtain a relationship between n, β, and $\Omega_{\rm M}$. Thus, if specifying the values of two of them the other is immediately fixed. In the analysis n and $\Omega_{\rm M}$ were treated as free parameters. The adopted values for the model parameters are taken from previously reported fits in the literature. Carvalho et al. (2008) obtained constraints on the (n, $\Omega_{\rm M}$) parameter space from the combination of BAO and CMB data with independent determinations of the Hubble parameter at different redshifts. Their best fit for the parameters was $n = 0.03$, $\beta = 4.7$ and $\Omega_{\rm M} = 0.26$ (black dashed-dotted line in Fig. 6.5), substantially different from our reconstruction.

In similar studies, other authors have combined SNe data with BAO and CMB. We consider here the numbers obtained by Fay et al. (2007) – red solid line – and Amarzguioui et al. (2006) – blue dashed line– using the SNLS and Gold samples, respectively. We find the latter model is in agreement with our

reconstruction although, from Fig. 6.5 it is evident that a strong degeneracy between n and $\Omega_{\rm M}$ is present.

This degeneracy will be studied in future work. We conclude that $f(R)$ cosmologies (at least the parameterisation considered here) should be kept as a possible theory of gravity.

Kinematic Models

Next, we consider kinematic models as described in Section 2.10. These are based only on a specific parameterisation of the deceleration parameter, q, or the jerk parameter, j. This means that no quantities coming from the dynamic description, such as the matter-energy content, are specified. We consider the five realizations specified in Sec. 2.10 and summarised in Table 6.1. For the different parameters we adopt the constraints obtained by Guimarães et al. (2009) with the previous Union compilation (Kowalski et al., 2008), and through a Bayesian marginal likelihood analysis. The comparison between the expansion history obtained from Union2.1 data and the theoretical expansion function calculated for each model is shown in Fig. 6.6. All these models make specific predictions for the cosmic expansion (see Guimarães et al., 2009, for the corresponding expressions of H) and they are of particular interest because no assumption on the matter-energy content present in the Universe is made.

We note that model M_2 can be rejected based on current SN Ia data because its shape differs greatly from the reconstructed expansion history. Also M_0 has a different slope which does not even fit the data at low redshifts. Models M_1, M_3 and M_4 agree with the SN data within the errors up to values of the scale factor $a \sim 0.6$ ($z \sim 0.66$). This is consistent with the transition redshifts $z_{\rm t}$ given in Guimarães et al. (2009). The good agreement may reflect the fact that the models were constructed in a way that mimics ΛCDM at low redshifts. At high redshifts $z > z_{\rm t}$, however, none of the models is consistent with our reconstructed expansion history.

Table 6.1: Summary of kinematic models.

Model Name	Parameterization
M_0	$q(z) = q_0$
M_1	$q(z) = q_0 + q_1 z$
M_2	$q(z) = q_0$ for $z \leq z_t$; $q(z) = q_1$ for $z > z_t$
M_3	$j(z) = j_0$
M_4	$D_L(z) = \frac{c}{H_0}\left[z + \frac{1}{2}(1-q_0)z^2 - \frac{1}{6}(1-q_0-3q_0^2-j_0)z^3\right] + O(z^4)$

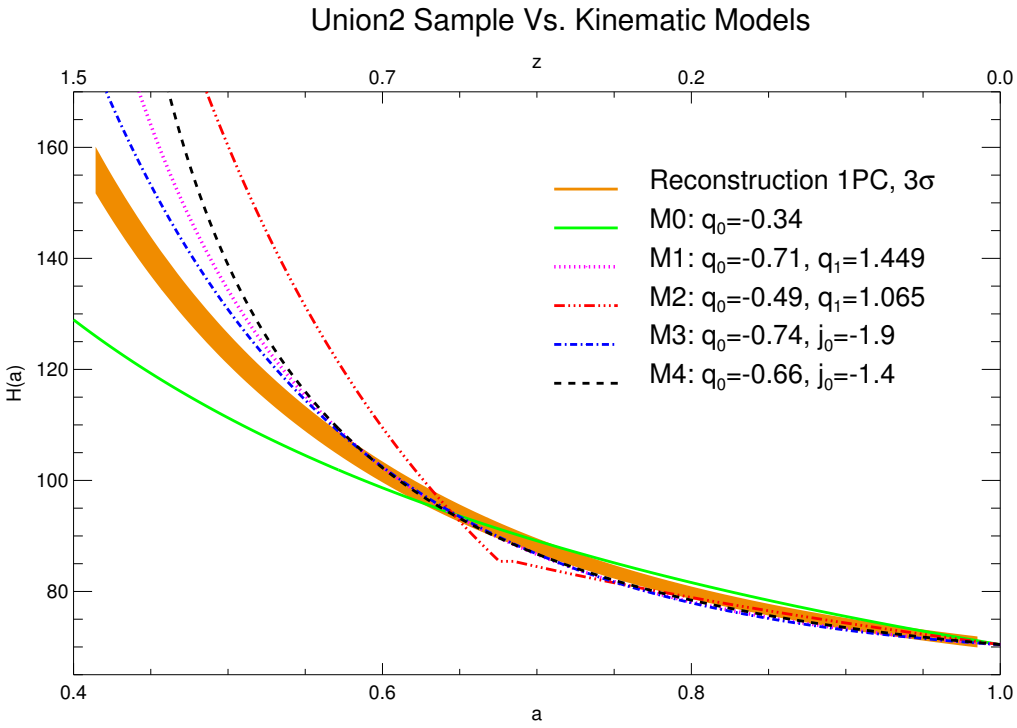

Figure 6.6: Recovered expansion rate extracted from the Union2.1 data with 1 PC and 3-σ errors (orange area) confronted with several kinematic models. The best fit parameter for the models were taken from previous studies in literature.

6.3 Alternative Cosmological Probes

After the analysis carried out in the previous Section, we conclude that it is still too early to accurately discriminate exotic alternatives from ΛCDM, although some of the scenarios can be ruled out from the current paradigm. However, taking only SNe into account may limit our ability to perform the reconstruction of the expansion rate. A comparison with other cosmological probes, such as BAO or CMB, could give tighter constraints for cosmological models.

As we saw in Sec. 2.6, the angular-distance diameter $D_{\rm A}$ can be translated into luminosity distances via the Etherington relation (Etherington, 1933). The use of BAO data, coming from surveys like the Baryon Oscillation Spectroscopic Survey (BOSS), will improve the performance of the method presented in this thesis and will provide higher accuracy in the calculation of $H(z)$. Indeed, some tentative work in this direction using simulated BOSS-like distance data has been carried out by Mignone (2009). As an illustration, Fig. 6.7 shows the expansion rate reconstructed from $D_{\rm A}$ data in the interval $0.6 < a < 1$ where most of the BOSS data concentrates. The accuracy in

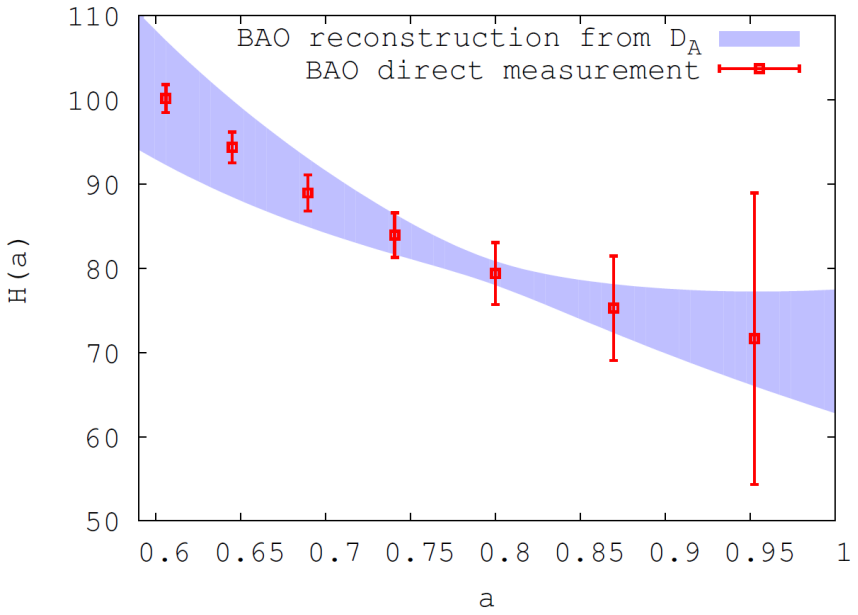

Figure 6.7: Recovered expansion rate extracted from BOSS-like distances (blue area) and estimated data points from the same survey (red points). From Mignone (2009).

the determination of $H(a)$ does not match the one reached with SNe due to the small number of BAO points available. The future BigBOSS will provide enough BAO data to be comparably used together with SNe Ia. Geometrical approaches as the one proposed here will greatly benefit from the combination of both probes.

Another idea would be to add directly measured $H(a)$ data to the reconstructed expansion derived from SN Ia. For example, Stern et al. (2010) present determinations of the cosmic expansion history from red-envelope galaxies. These are galaxies that formed their stellar population at high redshift $z > 2$ and whose stellar populations have been passively evolving since then, without further episodes of star formation. These galaxies are the oldest objects in the Universe at every redshift and their differential ages – i.e. the change in age of the Universe as a function of redshift dt/dz – should be good indicators for the expansion rate. The two data points obtained by the authors at $z \sim 0.5$ and $z \sim 0.9$, together with older determinations from the literature are plotted in Fig. 6.8 and compared with our reconstruction. Clearly, the errors in the $H(a)$ data are much bigger since they are affected by observational uncertainties and systematics in the determination of the stellar population. However, in general they agree with our result for the overall Hubble function.

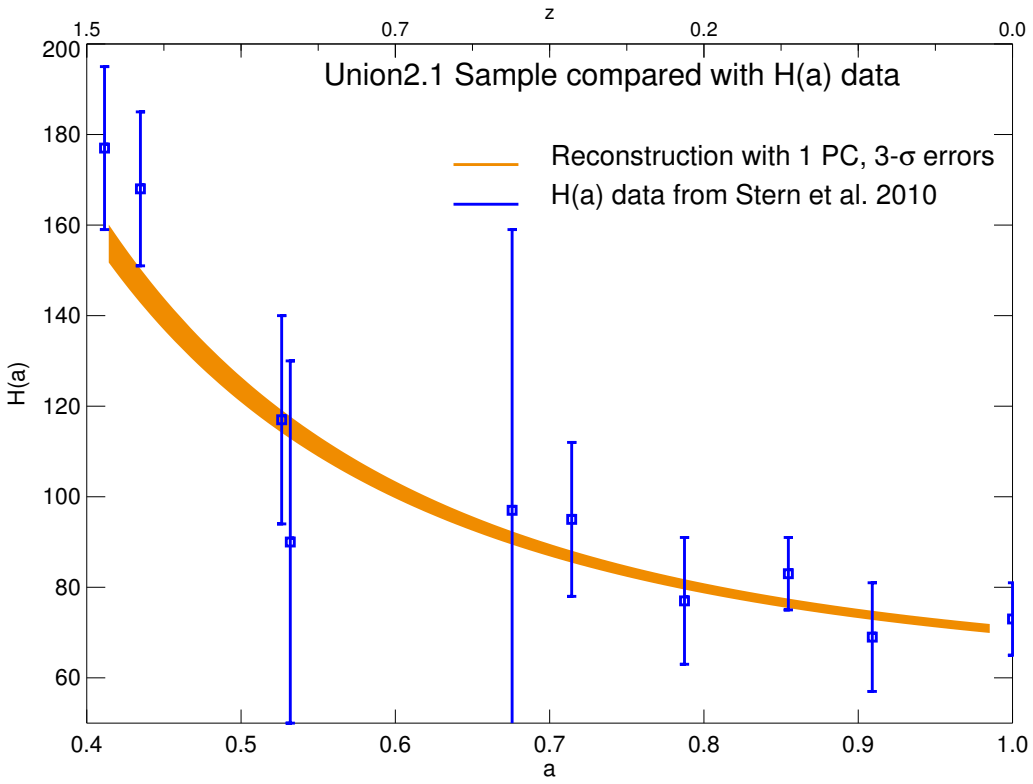

Figure 6.8: Recovered expansion rate extracted from the Union2.1 data compared with $H(a)$ data from passively evolving galaxies (Stern et al., 2010).

6.4 Other Interesting Applications

Our model-independent method to constrain the expansion history has other interesting applications. For instance, it offers a complementary way of detecting possible systematic effects such as possible uncertainties introduced by the light curve calibration, host galaxy extinction or intrinsic variations corresponding to different SN Ia populations, which could affect the data and would be overlooked within a traditional analysis based on physical parameterizations. The method is also a valuable tool that can be used to plan future Type Ia supernova cosmology campaigns, by testing redshift ranges in which it would be more relevant to collect data.

6.4.1 Checking for Systematics in the Supernova Samples

Given, for instance, some samples from different surveys, a question to ask is whether the respective cosmological parameters derived from both of them predict an expansion history that is consistent with the direct data analysis.

We tested this idea on the example of the Union2.1 data set which is a col-

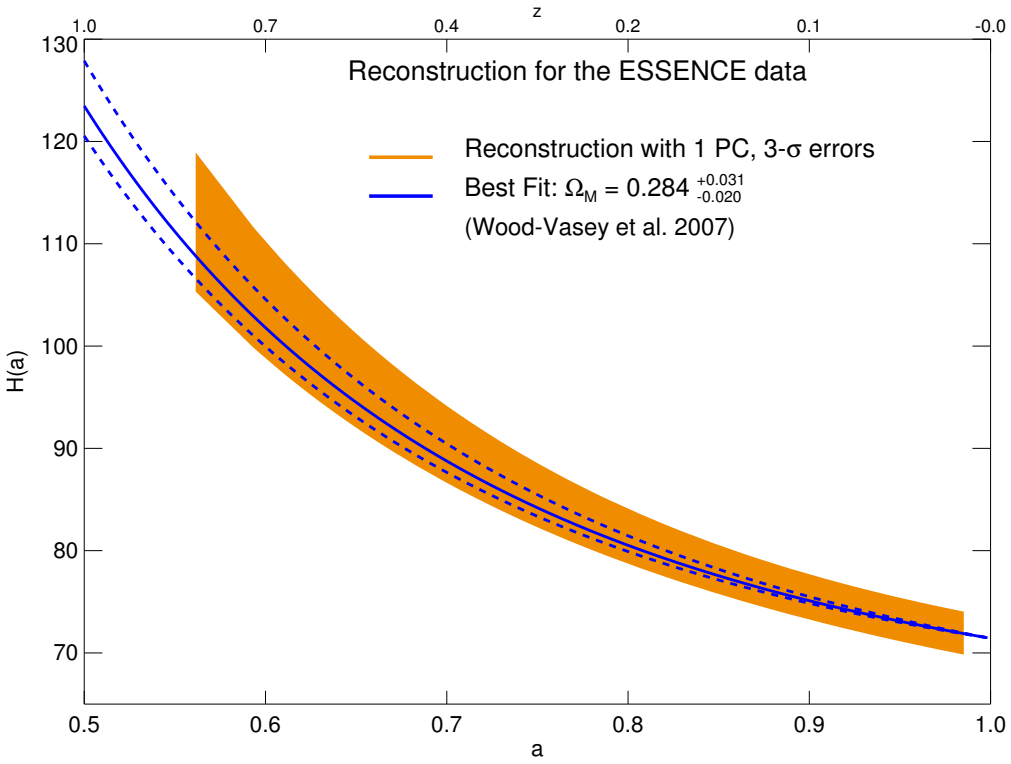

Figure 6.9: Recovered expansion rate extracted from the ESSENCE data with 1 PC and 3-σ errors (orange area). The blue solid line is the best fit encountered for this sample by Wood-Vasey et al. (2007). The dashed lines correspond to uncertainties on the best fit.

lection of data from various SN Ia surveys. Some tension amongst the several sub-samples in Union2.1 might exist, due to the different survey characteristics and handling of systematic errors, for example. In the most extreme case, one sub-sample alone could be responsible for introducing a bias in the entire data set. This can be identified by means of our reconstruction technique, which should detect discrepancies in the recovered expansion history of the individual sub-samples.

The three main components of the Union2.1 data set are the ESSENCE, the SNLS and the SDSS samples, as they cover a wide range in redshifts with a relatively large number of objects (see Fig. 5.1). The expansion histories of these three samples are compared with ΛCDM models based on the individual best-fit parameters found for them in Figures 6.9, 6.10 and 6.11. The errors are determined by the quality of each data set, being smaller for SNLS and SDSS.

It is worth noting that, in order to perform the reconstruction and avoid computational artifacts in the calculations, the three samples have been combined with low redshift data consisting on 57 SNe taken from Hicken et al. (2009a). All data sets show consistency of the reconstructed expansion with a

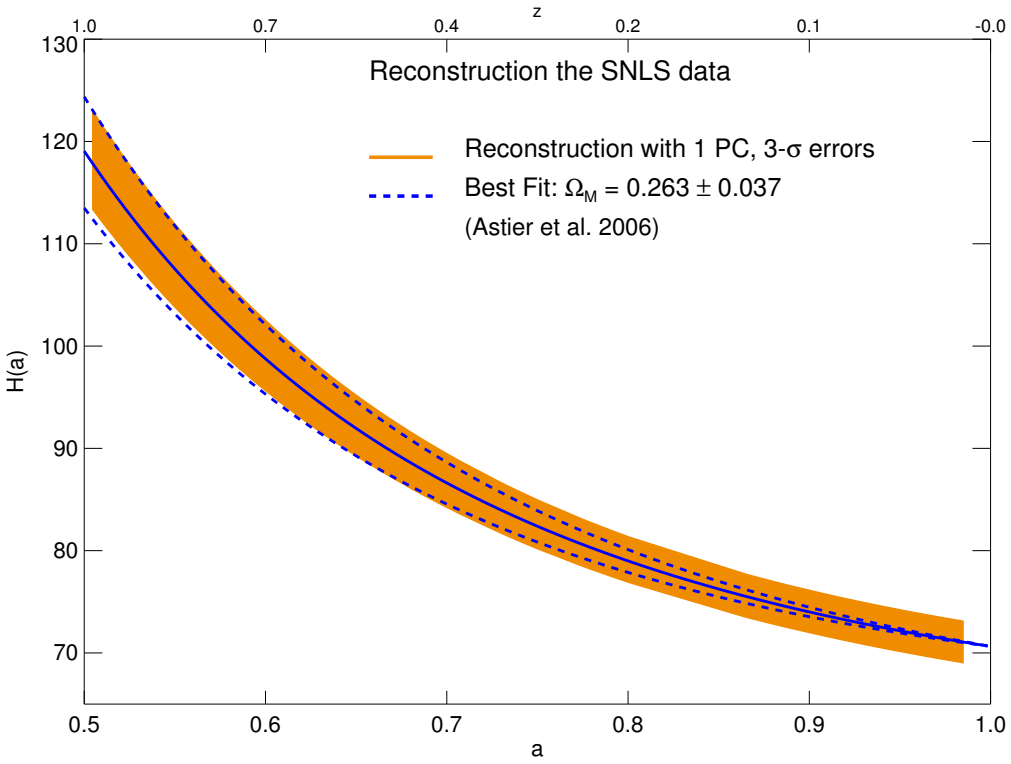

Figure 6.10: Recovered expansion rate extracted from the SNLS data with 1 PC and 3-σ errors (orange area). The blue solid line is the best fit encountered for this sample by Astier et al. (2006). The dashed lines corresponds to uncertainties on the best fit.

ΛCDM model, though the SDSS sample agrees marginally only with its best fit model obtained by Kessler et al. (2009). This could be due to the lack of high redshift SNe in this data sample, which counteracts the low-z sample giving the correct weight in the reconstruction. However, given the tests that have been performed on the method, even if such effect would exist, the deviation would not be that significant. This might indicate that the SDSS data are affected by some kind of unknown bias or that the ΛCDM best-fit model reported by Kessler et al. (2009), obtained with a traditional analysis, fails to represent some features of the underlying cosmology. Nonetheless, the data tested here correspond to the SDSS SNe contained in Union2.1 and not the original SDSS SNe, for which the best-fit was derived. This could also give a hint on how different frameworks to analyse the same data affect the cosmological results.

Plotting the extracted $H(a)$ from the three data sets together, we see in Fig. 6.12 that they are consisten with each other. However, the SDSS samples appears to have a different slope compared to the SNLS and ESSENCE reconstruction.

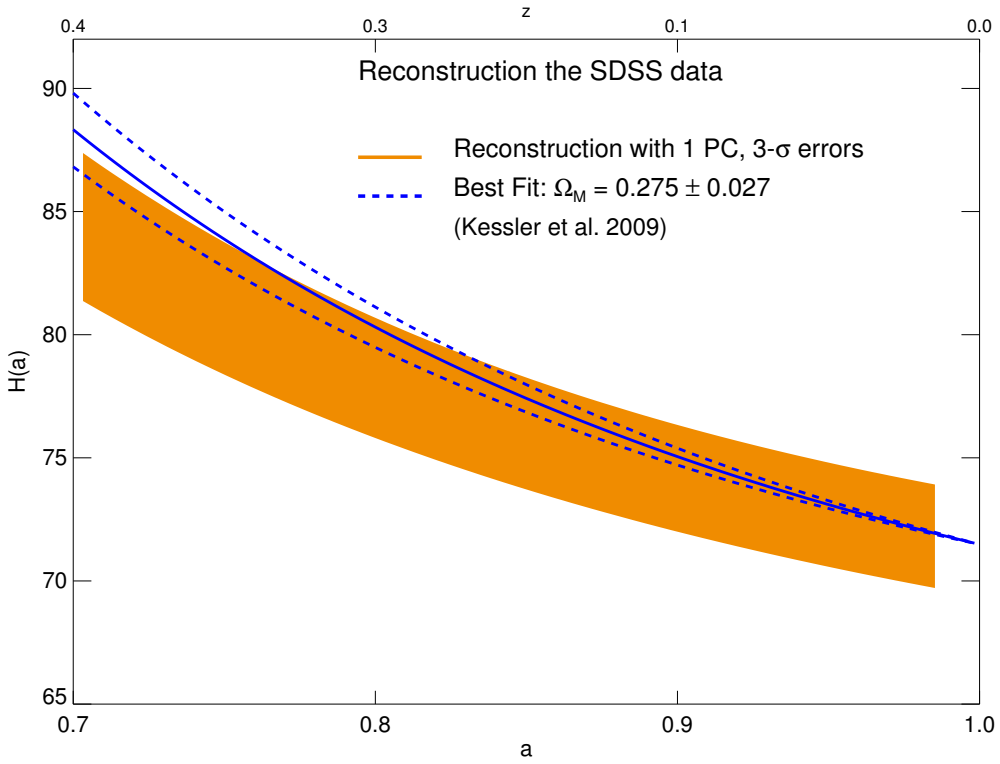

Figure 6.11: Recovered expansion rate extracted from the SDSS data with 1 PC and 3-σ errors (orange area). The blue solid line is the best fit encountered for this sample by Kessler et al. (2009). The dashed lines correspond to uncertainties on the best fit.

6.4.2 Testing Redshift Ranges for Supernova Campaign Planning

More data at various redshifts will be obtained in future SN Ia surveys. In order to test the effects new data may have on current data and on our reconstruction approach, we created high and low redshift mock data with very high signal to noise ($S/N \sim 2$) using SNANA. The distant SNe resemble those obtained with the *HST* regarding measurements errors, selection effects and filter system. We then combined each of these simulations with the Union2.1 sample individually and run the procedure to obtain $H(a)$. The approximate number of simulated data was 300, to roughly equal the number of nearby and distant SNe contained in Union2.1. Figure. 6.13 shows the results for the low-z sample combined with Union2.1 set. The recovered $H(a)$ for the high-z data plus Union2.1 is shown in Fig. 6.14.

The improvement of the reconstruction is apparent from the significant decrease in the error bars. This is not surprising, since the data were simulated with very high quality. In Figure 6.14 the errors for $z \gtrsim 0.8$ are specially small, which is consistent with the fact that the simulations abundantly populate that

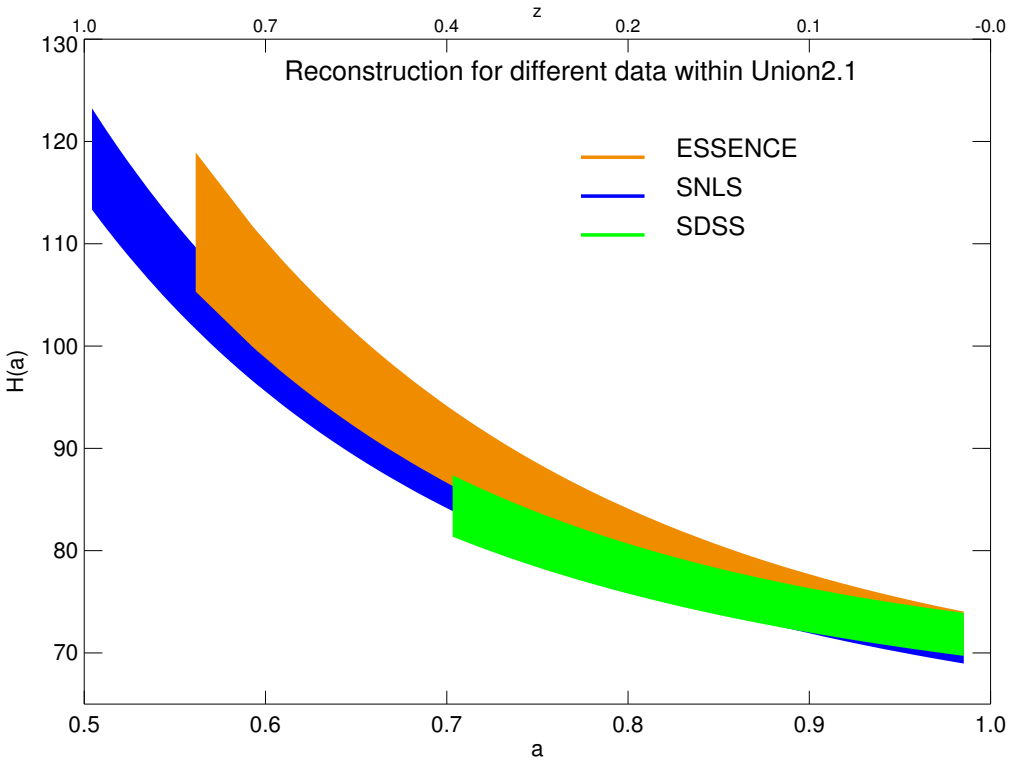

Figure 6.12: Comparison of the recovered expansion function from the ESSENCE (orange area), SNLS (blue area) and SDSS (green area) data samples with 1 PC and 3-σ errors.

area. It is also very interesting that, as observed in Fig. 6.13, high-redshift errors are greatly reduced when a large number of (quality) low-z SNe are included in current data sets. Good nearby data are easier to obtain and less subjected to systematic errors – such as survey selection effects – than their high-redshift counterparts. The advanced technology of future surveys will notably improve the observation and calibration procedures yielding very high signal-to-noise photometry and spectroscopy. We argue that SN campaigns – both ground and space-based – that focus on the low-z Universe might be more beneficial for SN cosmology than projects attempting to obtain thousands of SNe at high redshifts, where less control on the quality of the data and the systematic errors is achievable.

Moreover, spectroscopic classification becomes a hard and expensive task for high redshift SNe. Equally, accurate redshift determination of the host galaxies requires good spectroscopic data which is easier to obtain for nearby events. We discussed in Sec. 3.6.1 the possibility of accessing photometric redshifts from those high-redshift surveys, but this would probably carry a degradation in statistical accuracy, which is in contradiction with the needed quality, essential to improve present cosmological results. These reasons give an indication that more SN data in the nearby regime can help to signifi-

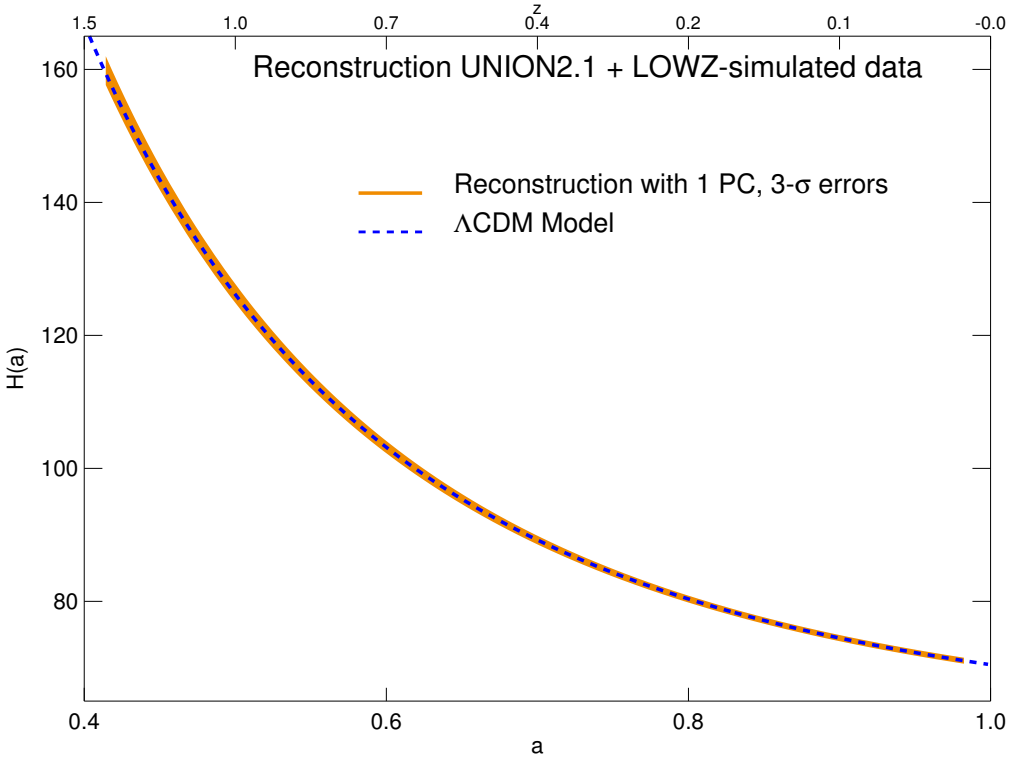

Figure 6.13: The reconstructed expansion rate with 3-σ errors extracted from the Union2.1 set plus around 300 simulated nearby SNe with high signal to noise. Our reconstruction (orange area) is compared with the underlying ΛCDM model (blue line).

cantly improve the constraints on cosmological models. We believe that such considerations may help with the design of future surveys.

6.5 Ongoing Work

An important aspect to take into account when dealing with SNe Ia is that they are not standard candles but have to be calibrated as distance indicators applying the empirical calibration discussed in Sec. 3.3.2. This calibration procedure introduces a dependence between the calibrated measurements that gives rise to finite non-diagonal entries in the covariance matrix for the distance modulus. Moreover, the parameters of the calibration and the derived distances may depend on the light-curve fitter employed for that purpose (Kessler et al., 2009). Though we demonstrated in Sec. 5.2.1 that with ideal (or good quality) data, the choice of light-curve fitter was irrelevant, actual data may still be affected by this limitation. Another complication, as was also mentioned in Sec. 3.4.1, is that the SALT2 fitter determines the calibration parameters simultaneously with the cosmological parameters assuming a ΛCDM model.

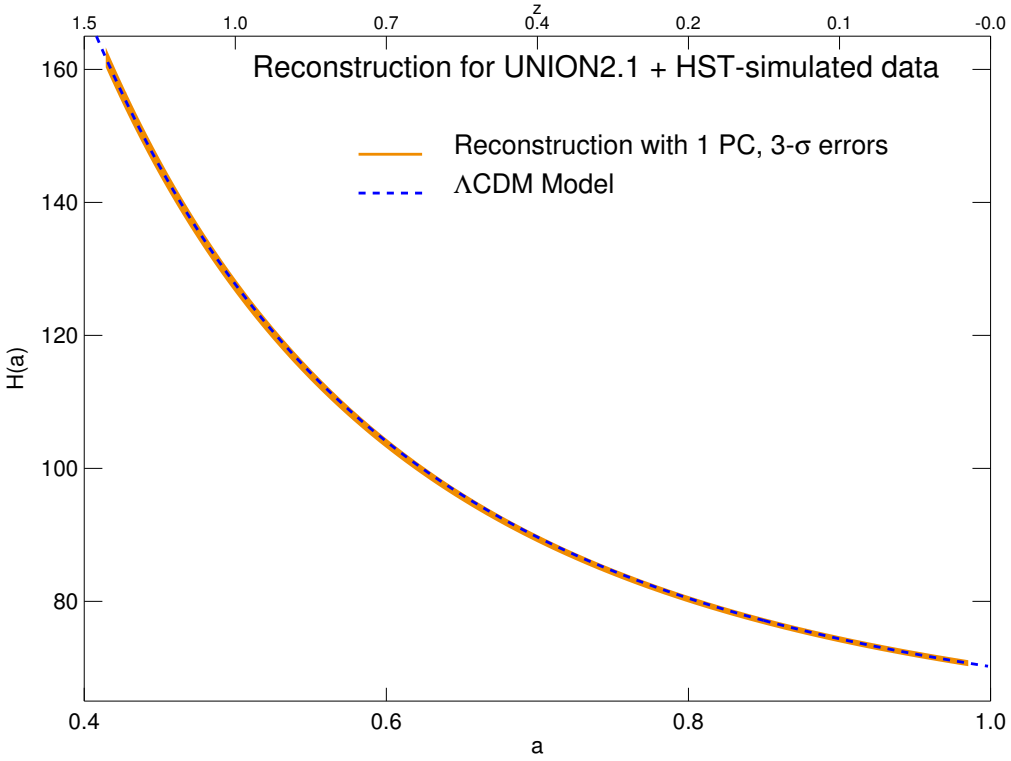

Figure 6.14: The reconstructed expansion rate with 3-σ errors extracted from the Union2.1 set plus around 300 simulated high-z SNe with high signal to noise. Our reconstruction (orange area) is compared with the underlying ΛCDM model (blue line).

As the Union2.1 sample was calibrated with SALT2, this applies also to the data and any cosmological result derived from them. This appears as a major contradiction to the intended model-independence of the method proposed in this thesis and has raised some constructive criticism.

Therefore, we saw the necessity of fitting the raw Union2 data using the MLCS fitter, which does provide *model-independent* luminosity-distance data, and compare the corresponding $H(a)$ reconstruction with our present results.[1] This may offer a interesting test for the SNe comunity since it will provide an independent assessment on the performance of the two most used light curve fitters on current data.

However, fitting the raw light curves is not a trivial task, since each of the sub-samples included in Union2 use a different set of filters, sometimes peculiar, for which correspondence with Bessell filters are not straightforward, or the same SN is observed by two telescopes, information that has to be

[1]Note that we refer here to the Union2 sample instead of the recent upgrade Union2.1, which was used throughout this thesis. The reason for this is that we only had access to the raw Union2 data. However, for our purposes, the difference should not be noticeable, since Union2.1 only containts around 20 SNe more than Union2.

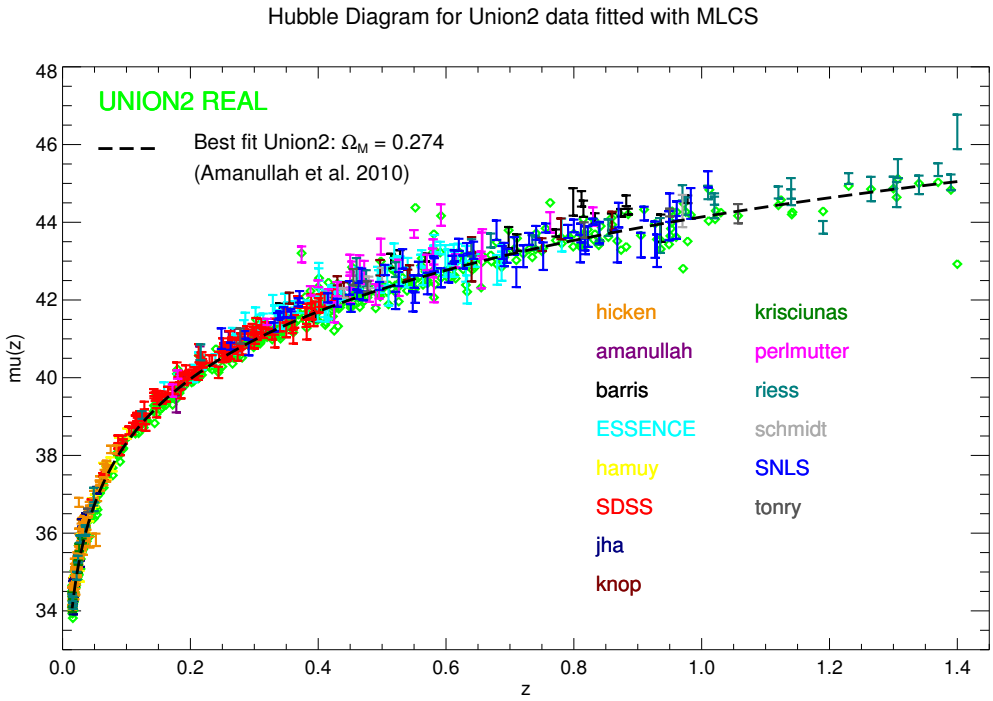

Figure 6.15: Our MLCS fit of the Union2 data (with errors) compared with the original SALT2 fit (without errors, green points). Here the modulus distance μ is plotted against redshift z. As a comparison the best fit cosmology for Union2 is also plotted (black dashed line).

included in the K-corrections. Doing this once and for all, and developing the necessary tools for new data that may be added to the compilation appears as a smart strategy.

A tentative, though not definitive, result for the MLCS fit is presented in Fig. 6.15 together with the SALT2 original fits. The plot shows distance modulus against redshift, following what is commonly displayed in the SN community (in contrast with $D_{\rm L}$ or H versus scale factor a, as was done in this thesis). In our fit, the (relative) distances obtained with MLCS are systematically higher than those derived with SALT2 (~ 0.5 mag. on average), which could point to errors in our fit. However, a comparison with the last reported MLCS fit to public data sets with 288 SNe from the SNLS, ESSENCE, SDSS and *HST* samples, shows good agreement with the fit we obtain (see Fig. 6.16). Moreover, the fit for $\Omega_{\rm M}$ is closer to what we obtain with our model-independent reconstruction than other supernova studies. We expect the reconstructed $H(a)$ to vary slightly donwards at high and intermediate redshifts from our result of Fig. 6.1, since our distances differ from the SALT2 estimates. But we do not foresee a significant change on the cosmological pa-

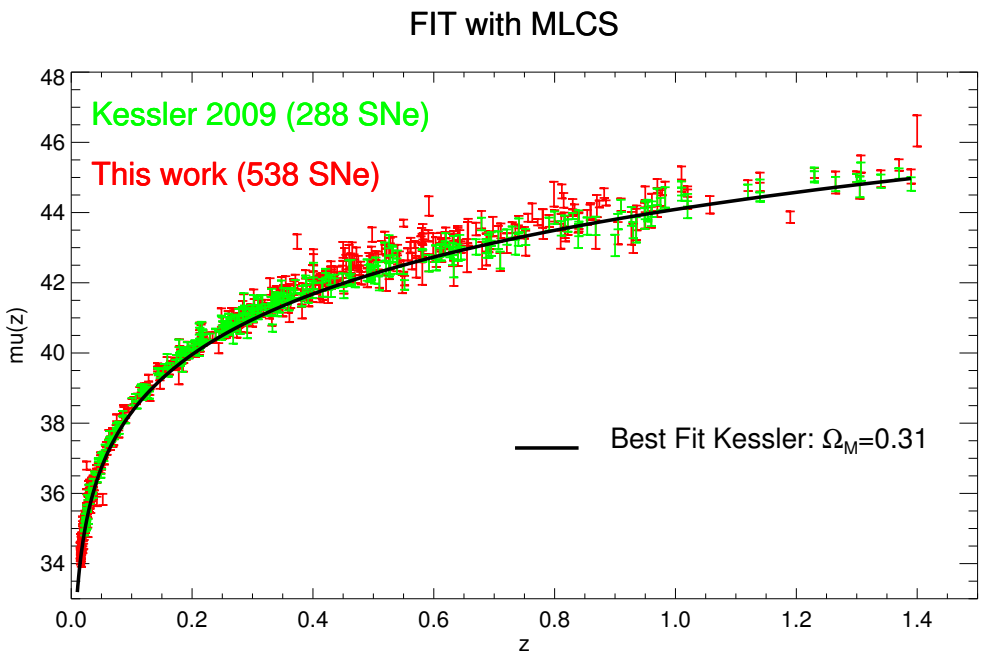

Figure 6.16: Our MLCS fit of the Union2 data compared with the fit of Kessler et al. (2009) with 288 SNe. Here the modulus distance μ is plotted against redshift z. The best cosmology obtained by Kessler et al. (2009) is also plotted in black.

rameters. More investigation is, however, needed in order to asses the validity of the fit and draw conclusions from the outcome.

Looking ahead into the future, when the number (and precision) of data from the upcoming surveys – as for example, the already started Dark Energy Survey or the future missions Euclid and LSST – allows it, we will explore the potential of the method for the analysis of possible local inhomogeneities through comparison of the expansion history in different directions.

7. Conclusions and Perspectives

The question of why the Universe is accelerating today is still not convincingly addressed within the current standard cosmological model. An uniformly distributed dark energy component, with equation of state $w = -1$ and exerting a negative pressure appears to be the most plausible explanation for the observed acceleration. A feasible candidate for dark energy is the cosmological constant Λ, understood as the zero point of all quantum fields or the vacuum energy. However, theoretical predictions result in an estimation of Λ that is between 120 to 55 orders of magnitude larger than suggested by astrophysical data. Other proposals for dark energy involve a dynamical scalar field rolling very slowly toward its lowest energy of state. Nowadays, even with the advent of very accurate cosmological data, the nature of dark energy and the reason for its relevance *now* remains unclear. Although general relativity can accommodate the detected acceleration of the Universe, it cannot give a deeper understanding about its cause, nor can it give robust solutions for the fine-tuning and the coincidence problem. In order to overcome these difficulties, non-standard cosmological models have been presented as alternative explanations for acceleration without dark energy. Modified gravity describes the late-time acceleration as a manifestation of new physics beyond General Relativity. Modified gravity theories advocate to introduce extra terms in Einstein's equations to allow for extra dimensions (braneworld models), or higher powers of the *Ricci* scalar ($f(R)$ models) in the Einstein-Hilbert action. Equally, pure kinematic approaches have been suggested based on parameterisations of the second and third derivatives of the scale factor, in an attempt to constraint the acceleration of the Universe. Such diverse scenarios are likely to diverge in their predictions for $H(z)$ from the standard ΛCDM model and therefore they can be constrained from the reconstructed expansion history of the Universe.

Since the detection of the acceleration of the Universe a decade ago, SN Ia cosmology has received an increasing attention. Due to their uniform luminosity, this class of supernovae can be used as very suitable (relative) distance indicators. They allow for the construction of modern versions of the *Hubble diagram*, using distance modulus instead of apparent brightness, and redshift instead of radial velocity. Different groups like the Supernova Cosmology Project, the Higher-Z or the CfA teams are putting great efforts in looking for more SNe Ia to extend both the nearby and the distant samples.

Currently, the largest, homogeneously reduced sample at hand is the Union2.1 data set, which includes many of the larger surveys, such as ESSENCE and SNLS and previous compilations from literature. Constraints from such compilations combined with other cosmological probes have yielded accurate values of the cosmological parameters which describe the Universe we live in. However, the uncertainties are still large. Statistical errors can be controlled if more supernovae are observed and included in the samples, but systematic uncertainties are not so easy to overcome. The main systematic errors come from the galaxy extinction, the calibration of the light curves to derive the distance estimations and a possible evolution in redshift of the supernova population. Data of better quality is mandatory in order to reliably improve the cosmological constraints inferred from SNe Ia.

In this thesis, we presented a method to recover the expansion history of the Universe in a model-independent fashion. The only assumption made is the validity of the FLRW metric and the Cosmological Principle. The luminosity distance measurements obtained from SNe Ia depend only on space-time geometry, and can be directly related to the *Hubble function* without assuming a dynamical model. This can be achieved by deriving the theoretical expression of the luminosity distance, as given by the FLRW metric, and transforming it into a Volterra integral equation of the second kind. A unique solution for this integral can be found in terms of Neumann series, providing the expansion rate within the accuracy allowed by the data. The drawback of the transformation to a Volterra integral is that the derivative of the luminosity distance is needed. However, taking the derivative directly from the data leads to unreliable results. The method employed here solves this problem through the expansion of the luminosity distance into an series of arbitrary orthonormal functions. In this way, fitting the expansion coefficients to the data and using the derivative of the series expansion instead of the derivative of the data we were able to recover the expansion history of the Universe. The only condition imposed here is that the minimum number of coefficients used on the reconstruction should be minimal.

Several basis were tested to reconstruct the *Hubble parameter* yielding acceptable results for the $H(a)$ function. Nevertheless, in an attempt to control the number of coefficients to be included in the reconstruction in a rigorous way, and avoid biases coming from the choice of the basis, we derived it from Principal Component Analysis. PCA is a well-known statistical tool traditionally used to reduce the dimensionality of large data sets and describe them in terms of a few features, which map the main characteristics contained in the data. Different approaches using PCA have been proposed to reconstruct the dark energy equation of state w or the expansion function $H(a)$.

The PC formalism employed here, defines a training set consisting of an ensemble of ΛCDM models with a particular reference vector as the origin of the new parameter space. The choice of this reference model is arbitrary and does not affect the nature of the basis or the reconstruction of $D_{\rm L}$. It

is generally identified with the mean of the training matrix. The principal components are found by solving the usual eigenvalue problem. The linear transformation leading to the PCs concentrates in only a few features all the information regarding deviations from the reference vector.

In contrast to others approaches in literature, we do not aim to model underlying physical quantities within a specific cosmological model, such as w. Instead, we aim at the Principal Components directly describing cosmological observables, e.g. luminosity distances. Moreover, the method also avoids redshift binning while smoothing the SN data. Although only results using SNe Ia data are presented in this thesis, it is possible to use the algorithm to analyse any type of observable which delivers standard candle or standard ruler measurements (e.g. CMB or BAO). A general parameterization (with independent parameters regardless of the underlying physical assumptions) could be achieved by considering the principal components as cosmological *eigen-cosmologies*.

We demonstrated that we are able to recover the main features underlying the cosmological expansion of the Universe, with only a few, mathematical, assumptions. The error budget in our reconstruction comes from the uncertainty in the determination of the coefficients and the *Hubble constant* H_0 due to the minimisation.

The strength of the method employed here to derive the expansion history of the Universe is that it provides a purely geometrical test. Contrary to other ways of analyzing cosmological data it does not revert to assumptions on the energy contents of the Universe nor its dynamics. We argue that, as long as the nature of dark energy remains unknown, model-independent analyses of the kind described here have more significance in deriving cosmological parameters than traditional parametric studies. This is due to the fact that no specific form of the equation of state w or the *Hubble* function is fixed in our approach.

Our analysis showed that SNe data point to a higher value of Ω_M, in contradiction with what was found with standard methods. Furthermore, this is in agreement with the last results driven by the Planck Satellite mission. In our approach, H_0, is considered a free parameter to be minimised with expansion coefficients. We obtained a value which is in agreement, within error bars, with the recent constraints obtained by other supernova studies.

The ultimate goal of this work was to discriminate among different cosmological models, such as dark energy or $f(R)$ and DGP cosmologies, based on very different physical assumptions, and, in this way, break the current degeneracy in the cosmological parameters. Testing the validity of the different scenarios is an important and challenging task. The reconstructed expansion rate can be used to consistently study those alternatives and provide constraints on their different cosmological parameters. By means of simulated data, we proved that our method is able to recover exotic cosmologies, even if they are not included in the original training matrix. In this cases, we often needed a larger number of components in order to recover the *true* expansion

history underlying the simulated data.

The issue of the number of PCs to include in the analysis is not trivial and is still a matter of current debate. Here we base our decision on the percentage of total variance carried by each eigenvalue and its corresponding eigenvector. This criteria proved to perform well in most cases, loosing only accuracy for very extreme cosmologies. Once we were sure of the robustness of out method, we investigated theoretical predictions from several cosmological scenarios by confronting them to the reconstructed expansion history obtained from the SN data. In this way, we were able to asses their validity by comparing the different predictions to our results for $H(a)$. We found that only a small set of cases remain consistent with the data within the $f(R)$ and DGP paradigms. In the context of kinematic models, which rely on different parameterizations of the jerk and the deceleration parameter, we found none of them fit the data well. Concerning dark energy models, it is not possible to discriminate between constant or evolving-in-time equation of state with current data, though this may change with new data released by future surveys.

Moreover, the model-independent method offers a complementary way of detecting possible systematic effects which could affect the data and be overlooked within a traditional analysis based on physically motivated parameterizations. Actual compilations of SNe Ia comprise data from different surveys and observed with disparate telescopes systems. It maybe the case, one sample could introduce a bias in the whole sample producing misleading results of the cosmological parameters. Discrepancies in the expansion history extracted from several samples within a compilation might help to identify these effects. We found general agreement in the reconstructed $H(a)$ obtained from the ESSENCE, SNLS and SDSS surveys, though we detected some deviation of the SDSS data from its best cosmological fit.

The application of the method to check for possible systematics within SN samples is specially relevant in the context of the different light curve fitters developed to calibrate the data. Though simulations with ideal and high quality data revealed no difference in the performance of the two mainstream light-curve fitters (MLCS and SALT2), a dependence of the derived distance moduli on the light curve model can still happen with current data. Therefore, it is important to test the performance of the available light-curve fitters on the base of model-independent approaches. It is important to keep in mind that the possible impact of the light curve fitter in the calculation of SN distances, and in our reconstruction technique, can be overcome by using near infrared data, a region where SN Ia are nearly standard candles. It would be interesting to apply the method to NIR data and investigate the effect on the constraints on the expansion history of the Universe and cosmological models.

An increasing body of high quality data will help to reduce systematic uncertainties affecting cosmological results obtained from SN data and will provide a better constraints on the expansion rate. We studied the effect that more nearby and distant SNe Ia will have on the reconstruction of $H(a)$. We

generated mock data resembling the *HST* and some low-z surveys with the SNANA software and added them to the Union2.1 sample. We found that, though distant SN are usefull for cosmological analysis, especially if one wants to map the time variation of the dark energy equation of state, a larger number of well-observed nearby data seems to be more essential. High redshift SN will always be affected by specific systematics, such as survey selection effects or inaccurate spectroscopic measurements, which can be easily overcome by concentrating on nearby data. We believe that our method stands as a valuable tool to plan future Type Ia supernova cosmology campaigns, by testing in which redshift ranges it is more important to collect new data.

In future work, we will consider not only SN Ia data but also other cosmological probes, such as the angular distances from BAO, in order to obtain tighter constrains on the expansion history of the Universe.

Finally, is it worthwhile noting the potential of the method for the analysis of possible local inhomogeneities through comparison of the expansion history in different directions.

8. Acknowledgments

First of all, I am indebted to my supervisor Wolfgang Hillebrandt who has constantly supported me through these three and a half years, even in the lowest moments of the PhD. I thank him for the patience and understanding, for encouraging me from the very beginning. Also, for giving me the opportunity of working on such a outstanding Institute as the MPA, where I have learned so much, earned so much experience and met so wonderful people.

Most warmly, I want to thank Emille Ishida, without whom this thesis could not have been accomplished. Thank you for the long discussions, many times through Skype with each of us in different continents in different time zones. For all the explanations, and offering them as many times as necessary. For making me value and appreciate the work we were doing.

I also thank Fritz Roepke for his guidance during the first years of my PhD, and for the delicious Feuerzangenbowle the last two Christmas at his "castle" in Wuerzburg.

I am equally obliged to our colleagues in Heidelberg: Claudia Mignone, Matteo Maturi and Matthias Bartelmann. This project could have not being completed without your valuable collaboration and your scientific advice.

It is a pleasure to thank A. Shafieloo, B. Leibundgut and M. Kowalski for providing helpful comments, suggestions and interesting challenges to the method.

This work was supported by Max-Planck Institute for Astrophysics (MPA), the Deutsche Forschungsgemeinschaft via the Transregional Collaborative Research Center "The Dark Universe" (TRR 33), the Emmy Noether Program (RO 3676/1-1) and the Excellence Cluster "Origin and Structure of the Universe" (EXC 153), institutions to which I thank most earnestly.

I am grateful to all the people at MPA for the memorable moments I have lived here. Special thanks to Irina and Rob for always being there, for being real friends. Thanks also to Nytia for her amiable chatting and her recommendations of Indian movies. The office is very lonely now!

To the people from the SN Ia group I thank for the support and always being ready to help and provide advice. Thanks to Markus and, specially to Stefan, for reading half of my thesis in only a few days and giving me very helpful comments and corrections. Thanks also for the kind words on the toughest moments. Also, I would like to thank Phillipe, Rob and my flatmate Mark for carefull reading the chapters presented here and their useful

suggestions.

I thank the people from GalileoMobile, who have shown me other ways in which Astrophysics is important and have lighthen on my heart the wish of sharing it with the young public.

To my Spanish friends in Munich thank you for being my family here, for bringing me back to reality when I was lost in deep space and making me laugh in the hardest moments. For always showing interest on what I was doing.

To my parents and my sister thank you so much for always, no matter what, supporting and encouraging me. I know it was hard for you to have me far away from home. Thank you for being there everytime I needed you. For looking after me even in the distance. For being absolutely sure – much more than myself – that I would make it. Thanks *Papa*, for those summer nights watching the sky when I was little, which motivated my fascination for the stars and the Universe, and led me to pursue a degree in Astrophysics. To my Mother, the second quote at the preface of this thesis is for you, because you made love literature and poetry almost as much as I love Astronomy.

Paula, *alma gemela*, thank you for always flying with me, for being the one that understands. *Hermana, te quiero hasta la locura, siempre.*

To Simon, thank you for the most happy time in my live. *Nunca olvidare lo que hiciste por mi en Heidelberg. Las estrellas nos unieron y espero que de nuevo, algun dia, nos vuelvan a juntar.*

Last but not least, I owe Albert Camus my gratitude for literally support me (more precisely one of the legs of my table) for the last year of the PhD. I absolutely believe that you inspired me somehow in the writing of this thesis.

Well, and now? Now, I look into the future...

Bibliography

Ahmed Z., et al., 2009, Physical Review Letters, 102, 011301

Aldering G., et al., 2002a, in Tyson J. A., Wolff S., eds, Society of Photo-Optical Instrumentation Engineers (SPIE) Conference Series Vol. 4836 of Society of Photo-Optical Instrumentation Engineers (SPIE) Conference Series, Overview of the Nearby Supernova Factory. pp 61–72

Aldering G., et al., 2002b, in Dressler A. M., ed., Society of Photo-Optical Instrumentation Engineers (SPIE) Conference Series Vol. 4835 of Society of Photo-Optical Instrumentation Engineers (SPIE) Conference Series, Overview of the SuperNova/Acceleration Probe (SNAP). pp 146–157

Aldering G., Knop R., Nugent P., 2000, AJ, 119, 2110

Alpher R. A., Bethe H., Gamow G., 1948, Physical Review, 73, 803

Alpher R. A., Herman R. C., 1948, Physical Review, 74, 1737

Amanullah R., et al., 2010, ApJ, 716, 712

Amanullah R., Stanishev V., Goobar A., Schahmaneche K., Astier P., Balland C., Ellis R. S., Fabbro S., Hardin D., Hook I. M., Irwin M. J., McMahon R. G., Mendez J. M., Mouchet M., Pain R., Ruiz-Lapuente P., Walton N. A., 2008, A&A, 486, 375

Amarzguioui M., Elgarøy Ø., Mota D. F., Multamäki T., 2006, A&A, 454, 707

Amendola L., Kainulainen K., Marra V., Quartin M., 2010, Physical Review Letters, 105, 121302

Angloher G., et al., 2012, European Physical Journal C, 72, 1971

Arfken G. B., Weber H. J., 1995, Mathematical methods for physicists. Academic Press

Arnett W. D., 1969, Astr. Sp. Sc., 5, 180

Astier P., et al., 2006, A&A, 447, 31

Baade W., 1956, PASP, 68, 5

Baade W., Zwicky F., 1934, Physical Review, 46, 76

Barausse E., Sotiriou T. P., Miller J. C., 2008, Classical and Quantum Gravity, 25, 105008

Barone-Nugent R. L., Lidman C., Wyithe J. S. B., Mould J., Howell D. A., Hook I. M., Sullivan M., Nugent P. E., Arcavi I., Cenko S. B., Cooke J., Gal-Yam A., Hsiao E. Y., Kasliwal M. M., Maguire K., Ofek E., Poznanski D., Xu D., 2012, MNRAS, 425, 1007

Barris B. J., et al., 2004, ApJ, 602, 571

Beckers J. M., 1993, ARAA, 31, 13

Begeman K. G., 1989, A&A, 223, 47

Benitez-Herrera et al., 2012, MNRAS, 419, 513

Benitez-Herrera et al., 2013, accepted for publication at MNRAS

Bernstein J. P., et al., 2012, ApJ, 753, 152

Bertone G., Hooper D., Silk J., 2005, PhRep, 405, 279

Bessell M. S., 1990, PASP, 102, 1181

Blake C., Glazebrook K., 2003, ApJ, 594, 665

Blondin S., Dessart L., Hillier D. J., Khokhlov A. M., 2013, MNRAS, 429, 2127

Blondin S., et al., 2006, AJ, 131, 1648

Boyarsky A., Lesgourgues J., Ruchayskiy O., Viel M., 2009, JCap, 5, 12

Branch D., 1998, ARAA, 36, 17

Branch D., Baron E., Hall N., Melakayil M., Parrent J., 2005, PASP, 117, 545

Branch D., Fisher A., Nugent P., 1993, AJ, 106, 2383

Branch D., Tammann G. A., 1992, ARAA, 30, 359

Buchdahl H. A., 1970, MNRAS, 150, 1

Caldwell R. R., Dave R., Steinhardt P. J., 1998, Astr. Sp. Sc., 261, 303

Campbell H., et al., 2013, ApJ, 763, 88

Cardelli J. A., Clayton G. C., Mathis J. S., 1989, ApJ, 345, 245

Carroll B. W., Ostlie D. A., 1996, An Introduction to Modern Astrophysics. Addison-Wesley, Reading, MA

Carroll S. M., 1998, Physical Review Letters, 81, 3067

Carvalho F. C., Santos E. M., Alcaniz J. S., Santos J., 2008, Journal of Cosmology and Astro-Particle Physics, 9, 8

Cattell F. C., 1966, The journal of the Society of Multivariate Experimental Psychology

Chandrasekhar S., 1931, ApJ, 74, 81

Chevallier M., Polarski D., 2001, International Journal of Modern Physics D, 10, 213

Chotard N., et al., 2011, A&A, 529, L4

Clocchiatti A., et al., 2006, ApJ, 642, 1

Clowe D., Bradač M., Gonzalez A. H., Markevitch M., Randall S. W., Jones C., Zaritsky D., 2006, ApJL, 648, L109

Coil A. L., et al., 2000, ApJL, 544, L111

Colgate S. A., 1979, ApJ, 232, 404

Colgate S. A., McKee C., 1969, ApJ, 157, 623

Colless M., et al., 2001, MNRAS, 328, 1039

Collins II G. W., 1978, The virial theorem in stellar astrophysics

Conley A., et al., 2006, AJ, 132, 1707

Conley A., et al., 2011, ApJS, 192, 1

Contreras C., et al., 2010, AJ, 139, 519

Cooray A., Caldwell R. R., 2006, PhRvD, 73, 103002

Copin Y., et al., 2006, New Astronomy Review, 50, 436

Corasaniti P. S., Bassett B. A., Ungarelli C., Copeland E. J., 2003, Physical Review Letters, 90, 091303

Cyburt R. H., 2004, PhRvD, 70, 023505

Daly R. A., Djorgovski S. G., 2003, ApJ, 597, 9

Daly R. A., Djorgovski S. G., 2004, ApJ, 612, 652

Davis T. M., et al., 2007, ApJ, 666, 716

Davis T. M., Schmidt B. P., Kim A. G., 2006, PASP, 118, 205

de Bernardis P., et al., 1999, Nar, 43, 289

Deffayet C., 2001, Physics Letters B, 502, 199

Dunkley J., et al., 2009, ApJS, 180, 306

Durrer R., Maartens R., 2008, ArXiv e-prints

Dvali G., Gabadadze G., Kolanović M., Nitti F., 2001, PhRvD, 64, 084004

Dvali G., Turner M. S., 2003, ArXiv Astrophysics e-prints

Einstein A., 1916, Annalen der Physik, 354, 769

Eisenstein D. J., et al., 2005, ApJ, 633, 560

Elgarøy Ø., Multamäki T., 2006, Journal of Cosmology and Astro-Particle Physics, 9, 2

Etherington I. M. H., 1933, Philosophical Magazine, 15, 761

Fairbairn M., Goobar A., 2006, Physics Letters B, 642, 432

Faraoni V., Jensen M. N., Theuerkauf S. A., 2006, Classical and Quantum Gravity, 23, 4215

Fay S., Tavakol R., 2006, PhRvD, 74, 083513

Fay S., Tavakol R., Tsujikawa S., 2007, PhRvD, 75, 063509

Filippenko A. V., 1997a, ARAA, 35, 309

Filippenko A. V., 1997b, in Ruiz-Lapuente P., Canal R., Isern J., eds, Thermonuclear Supernovae Vol. 486 of NATO ASIC Proc., Type Ia supernovae: observational overview. Kluwer Academic Publishers, Dordrecht, pp 1–32

Filippenko A. V., Li W. D., Treffers R. R., Modjaz M., 2001, in Paczynski B., Chen W.-P., Lemme C., eds, IAU Colloq. 183: Small Telescope Astronomy on Global Scales Vol. 246 of Astronomical Society of the Pacific Conference Series, The Lick Observatory Supernova Search with the Katzman Automatic Imaging Telescope. pp 121–+

Filippenko A. V., Richmond M. W., Matheson T., Shields J. C., Burbidge E. M., Cohen R. D., Dickinson M., Malkan M. A., Nelson B., Pietz J., Schlegel D., Schmeer P., Spinrad H., Steidel C. C., Tran H. D., Wren W., 1992, ApJL, 384, L15

Filippenko A. V., Shields J. C., Wheeler J. C., Harkness R. P., McNaught R. H., 1986, IAU Circ., 4288, 1

Folatelli G., et al., 2010, AJ, 139, 120

Freeman P. E., Newman J. A., Lee A. B., Richards J. W., Schafer C. M., 2009, MNRAS, 398, 2012

Freese K., Adams F. C., Frieman J. A., Mottola E., 1987, Nuclear Physics B, 287, 797

Frieman J. A., 1996, Comments on Astrophysics, 18, 323

Frieman J. A., Hill C. T., Stebbins A., Waga I., 1995, Physical Review Letters, 75, 2077

Frieman J. A., Turner M. S., Huterer D., 2008, ARAA, 46, 385

Fukugita M., Ichikawa T., Gunn J. E., Doi M., Shimasaku K., Schneider D. P., 1996, AJ, 111, 1748

Gallagher J. S., Garnavich P. M., Caldwell N., Kirshner R. P., Jha S. W., Li W., Ganeshalingam M., Filippenko A. V., 2008, ApJ, 685, 752

Gamezo V. N., Khokhlov A. M., Oran E. S., Chtchelkanova A. Y., Rosenberg R. O., 2003, Science, 299, 77

Garavini G., et al., 2007, A&A, 470, 411

Garnavich P. M., et al., 1998, ApJL, 493, L53+

Goldhaber G., et al., 1997, in Ruiz-Lapuente P., Canal R., Isern J., eds, NATO ASIC Proc. 486: Thermonuclear Supernovae Observation of cosmological time dilation using Type Ia supernovae as clocks. pp 777–+

Goldhaber G., et al., 2001, ApJ, 558, 359

Goobar A., 2008, ApJL, 686, L103

Goobar A., Leibundgut B., 2011, Annual Review of Nuclear and Particle Science, 61, 251

Guimarães A. C. C., Cunha J. V., Lima J. A. S., 2009, ArXiv e-prints

Guo Z.-K., Zhu Z.-H., Alcaniz J. S., Zhang Y.-Z., 2006, ApJ, 646, 1

Guth A. H., 1981, PhRvD, 23, 347

Guy J., Astier P., Nobili S., Regnault N., Pain R., 2005, A&A, 443, 781

Guy J., et al., 2007, A&A, 466, 11

Hachinger S., Mazzali P. A., Taubenberger S., Fink M., Pakmor R., Hillebrandt W., Seitenzahl I. R., 2012, MNRAS, 427, 2057

Hamuy M., et al., 1993, AJ, 106, 2392

Hamuy M., et al., 1994, AJ, 108, 2226

Hamuy M., et al., 2006, PASP, 118, 2

Hamuy M., Phillips M. M., Maza J., Suntzeff N. B., Schommer R. A., Aviles R., 1995, AJ, 109, 1

Hamuy M., Phillips M. M., Suntzeff N. B., Maza J., González L. E., Roth M., Krisciunas K., Morrell N., Green E. M., Persson S. E., McCarthy P. J., 2003, Nature, 424, 651

Hamuy M., Phillips M. M., Suntzeff N. B., Schommer R. A., Maza J., Aviles R., 1996, AJ, 112, 2391

Hansen S. H., Macció A. V., Romano-Diaz E., Hoffman Y., Brüggen M., Scannapieco E., Stinson G. S., 2011, ApJ, 734, 62

Harkness R., 1991, in Woosley S. E., ed., Supernovae A Comparison of Carbon Deflagration Models for Supernova Type-Ia. pp 454–+

Harrison E. R., 1970, PhRvD, 1, 2726

Haugbølle T., Hannestad S., Thomsen B., Fynbo J., Sollerman J., Jha S., 2007, ApJ, 661, 650

Hayden B., Garnavich P., Survey C. S., 2012, in American Astronomical Society Meeting Abstracts Vol. 219 of American Astronomical Society Meeting Abstracts, Host Galaxies Near And Far: The Candels Sn Survey. p. 429.01

Hicken M., Challis P., Kirshner R. P., Modjaz M., Wood-Vasey M., Berlind P., Calkins M., Stubbs C., Matheson T., Rest A., Jha S., 2006, in American Astronomical Society Meeting Abstracts Vol. 208 of American Astronomical Society Meeting Abstracts, CFA Supernova Observing Program and Light Curves. p. 72.04

Hicken M., Wood-Vasey W. M., Blondin S., Challis P., Jha S., Kelly P. L., Rest A., Kirshner R. P., 2009a, ApJ, 700, 1097

Hicken M., Wood-Vasey W. M., Blondin S., Challis P., Jha S., Kelly P. L., Rest A., Kirshner R. P., 2009b, ApJ, 700, 1097

Hilbert D., 1924, MatAnn, 92, 1

Hillebrandt W., Kromer M., Röpke F. K., Ruiter A. J., 2013, Frontiers of Physics, 8, 116

Hillebrandt W., Niemeyer J. C., 2000, ARAA, 38, 191

Hinshaw G., et al., 2012, ArXiv e-prints

Höflich P., Khokhlov A., 1996, ApJ, 457, 500

Holsclaw T., Alam U., Sansó B., Lee H., Heitmann K., Habib S., Higdon D., 2010, Physical Review Letters, 105, 241302

Holtzman J. A., et al., 2008, AJ, 136, 2306

Hook I. M., et al., 2005, AJ, 130, 2788

Howell D. A., et al., 2005, ApJ, 634, 1190

Hoyle F., Fowler W. A., 1960, ApJ, 132, 565

Hsiao E. Y., Conley A., Howell D. A., Sullivan M., Pritchet C. J., Carlberg R. G., Nugent P. E., Phillips M. M., 2007, ApJ, 663, 1187

Hu W., Sawicki I., 2007, PhRvD, 76, 064004

Hubble E. P., 1936, Realm of the Nebulae. Yale University Press

Hui L., Greene P. B., 2006, PhRvD, 73, 123526

Huterer D., Peiris H. V., 2007, PhRvD, 75, 083503

Huterer D., Starkman G., 2003, Physical Review Letters, 90, 031301

Huterer D., Turner M. S., 1999, PhRvD, 60, 081301

Huterer D., Turner M. S., 2000, PhRvD, 62, 063503

Iocco F., Mangano G., Miele G., Pisanti O., Serpico P. D., 2009, PhRep, 472, 1

Ishida E. E. O., de Souza R. S., 2011, A&A, 527, A49

Ishida E. E. O., de Souza R. S., Ferrara A., 2011, MNRAS, 418, 500

Jeffery D. J., Branch D., Baron E., 2006, ArXiv Astrophysics e-prints

Jeffery D. J., Leibundgut B., Kirshner R. P., Benetti S., Branch D., Sonneborn G., 1992, ApJ, 397, 304

Jha S., et al., 1999, ApJS, 125, 73

Jha S., et al., 2006, AJ, 131, 527

Jha S., Riess A. G., Kirshner R. P., 2007, ApJ, 659, 122

John M. V., 2005, ApJ, 630, 667

Jollife I., 2002, A&A

Kaiser N., Pan-STARRS Team 2002, in American Astronomical Society Meeting Abstracts Vol. 34 of Bulletin of the American Astronomical Society, The Pan-STARRS Optical Survey Telescope Project. p. 122.07

Kasen D., 2006, ApJ, 649, 939

Kasen D., Woosley S. E., 2007, ApJ, 656, 661

Kelly P. L., Hicken M., Burke D. L., Mandel K. S., Kirshner R. P., 2010, ApJ, 715, 743

Kessler R., Bernstein J. P., Cinabro D., Dilday B., Frieman J. A., Jha S., Kuhlmann S., Miknaitis G., Sako M., Taylor M., Vanderplas J., 2009, PASP, 121, 1028

Kessler R., et al., 2009, ApJS, 185, 32

Khokhlov A. M., 1991, A&A, 245, 114

Kim A., Goobar A., Perlmutter S., 1996, PASP, 108, 190

Kim A. G., Miquel R., 2006, Astroparticle Physics, 24, 451

Knop R. A., et al., 2003, ApJ, 598, 102

Komatsu E., et al., 2009, ApJS, 180, 330

Komatsu E., et al., 2011, ApJS, 192, 18

Kowal C. T., 1968, AJ, 73, 1021

Kowalski M., et al., 2008, ApJ, 686, 749

Krisciunas K., Phillips M. M., Stubbs C., Rest A., Miknaitis G., Riess A. G., Suntzeff N. B., Roth M., Persson S. E., Freedman W. L., 2001, AJ, 122, 1616

Krisciunas K., Phillips M. M., Suntzeff N. B., 2004, ApJL, 602, L81

Kuchner M. J., Kirshner R. P., Pinto P. A., Leibundgut B., 1994, ApJL, 426, L89

Larson D., et al., 2011, ApJS, 192, 16

Law N. M., et al., 2009, PASP, 121, 1395

Leibundgut B., 2000, A&ApRv, 10, 179

Leibundgut B., 2008, General Relativity and Gravitation, 40, 221

Leibundgut B., et al., 1993, AJ, 105, 301

Leibundgut B., Pinto P. A., 1992, ApJ, 401, 49

Leibundgut B., Schommer R., Phillips M., Riess A., Schmidt B., Spyromilio J., Walsh J., Suntzeff N., Hamuy M., Maza J., Kirshner R. P., Challis P., Garnavich P., Smith R. C., Dressler A., Ciardullo R., 1996, ApJL, 466, L21+

Leitch E. M., Kovac J. M., Pryke C., Carlstrom J. E., Halverson N. W., Holzapfel W. L., Dragovan M., Reddall B., Sandberg E. S., 2002, Nature, 420, 763

Li W., Leaman J., Chornock R., Filippenko A. V., Poznanski D., Ganeshalingam M., Wang X., Modjaz M., Jha S., Foley R. J., Smith N., 2011, MNRAS, 412, 1441

Li W. D., Filippenko A. V., Riess A. G., Treffers R. R., Hu J. Y., Qiu Y. L., 2000, in Holt S. S., Zhang W. W., eds, Cosmic Explosions: Tenth Astrophysics Conference Vol. 522 of AIP Conference Proceedings, A high peculiarity rate for Type Ia SNe. American Institute of Physics, Melville, New York, pp 91–94

Liang N., Zhu Z.-H., 2011, Research in Astronomy and Astrophysics, 11, 497

Liddle A. R., Lyth D. H., Viana P. T. P., White M., 1996, MNRAS, 282, 281

Lidman C., others The Supernova Cosmology Project 2005, A&A, 430, 843

Linde A. D., 1982, Physics Letters B, 108, 389

Linder E. V., 2003, Physical Review Letters, 90, 091301

LSST Science Collaboration Abell P. A., Allison J., Anderson S. F., Andrew J. R., Angel J. R. P., Armus L., Arnett D., Asztalos S. J., Axelrod T. S., et al. 2009, ArXiv e-prints

Maartens R., Majerotto E., 2006, PhRvD, 74, 023004

Mandel K. S., Wood-Vasey W. M., Friedman A. S., Kirshner R. P., 2009, ApJ, 704, 629

Marriner J., Bernstein J. P., Kessler R., Lampeitl H., Miquel R., Mosher J., Nichol R. C., Sako M., Schneider D. P., Smith M., 2011, ApJ, 740, 72

Matheson T., et al., 2005, AJ, 129, 2352

Maturi M., Mignone C., 2009, ArXiv e-prints

Mazzali P. A., Chugai N., Turatto M., Lucy L. B., Danziger I. J., Cappellaro E., della Valle M., Benetti S., 1997, MNRAS, 284, 151

Meikle W. P. S., et al. 1997, in Ruiz-Lapuente P., Canal R., Isern J., eds, NATO ASIC Proc. 486: Thermonuclear Supernovae Infrared and optical spectroscopy of Type Ia Supernovae. pp 53–+

Mignone C., 2009, PhD thesis, Univ. Heidelberg

Mignone C., Bartelmann M., 2008, A&A, 481, 295

Miknaitis G., et al., 2007, ApJ, 666, 674

Minkowski R., 1941, PASP, 53, 224

Minkowski R., 1964, ARAA, 2, 247

Narlikar J. V., 2002, An introduction to cosmology. Cambridge University Press

Niemeyer J. C., Hillebrandt W., Woosley S. E., 1996, ApJ, 471, 903

Nobili S., Goobar A., 2008, A&A, 487, 19

Noterdaeme P., Petitjean P., Srianand R., Ledoux C., López S., 2011, A&A, 526, L7

Nugent P., Kim A., Perlmutter S., 2002, PASP, 114, 803

Olive K. A., 1990, PhRep, 190, 307

Olmo G. J., 2007, PhRvD, 75, 023511

Ostriker J. P., Steinhardt P. J., 1995, Nature, 377, 600

Pakmor R., Kromer M., Taubenberger S., Sim S. A., Röpke F. K., Hillebrandt W., 2012, ApJL, 747, L10

Palatini A., 1919, in Bergmann P. G., de Sabbata V., eds, NATO ASIB Proc. 58: Cosmology and Gravitation: Spin, Torsion, Rotation, and Supergravity Invariant Deduction of the Gravitational Equations from the Principle of Hamilton. p. 479

Patat F., Benetti S., Cappellaro E., Danziger I. J., della Valle M., Mazzali P. A., Turatto M., 1996, MNRAS, 278, 111

Peacock J. A., 1999, Cosmological Physics. Cambridge University Press

Peebles P. J. E., 1993, Principles of physical cosmology. Princeton University Press

Peebles P. J. E., Yu J. T., 1970, ApJ, 162, 815

Percival W. J., Cole S., Eisenstein D. J., Nichol R. C., Peacock J. A., Pope A. C., Szalay A. S., 2007, MNRAS, 381, 1053

Perivolaropoulos L., 2005, PhRvD, 71, 063503

Perlmutter S., et al., 1995, ApJL, 440, L41

Perlmutter S., others Couch W. J., The Supernova Cosmology Project 1997, ApJ, 483, 565

Perlmutter S., others The Supernova Cosmology Project 1999, ApJ, 517, 565

Perlmutter S., Schmidt B. P., 2003, in Weiler K., ed., Supernovae and Gamma-Ray Bursters Vol. 598 of Lecture Notes in Physics, Berlin Springer Verlag, Measuring Cosmology with Supernovae. pp 195–217

Phillips M. M., 1993, ApJL, 413, L105

Phillips M. M., Lira P., Suntzeff N. B., Schommer R. A., Hamuy M., Maza J., 1999, AJ, 118, 1766

Planck Collaboration Ade P. A. R., Aghanim N., Armitage-Caplan C., Arnaud M., Ashdown M., Atrio-Barandela F., Aumont J., Baccigalupi C., Banday A. J., et al. 2013, ArXiv e-prints

Pratt J., 1976, AStat, 4, 501

Randall L., Sundrum R., 1999, Physical Review Letters, 83, 4690

Rapetti D., Allen S. W., Amin M. A., Blandford R. D., 2007, MNRAS, 375, 1510

Rapetti D., Allen S. W., Weller J., 2005, MNRAS, 360, 555

Reinecke M., Hillebrandt W., Niemeyer J. C., Klein R., Gröbl A., 1999, A&A, 347, 724

Reinecke M., Hillebrandt W., Niemeyer J. C., Röpke F., Schmidt W., Sauer D., 2002, in Hillebrandt W., Müller E., eds, Proceedings of the 11th Workshop on "Nuclear Astrophysics", Ringberg Castle MPA/P13, Recent progress in multidimensional SN Ia simulations. Max-Planck-Institut für Astrophysik, Garching, pp 54–56

Riess A. G., et al., 1998, AJ, 116, 1009

Riess A. G., et al., 2000, ApJ, 536, 62

Riess A. G., et al., 2004, ApJ, 607, 665

Riess A. G., et al., 2007, ApJ, 659, 98

Riess A. G., Filippenko A. V., Leonard D. C., Schmidt B. P., Suntzeff N., Phillips M. M., Schommer R., Clocchiatti A., Kirshner R. P., Garnavich P., Challis P., Leibundgut B., Spyromilio J., Smith R. C., 1997, AJ, 114, 722

Riess A. G., Filippenko A. V., Li W., Treffers R. R., Schmidt B. P., Qiu Y., Hu J., Armstrong M., Faranda C., Thouvenot E., Buil C., 1999, AJ, 118, 2675

Riess A. G., Livio M., 2006, ApJ, 648, 884

Riess A. G., Macri L., Casertano S., Lampeitl H., Ferguson H. C., Filippenko A. V., Jha S. W., Li W., Chornock R., 2011, ApJ, 730, 119

Riess A. G., Press W. H., Kirshner R. P., 1995, ApJL, 445, L91

Riess A. G., Press W. H., Kirshner R. P., 1996, ApJ, 473, 88

Roberts M. S., Rots A. H., 1973, A&A, 26, 483

Robertson H. P., 1933, Reviews of Modern Physics, 5, 62

Röpke F. K., Hillebrandt W., 2005, A&A, 429, L29

Röpke F. K., Hillebrandt W., Niemeyer J. C., Woosley S. E., 2006, A&A, 448, 1

Röpke F. K., Woosley S. E., Hillebrandt W., 2007, ApJ, 660, 1344

Rubin V. C., Ford W. K. J., . Thonnard N., 1980, ApJ, 238, 471

Ruiz-Lapuente P., Cappellaro E., Turatto M., Gouiffes C., Danziger I. J., della Valle M., Lucy L. B., 1992, ApJL, 387, L33

Sachs R. K., Wolfe A. M., 1967, ApJ, 147, 73

Sahni V., 2002, Classical and Quantum Gravity, 19, 3435

Sahni V., Starobinsky A., 2000, International Journal of Modern Physics D, 9, 373

Sako M., et al., 2008, AJ, 135, 348

Sandage A., 1961, ApJ, 134, 916

Sandage A., 1988, ApJ, 331, 583

Sarkar D., Amblard A., Cooray A., Holz D. E., 2008, ApJL, 684, L13

Schmidt B. P., et al., 1998, ApJ, 507, 46

Schwarzschild K., 1916, Abh. Konigl. Preuss. Akad. Wissenschaften Jahre 1906,92, Berlin,1907, pp 189–196

Seikel M., Clarkson C., Smith M., 2012, JCap, 6, 36

Seikel M., Schwarz D. J., 2009, Journal of Cosmology and Astro-Particle Physics, 2, 24

Seo H.-J., Eisenstein D. J., 2003, ApJ, 598, 720

Shafieloo A., Alam U., Sahni V., Starobinsky A. A., 2006, MNRAS, 366, 1081

Shafieloo A., Kim A. G., Linder E. V., 2012, PhRvD, 85, 123530

Shafieloo A., Souradeep T., Manimaran P., Panigrahi P. K., Rangarajan R., 2007, PhRvD, 75, 123502

Shapiro C., Turner M. S., 2006, ApJ, 649, 563

Sievers J. L., et al., 2013, ArXiv e-prints

Sigurdson K., Doran M., Kurylov A., Caldwell R. R., Kamionkowski M., 2004, PhRvD, 70, 083501

Silk J., 1968, ApJ, 151, 459

Simon J. D., et al., 2009, ApJ, 702, 1157

Simpson F., Bridle S., 2006, PhRvD, 73, 083001

Smoot G. F., et al., 1992, ApJL, 396, L1

Sneden C., Gehrz R. D., Hackwell J. A., York D. G., Snow T. P., 1978, ApJ, 223, 168

Song Y.-S., Peiris H., Hu W., 2007, PhRvD, 76, 063517

Sotiriou T. P., Liberati S., 2007, Annals of Physics, 322, 935

Springel V., 2005, MNRAS, 364, 1105

Starobinsky A. A., 1980, Physics Letters B, 91, 99

Starobinsky A. A., 1998, Soviet Journal of Experimental and Theoretical Physics Letters, 68, 757

Stehle M., Mazzali P. A., Benetti S., Hillebrandt W., 2005, MNRAS, 360, 1231

Steigman G., Romano D., Tosi M., 2007, MNRAS, 378, 576

Steinhardt P. J., 1999, Physics Letters B, 462, 41

Stern D., Jimenez R., Verde L., Kamionkowski M., Stanford S. A., 2010, JCap, 2, 8

Stritzinger M., et al., 2002, AJ, 124, 2100

Stubbs C. W., Tonry J. L., 2006, ApJ, 646, 1436

Sullivan M., et al., 2003, MNRAS, 340, 1057

Sullivan M., et al., 2006, ApJ, 648, 868

Sullivan M., et al., 2010, MNRAS, 406, 782

Sullivan M., et al., 2011, ApJ, 737, 102

Suntzeff N. B., 1996, in McCray R., Wang Z., eds, Supernovae and Supernova Remnants Vol. 145 of IAU Colloq., Observations of Type Ia supernovae. Cambridge University Press, Cambridge, pp 41–48

Sunyaev R. A., 1978, in Longair M. S., Einasto J., eds, Large Scale Structures in the Universe Vol. 79 of IAU Symposium, Fluctuations of the microwave background radiation. pp 393–402

Sunyaev R. A., Zeldovich Y. B., 1970, Astr. Sp. Sc., 7, 3

Suzuki N., others Supernova Cosmology Project T., 2012, ApJ, 746, 85

Tammann G. A., 1978, Memorie della Societa Astronomica Italiana, 49, 315

Tammann G. A., Leibundgut B., 1990, A&A, 236, 9

Tang J.-Y., Weller J., Zablocki A., 2006, ArXiv Astrophysics e-prints

Taylor A. N., Dye S., Broadhurst T. J., Benitez N., van Kampen E., 1998, ApJ, 501, 539

Tegmark M., 2002, PhRvD, 66, 103507

The Dark Energy Survey Collaboration 2005, ArXiv Astrophysics e-prints

Thomas S. A., Abdalla F. B., Weller J., 2009, MNRAS, 395, 197

Tonry J. L., et al., 2003, ApJ, 594, 1

Tripp R., 1998, A&A, 331, 815

Truran J. W., Arnett W. D., Cameron A. G. W., 1967, Canadian Journal of Physics, 45, 2315

Turatto M., 2003, in Weiler K., ed., Supernovae and Gamma-Ray Bursters Vol. 598 of Lecture Notes in Physics, Berlin Springer Verlag, Classification of Supernovae. pp 21–36

Turatto M., Benetti S., Cappellaro E., Danziger I. J., Della Valle M., Gouiffes C., Mazzali P. A., Patat F., 1996, MNRAS, 283, 1

Turatto M., Cappellaro E., Benetti S., 1994, AJ, 108, 202

Turner M. S., 1983, PhRvD, 28, 1243

Turner M. S., 1991, Physica Scripta Volume T, 36, 167

Turner M. S., 1997, Nuclear Physics A, 621, 522

Turner M. S., 1999, in Gibson B. K., Axelrod R. S., Putman M. E., eds, The Third Stromlo Symposium: The Galactic Halo Vol. 165 of Astronomical Society of the Pacific Conference Series, Dark Matter and Dark Energy in the Universe. p. 431

Turner M. S., Huterer D., 2007, Journal of the Physical Society of Japan, 76, 111015

Turner M. S., Riess A. G., 2002, ApJ, 569, 18

Turner M. S., Steigman G., Krauss L. M., 1984, Physical Review Letters, 52, 2090

Turner M. S., White M., 1997, PhRvD, 56, 4439

Walker A. G., 1933, MNRAS, 94, 159

Wang Y., 1999, ApJ, 525, 651

Wang Y., Chuang C.-H., Mukherjee P., 2012, PhRvD, 85, 023517

Wang Y., Tegmark M., 2005, PhRvD, 71, 103513

Weinberg D. H., Davé R., Katz N., Kollmeier J. A., 2003, in Holt S. H., Reynolds C. S., eds, The Emergence of Cosmic Structure Vol. 666 of American Institute of Physics Conference Series, The Lyman-α Forest as a Cosmological Tool. pp 157–169

Weinberg D. H., Mortonson M. J., Eisenstein D. J., Hirata C., Riess A. G., Rozo E., 2012, ArXiv e-prints

Wetterich C., 1995, A&A, 301, 321

Wetterich C., 1998, General Relativity and Gravitation, 30, 159

Wheeler J. C., Harkness R. P., 1990, Reports of Progress in Physics, 53, 1467

Wheeler J. C., Levreault R., 1985, ApJL, 294, L17

Wilson O. C., 1939, ApJ, 90, 634

Wood-Vasey W. M., et al., 2004, New Astronomy Review, 48, 637

Wood-Vasey W. M., et al., 2007, ApJ, 666, 694

York D. G. t. S., et al., 2000, AJ, 120, 1579

Zehavi I., Riess A. G., Kirshner R. P., Dekel A., 1998, ApJ, 503, 483

Zeldovich Y. B., 1972, MNRAS, 160, 1P

Zwicky F., 1937, ApJ, 86, 217